ETH zürich

Diss. ETH No. 29187

Roman Indergand

Finite-Temperature Phase-Field Investigation of Switching Kinetics in Ferroelectric Ceramics

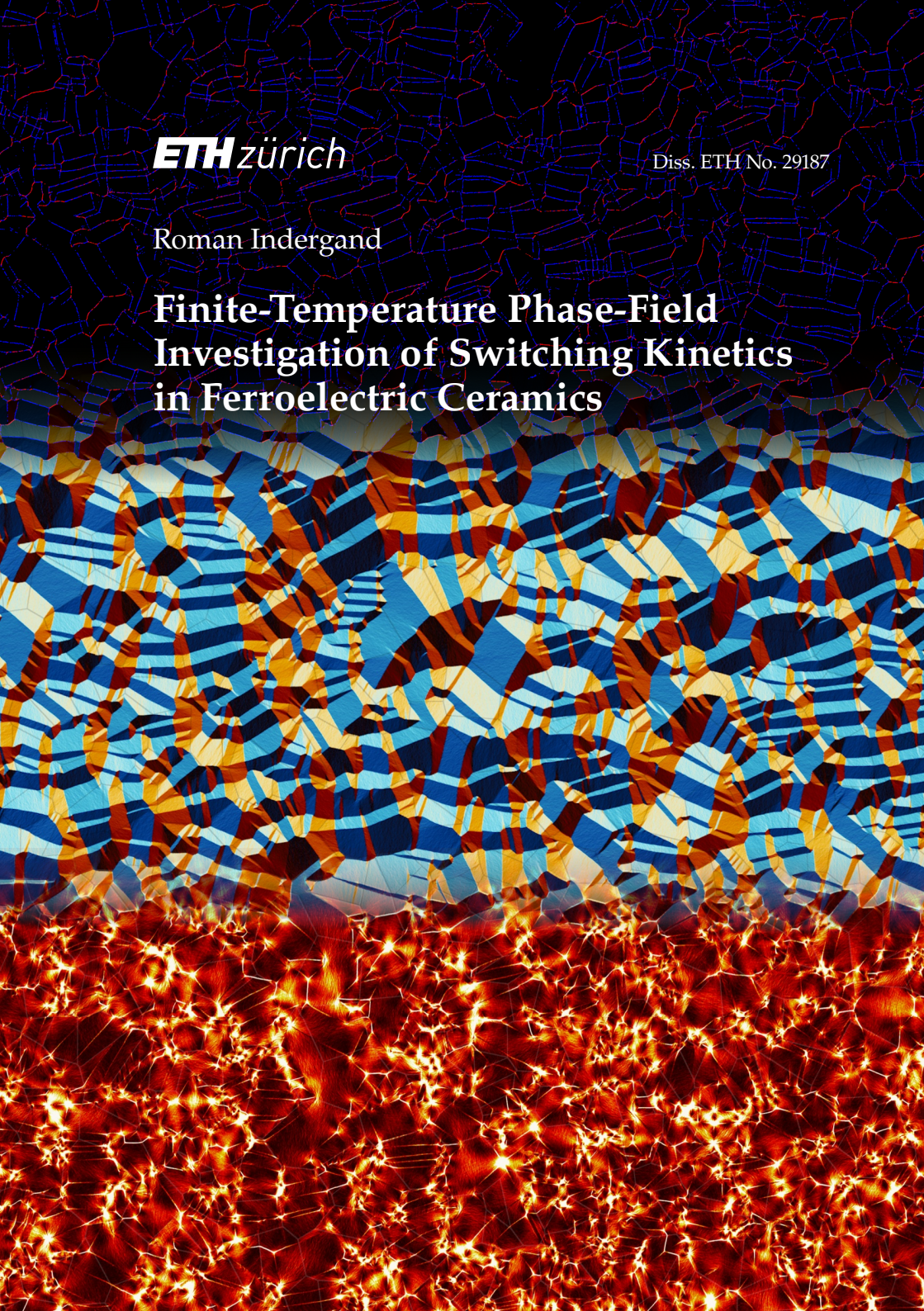

Front cover: Ferroelectric microstructure of a tetragonal PZT ceramic computed with the finite-temperature phase-field model, showing ferroelectric domain walls (upper third), domain pattern formations visualized by the polarization orientation (middle third), and local stress concentrations indicated by the elastic strain energy (lower third).

A digital version of this thesis is available for download at
https://doi.org/10.3929/ethz-b-000620715

DISS. ETH NO. 29187

FINITE-TEMPERATURE PHASE-FIELD INVESTIGATION OF SWITCHING KINETICS IN FERROELECTRIC CERAMICS

A dissertation submitted to attain the degree of

DOCTOR OF SCIENCES of ETH ZURICH
(Dr. sc. ETH Zurich)

presented by

ROMAN INDERGAND
MSc ETH ME, ETH Zurich

born on 29 August 1986

accepted on the recommendation of

Prof. Dr. Dennis M. Kochmann, examiner
Prof. Dr. Nicola A. Spaldin, co-examiner
Prof. Dr. Martín I. Idiart, co-examiner
Prof. Dr. Laurent Guin, co-examiner

2023

DOI: 10.3929/ethz-b-000620715

ABSTRACT

Ferroelectric materials exhibit an atomic-level electric dipole moment, known as spontaneous polarization, which can be reoriented by an applied electric field. Furthermore, ferroelectrics tend to form a microstructure consisting of regions of identical polarization orientation, called domains, separated by domain walls. This thesis aims to enhance the predictability of ferroelectric material response at the macroscale by gradually refining our understanding of the kinetics of polarization switching at lower length scales. This is achieved by examining the intricate interaction between ferroelectric microstructure evolution, which occurs through the nucleation and growth of domains, and structural defects, such as pores and grain boundaries. In addition, finite-temperature effects play a crucial role in the formation and evolution of ferroelectric domain patterns. To accurately predict the effective material behavior at the device-level, it is essential to consider all of these factors in our models.

The first part of this thesis details a novel finite-temperature constitutive model for ferroelectric lead zirconate titanate (PZT) ceramics that accounts for the temperature dependence of the first-principles-informed polarization potential and the effect of thermal lattice vibrations. Based on statistical mechanics, a temperature-dependent Gaussian noise is introduced to the evolution equation for the polarization, which mimics atomic-level lattice vibrations at the continuum scale. The theoretical derivation and Fourier-based implementation are discussed, along with numerical examples and experimental observations. Results show that thermal fluctuations can induce branching of existing domains and nucleation of new domains. These finite-temperature effects stimulate the effective switching kinetics and promote the formation of realistic domain patterns, reminiscent of ferroelectric microstructure observed in experiments.

The second part of the thesis investigates the combined effect of porosity and temperature on porous, single-crystalline PZT by utilizing the developed finite-temperature model. Circular pores are modeled, and their impact on an approaching ferroelectric domain wall is investigated. The results show that larger pore sizes and higher densities impede the kinetics of domain walls, while an increase in temperature mitigates the pinning

effect of pores, enhancing the mobility of domain walls. These findings are generally consistent with experimental reports and emphasize the importance of considering finite-temperature effects on effective switching kinetics.

The third part of this thesis presents a high-resolution phase-field analysis of complex domain pattern formation in tetragonal PZT ceramics, showing well-known lamellar bands within grains and wedged-shaped domains near grain boundaries. The simulations of polycrystalline PZT, which combined more than 12,000 grain samples, revealed distinct correlations between grain orientation and the grain-averaged polarization, strain, and domain density that are consistent with experimental reports and theoretical models. In addition, we discuss novel computational techniques for domain wall identification and tracking, and demonstrate their ability to assess the domain wall density and effective switching mechanism of an evolving ferroelectric microstructure.

In summary, the newly introduced models and findings help predict and understand domain switching mechanisms in ferroelectric materials by considering crucial effects of structural defects and temperature. The finite-temperature phase-field framework presents a powerful tool to efficiently studying the lower-scale mechanics of domain evolution, which play a key role in the macroscopic switching kinetics and are challenging to capture with experimental techniques in this detail.

ZUSAMMENFASSUNG

Ferroelektrische Materialien besitzen ein elektrisches Dipolmoment auf atomarer Ebene, das als spontane Polarisation bezeichnet wird. Die Polarisation kann durch ein angelegtes elektrisches Feld beliebig zwischen den polaren Achsen des ferroelektrischen Kristalles umgepolt werden. Des Weiteren bildet sich in Ferroelektrika eine Mikrostruktur, bestehend aus Regionen mit identischer Orientierung der Polarisation, welche als Domäne bezeichnet werden und durch Domänenwände getrennt sind. Das Ziel der vorliegenden Dissertation ist es, die Vorhersagbarkeit der ferroelektrischen Materialantwort auf der Makroebene zu verbessern, indem die Kinetik der Polarisationsumschaltung auf niedrigeren Längenskalen untersucht wird, um den derzeitigen Wissensstand dazu zu erweitern. Dies wird durch die Erforschung der komplexen Wechselwirkung zwischen der Evolution der ferroelektrischen Mikrostruktur, die durch die Keimbildung und das Wachstum von ferroelektrischen Domänen entsteht, und strukturellen Defekten, wie Poren und Korngrenzen, erreicht. Darüber hinaus spielen Temperatureffekte eine entscheidende Rolle bei der Bildung und Evolution ferroelektrischer Domänstrukturen. Um das effektive Materialverhalten in ferroelektrischen Anwendungen möglichst präzise vorhersagen zu können, ist es unerlässlich, all diese Faktoren in unseren Modellen zu berücksichtigen.

Der erste Teil dieser Dissertation beschreibt ein innovatives Konstitutivmodell für ferroelektrische Blei-Zirkonat-Titanat (PZT) Keramiken, das die Temperaturabhängigkeit des Polarisationspotenzials und die Auswirkungen thermischer Gitterschwingungen berücksichtigt. Auf der Grundlage der Statistischen Mechanik wird ein temperaturabhängiges Gauß'sches Rauschen in die Evolutionsgleichung für die Polarisation eingeführt, welches auf der Kontinuumsebene Gitterschwingungen nachahmt, die auf der atomarer Ebene auftreten. Die theoretische Herleitung und die Fourierbasierte Implementierung werden zusammen mit numerischen Beispielen und experimentellen Beobachtungen diskutiert. Die Ergebnisse zeigen, dass thermische Schwingungen zur Verzweigung bestehender Domänen und zur Keimbildung neuer Domänen führen können. Diese Temperatureffekte stimulieren die effektive Umschaltkinetik und fördern die Bildung

realistischer Domänstrukturen, die mit den beobachteten ferroelektrische Mikrostrukturen aus Experimenten vergleichbar sind.

Der zweite Teil der Dissertation untersucht die kombinierte Wirkung von Porosität und Temperatur auf poröses, einkristallines PZT unter Verwendung des entwickelten temperaturabhängigen Konstitutivmodells. Es werden kreisförmige Poren modelliert und ihr Einfluss auf eine sich nähernde ferroelektrische Domänenwand untersucht. Die Ergebnisse zeigen, dass größere Porendurchmesser und höhere Porendichten die Kinetik der Domänenwände behindern, während andererseits ein Temperaturanstieg den Pinning-Effekt der Poren abschwächt und die Mobilität der Domänenwände erhöht. Diese Ergebnisse stimmen im Allgemeinen mit experimentellen Berichten überein und unterstreichen die Bedeutung der Berücksichtigung von Temperatureffekten auf die effektive Umschaltkinetik der Polarisation.

Im dritten Teil dieser Dissertation wird eine umfangreiche und hochauflösende Phasenfeldanalyse zur Bildung komplexer Domänenstrukturen in tetragonalen PZT-Keramiken vorgestellt, welche die typischen lamellenförmigen Strukturen innerhalb der Körner und keilförmige Strukturen nahe der Korngrenzen aufweist. Die Simulationsergebnisse zu polykristallinem PZT, die insgesamt mehr als 12'000 Körner umfassen, zeigen deutliche Korrelationen zwischen der Kornorientierung und der über das Korn gemittelten Polarisation, Dehnung und Domänendichte, die mit experimentellen Berichten und theoretischen Modellen gut übereinstimmen. Des Weiteren werden neue computergestützte Verfahren zur automatischen Identifizierung von Domänenwänden vorgestellt und deren Fähigkeit demonstriert, die Dichte von Domänenwänden und den effektiven Umschaltmechanismus einer sich ändernden ferroelektrischen Mikrostruktur zu bestimmen.

Insgesamt tragen die neu eingeführten Modelle und Erkenntnisse dazu bei, die Mechanismen der Domänenumschaltung in ferroelektrischen Materialien vorherzusagen und zu verstehen, indem die wichtigen Auswirkungen von Strukturdefekten und Temperatur berücksichtigt werden. Das temperaturabhängige Phasenfeldmodell stellt ein leistungsfähiges Werkzeug zur effizienten Untersuchung der Mechanik der Domänenentwicklung auf niedrigerer Längenskalen dar, die eine Schlüsselrolle in der makroskopischen Umschaltkinetik spielt und mit experimentellen Methoden nur schwer in diesem Detail zu erfassen ist.

ACKNOWLEDGEMENTS

First, I would like to express my deepest gratitude to Prof. Dennis Kochmann for his invaluable support throughout all these years. It has been a very enlightening journey that started with my Master's thesis in 2018 and eventually resulted in this dissertation. Dennis is a very open-minded person, an understanding supervisor, and an inspiring mentor. Thank you very much, Dennis, for having granted me this opportunity.

Next, I would like to extend my gratitude to my thesis committee. I am grateful for the support of my second supervisor, Prof. Nicola Spaldin, who taught me the basics of ferroelectrics in her lectures and was always ready to answer my questions. I have also appreciated honest feedback and advice from Prof. Laurent Guin during our weekly meetings and the fruitful discussions I have had with Prof. Martín Idiart during his visit at ETH Zürich; thank you all for sharing your expertise and knowledge with me.

Furthermore, I would like to express my appreciation of my fellow researchers at the Mechanics and Materials Lab for their support, encouragement, and the enjoyable moments we have shared together. I am especially thankful to Abbas Tutcuoglu, Siddhant Kumar, and Manuel Weberndorfer, who provided support with the computational implementation and optimization in C++. Special gratitude goes also to Vignesh Kannan and Hsu-Cheng Cheng for their kind advice and continuous support during my work toward the doctorate; it has been a pleasure working with you all.

Of course, this work would not have been possible without unwavering support from my friends and family. Their love and encouragement throughout my life allowed me to immerse myself unconditionally in my research, free from any burden. For this I am deeply grateful and would like to express my heartfelt thanks. I am also grateful to Kim Hays for her kind advice on the thesis text.

Finally, I would like to extend my appreciation for the financial support of the Swiss National Science Foundation (SNSF) and for the computational resources provided by the Euler cluster within the Swiss National Supercomputing Center (CSCS).

CONTENTS

1

INTRODUCTION

In this thesis, we investigate the material behaviour of a special type of active materials called *ferroelectrics*. Ferroelectric materials are among the most promising active, multifunctional materials. They demonstrate a variety of physical effects such as piezoelectricity (Curie & Curie, 1880), pyroelectricity (Brewster, 1824), electrocaloric (Olsen et al., 1985), electrooptic, and catalytic effects (Parravano, 1952), which have been studied and utilized in sensors, actuators, or micro- and nano-electromechanical systems. Their applications extend across aerospace, medicine, communication, automotive and military industries (Park et al., 2016; Uchino, 2009).

Since the discovery of ferroelectricity in 1921 (Valasek, 1921), numerous ferroelectric materials have been found, among which the family of perovskite oxides is the technically most relevant. At the Curie temperature, the crystallographic structure of perovskites exhibits a phase transition from a high-symmetry, cubic lattice to a lower-symmetry, e.g., tetrahedral, orthorhombic, and rhombohedral phase (Bernhard Jaffe, 1971; Jona et al., 1957; Shirane & Hoshino, 1954). As a result, individual ions shift from their centrosymmetric positions, which leads to spontaneous polarization and spontaneous strains below the Curie temperature (Lines & Glass, 2001). Above the Curie temperature, crystals are centrosymmetric; hence, the electric dipole vanishes in the absence of an applied electric field – a quality of the material referred to as paraelectricity. Below the Curie point, the atomic-level polarization of perovskite oxides is electrically alterable, and many are also mechanically alterable (Chaplya & Carman, 2001) – these properties are referred to as ferroelectricity and ferroelasticity, respectively.

At the mesoscale, long-range ordering of spontaneous polarization in adjacent unit cells leads to the formation of regions with homogeneous polarization orientation, which are called ferroelectric domains. In this regime, any microstructural rearrangement is accommodated by the nucleation and growth of an intricate network of ferroelectric domains, where Fig. 1.1 gives an illustrative overview of different ferroelectric microstructures. Although the observed microstructures show very different patterns, they all arise as a result of an energy relaxation of their respective systems, whose crystallo-

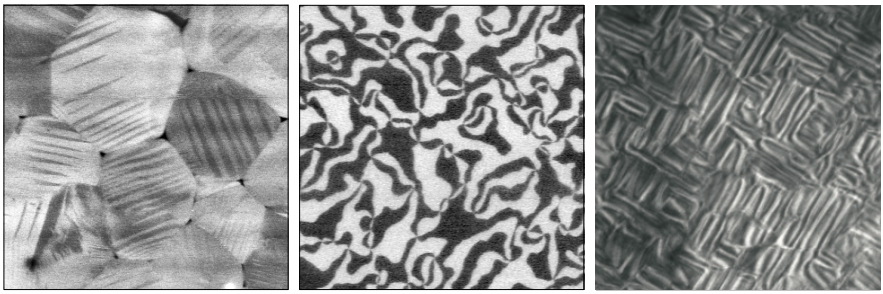

(a) (b) (c)

Figure 1.1: Examples of ferroelectric microstructures: (a) lamellar domain patterns in tetragonal $BaTiO_3$, (b) trimerization domain patterns in hexagonal $YMnO_3$ (Jungk et al., 2010), and (c) rectangular domain patterns in orthorhombic $TbMnO_3$ (Daumont et al., 2009). All images reprinted with permission. (a) Courtesy of V. Kannan, ETH Zürich, (b) reprinted from Jungk et al. (2010), with the permission of AIP Publishing, and (c) used with permission of IOP Publishing, Ltd from Daumont et al. (2009); permission conveyed through Copyright Clearance Center, Inc.

graphic structures are (a) tetragonal, (b) hexagonal, and (c) orthorhombic. The symmetry of the underlying crystal lattice apparently affects the way individual domains arrange themselves within ferroelectrics (for reasons of compatibility) (Fousek & Janovec, 1969; Janovec & Privratska, 2013).

Similar domain pattern formations can be observed in the microstructures of other members of the family of ferroic materials, to which ferroelectrics belong to. For instance, Fig. 1.2(a) shows striped patterns of ferroelastic domains in Cu-Ni martensite, reminiscent of ferroelectric laminates, depicted in Fig. 1.1(a). Other examples of ferromagnetic microstructures illustrate the link between domain pattern formation and macroscopic material behavior. On the one hand, domain structures in soft magnets, such as multiaxial SiFe electric steel, are driven by the principle of flux closure due to their weak magnetic anisotropy (Hubert & Schäfer, 2008), which becomes apparent by the typical vortex-like arrangements visible in Fig. 1.2(b). On the other hand, domain patterns in permanent magnets, such as uniaxial $Nd_2Fe_{14}B$, which exhibit high magnetic anisotropy, form intricate fine surface patterns due to gradual branching of domains in the interior and refinement towards the surface (Hubert & Schäfer, 2008), shown in Fig. 1.2(c).

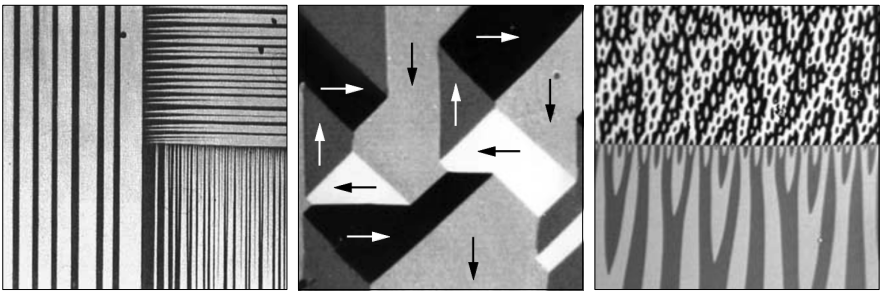

(a) (b) (c)

Figure 1.2: Micrographs of various natural patterns emerging in ferroic materials: (a) twin patterns of ferroelastic domains in Cu-Ni martensite (Abeyaratne & Knowles, 1991), (b) vortex patterns of ferromagnetic domains in cubic SiFe (Hubert & Schäfer, 2008), and (c) branching patterns of ferromagnetic domains in tetragonal NdFeB (Hubert & Schäfer, 2008), where the upper and lower half of the depicted pattern show the top and side view of the microstructure, respectively. All images reprinted with permission. (a) reprinted from Abeyaratne and Knowles (1991) © 1991 by permission of Informa UK Limited, trading as Taylor & Taylor & Francis Group, http://www.tandfonline.com, (b) reproduced from Hubert and Schäfer (2008) with permission from Springer Nature, and (c) reproduced from Hubert and Schäfer (2008) with permission from Springer Nature.

Besides its effect on the appearance of microstructures, the crystallographic lattice structure at the lower scales and the complex formation of ferroelastic and ferroelectric domain patterns have a great impact on the effective properties at the macroscale, such as the piezoelectric and dielectric constants in ferroelectric oxides (Cao & Randall, 1996; Janovec & Privratska, 2013; Lines & Glass, 2001; Pramanick et al., 2011). Therefore, a profound understanding of the origin and subsequent evolution of domain pattern formation is key to predicting realistic ferroelectric microstructures in order to improve the properties of existing and future ferroelectric materials.

The intricate coupling mechanisms between the lower-scales spontaneous polarization and the effective properties in ferroelectric devices require us to account for multiple length scales ranging from the atomic level across the polycrystalline mesoscale to the macroscopic device level, which makes it challenging to model the electromechanical behavior of ferroelectric oxides properly. Therefore, a broad range of models suitable for specific length scales exists, starting with *ab initio* atomistic calculations (subject to the

fundamental laws of quantum mechanics) at the lowest scales and progressing from continuum models (based on thermodynamic potentials) to phenomenological macroscale approaches (built on empirical observations). Here, we pursue multiscale modeling by utilizing inputs from atomistics to model the ferroelectric microstructure at the continuum scale in order to bridge the gap between zero-temperature energetics at the lower scales and the effective hysteresis of ferroelectric ceramics at the macroscopic device level.

1.1 INTRODUCTION TO FERROELECTRIC MATERIALS

1.1.1 *Material symmetry*

Various physical properties of crystalline materials, such as the material's anisotropy or its electromechanical and electrooptical coupling, are reflected in the symmetry of their underlying crystal structure, known as *crystallographic point group*. A point group is a set of symmetry operations (rotations, mirror planes, and inversions) that leaves the overall structure of the crystal unchanged, i.e., each atom maps to a position occupied by an atom of the same type prior to the transformation. Fig. 1.3 provides an overview of the 32 possible point groups of crystalline materials in three dimensions, which can be categorized into seven lattice systems: triclinic, monoclinic, orthorhombic, tetragonal, rhombohedral, hexagonal, and cubic, depicted in Fig. 1.4.

An important subgroup of the 32 point groups are the 21 *non-centrosymmetric* crystals, which possess no inversion point. Among those, 20 crystal classes can be polarized upon application of mechanical stress, known as *piezoelectric* point group (Lines & Glass, 2001). Crystals of the piezoelectric point group exhibit an electric dipole moment, called *polarization* when normalized by the volume, due to a non-centrosymmetric shift of the positive and negative centers of charge during the deformation of the unit cell, which is called *piezoelectric effect*. Both the piezoelectric effect and the inverse piezoelectric effect, i.e, the induction of mechanical strains under an applied electric field, are linear and reversible, i.e., the induced polarization and strains disappear upon removal of the applied mechanical and electric field, respectively.

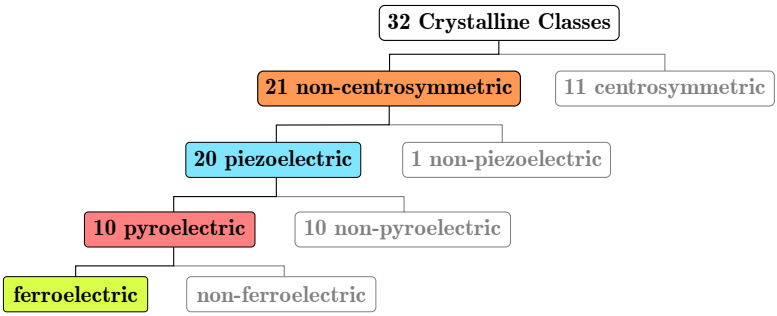

Figure 1.3: Crystalline classes showing the ferroelectric class (green) as a special subgroup of the 21 non-centrosymmetric crystal classes (orange), the 20 piezoelectric crystal classes (blue), and the 10 pyroelectric crystal classes (red).

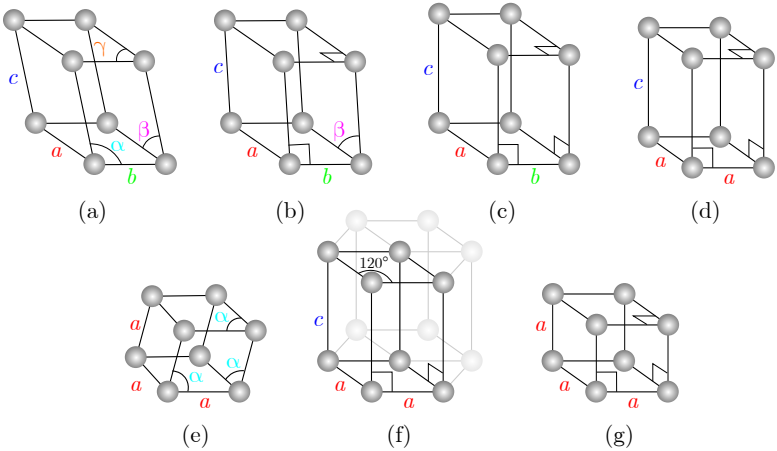

Figure 1.4: Lattice systems: (a) triclinic, (b) monoclinic, (c) orthorhombic, (d) tetragonal, (e) rhombohedral, (f) hexagonal, and (g) cubic. The independent lattice lengths and angles are denoted by $\{a, b, c\}$ and $\{\alpha, \beta, \gamma\}$, respectively. This overview shows only the primitive (Bravais) lattice, other types of centerings are omitted for simplicity.

Moreover, the subgroup of the 10 *pyroelectric* crystal classes, also known as *polar point group*, have a permanent polarization referred to as *spontaneous polarization*. Crystals of this group have a polar axis, which is an axis of rotational symmetry with no existing mirror plane perpendicular to this axis. Out of the seven lattice systems, all except the cubic lattice satisfy this requirement. The *pyroelectric effect* is defined as the change of spontaneous

polarization vector $\boldsymbol{p}_0$ with temperature θ at zero electric field (Damjanovic, 1998), viz.

$$\boldsymbol{\pi} = \left(\frac{\partial \boldsymbol{p}_0}{\partial \theta} \right), \tag{1.1.1}$$

where $\boldsymbol{\pi}$ denotes the pyroelectric coefficient vector.

Ferroelectric crystals are also *polar*, like pyroelectric crystals, but with the additional feature that the *spontaneous polarization* can be reoriented by an applied electric field. Since ferroelectrics are derivatives of the parenting point groups, they own the same physical properties, i.e., ferroelectrics have no inversion center (*non-centrosymmetric*) and exhibit electromechanical coupling (*piezoelectric*) and a temperature-dependent, spontaneous polarization (*pyroelectric*), which is stable in multiple orientations and can be reoriented by an imposed electric field (*ferroelectric*).

1.1.2 *Ferroelectric phase transformation*

In our previous definition of ferroelectrics, we required the material to have more than one stable state (orientation), between which the polarization can be switched (reoriented). In this section, we introduce the fundamental concepts of a phase transformation and its connection to the different ferroelectric states based on a symmetry approach by following (Janovec & Privratska, 2013; L. Landau, 1937; Tagantsev et al., 2010).

Many crystalline materials undergo a structural phase transformation, which is a transformation between different point groups (Tomaszewski, 1992a, 1992b; Tonkov & Tonkov, 1992), and are categorized based on the following properties:

We differentiate between two types of phase transformations: *distortive* and *reconstructive transitions* (Gränicher & Müller, 1971). While in a reconstructive transition, the existing interatomic bonds can break apart and individual atoms rearrange themselves to form a new atomic structure, in a distortive transition, the chemical bonds remain intact, because atoms shift only slightly and in a coordinated fashion, such that the overall crystal structure exhibits a minor shape change. Examples of a reconstructive transition can be found in titanium (Ti) between the (body-centered) cubic phase and hexagonal/rhombohedral phases and in zinc sulfide (ZnS) between sphalerite- and wurtzite-type structures.

Most technically relevant ferroelectrics exhibit a distortive transition, which can be induced by the change in temperature and pressure to which the material is exposed . In contrast to the reconstructive transition, where no general relation between the two structures involved in the transition exists (except for the chemical composition), the distortive transition can be described as a change in the symmetry of the crystal structures. Consider two crystal structures S_G and S_F where the subscripts G and F indicate a crystal class of the 32 point groups (see Fig. 1.3), and the crystal class F has lower symmetry than G. Based on symmetry arguments, we can define a *distortive transition* as

$$F \subset G, \tag{1.1.2}$$

where the low-symmetry phase F is a subset of the high-symmetry phase G, such that the structure S_F arises from distortion of the structure S_G. Any phase transformation that complies with (1.1.2) and results in a change of its point group ($F \neq G$) is referred to as *ferroic transition*, where F denotes the point group of the *ferroic phase*.

For the sake of completeness, we dive one step deeper into *distortive transitions* by distinguishing between *displacive* and *order–disorder* transitions. In the former transition, thermal fluctuations cause atoms to oscillate harmonically around their equilibrium positions at the transition, while in the latter transition, thermal motion enables atoms to switch between two or more equilibrium positions. Classical examples for a *displacive* transition and a *order-disorder* transition are the cubic-tetragonal transition (with $F = 4mm$ and $G = m\bar{3}m$) of barium titanate ($BaTiO_3$) and the orthorhombic-orthorhombic transition (with $F = mm2$ and $G = mmm$) of sodium nitrite ($NaNO_2$), respectively. Of course, these are not the only mechanisms that can give rise to ferroelectricity. Recent advances in multiferroics research to design materials that combine ferromagnetic and ferroelectric properties, which are mutually exclusive, stimulated the search for alternative ferroelectric mechanisms (Spaldin & Fiebig, 2005), e.g., based on stereochemically active electron lone pairs (Seshadri & Hill, 2001) or geometrically driven distortions (Van Aken et al., 2004). Materials which own multiple ferroic properties, such as ferromagnetic, ferroelectric, and ferroelastic, are called *multiferroics*.

A *ferroelectric phase transition* is commonly defined as a transition from a high-symmetry, non-polar phase G to a low-symmetry polar phase F at the Curie temperature θ_C. This polar transition gives rise to a sponta-

neous polarization (vector) whose components can be defined through the temperature-dependent piezoelectric coefficient π (1.1.1), viz.

$$p_0(\theta) = \int_{\theta}^{\theta_C} \pi(\theta)\, \mathrm{d}\theta, \tag{1.1.3}$$

where θ denotes any temperature below the Curie temperature θ_C. Furthermore, the spontaneous polarization needs to be switchable by an applied electric field. While this holds for the majority of cases, it excludes ferroelectrics, whose polarization cannot be reoriented, due to practical reasons (mechanical integrity, electric field limitations, etc.) and transitions between polar phases. To circumvent this issue, we point to an alternative definition based on the pyroelectric coefficient (Tagantsev et al., 2010), which is: *"A phase transition is called ferroelectric if it results in a lower symmetry phase, in which the vector of pyroelectric coefficients acquires new components which were zero, by symmetry, in the high-symmetry phase."*

1.1.3 *Ferroelastic phase transformation*

Analogous to the definition of a *ferroelectric phase transition* based on new non-zero components in the pyroelectric coefficient vector π, one may use symmetry arguments on the symmetric, second-order thermal dilation tensor α_{ij} (with $i, j = 1, 2, 3$) to define a *ferroelastic phase transition*. For example, in the high-symmetry cubic phase, the thermal dilation tensor $\alpha_{ij} = \mathrm{diag}\,(a_c, a_c, a_c)$ can be described by only one independent component a_c, whereas in the low-symmetry tetragonal phase, two independent components a and c are required to describe the three possible deformation states: $\alpha^1_{ij} = \mathrm{diag}\,(a, a, c)$, $\alpha^2_{ij} = \mathrm{diag}\,(a, c, a)$, and $\alpha^3_{ij} = \mathrm{diag}\,(c, a, a)$, which are illustrated in Fig. 1.5(c). Any transition between a high-symmetry phase G and a low-symmetry phase F in which the number of independent components in the thermal dilation tensor α_{ij} change, is called *ferroelastic phase transition* and F, a *ferroelastic phase* (Aizu, 1969). In contrast to *ferroelectric phase transitions*, transitions among point groups of the same crystal class are not *ferroelastic*, since they share the same number of independent components in the thermal dilation tensor. Only transitions between different crystal families are *ferroelastic* (Nye et al., 1985).

Similar to the *ferroelectric phase transition*, we use the concept of spontaneous strains which describe the deformation of the unit cell associated with

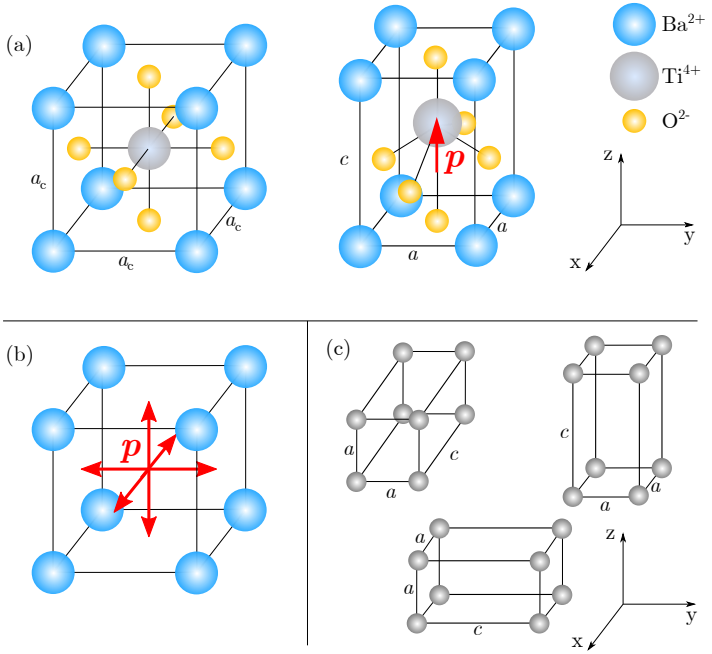

Figure 1.5: (a) Perovskite structure of $BaTiO_3$, showing the unit cell of the non-polar, centrosymmetric cubic phase (left) and the polar, low-symmetry tetragonal phase (right). (b) Ferroelectric states indicated by the six possible directions in which the spontaneous polarization vector $\boldsymbol{p}$ (red arrow) can align, and (c) ferroelastic states visualized by the three deformations of the tetragonal unit cell.

a *ferroelastic phase transitions* as the difference of thermal strains between the low-symmetry phase F and high-symmetry phase G as

$$\varepsilon_{ij}^{0}(\theta) = \int_{\theta}^{\theta_C} \left(\alpha_{ij}^{F}(\theta) - \alpha_{ij}^{G}(\theta)\right) \mathrm{d}\theta, \tag{1.1.4}$$

where $\theta \leq \theta_C$ denotes the temperature of the ferroelastic phase F and θ_C the Curie temperature.

1.1.4 *Domains, domain walls, and compatibility*

As discussed in the previous sections, the number of *ferroelectric* and *ferroelastic states* differs depending on the symmetry of the crystal lattice

associated with the high- and low-symmetry phases. In general, regions of homogeneous spontaneous polarization and spontaneous strain are called *ferroelectric domains* and *ferroelastic domains*, respectively. Analogously, adjacent domains with different spontaneous polarization or strain are separated by typically nanometer-thin interfaces, referred to as *ferroelectric domain walls* and *ferroelastic domain walls*, respectively.

This section provides a brief overview of possible combinations of domains that form compatible domain pairs, with a focus on the tetragonal crystal symmetry. According to Tagantsev et al. (2010), four elements are particularly crucial in determining the orientation of a *domain wall*. First, each domain should be in a spontaneous state to minimize the total energy of the material. Second, the electrostatic energy associated with differences in polarization orientation at the wall, also known as *electrical compatibility*, should be minimized. Third, reducing the strain mismatch at the interface minimizes the elastic strain energy, known as *mechanical compatibility*. Finally, the energy contained in the domain wall is referred to as *interface energy*.

The *electrical compatibility condition* demands electrical neutrality at the interface. Uncompensated bound charges at interface (whose density is $\rho_b = -\nabla \cdot \boldsymbol{p}$) increase the electric energy and are therefore unfavorable. To comply with electrical neutrality at the interface ($\rho_b = 0$), the normal component of the jump in polarization across the interface has to vanish, such that the *electrical compatibility condition* reads (Davi & Rizzoni, 2004; Shu & Bhattacharya, 2001)

$$\left(\boldsymbol{p}^I - \boldsymbol{p}^{II}\right) \cdot \boldsymbol{n} = 0, \tag{1.1.5}$$

where $\boldsymbol{n}$ denotes the interface normal vector and $\boldsymbol{p}^I$ and $\boldsymbol{p}^{II}$ the polarization vectors inside domain I and II, respectively. In the absence of free charge carriers, which could neutralize any uncompensated bound charges, the electrical compatibility plays a dominant role in the formation of domain patterns. Domain walls, domain pairs, and domain patterns are usually denoted based on the difference of their respective polarization orientations. Classic examples of electrically compatible domain pairs are 180°-domain walls and 90°-domain walls of tetragonally oriented $BaTiO_3$, shown in Fig. 1.6(a) and (b), respectively. Of course, the exact number of admissible domain walls depends on the underlying crystallographic structure. A complete overview of possible compatible domain pairs for different crystal symmetries that satisfy average compatibility and exact compatibility (i.e.,

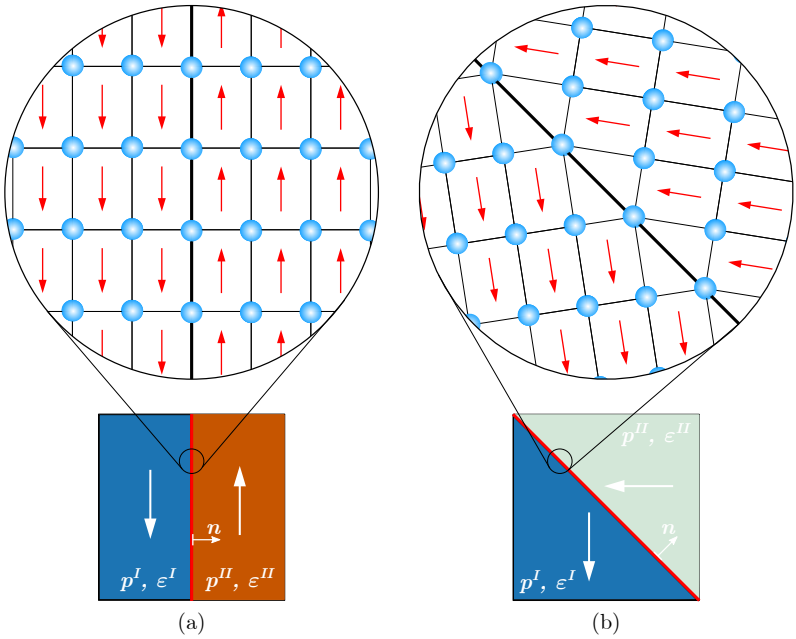

Figure 1.6: Two types of domain walls in a tetragonal crystal: (a) the ferroelectric 180°-domain wall, where the polarization vectors in adjacent domains are antiparallel aligned, and (b) the ferroelectric/ferroelastic 90°-domain wall, where the polarization vectors of neighboring domains are approximately perpendicular. Different domains (colors) are indicated by the orientation of the spontaneous polarization $\boldsymbol{p}$ (white arrow) and are separated through a domain wall (red line), whose normal vector is denoted as $\boldsymbol{n}$ (small white arrow). At the top, a magnified schematic of the lattice structure in the proximity of a domain wall is depicted, showing the domain wall (thick black line), polarization vectors (red arrows), and the A-site cations (blue circles) of the tetragonal unit cell.

local compatibility) can be found in Shu and Bhattacharya (2001) and Tsou et al. (2011), respectively.

Analogously for *ferroelastic domain* pairs, the *mechanical compatibility* must be fulfilled in order to minimize the elastic strain energy of the material. Following Ball and James, 1987; DeSimone and James, 2002; Shu and Bhattacharya, 2001, we assume homogeneous strain states $\boldsymbol{\varepsilon}^I$ and $\boldsymbol{\varepsilon}^{II}$ in the neighboring domains I and II, respectively, which are separated by a planar domain wall with interface normal vector $\boldsymbol{n}$. Furthermore, we require a continuous deformation across the wall, such that the strains of the two

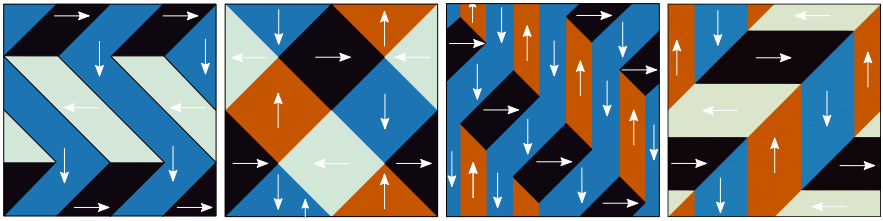

Figure 1.7: Exactly compatible rank-2 laminate domain patterns of a tetragonal crystal (Tsou et al., 2011), illustrated by the four unit cells (a) through (d) showing differently oriented domains (colors) and the corresponding polarization vectors (white arrows).

adjacent domains are subject to the *Hadamard jump condition* (Gurtin, 1982), which reads, for small-strain kinematics,

$$\boldsymbol{\varepsilon}^I - \boldsymbol{\varepsilon}^{II} = \frac{1}{2}\left(\boldsymbol{a} \otimes \boldsymbol{n} + \boldsymbol{n} \otimes \boldsymbol{a}\right), \tag{1.1.6}$$

where $\boldsymbol{a}$ is an arbitrary vector. For given pairs of $\left(\boldsymbol{\varepsilon}^I, \boldsymbol{p}^I\right)$ and $\left(\boldsymbol{\varepsilon}^{II}, \boldsymbol{p}^{II}\right)$, compatible domain pairs can be found, e.g., by solving the corresponding eigenvalue problem of (1.1.6) (Ball & James, 1987) and subsequently checking for electrical compatibility (1.1.5). Domain patterns that satisfy mechanical and electrical compatibility can be considered as energy-minimizing patterns, although additional contributions from strain-mismatch at domain walls and disarrangement of lattices in adjacent domains will further increase the interface and elastic strain energy, respectively (Jona & Shirane, 1962; Salje, 1990; Surowiak et al., 1993). Most prominent examples are lamellar domain structures, which are frequently observed in experiments and depicted in Fig. 1.1(a). By combining multiple compatible domain pairs, one can construct more complex domain structures, such as rank-2 laminate structures, which are well-known from experiments (Arlt, 1990; Merz, 1954). Fig. 1.7 shows four rank-2 laminate structures of a tetragonal crystal that satisfy (exact) compatibility, e.g., the well-established (a) herringbone pattern and (b) vortex pattern; see Tsou et al. (2011) for a recent overview of compatible laminate patterns.

1.2 EXPERIMENTAL TECHNIQUES

Several experimental techniques have been established to study ferroelectric materials ranging from the crystalline structure at the lowest scales to simple laminate patterns at the mesoscale. Here, we provide a brief (and by no means exhaustive) overview of the most common methods for the characterization of ferroelectric microstructures, based on the book of Tagantsev et al. (2010).

In *polarized light microscopy* (PLM), the interference of polarized light with ferroelectric domains and differences in the optical properties of domains are used to reveal the ferroelectric microstructure, by contrasting domains differently depending on their polarization orientation. By analyzing the changes in polarization of light passing through the ferroelectric material, known as birefringence, it is possible to capture the domains' pattern and measure their size and shape. PLM is a nondestructive method that enables in-situ observation of the domain evolution (Merz, 1954; Mulvmill et al., 1996; Tu et al., 2001) with tens-of-micrometers precision.

More advanced techniques utilize the nonlinear optical properties of non-centrosymmetric materials (such as ferroelectrics) to measure the polarization vector of the domain pattern formation. *Second-harmonic generation* (SHG) is a physical mechanism in nonlinear optical media where two photons with the same frequency combine to produce a photon with double the frequency (Franken et al., 1961). This effect is used in SHG microscopy to probe the components of the electric susceptibility tensor, which is a measure of the underlying polarization state, through the incident and detected light waves (Fiebig et al., 2005). SHG microscopy is a promising, noninvasive method that has been used to study various ferroic materials such as ferroelectrics (Lummen et al., 2014), ferromagnetics (Regensburger et al., 2000), antiferromagnetics (Schoenherr et al., 2017), and multiferroics (Manz et al., 2016).

Scanning force microscopy-based techniques allow for a nondestructive mapping of the sample's surface with nanometer precision by using a probing tip mounted on a cantilever beam to measure interaction forces between the tip and the specimen (Bonnell, 2000). Depending on the type of interaction force that is measured, different methods are available. In the non-contact mode of the scanning tip, spontaneous polarization can be measured through the electrostatic field induced by the bound charges, which is called *electrostatic force microscopy* (EFM) (Saurenbach & Terris, 1990).

Alternatively, if the probing tip is in mechanical contact with the surface, ferroelastic domain walls can be detected by scanning the topology of the sample via the deflection of the cantilever beam, known as *atomic force microscopy* (AFM) (Binnig et al., 1986; Nakatani, 1979). A powerful extension of AFM is built on applying an additional alternating electric current through the tip to induce a mechanical deformation by the inverse piezoelectric effect, which provides valuable information on the polarization orientation and is a well-established method called *piezoresponse force microscopy* (PFM) (Güthner & Dransfeld, 1992). Finally, by conducting angular-resolved PFM measurements, i.e., through subsequent measurements under different angles of the cantilever beam, not only the 2D landscape of the domain pattern formation can be revealed, but also the corresponding 3D polarization vector is obtained.

At lower scales, electron microscopy-based techniques make use of the interaction of electron beams with ferroic domains and can be divided into two methods, based on which type of electrons are being detected. First, *scanning electron microscopy* (SEM) enables direct observation of domains (Robinson & White, 1967) at different temperatures and during slowly evolving switching processes, with a major downside of accumulating charges from the electron beam, which can alter the ferroelectric microstructure (Nakatani, 1973). SEM can be operated in two modes: (i) detection of *secondary electrons* emitted by atoms that have been excited by the electron beam and (ii) *backscattered electrons* originating from elastic scattering interactions of the electron beam with specimen atoms. While the former mode is generally used to create high-resolution images of the domain pattern formation on the surface, the latter mode provides valuable information about microstructural properties such as the composition and crystalline structure, which is of particular interest in ferroelectric ceramics (Tagantsev et al., 2010). SEM is a common method to capture the ferroelectric microstructure with tens-of-nanometers precision, but it does not provide further details on the domain orientation and requires an appropriate treatment of the surface (etching and polishing), which may affect the domain pattern formation.

Second, *transmission electron microscopy* (TEM) works similarly to SEM by utilizing an electron beam but with a smaller wave length and, instead of using electrons backscattered from the surface, information on the crystal structure is obtained by electrons that are passing through the specimen. Furthermore, electrons are scattered by various elastic and inelastic scattering processes and their diffraction pattern is measured on a detector on

the opposite side of the sample. Depending whether only the transmitted beam or the diffracted beam is used, the bright field or dark field image is acquired, respectively. Moreover, in *high-resolution transmission electron microscopy* (HRTEM), a combination of many diffracted beams and the transmitted beam is utilized. HRTEM is a potent tool to study domain pattern formation with the atomic-level resolution that allows characterization domain walls in terms of structure, thickness, and roughness, e.g., in $BaTiO_3$ (Floquet et al., 1997; Shiojiri et al., 1992) and $PbTiO_3$ (Foeth et al., 1999; Stemmer et al., 1995). However, TEM is limited to thin samples with thicknesses of less than $5 - 20\,\text{nm}$ for HRTEM and $100\,\text{nm}$ for classical TEM (Tagantsev et al., 2010).

1.3 MODELLING TECHNIQUES

A wide variety of theoretical and numerical models have been used to describe ferroelectric material behavior. Because of the broad range of length scales involved in a ferroelectric material, different models focus primarily on a specific range of time and length scales, considering only interactions relevant within those particular scales, while less dominant physical effects are often neglected or modeled appropriately only when necessary. The majority of theoretical approaches to characterize ferroelectrics can be divided into three main groups depending on the length scale of interest.

1.3.1 *Atomic-level approaches*

At the lower scales, various atomistic modelling techniques have been established to study ferroelectrics, based on the fundamental laws of quantum mechanics and electrostatics. Among the first-principle (*ab-initio*) approaches, *density functional theory* (DFT) (Hohenberg & Kohn, 1964; W. Kohn & Sham, 1965) is perhaps one of the most widely used methods, which has been successfully applied to various ferroelectric oxides to improve our understanding of the behavior of bulk crystals (Resta, 2003; Vanderbilt, 1997) and thin films (Ghosez & Rabe, 2000; Junquera & Ghosez, 2003; Meyer & Vanderbilt, 2002; Rondinelli & Spaldin, 2011). Although DFT methods provide valuable insights into quantum mechanical interactions of ferroelectrics, they come with certain limitations. First, only a few hundred atoms can be considered in a first-principle DFT calculation due to computational

limitations, which makes it challenging to assess solid solutions, such as $PbZr_{1-x}Ti_xO_3$ (PZT), $Ba_{1-x}Sr_xTiO_3$ (BST), and relaxor ferroelectrics. Second, first-principle DFT calculations are restricted to conditions at the athermal limit (at 0 K), since thermal vibrations are not feasible, which prevents a direct comparison with experiments conducted at finite temperatures.

Interpolative methods, by contrast, do consider finite-temperature effects. These include the *effective Hamiltonian approach* (Rabe & Joannopoulos, 1987; Zhong et al., 1994, 1995), where the Hamiltonian is obtained from a Taylor expansion around the (non-polar) paraelectric phase in terms of the soft-mode degrees of freedom and the homogeneous strain, and the expansion coefficients are fitted based on inputs from DFT calculations. Such models have been used to study the temperature dependence of the dielectric (Waghmare & Rabe, 2005), piezoelectric (Garcia & Vanderbilt, 1998), and optical (Veithen et al., 2005) properties and phase transitions (Iniguez et al., 2001; Marton et al., 2017; Zhong et al., 1995). Similarly, *shell models* (Bilz et al., 1987; Sepliarsky et al., 2001) use interatomic potentials that are adjusted based on first-principle calculations to provide a more complete atomistic description, including all phonon branches (not just soft modes). These models have been applied successfully to study various ferroelectric oxides (Sepliarsky et al., 2004; Tinte et al., 1999; Völker et al., 2011).

A major advantage of first-principle calculations is that they do not require any empirical inputs, which makes them a useful tool in the search for new materials with interesting properties, e.g., Pb_2TiO_4 (Fennie & Rabe, 2005), $BaTi_2O_5$ (Waghmare et al., 2004), $BiFeO_3$ (J. Wang et al., 2003), $BiAlO_3$, and $BiGaO_3$ (Baettig et al., 2005) or in the investigation of new structures of established ferroelectric oxides, e.g., $PbZrO_3$ (Johannes & Singh, 2005). These benefits come at the cost of severe limitations in the number of atoms that can be included in atomistic calculations, due to extensive computations required in these methods.

1.3.2 *Mesoscale approaches*

At the continuum level, ferroelectric microstructures can be described as solutions of a non-convex variational problem (Su & Landis, 2007; W. Zhang & Bhattacharya, 2005) based on Landau-Devonshire theory (Devonshire, 1949; L. Landau, 1937) where the low-symmetry crystal structure is modeled phenomenologically by using thermodynamic potentials. The nonexistence of homogeneous minimizers results in the formation of energy-minimizing

sequences upon relaxation of the energy, such as intricate laminate patterns (Ball & James, 1987; Bhattacharya, 1991). Such a description of ferroelectricity is used in diffuse-interface and sharp-interface models, which are discussed below.

The introduction of an interface energy term regularizes gradients (in the polarization field) by smearing out sharp contrasts, which gives rise to a finite thickness and energy cost associated with an interface (Gurtin, 1987). This diffuse-interface approach is utilized in *phase-field models* where the polarization vector generally acts as the order parameter in the expansion of the (Landau) energy, which holds crucial material properties, such as spontaneous polarization, permittivity, energy levels and barriers (Devonshire, 1949, 1951; L. Landau, 1937). Phase-field models simulate the evolution of the ferroelectric microstructure by resolving the diffuse interface with a typical thickness in the order of nanometers. While diffuse-interface models enable us to compute intricate networks of domain patterns in ceramics with no prior assumption of the domain structure, they requires sufficient spatial resolution to track individual domain walls. This constraint renders phase-field models computationally expensive, and they are typically used at the (intermediate) mesoscale, ranging from (sub)nanometers to a few micrometers. In the seminal work of Su and Landis (2007) and W. Zhang and Bhattacharya (2005), the phase-field approach was established to model ferroelectric domain pattern formations at the mesoscale within a finite-element (FE) framework. Later, researchers suggested solving the electromechanically coupled boundary value problem (BVP) more efficiently in Fourier space by utilizing a spectral solution scheme (Chen, 2008; Vidyasagar et al., 2017) or others focused on the effect of depolarization fields in thin films by using boundary element methods (Dayal & Bhattacharya, 2007). Alternative phase-field models used the spontaneous polarization as an order parameter to enhance the physical interpretation of material parameters (Schrade et al., 2013) and to derive a general kinetics model (Guin & Kochmann, 2022). Independent of the particular formulation, phase-field models have been used extensively to study various applications of ferroelectric materials such as switching in polycrystals (Choudhury et al., 2005; Vidyasagar et al., 2017), thin films (Dayal & Bhattacharya, 2007; Gao et al., 2014), temperature-induced phase-transformations in $BaTiO_3$ (Franzbach et al., 2012; J. Wang et al., 2010), coexisting crystal phases in lead-based ferroelectrics (Franzbach et al., 2014; Seo et al., 2013), space charges (Xiao et al., 2005), oxygen vacancy migration (Suryanarayana & Bhattacharya,

2012; Xiao & Bhattacharya, 2008), and charged domain walls (Shenoy et al., 2012; Sluka et al., 2012; Zuo et al., 2014).

By contrast, *sharp-interface models* treat domain walls in a more efficient fashion. Here, domain walls are represented as sharp interfaces, across which polarization, strain, and electric fields may jump. Within this framework, the motion of domain walls is described by a kinetic relation (Abeyaratne & Knowles, 1991; Logé & Suo, 1996) that links the velocity of interfaces with the driving traction, commonly obtained by the jump in the Eshelby energy momentum tensor (Eshelby, 1975) and any additional contributions, e.g., due to the curvature of the domain wall (Salje & Ishibashi, 1996). While sharp-interface models offer mathematical advantages, they require an additional model to account for the nucleation of new domains and intensive computations for large numbers of interfaces, which makes them in practice unsuitable for predicting the complex domain patterns in polycrystalline materials. Nevertheless, sharp interface models have been used extensively to improve our understanding of, e.g., energy-minimizing domain pairs (Shu & Bhattacharya, 2001), laminates (Tsou et al., 2011; Tsou & Huber, 2010; Weng & Wong, 2009), herringbone structures (Shilo et al., 2007) and vortices (Weng & Wong, 2009), the transition between different laminate structures (Tsou et al., 2013), hysteresis response using variational principles (J. E. Huber & Cocks, 2008; Yen et al., 2008), and rate-dependent effects based on general kinetics models (Guin & Kochmann, 2022).

1.3.3 *Macroscale approaches*

Finally, *phenomenological macroscale models* focus on the macroscale material response of bulk polycrystalline ferroelectric ceramics, without resolving the ferroelectric microstructure at lower scales, by utilizing an efficient material description, suitable for numerical implementation in finite element codes applicable at the ferroelectric device level (Miehe & Rosato, 2011).

A popular approach (Landis, 2002; McMeeking & Landis, 2002; Miehe & Rosato, 2011) is built on a decomposition of polarization and strain into reversible and irreversible parts, where the irreversible contribution is treated as internal variables. *Micro-electromechanical* models provide a description of the kinematics and evolution of these internal variables, i.e., remnant polarization and remnant strains (Landis, 2004). While early studies (Hwang et al., 1995; Lu et al., 1999) assumed a single domain within a grain, whose state is governed by a switching criterion, more

recent models account for grains comprised of multiple domains by using domain volume fractions (J. Huber et al., 1999; Stark et al., 2016; W. L. Tan & Kochmann, 2017) and orientation distribution functions (Idiart & Bottero, 2020) as internal variables.

Alternatively, stochastic models, such as the well-established Kolmogorov-Avrami-Ishibashi (KAI) model (Avrami, 1940; Ishibashi & Takagi, 1971), are based on the assumption of a random and statistically independent nucleation of domains within a homogeneous medium and constant nucleation rate, such that switching kinetics are limited by the motion of domain walls, which is described by a characteristic switching time. Later, strong qualitative disagreement of the predictions in bulk polycrystals (Zhukov et al., 2010) and PZT thin films (Gruverman et al., 2005; Tagantsev et al., 2002) led to an extension to a statistical distribution of switching times to characterize different regions in heterogeneous materials, such as grains in a polycrystal, which improved the accuracy of predictions (Genenko et al., 2012; Jo et al., 2007). Analogously, nucleation limited switching (NLS) models assume that switching kinetics in a certain region is limited by the nucleation of new domains instead by domain wall motion, which is characterized by an exponential distribution of nucleation waiting times. Experimentally measured polarization switching curves fitted well with the NLS model in polycrystalline thin films (Dabra et al., 2010; Duiker & Beale, 1990). While stochastic models generally capture the kinetics of polarization switching reasonably well, their connection to the underlying microstructure is mainly phenomenological, based on the fundamental assumption that switching occurs in a uncorrelated fashion, which is not in agreement with experimental observations (Schultheiß et al., 2018).

1.4 MOTIVATION

A key property of ferroelectric ceramics is the coupling of electric and mechanical fields. While primarily used in the linear regime (Taylor, 1985; J. Yang, 2006), ferroelectric ceramics under sufficiently large electric or mechanical loading enter a nonlinear regime, where a remnant polarization remains after the load is removed (Bhattacharya & Ravichandran, 2003; Chaplya & Carman, 2001). Such permanent changes in the atomic-level dipole structure offer avenues to adjust material properties (le Graverend et al., 2015), induce significant shape changes (Burcsu et al., 2004), or store information (Buck, 1952).

Early studies (Abe, 1959; Drougard, 1960; Miller & Weinreich, 1960) suggested that the motion of a 180°-domain wall in a defect-free single crystal is driven by the nucleation and growth of triangular shaped domains in a staggered manner. Although such nucleation-driven domain wall motion explains certain experimental observations, it unfortunately fails to predict the required activation fields for nucleation (Paruch et al., 2006; Tybell et al., 2002) and the absolute wall velocity. To fill this gap, Hayashi, 1972 proposed an analytical model to account for the kinetics of domain wall motion based on the theory of absolute reaction rates, whereas Logé and Suo, 1996 described ferroelectric domain wall motion as a non-equilibrium thermodynamic process, deriving a kinetic model based on variational principles. While the quasistatic material response of idealized ferroelectric ceramics is generally well understood and captured by such models, the complex microstructural mechanisms in real materials – from oxygen vacancies on the atomic level to grain boundary (GB) mechanisms on the polycrystalline mesoscale to boundary conditions on the macroscopic device level – and their influence on the switching kinetics is far less established. As an example, consider the intricate effect of stress concentrations near defects, cracks, and GBs, which promote switching and interfere with domain wall motion (Lambeck & Jonker, 1986; Marincel, Zhang, et al., 2015; Rodriguez et al., 2008).

Moreover, recent studies revealed that the homogenized polarization switching kinetics at the macroscale can be traced back to the collective motion (Bintachitt et al., 2010; Gorfman et al., 2018) of domain walls at smaller scales (Bassiri-Gharb et al., 2007; Pramanick et al., 2011). Hence, a profound understanding of the mechanism of nucleation and growth of domains and their interaction with microstructural defects in realistic materials (which typically posses an abundance of GBs, cracks, and pores (Mercadelli et al., 2010) is crucial to make reliable predictions of polycrystalline and porous materials. Structural defects, such as pores, can induce considerable mechanical and electric fields (Johnson-Wilke et al., 2015; Xu & Wang, 2015) in their proximity, which can cause domain wall pinning and therefore have an impact on the effective properties in bulk materials (Schultheiß et al., 2019a; Skinner et al., 1978) and thin films (Johnson-Wilke et al., 2015). Although several studies investigated the effect of space charges and oxygen vacancy migration (Xiao & Bhattacharya, 2008), dislocations (Kontsos & Landis, 2009), GBs (N. Liu & Su, 2014), and voids (J. Wang & Kamlah, 2009), the domain wall kinetics associated with domain wall pinning and depinning due to finite-temperature effects is largely unknown, despite experimental

reports underlining its importance (Savage & Miller, 1960; Stadler & Zachmanidis, 1964). For better accessibility using TEM imaging, experimental research has focused on ferroelectric switching in thin films (Chen, 2008; Lohse et al., 2001; Tagantsev et al., 2002). The thus observed response, however, does not necessarily capture the behavior of bulk ferroelectrics, since it involves both material and structural effects. Recent experiments by Schultheiß et al. (2018) studied bulk PZT using a fast high-voltage switch setup; the step response of polarization and strain was measured, providing insight into fast-switching kinetics and demonstrating not only clear rate dependence but also a dependence on grain size and texture.

Another open challenge is the rate- and temperature-dependent kinetics of ferroelectric switching (Arlt & Dederichs, 1980; Merz, 1956; Schultheiß et al., 2018; Wojnar et al., 2014; Zhou et al., 2001), which emerges on the atomic level but is strongly influenced by the mesoscale defect network through its impact on domain wall motion and nucleation. The broad range of length and time scales involved presents a challenge for both experimental observation and computational modeling. Although recent attempts (Vidyasagar et al., 2017) demonstrated the bridging of the gap between numerical results based on first-principle inputs (Völker et al., 2011) and macroscale experiments (W. L. Tan & Kochmann, 2017), these attempts failed to account for the crucial effect of finite-temperature kinetics, resulting in inaccurate predictions.

Furthermore, rising interest in the unique properties of domain walls, e.g., domain-wall conductivity (Guyonnet et al., 2011; Meier et al., 2012; Rojac et al., 2017) and domain-wall polarity in non-polar materials (Goncalves-Ferreira et al., 2008; Nataf et al., 2017; Salje et al., 2013; Yokota et al., 2019) gave rise to a new research branch with exciting applications, known as *domain wall engineering*. Therefore, an in-depth understanding of the underlying physics of the domain pattern formation is essential for future applications of ferroelectrics in domain-wall nanoelectronics (Catalan et al., 2012), e.g., as non-volatile memory devices, whose data storage capacity correlates with the domain wall density (Nataf et al., 2020).

Many exciting new domain structures, such as polarization flux-closure vorticies (Yadav et al., 2016), polar-skyrmion bubble domains (Das et al., 2019), and polarization flux-closure domains (Jia et al., 2011), have been reported, the latter being a well-examined structure in ferromagnetic materials (Kittel, 1946; L. Landau & Lifshitz, 1935). Despite some existing knowledge and analogies of common patterns in other ferroic materials, the

underlying cause and physical mechanism that give rise to these structures can vary, which necessitates a specific review within the context of ferroelectric materials. So far, different theoretical models have been utilized to study ferroelectric microstructures, e.g., sharp-interface models to investigate energy-minimizing domain patterns in equilibrium conditions (Davi & Rizzoni, 2004; J. Li & Liu, 2004; Shu & Bhattacharya, 2001; Tsou et al., 2011) and diffuse-interface models to simulate domain pattern evolution (Su & Landis, 2007; Vidyasagar et al., 2017; W. Zhang & Bhattacharya, 2005), but those are limited either to predefined domain structures or to simple domain patterns in nanometer-sized polycrystals; hence, previous attempts have been largely unable to simulate realistic domain pattern formations occurring in ferroelectric ceramics with no prior assumption of the domain configuration.

1.5 OUTLINE

The ultimate goal of this thesis is to improve the predictability of ferroelectric material behavior at the macroscale by continually improving our current understanding of the kinetics of polarization switching. This is accomplished by resolving the intricate interplay between ferroelectric domain evolution, which is facilitated by the nucleation and growth of domains at the mesoscale, and the surrounding polycrystalline microstructure. Furthermore, structural defects, such as pores and grain boundaries, along with finite-temperature effects, determine the domain pattern formation. All these factors need to be taken into account for an accurate prediction of the effective material response.

Chapter 2 details the continuum-level diffuse-interface approach used to simulate the ferroelectric microstructure. Here, a novel ferroelectric constitutive model is proposed by using statistical mechanics to account for atomic-level thermal fluctuations and by modifying the underlying Devonshire-Landau potential to depend on temperature. We discuss the analytical derivation, numerical implementation, and experimental validation of the finite-temperature phase-field framework for ferroelectric ceramics.

Chapter 3 discusses the influence of pores on ferroelectric domain wall motion at finite temperatures by leveraging our established finite-temperature phase-field framework. Manufacturing-induced porosity introduces local stress and electric fields that interfere with domain wall motion, which affects the ferroelectric material properties. Therefore, we study the mesoscale

motion of 180°-domain walls in porous PZT as a function of pore size and concentration at various temperatures, which is in reasonable agreement between simulated results and experimental reports.

Chapter 4 investigates the intricate domain pattern formation in ferroelectric ceramics where the size and orientation distribution of the crystallites are decisive factors in determining the effective properties of polycrystals. We discuss a novel method to identify and track domain walls in phase-field models, reveal distinct correlations between the grain orientation and polarization, strain, and domain density within a grain, and qualitatively assess the influence of grain boundaries on the domain pattern formation in comparison with experiments.

Chapter 5 summarizes the presented work and draws conclusions from the most important results. Additionally, recommendations for enhancing the simulation model and potential future research directions are discussed.

2

FINITE-TEMPERATURE FERROELECTRIC CONSTITUTIVE MODEL

This Chapter has been adapted from:

Indergand, R., Vidyasagar, A., Nadkarni, N., and Kochmann, D.M. (2020). "A phase-field approach to studying the temperature-dependent ferroelectric response of bulk polycrystalline PZT." *Journal of the Mechanics and Physics of Solids*, Vol. 144, 104098, URL: https://doi.org/10.1016/j.jmps.2020.104098

Indergand, R. and Kochmann, D.M. (2021). "Effect of temperature on domain wall–pore interactions in lead zirconate titanate: A phase-field study." *Applied Physics Letters*, Vol. 119, 222901, URL: https://doi.org/10.1063/5.0066612

2.1 INTRODUCTION

Temperature plays a crucial role in the behavior of ferroelectric oxides since it affects various important material properties such as the spontaneous polarization (Samara, 1971), thermal and electric conductivity (Bhide et al., 1962; Mante & Volger, 1967), elasticity (Z. Li et al., 1996), domain wall pinning (depinning field) (Jo et al., 2009), and hysteresis properties (coercive field, remnant polarization, dielectric and piezoelectric constants) (Hooker, 1998). Therefore, a profound understanding of the underlying mechanisms driving the temperature dependence of the material response is a requirement for predicting and optimizing the ferroelectric properties of these materials.

The influence of temperature on the ferroelastic and ferroelectric material response has been assessed experimentally. For the ferroelectric case, the temperature dependence of the piezoelectric and dielectric coefficients of PZT has been measured by electric cycling from room temperature to (or close to) the athermal limit (Q. Zhang et al., 1994). Hooker (1998) performed

high-temperature experiments reaching up to 500 K. More recent measurements with co-doped soft PZT covered an even broader temperature range that approached the Curie temperature (Kaeswurm et al., 2018). The influence of temperature on the ferroelastic material properties has been measured in uniaxial compression experiments, e.g., by Ji and Kim (2013), Kaeswurm et al. (2018), Marsilius et al. (2010), and Webber et al. (2009).

When modeling ferroelectric ceramics, three approaches are popular: phenomenological macroscale models, sharp-interface models, and diffuse-interface phase-field models; see, e.g., Vidyasagar et al., 2017 for a discussion and examples. Since we are interested in domain evolution at the mesoscale, we here follow the phase-field approach of W. Zhang and Bhattacharya (2005) and Su and Landis (2007), who first modeled ferroelectric domain structures at the mesoscale by solving the electro-mechanically coupled boundary value problem (BVP) based on a finite-element (FE) discretization. By contrast, we adopt Chen's (2008) spectral strategy to solve the BVP efficiently in Fourier space and specifically adopt the formulation of Vidyasagar et al. (2017). Our ferroelectric constitutive model is derived from the thermodynamic potentials of Völker et al. (2011), who used first-principles data based on density functional theory (DFT) and atomistic simulations to calibrate the (zero-temperature) electric enthalpy density. While those studies all neglected thermal effects, Woldman and Landis (2016, 2019) used phase-field methods to characterize the structure of ferroelectric-to-paraelectric phase boundaries near the Curie temperature and derived a thermodynamic framework that accounts for spatially heterogeneous temperature fields. Vopsaroiu et al. (2010) investigated thermally activated switching kinetics by using a non-equilibrium statistical model that describes the polarization switching of a nucleus. S. Liu et al. (2016) performed molecular dynamics simulations to investigate ferroelectric domain wall motion at finite temperature beyond Merz's law (Merz, 1956). Finite-temperature effects in the continuum phase-field framework, however, have remained a rare find.

In our approach presented here, temperature enters the phase-field description of ferroelectric ceramics in two ways. First, the underlying polarization potential is adjusted to depend on temperature by interpolating between the first-principles-informed energy landscape at zero temperature (Völker et al., 2011) and the convex energy potential at the Curie temperature – taking inspiration from the temperature dependence of the order parameter in continuous phase transitions close to the transition point being characterized by a power law and an associated critical exponent (Toda et al., 1983). Such interpolation models, have previously been proposed in the con-

text of, e.g., lambda phase transitions of liquid helium (Ferrell et al., 1968), liquid-gas phase transitions in nuclear reactors (Panagiotou et al., 1984), glass transitions of amorphous oxides (Ojovan & Lee, 2006), paramagnetic-ferromagnetic phase transitions (Mohan et al., 1998), and ferroelectric phase transitions in single-crystalline barium titanate (Y. Li et al., 2005; J. Wang et al., 2010; Woldman & Landis, 2016). Second, we account for thermal lattice vibrations by a statistical mechanics-based thermalization of the Allen-Cahn evolution equation through temperature-dependent random noise (Funaki, 1995; Rolland et al., 2016; Shardlow, 2000). Related stochastic phase-field models haven been employed to model, e.g., the microstructure evolution in magnetic materials (Koyama, 2008), dendritic crystal growth (Karma & Rappel, 1999; Shang et al., 2016), confined nanoferroelectrics (Slutsker et al., 2008), solidification of austenitic nickel-chromium-based superalloys (Radhakrishnan et al., 2019), plasticity in Ti-alloys (Zhu et al., 2017), and GB motion (Baruffi et al., 2019). Here, we introduce thermal fluctuations to affect the polarization evolution. The resulting finite-temperature phase-field model is validated against experimental measurements (in terms of the ferro- and piezoelectric properties), and we discuss the predicted influence of temperature on ferroelectric microstructures and the associated switching kinetics.

2.2 FERROELECTRIC CONSTITUTIVE MODEL AND RVE-PROBLEM AT ZERO TEMPERATURE

We adopt and extend the constitutive model of Vidyasagar et al. (2017), which was introduced for zero-temperature simulations and which we here summarize briefly to present our modifications and extensions in the proper context. We consider tetragonal perovskite ceramics below their Curie temperature and use continuum mechanics to describe a body $\boldsymbol{\Omega} \subset \mathbb{R}^n$ in n-dimensional space. The small strains in brittle ceramics allow the use of linearized kinematics with an infinitesimal strain tensor $\boldsymbol{\varepsilon} = \mathrm{sym}(\nabla \boldsymbol{u})$ derived from a (mechanical) displacement field $\boldsymbol{u}(\boldsymbol{x}, t) : \Omega \times \mathbb{R} \to \mathbb{R}^n$, depending on position $\boldsymbol{x} \in \boldsymbol{\Omega}$ and time $t > 0$. If inertial and body forces are neglected (as in our applications), the *mechanical problem* is governed by the balance of linear momentum, which requires

$$\nabla \cdot \boldsymbol{\sigma} = 0, \tag{2.2.1}$$

with the infinitesimal Cauchy stress tensor $\boldsymbol{\sigma}$ (and appropriate Dirichlet and Neumann boundary conditions in terms of prescribed displacements

and tractions, respectively). The governing equations for the *electric problem* are derived from Maxwell's equations. Gradients in the voltage potential $\phi : \mathbb{R}^n \times \mathbb{R} \to \mathbb{R}$ produce an electric field $\boldsymbol{e} = -\nabla\phi$, which is connected to the electrical displacement field $\boldsymbol{d} : \Omega \times \mathbb{R} \to \mathbb{R}^n$ and the polarization field $\boldsymbol{p} : \Omega \times \mathbb{R} \to \mathbb{R}^n$ through $\boldsymbol{d} = \kappa_0 \boldsymbol{e} + \boldsymbol{p}$, where κ_0 is the permittivity in vacuum. By assuming that no free charges are present within the body $\boldsymbol{\Omega}$, Gauss' law reduces to

$$\nabla \cdot \boldsymbol{d} = 0, \tag{2.2.2}$$

again assuming appropriate Dirichlet and Neumann boundary conditions (in terms of prescribed voltages and surface charges, respectively).

In order to close the above system of equations, we require constitutive relations as well as a dissipative evolution equation for the polarization field. We derive all constitutive relations from the electric enthalpy density W, which for a ferroelectric perovskite decomposes as (Su & Landis, 2007; W. Zhang & Bhattacharya, 2005)

$$\begin{aligned} W(\boldsymbol{\varepsilon}, \boldsymbol{e}, \boldsymbol{p}, \nabla \boldsymbol{p}) = \Psi_{\text{mech}}(\boldsymbol{\varepsilon}) + \Psi_{\text{coupl}}(\boldsymbol{\varepsilon}, \boldsymbol{p}) + \Psi_{\text{pol}}(\boldsymbol{p}) + \Psi_{\text{inter}}(\nabla \boldsymbol{p}) \\ + \Psi_{\text{el}}(\boldsymbol{e}) - \boldsymbol{e} \cdot \boldsymbol{p}, \end{aligned} \tag{2.2.3}$$

such that

$$\boldsymbol{\sigma} = \frac{\partial W}{\partial \boldsymbol{\varepsilon}} \quad \text{and} \quad \boldsymbol{d} = -\frac{\partial W}{\partial \boldsymbol{e}}. \tag{2.2.4}$$

The first two terms in (2.2.3) arise from decomposing the linear elastic strain energy density into a purely mechanical strain energy Ψ_{mech} and an electrostrictive coupling contribution Ψ_{coupl}. The electrostriction is modeled by a quadratic approach (Mason, 1948; Völker et al., 2011)

$$\varepsilon^{\text{r}}_{ij} = \mathbb{Q}_{ijkl} p_k p_l \quad \text{with} \quad \mathbb{Q} = \begin{cases} Q_{11}, & i = j = k = l \\ Q_{12}, & i = j \neq k = l \\ Q_{44}, & i = k \neq j = l \\ 0, & \text{otherwise.} \end{cases} \tag{2.2.5}$$

Writing $\varepsilon_{ij} = \varepsilon^{\text{e}}_{ij} + \varepsilon^{\text{r}}_{ij}$, where $\varepsilon^{\text{e}}_{ij}$ denotes elastic strains and $\varepsilon^{\text{r}}_{ij}$ remnant strains, we have $\Psi_{\text{elastic}}(\boldsymbol{\varepsilon}) = \frac{1}{2}(\varepsilon_{ij} - \varepsilon^{\text{r}}_{ij})\mathbb{C}_{ijkl}(\varepsilon_{kl} - \varepsilon^{\text{r}}_{kl})$ with fourth-order elasticity tensor $\mathbb{C}_{ijkl}$, such that the resulting mechanical energy density Ψ_{mech} reads

$$\Psi_{\text{mech}}(\boldsymbol{\varepsilon}) = \frac{1}{2} \varepsilon_{ij} \mathbb{C}_{ijkl} \varepsilon_{kl}, \tag{2.2.6}$$

whereas the anisotropic electro-mechanical coupling energy, according to Völker et al. (2011), is expressed as

$$\begin{aligned}\Psi_{\text{coupl}}(\boldsymbol{\varepsilon}, \boldsymbol{p}) = q_{11} &\left(\varepsilon_{11} p_1^2 + \varepsilon_{22} p_2^2 + \varepsilon_{33} p_3^2\right) \\ &+ q_{12} \left[\varepsilon_{11}\left(p_2^2 + p_3^2\right) + \varepsilon_{22}\left(p_1^2 + p_3^2\right) + \varepsilon_{33}\left(p_1^2 + p_2^2\right)\right] \\ &+ q_{44}\left(p_1 p_2 \varepsilon_{12} + p_1 p_3 \varepsilon_{13} + p_2 p_3 \varepsilon_{23}\right) \\ &+ \beta_1\left(p_1^4 + p_2^4 + p_3^4\right) + \beta_2\left(p_1^2 p_2^2 + p_1^2 p_3^2 + p_2^2 p_3^2\right),\end{aligned} \tag{2.2.7}$$

with coefficients

$$\begin{aligned} q_{11} &= -C_{11} Q_{11} - 2 C_{12} Q_{12}, \\ q_{12} &= -C_{12}(Q_{11} + Q_{12}) - C_{11} Q_{12}, \\ q_{44} &= -4 C_{44} Q_{44}, \\ \beta_1 &= \frac{C_{11} Q_{11}^2}{2} + 2 C_{12} Q_{11} Q_{12} + C_{11} Q_{12}^2 + C_{12} Q_{12}^2, \\ \beta_2 &= C_{11} Q_{12}(2 Q_{11} + Q_{12}) + C_{12}(Q_{11}^2 + Q_{11} Q_{12} + 3 Q_{12}^2) + 2 C_{44} Q_{44}^2. \end{aligned}$$

For convenience, we make use of a more compact notation

$$\Psi_{\text{coupl}}(\boldsymbol{\varepsilon}, \boldsymbol{p}) = \varepsilon_{ij} \mathbb{B}_{ijkl} p_k p_l + p_i p_j \mathbb{A}_{ijkl} p_k p_l, \tag{2.2.9}$$

which concentrates the electro-mechanical coupling coefficients q_{11}, q_{12}, q_{44}, and β_1, β_2 in fourth-order coupling tensors $\mathbb{B}$ and $\mathbb{A}$ with components

$$\mathbb{B}_{ijkl} = \begin{cases} q_{11} & \text{if } i = j = k = l, \\ q_{12} & \text{if } i = j \neq k = l, \\ q_{44} & \text{if } i = k \neq j = l, \\ 0 & \text{else} \end{cases} \quad \text{and} \quad \mathbb{A}_{ijkl} = \begin{cases} \beta_1 & \text{if } i = j = k = l, \\ \beta_2/6 & \text{if } i = j \neq k = l, \\ & \text{or } i = k \neq j = l, \\ & \text{or } i = l \neq j = k, \\ 0 & \text{else.} \end{cases} \tag{2.2.10}$$

Higher-order coupling tensors $\mathbb{F}_{ijklmn}$ and $\mathbb{G}_{ijklmn}$, introduced by Su and Landis (2007), are not here considered to enforce stress-free conditions on average (as described below). Here and in the following, we use classical index notation with Einstein's summation convention.

The non-convex polarization energy for tetragonal PZT is described by a Landau-Devonshire polarization potential Ψ_{pol}, which is assumed as a sixth-order polynomial

$$\Psi_{\text{pol.}}(\boldsymbol{p}) = p_i \mathbb{A}^1_{ij} p_j + p_i p_j \mathbb{A}^2_{ijkl} p_k p_l + p_i p_j p_k \mathbb{A}^3_{ijklmn} p_l p_m p_n. \tag{2.2.11}$$

We here adopt the potential proposed by Völker et al. (2011), who calibrated the polynomial coefficients using first-principles DFT data at the athermal limit and exploiting the known crystal symmetries; see Vidyasagar et al. (2017) for a discussion and Fig. 2.1 for a 2D visualization of the polarization potential $\Psi_{\text{pol.}}$.

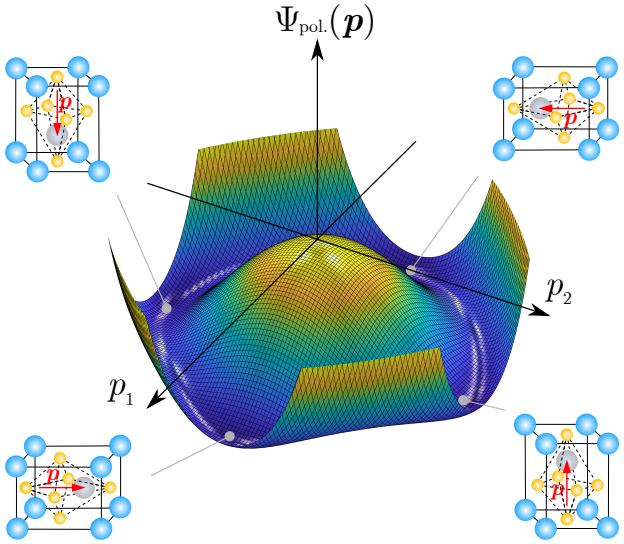

Figure 2.1: Visualization of the polarization potential $\Psi_{\text{pol.}}(\boldsymbol{p})$ as a function of the polarization vector $\boldsymbol{p} = (p_1, p_2)^{\mathrm{T}}$, where each minima in the energy landscape corresponds to one of the four (spontaneous) polarization states (in 2D). Each state is visualized by a tetragonally distorted unit cell, which are, e.g., in case of lead titanate oxide $PbTiO_3$, composed of four lead cations Pb^{2+} (blue) at the corners, one off-centered titanium cation Ti^{4+} (gray) at the center, which is octahedrally coordinated by six oxygen anions O^{2-} (yellow). The electric dipole is indicated by a red arrow.

The energy contained in domain walls is considered by the regularizing interface energy (Völker et al., 2011)

$$\Psi_{\text{inter}}(\nabla \boldsymbol{p}) = \frac{1}{2} p_{i,j} \mathbb{G}_{ijkl} p_{k,l} \quad \text{with} \quad \mathbb{G}_{ijkl} = \begin{cases} G_{11} & \text{if } i=j=k=l, \\ G_{12} & \text{if } i=j \text{ and } k=l, \\ G_{44} & \text{if } i=k \text{ and } j=l, \\ & \text{or } i=l \text{ and } j=k, \\ 0 & \text{else,} \end{cases} \tag{2.2.12}$$

which is generally anisotropic, described by the 4th-order tensor $\mathbb{G}$. Finally, the electric energy density writes

$$\Psi_{\text{el}}(\boldsymbol{e}) = -\frac{\kappa_0}{2} \boldsymbol{e} \cdot \boldsymbol{e}, \tag{2.2.13}$$

where κ_0 denotes the permittivity of free space. In polycrystals the energy density Ψ is rotated into the local coordinate system of each grain, transforming all vector- and tensor-valued fields according to the local rotation $\boldsymbol{R} \in \mathrm{SO}(n)$.

For a fixed polarization $\boldsymbol{p}$, (2.2.1) and (2.2.2) – along with constitutive relations (2.2.4) – provide an equilibrium solution of the unknown fields $\boldsymbol{u}(\boldsymbol{x}, t) \to \boldsymbol{u}_{\text{eq}}(\boldsymbol{x})$ and $\phi(\boldsymbol{x}, t) \to \phi_{\text{eq}}(\boldsymbol{x})$ as $t \to \infty$. In reality, the polarization $\boldsymbol{p}(\boldsymbol{x}, t)$ evolves over time in a dissipative manner and requires a kinetic evolution law. The latter is usually modeled by the Allen-Cahn equation of a linear gradient flow (Su & Landis, 2007; W. Zhang & Bhattacharya, 2005):

$$\mu \dot{\boldsymbol{p}} = -\frac{\delta W}{\delta \boldsymbol{p}} = -\frac{\partial W}{\partial \boldsymbol{p}} + \nabla \cdot \frac{\partial W}{\partial \nabla \boldsymbol{p}} \tag{2.2.14}$$

with an inverse mobility (or drag coefficient) $\mu > 0$. The unknown fields $\boldsymbol{u}(\boldsymbol{x}, t)$, $\phi(\boldsymbol{x}, t)$, and $\boldsymbol{p}(\boldsymbol{x}, t)$ are now obtained from simultaneously solving linear momentum balance (2.2.1), Gauss' law (2.2.2), and the kinetic evolution law (2.2.14), based on the enthalpy (2.2.3) and constitutive relations (2.2.4). All material parameters used are listed in Tab. 2.1.

Table 2.1: Material constants for tetragonal PZT 50/50 at 0 K from Völker et al. (2011) and simulation parameters used in numerical examples.

material constants used for PZT			
parameter	value	units	source
G_0	$7.0 \cdot 10^{-11}$	$\mathrm{Vm^3/C}$	this work
α_1	$-8.499 \cdot 10^{8}$	Vm/C	Völker et al., 2011
α_{11}	$1.950 \cdot 10^{8}$	$\mathrm{Vm^5/C^3}$	Völker et al., 2011
α_{12}	$-9.750 \cdot 10^{8}$	$\mathrm{Vm^5/C^3}$	Völker et al., 2011
α_{111}	$2.117 \cdot 10^{9}$	$\mathrm{Vm^9/C^5}$	Völker et al., 2011
α_{112}	$1.687 \cdot 10^{10}$	$\mathrm{Vm^{13}/C^7}$	Völker et al., 2011
α_{123}	$4.823 \cdot 10^{9}$	$\mathrm{Vm^9/C^5}$	Völker et al., 2011
Q_{11}	$-2.3386 \cdot 10^{10}$	Vm/C	Völker et al., 2011
Q_{12}	$-3.1528 \cdot 10^{9}$	Vm/C	Völker et al., 2011
Q_{44}	$-1.892 \cdot 10^{10}$	Vm/C	Völker et al., 2011
μ_e	123	GPa	Völker et al., 2011
λ_e	115	GPa	Völker et al., 2011
$a_\mathrm{cub.}$	$4.0119 \cdot 10^{-10}$	m	Völker et al., 2011
$a_\mathrm{tetr.}$	$4.0047 \cdot 10^{-10}$	m	Völker et al., 2011
$c_\mathrm{tetr.}$	$4.0602 \cdot 10^{-10}$	m	Völker et al., 2011
κ_0	$8.854 \cdot 10^{-12}$	F/m	Haynes, 2014
k_B	$1.380 \cdot 10^{-23}$	J/K	Haynes, 2014
θ_C	650	K	Bernhard Jaffe, 1971
μ	$1.0 \cdot 10^{9}$	$\mathrm{kg\ m^3/C^2\ s}$	this work
Δx	$4.0047 \cdot 10^{-10}$	m	this work
Δy	$4.0047 \cdot 10^{-10}$	m	this work

2.3 EXTENSION TO AND EFFECTS OF FINITE TEMPERATURE

To account for temperature dependent material behavior, we modify the above constitutive model as follows: first, we render the *polarization potential* Ψ_pol temperature-dependent; second, we append the *Allen-Cahn evolution*

law (2.2.14) by a stochastic noise term to mimic the effects of thermally induced lattice vibrations. We acknowledge that this is a first-order approximation; i.e., we modify those terms which, in our view, show the strongest influence on the resulting predicted material response. In principle, we could also account for temperature-dependent elastic and coupling coefficients as well as mobility. Further, one could consider heat conduction, thermal expansion, and thermal heating due to the dissipative evolution kinetics. Here, we assume that all these contributions have a marginal impact on the ferroelectric hysteresis and the microstructural domain evolution compared to the two former aspects taken into account. We therefore assume a uniform known temperature across the RVE and simulate the material response at different temperatures. We note that, for more accurate predictions, the effects of thermal expansion should be included in the model in order to account for secondary pyroelectricity and for thermally induced stresses at GBs in the polycrystalline case. As we simulate unconstrained, elastically isotropic samples under isothermal conditions, we neglect thermal expansion.

2.3.1 *Temperature-dependent polarization potential*

We exploit our knowledge of the zero-temperature polarization potential of tetragonal PZT from Völker et al. (2011) as well as of the paraelectric phase implying a convex potential landscape at the Curie temperature θ_C. In general, the polarization potential at a finite temperature θ is unknown and must be modeled properly between $\theta = 0\text{K}$ and $\theta = \theta_C$. Following L. D. Landau (1908) and Devonshire (1949), we introduce a linear interpolation of the polarization potential with respect to temperature θ, such that the polarization enthalpy density in 3D becomes

$$\begin{aligned} W_{\text{pol}}(\boldsymbol{p}, \boldsymbol{e}, \theta) &= \Psi_{\text{pol}}(\boldsymbol{p}, \theta) - \boldsymbol{e} \cdot \boldsymbol{p} \\ &= \alpha_1 \frac{\theta_C - \theta}{\theta_C} (p_1^2 + p_2^2 + p_3^2) + \alpha_{11} (p_1^4 + p_2^4 + p_3^4) \\ &\quad + \alpha_{12} \frac{\theta_C - \theta}{\theta_C} (p_1^2 p_2^2 + p_2^2 p_3^2 + p_1^2 p_3^2) + \alpha_{111} (p_1^6 + p_2^6 + p_3^6) \\ &\quad + \alpha_{112} \left[p_1^4 (p_2^2 + p_3^2) + p_2^4 (p_1^2 + p_3^2) + p_3^4 (p_1^2 + p_2^2) \right] \\ &\quad + \alpha_{123}\, p_1^2 p_2^2 p_3^2 - \boldsymbol{e} \cdot \boldsymbol{p}, \end{aligned} \tag{2.3.1}$$

where $p_i = \boldsymbol{p} \cdot \hat{\boldsymbol{e}}_i$ denotes the polarization component in the x_i-direction, and the Cartesian unit vectors $\hat{\boldsymbol{e}}_i$ ($i = 1, 2, 3$ in three dimensions) are chosen to align with the tetragonal crystal axes $\langle 100 \rangle$, $\langle 010 \rangle$, and $\langle 001 \rangle$. α_1 through α_{123} are material constants adopted from the DFT-based 0K potential of Völker et al. (2011), see Tab. 2.1.

Due to symmetry of the tetragonal unit cell, the polarization potential $\Psi_{\text{pol}}(\boldsymbol{p}, \theta)$ has six minima (and $2n$ minima in n dimensions in general). In those polarization states, the polarization is aligned with one of the tetragonal crystal axes and $\boldsymbol{p}(\theta) = \pm p_0(\theta)\, \hat{\boldsymbol{e}}_i$, where $p_0(\theta) > 0$ denotes the (now temperature-dependent) spontaneous polarization. Consider now a ferroelectric single-crystal forming a single, homogeneous domain, whose polarization is aligned with one of the tetragonal crystal axes. In the absence of any external mechanical or electrical loading ($\boldsymbol{e} = \boldsymbol{0}$), minimizing the electric enthalpy (which is equivalent to minimizing (2.3.1)) with respect to the polarization and considering only positive and real solutions $p_0 \in \mathbb{R}^+$ identifies the temperature-dependent spontaneous polarization as

$$p_0(\theta) = \sqrt{\frac{\sqrt{\alpha_{11}^2 - 3\alpha_1\alpha_{111}\frac{\theta_C - \theta}{\theta_C}} - \alpha_{11}}{3\alpha_{111}}} \qquad \text{for} \quad \theta \leq \theta_C. \tag{2.3.2}$$

We note that (2.3.2) is identical to the theory of Devonshire (1949) only in the limit $|(\theta_C - \theta)/\theta_C| \ll 1$, in which case a Taylor expansion of (2.3.2) results in the classical relation $p_0^2 = \beta(\theta_C - \theta)/\alpha_{11}$ with a constant $\beta > 0$. By contrast, we here do not make this simplifying assumption since we aim to cover the full temperature range from 0K to the Curie point (and we will demonstrate that retaining the exact form (2.3.2) is important to arrive at accurate predictions).

A further intrinsic ferroelectric property, which is predicted by Landau-Devonshire theory, is the coercive field e_c, which refers to the electric field required in a single-crystal for complete 180° polarization reversal. Considering a stress-free single-domain single-crystal with an applied electric field (aligned with a tetragonal crystal axis), we solve $\partial W_{\text{pol}}(\boldsymbol{p}, \boldsymbol{e}, \theta)/\partial p_i = 0$ using (2.3.1) with $\boldsymbol{p} = p\hat{\boldsymbol{e}}_i$, $\boldsymbol{e} = e\hat{\boldsymbol{e}}_i$, to find a relation between the electric field e and the equilibrium polarization p (at a given temperature θ), viz.

$$e(p, \theta) = 2\alpha_1 \frac{\theta_C - \theta}{\theta_C} p + 4\alpha_{11} p^3 + 6\alpha_{111} p^5. \tag{2.3.3}$$

This relation is visualized in Fig. 2.2 for various temperatures. The coercive field corresponds to the local maximum in the electric field (illustrated as

dashed lines in Fig. 2.2) and hence follows from solving $\partial^2 W_{\mathrm{pol}}/\partial p_i^2 = 0$ for $p^* = p^*(\theta)$ and inserting the solution into (2.3.3) so $e_{\mathrm{c}}(\theta) = |e(p^*(\theta), \theta)|$. We omit the lengthy analytical solution here. For this 1D scenario, the temperature-dependent polarization potential and its corresponding electric field are plotted as functions of the polarization for various temperatures in Fig. 2.2. The minima in the polarization potential are located at $\pm\, p_{\mathrm{o}}(\theta)$, whereas the coercive field is identified as the points of bifurcation in the electric hysteresis.

2.3.2 *Thermal fluctuations via stochastic noise*

While the above temperature-dependent potential reflects variations in the spontaneous polarization and coercive field, it affects the kinetics of ferroelectric switching only through changes in the driving force (due to changes in the energy landscape). This, however, neglects another important effect of temperature. In any ferroelectric sample, the abundant network of defects (including point defects such as oxygen vacancies as well as higher-dimensional defects such as GBs and existing domain walls)

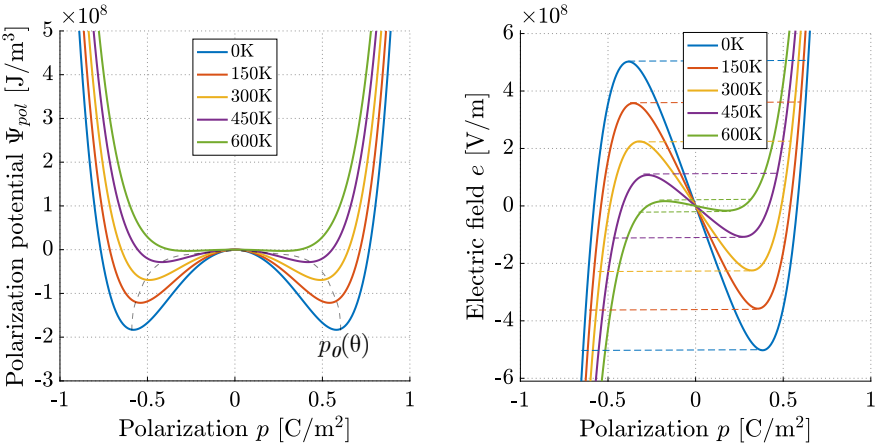

Figure 2.2: Influence of temperature on the polarization potential $\Psi_{\mathrm{pol}}(p, \theta)$ (left) and the corresponding electric field $e(p, \theta)$ (right) for a single-domain single-crystal and an electric field parallel to the polarization. The minima of $\Psi_{\mathrm{pol}}(p, \theta)$ are at $\pm p_0(\theta)$, whereas the local maxima/minima of the electric field represent the coercive field $\pm e_{\mathrm{c}}(\theta)$ (indicated as dashed lines).

serves as nucleation sites for the heterogeneous nucleation of new domains, while also impeding domain wall motion through pinning and drag effects (Jo et al., 2009; Puchberger et al., 2017). Such mechanisms are generally temperature-dependent, and one underlying causal mechanism are atomic lattice vibrations whose amplitude grows with temperature. Although generally being of small amplitude compared to the atomic unit cell rearrangements during ferroelectric switching, these small perturbations can be sufficient for promoting nucleation and growth of domains by helping the material locally overcome the respective energy barriers. Simply put, not only do energy wells in the potential of Fig. 2.2 become shallower with increasing temperature, but also do atoms fluctuate at higher amplitude within those wells, which promotes switching to the respective other well and hence increases the escape rate, especially near lattice defects.

Because it is neither possible nor desirable to compute the motion of individual atoms inside the RVE, we here use a statistical mechanics-based approach to capture the influence of atomic vibrations by amending the polarization kinetics to include a term of Brownian motion at the RVE-/mesoscale. Specifically, we turn the Allen-Cahn equation (2.2.14) into the stochastic form in the following Section.

2.3.2.1 *Derivation of the stochastic noise term*

To account for the effect of thermal fluctuations in the ferroelectric constitutive model, we briefly revisit the random walk concept and Brownian motion, starting in 1D for simplicity. We begin with the Langevin equation (Langevin, 1908), considering only the overdamped solution (inertial terms are neglected) with a polarization p that is attached to its equilibrium position p_0 through a potential $W(p)$ and has an inverse mobility μ. With the added random-walk term $\eta(t)$, the equation of motion becomes

$$0 = -\frac{\partial W}{\partial p} - \mu\dot{p} + \mu\eta \qquad \Leftrightarrow \qquad \dot{p} = -\frac{1}{\mu}\frac{\partial W}{\partial p} + \eta. \tag{2.3.4}$$

The double-well potential $W(p)$ keeps the polarization close to the spontaneous polarization p_0 and prevents it from drifting over time. Therefore, we expect that the variance of the polarization does not diffuse to zero over time but that the distance from the equilibrium position remains bounded, so that states far from p_0 (of high energy) become unlikely (even more so than before). The viscous damping slows down the polarization motion and we expect that over long times the polarization may not assume an

equilibrium position (the random noise prevents this) but will attain an equilibrium distribution with constant mean and variance.

One may expect that over long times ($t \to \infty$) this process attains a thermal equilibrium, for which the probability of finding a polarization p is given by a Boltzmann distribution (Boltzmann, 1868; Gibbs, 1902)

$$\rho(p) = \frac{1}{Z} \exp\left(-\frac{V(p)}{k_\mathrm{B}\theta}\right) \qquad \text{with} \qquad Z = \int_{-\infty}^{\infty} \exp\left(-\frac{V(p)}{k_\mathrm{B}\theta}\right) \mathrm{d}p \tag{2.3.5}$$

with temperature θ, Boltzmann's constant k_B and the energy $V(p) = V_\mathrm{char} W(p)$, where V_char denotes a characteristic volume used for normalization (since W is an energy density, V_char is required to arrive at an energy and may be interpreted as the volume of the material or grid point of interest). The question now is how to choose $\eta(t)$ such that we indeed attain thermal equilibrium in the long-term limit as $t \to \infty$.

Let us discretize the governing equation (2.3.4) in time with a constant step size $\Delta t > 0$, so that applying a first-order forward-Euler finite-difference stencil leads to

$$\begin{aligned} \frac{p(t+\Delta t) - p(t)}{\Delta t} &= -\frac{1}{\mu}\frac{\partial W}{\partial p}\big(p(t)\big) + \eta(t) \\ \Rightarrow \qquad p(t+\Delta t) &= p(t) + v\big(p(t)\big)\Delta t + \eta_{\Delta t}(t), \end{aligned} \tag{2.3.6}$$

where we defined

$$v(p) = -\frac{1}{\mu}\frac{\partial W}{\partial p}(p) \tag{2.3.7}$$

and $\eta_{\Delta t}(t) = \Delta t\, \eta(t)$ is a short notation for the random fluctuation (whose amplitude needs to be found, so multiplication by the time step does not affect the final result).

If we look only at the stochastic contribution to the polarization change, then

$$p(t+\Delta t) = p(t) + \eta_{\Delta t}(t). \tag{2.3.8}$$

As for a random walk, we require the random noise term to have zero mean and to be uncorrelated, i.e., respectively,

$$\begin{aligned} \langle \eta_{\Delta t}(t) \rangle &= \int_0^\infty \eta_{\Delta t}(t)\, \mathrm{d}t = 0 \qquad \text{and} \\ \langle \eta_{\Delta t}(t)\eta_{\Delta t}(t') \rangle &= \int_0^\infty \eta_{\Delta t}(\tau)\eta_{\Delta t}(\tau + t - t')\, \mathrm{d}\tau = 2D^*\delta(t-t') \end{aligned} \tag{2.3.9}$$

with some constant diffusion coefficient $D^* \geq 0$ that captures the (yet to be determined) noise amplitude. After n time steps, the random noise has altered the solution by

$$\begin{aligned} p(t+n\Delta t) &= p(t) + \eta_{\Delta t}(t) + \eta_{\Delta t}(t+\Delta t) + \ldots + \eta_{\Delta t}\big(t+(n-1)\Delta t\big) \\ &= p(t) + \sum_{i=0}^{n-1} \eta_{\Delta t}(t+i\Delta t). \end{aligned} \tag{2.3.10}$$

By exploiting the uncorrelated nature of noise from distinct time steps, we conclude that the mean squared difference between the initial and final position over the above n steps is

$$\begin{aligned} \Big\langle [p(t+n\Delta t) - p(t)]^2 \Big\rangle &= \left\langle \left[\sum_{i=0}^{n-1} \eta_{\Delta t}(t+i\Delta t) \right]^2 \right\rangle \\ &= \sum_{i=0}^{n-1} \langle \eta_{\Delta t}^2(t+i\Delta t) \rangle = n \, \langle \eta_{\Delta t}^2(t) \rangle. \end{aligned} \tag{2.3.11}$$

Assuming an unbiased random walk, this implies that, with the total elapsed time $n\,\Delta t$,

$$\Big\langle [p(t+n\Delta t) - p(t)]^2 \Big\rangle = 2D\, n\, \Delta t, \tag{2.3.12}$$

so that a comparison of (2.3.11) and (2.3.12) yields

$$\langle \eta_{\Delta t}^2(t) \rangle = 2D\Delta t. \tag{2.3.13}$$

Such a scenario is achieved by choosing a Gaussian noise of average 0 and amplitude $2D\Delta t$, whose probability distribution is (Gauss, 1809; Laplace, 1774)

$$\rho(\eta_{\Delta t}) = \frac{1}{\sqrt{4\pi D \Delta t}} \exp\left(-\frac{\eta_{\Delta t}^2}{4D\Delta t} \right). \tag{2.3.14}$$

Next, we consider the full governing equation (2.3.6), including the non-convex potential, to identify the unknown constant D. We start with

$$p(t+\Delta t) = p(t) + v(p)\Delta t + \eta_{\Delta t}(t). \tag{2.3.15}$$

Using a generalized version of the time evolution of the probability distribution, we may write

$$\rho(p, t+\Delta t) = \int_{-\infty}^{\infty} P_{\Delta t}(p,q)\rho(q,t)\,\mathrm{d}q, \tag{2.3.16}$$

where $P_{\Delta t}(p,q)$ is the probability that the particle moves from q at time t to the position p at time $t+\Delta t$, and we integrate over all possible positions q. (2.3.16) is known as the *Chapman-Kolmogorov equation* (Kampen, 2007). Moving from q to p in our scenario implies that $p = q + v(q)\Delta t + \eta_{\Delta t}(t)$, cf. (2.3.15). Simply speaking, the random noise term has the right magnitude to help move the particle from q to p (while the potential is also acting). The probability that the noise has exactly a magnitude of $\eta_{\Delta t} = p - q - v(q)\Delta t$ is defined by the Gaussian distribution (2.3.14):

$$P_{\Delta t}(p,q) = \frac{1}{\sqrt{4\pi D\Delta t}} \exp\left(-\frac{[p-q-v(q)\Delta t]^2}{4D\Delta t}\right). \tag{2.3.17}$$

A *Kramers-Moyal expansion* (Kramers, 1940; Moyal, 1949) of the *master equation* (Kampen, 2007) is used to finally derive the well-known *Fokker-Planck equation* (Fokker, 1914; Kolmogoroff, 1931; Planck, 1917)

$$\begin{aligned}\frac{\mathrm{d}\rho}{\mathrm{d}t}(p,t) &= -\frac{\partial\, v(p)\rho(p,t)}{\partial p} + D\frac{\partial^2\rho(p,t)}{\partial p^2} \\ &= \frac{1}{\mu}\frac{\partial}{\partial p}\left[\frac{\partial W(p(t))}{\partial p}\rho(p,t)\right] + D\frac{\partial^2\rho(p,t)}{\partial p^2},\end{aligned} \tag{2.3.18}$$

where we inserted the definition of ν from (2.3.7).

If we assume that this probability distribution will – over long time – evolve into a *steady state*

$$\rho_{\mathrm{eq}}(p) = \lim_{t\to\infty}\rho(p,t), \tag{2.3.19}$$

then we may find that equilibrium distribution by solving

$$0 = \frac{1}{\mu}\frac{\partial}{\partial p}\left[\frac{\partial W}{\partial p}(p)\,\rho_{\mathrm{eq}}(p)\right] + D\frac{\partial^2\rho_{\mathrm{eq}}(p)}{\partial p^2}. \tag{2.3.20}$$

It is straightforward to verify by substitution that the following presents a solution:

$$\rho_{\mathrm{eq}}(p) = \frac{1}{Z}\exp\left(-\frac{W(p)}{\mu D}\right) \qquad \text{with} \qquad Z = \int_{-\infty}^{\infty}\exp\left(-\frac{W(p)}{\mu D}\right)\mathrm{d}p. \tag{2.3.21}$$

Notice that solution (2.3.21) has exactly the form of the Boltzmann distribution (2.3.5) if we choose

$$D = \frac{k_{\mathrm{B}}\theta}{\mu V_{\mathrm{char}}}. \tag{2.3.22}$$

Therefore, in the limit of long times, the probability distribution approaches the steady-state Boltzmann distribution

$$\rho_{\mathrm{eq}}(p) = \frac{1}{Z}\exp\left(-\frac{V(p)}{k_{\mathrm{B}}\theta}\right) \qquad \text{with} \qquad Z = \int_{-\infty}^{\infty}\exp\left(-\frac{V(p)}{k_{\mathrm{B}}\theta}\right)\mathrm{d}p, \tag{2.3.23}$$

if we choose the random noise (using (2.3.13)) according to

$$\langle \eta_{\Delta t}(t)\rangle = 0 \qquad \text{and} \qquad \langle \eta_{\Delta t}(t)\eta_{\Delta t}(t')\rangle = \frac{2k_{\mathrm{B}}\theta}{\mu V_{\mathrm{char}}}\Delta t\,\delta(t-t'). \tag{2.3.24}$$

This defines the temperature-dependent random noise term in 1D. Since the random noise term must satisfy these relations in each direction (and at every point inside the RVE), the generalization to 3D leads directly to the following relation

$$\mu\dot{\boldsymbol{p}} = -\frac{\delta W}{\delta \boldsymbol{p}} + \mu\boldsymbol{\eta} = -\frac{\partial W}{\partial \boldsymbol{p}} + \nabla\cdot\frac{\partial W}{\partial \nabla\boldsymbol{p}} + \mu\boldsymbol{\eta}, \tag{2.3.25}$$

in which $\boldsymbol{\eta}(\boldsymbol{x},\theta)$ represents a random noise term that mimics the effect of lattice vibrations. To comply with the second law of thermodynamics, we consider only conditions of constant uniform temperature θ within the RVE. Furthermore, we require that the noise term satisfies the following constraints:

1. For a truly stochastic noise that does not bias the evolution of the polarization field $\boldsymbol{p}$ in any direction, the random noise must average to zero over time at any point within the simulated RVE:

$$\langle \boldsymbol{\eta}(\boldsymbol{x},t)\rangle_t = \int_0^{\tau}\boldsymbol{\eta}(\boldsymbol{x},t)\,\mathrm{d}t = \boldsymbol{0} \qquad \text{for all } \boldsymbol{x}\in\Omega, \tag{2.3.26}$$

   with any sufficiently large time window $\tau > 0$.

2. The random noise must average to zero over the RVE at any given time:

$$\langle \boldsymbol{\eta}(\boldsymbol{x},t)\rangle_\Omega = \int_\Omega \boldsymbol{\eta}(\boldsymbol{x},t)\,\mathrm{d}V = \boldsymbol{0} \qquad \text{for all } t\geq 0. \tag{2.3.27}$$

3. The random noise is uncorrelated in space and time, and its variance σ^2 depends on temperature θ and time increment Δt according to

$$\langle \boldsymbol{\eta}(\boldsymbol{x},t),\boldsymbol{\eta}(\boldsymbol{x}',t')\rangle_{t,\Omega} = \frac{2k_{\mathrm{B}}\theta}{\mu V_{\mathrm{char}}\Delta t}\delta(t-t')\,\delta(\boldsymbol{x}-\boldsymbol{x}'), \tag{2.3.28}$$

where $V_{\text{char}} = a_{\text{tetr}}^2 c_{\text{tetr}}$ is the volume of the perovskite's atomic unit cell, which is used for normalization of the thermodynamic potential. We do not account for local variations in the lattice volume V_{char}, which could be important for a more accurate representation of GBs and multiple, low-symmetry phases. As detailed in the above derivation of the random noise term, the correlation constraint (2.3.28) stems from a statistical mechanics consideration, interpreting the random noise term analogous to a random walk whose overall effect, over sufficiently long times, obeys a Boltzmann-type equilibrium probability distribution. By solving the associated Fokker-Planck equation in the equilibrium limit, the above condition (2.3.28) emerges.

The modified Allen-Cahn equation (2.3.25) for the polarization field, along with the conditions (2.3.26)-(2.3.28), effects a kinetic evolution of the polarization that depends on temperature in a stochastic sense – and the thermal fluctuations grow with increasing temperature according to (2.3.28). To enforce the above conditions in practice, we pick real, uncorrelated random numbers out of a standard normal distribution $\mathcal{N}(\mu, \sigma^2)$ with mean $\mu = 0$ and variance $\sigma^2 = 1$. This is achieved, e.g., by the Muller-Box sampling (Muller, 1958) or the polar method of Marsaglia and Bray (1964). For 3D simulations, noise is generated by picking random numbers $\{x_1, x_2, x_3\}$ at each time step and for each point inside the RVE, so that rescaling gives the sought random noise (at each discrete time step and at each point) as

$$\boldsymbol{\eta}_{\Delta t} = \sqrt{\frac{2k_{\text{B}}\theta\,\Delta t}{\mu V_{\text{char}}}} \sum_{i=1}^{3} x_i \hat{\boldsymbol{e}}_i \qquad \text{with} \qquad \{x_1, x_2, x_3\} \sim \mathcal{N}(0,1). \tag{2.3.29}$$

We point out that the stochastic Allen-Cahn equation is assumed ill-posed for dimensions $n \geq 2$ (i.e., its continuum limit does not have a reasonable meaning), which may introduce mesh dependence (Ryser et al., 2012). In our scenario, however, there exists a natural, finite length scale, since the electric dipole within the atomic unit cell is the smallest unit exposed to lattice vibrations acting on the surrounding ions. Hence, the size of the atomic-level unit cell (of volume V_{char}) provides a physical length scale that relates the random noise to the numerical discretization Δx used in simulations. Choosing Δx at the level of the atomic unit cell hence provides a reasonable solution. (While shrinking the mesh size below the atomic unit cell is physically questionable, coarser grids generally underestimate the number of possible nucleation sites and therefore slow down the switching

kinetics.) An alternative would be to regularize the noise with a correlation length that depends on the length scale of the dipole-dipole interactions (see, e.g., R. V. Kohn et al. (2007) for an investigation of the stochastic Allen-Cahn equation at the sharp-interface limit by using large-deviation theory). Here, the interface energy introduces a characteristic length scale for dipole-dipole interactions, which acts as a natural regularization by limiting the impact of a unit cell's noise on its neighbors.

2.4 HOMOGENIZATION PROBLEM

The constitutive material law introduced in Sections 2.2 to 2.3 describes the behavior of a ferroelectric perovskite at the single-crystal, single-domain level. The transition from that scale to the macroscale is accomplished by computing the effective response of a Representative Volume Element (RVE), as is customary in classical first-order homogenization (see e.g. Miehe et al. (2002) and Schröder (2009)). For a sample with an approximately statistically homogeneous microstructure, we hence define an effective property as the volume average over the RVE, writing

$$\langle \cdot \rangle = \frac{1}{|\Omega|} \int_{\Omega} (\cdot) \, \mathrm{d}V, \tag{2.4.1}$$

where $|\Omega|$ denotes the volume of the RVE. We solve the balance of linear momentum (2.2.1) and Gauss' law (2.2.2), while imposing periodic boundary conditions over the surface (or boundary in 2D) of the RVE. Technically, we decompose the RVE boundary into opposite parts such that $\partial\Omega = \partial\Omega^+ \cup \partial\Omega^-$, and we enforce

$$\begin{aligned} \boldsymbol{u}(\boldsymbol{x}^+,t) - \boldsymbol{u}(\boldsymbol{x}^-,t) &= \boldsymbol{\varepsilon}^0 \left(\boldsymbol{x}^+ - \boldsymbol{x}^-\right) \quad \text{and} \quad \boldsymbol{t}(\boldsymbol{x}^+,t) = -\boldsymbol{t}(\boldsymbol{x}^-,t) \quad \text{on } \partial\Omega, \\ \phi(\boldsymbol{x}^+,t) - \phi(\boldsymbol{x}^-,t) &= \boldsymbol{e}^0 \cdot \left(\boldsymbol{x}^+ - \boldsymbol{x}^-\right) \quad \text{and} \quad \boldsymbol{d}(\boldsymbol{x}^+,t) = -\boldsymbol{d}(\boldsymbol{x}^-,t) \quad \text{on } \partial\Omega, \end{aligned} \tag{2.4.2}$$

where $\boldsymbol{x}^+$ and $\boldsymbol{x}^-$ are pairs of opposing points on $\partial\Omega^+$ and $\partial\Omega^-$, respectively. The volume-averaged strain is denoted by $\boldsymbol{\varepsilon}^0 = \langle \boldsymbol{\varepsilon} \rangle$ and volume-averaged electric field is $\boldsymbol{e}^0 = \langle \boldsymbol{e} \rangle$. For homogenization to work, we assume a separation of scales and we postulate that body and inertial forces are negligible since we are interested in the quasistatic material behavior; hence the mechanical and electrical RVE problems are solved quasi-statically.

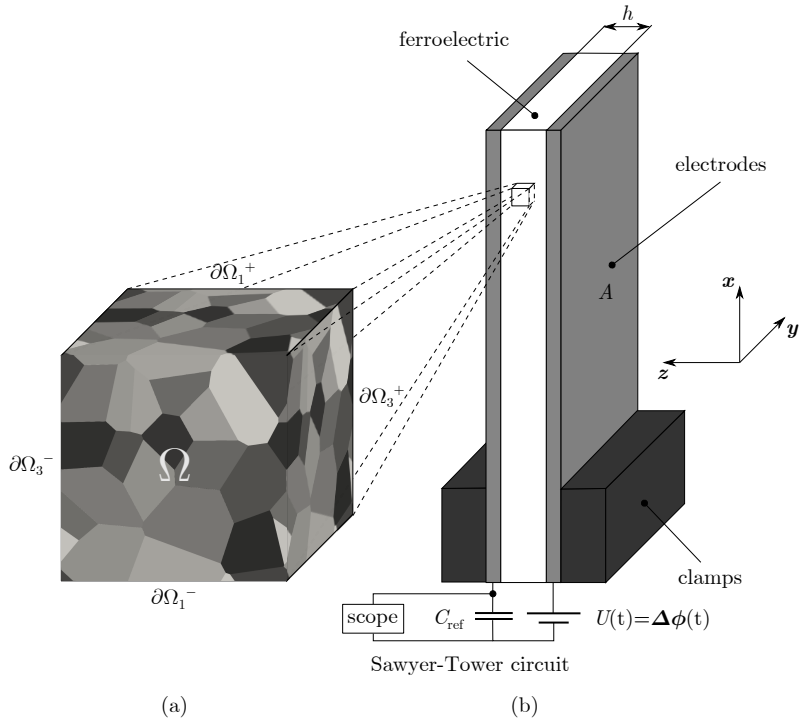

Figure 2.3: Schematic of (b) the experimental setup showing a ferroelectric specimen (white) coated with two metallic electrodes on opposite sides (gray) and clamped on the bottom end (black) and (a) the numerical setup visualized by the polycrystalline RVE, which corresponds to the cubic-shaped volume $V = L^3$ of the bulk material indicated in (b). In the Sawyer-Tower circuit, the accumulated charges Q at a reference capacitor with capacitance C_{ref} are measured over time along with the applied voltage $U(t)$ across the sample thickness h.

The only time-dependent governing equation, the modified Allen-Cahn equation (2.3.25), is solved by assuming the periodic boundary conditions

$$\boldsymbol{p}(\boldsymbol{x}^+, t) = \boldsymbol{p}(\boldsymbol{x}^-, t), \tag{2.4.3}$$

which does not impose an average but instead allows the polarization field to evolve freely (aside from periodicity on the RVE surfaces).

In our experiments (Kannan & Kochmann, 2022; Kannan et al., 2022; le Graverend et al., 2015; W. L. Tan et al., 2019; Wojnar et al., 2014), a uniform electric field $\bar{e} = \Delta\phi/h$ is applied over the specimen thickness h, with $\Delta\phi$

denoting the corresponding voltage differential. In this setup, the electric field is applied at the macroscale, thus we assume a separation of scales. The measured electric charge Q can be directly linked to the average electric displacement $\bar{d} = Q/A$, viz. (Vidyasagar et al., 2017)

$$\begin{aligned} \frac{Q}{A}\boldsymbol{z} = \frac{Q}{V}h\boldsymbol{z} = \frac{1}{V}\int_{\partial\Omega} q_s \boldsymbol{x}\, \mathrm{d}s = \frac{1}{V}\int_{\Omega} \nabla\cdot(\boldsymbol{x}\otimes\boldsymbol{d})\, \mathrm{d}v \\ = \frac{1}{V}\int_{\Omega} (\boldsymbol{x}\,\nabla\cdot\boldsymbol{d} + \boldsymbol{d})\, \mathrm{d}v = \frac{1}{V}\int_{\Omega} \boldsymbol{d}\, \mathrm{d}v = \langle \boldsymbol{d}\rangle, \end{aligned} \tag{2.4.4}$$

where A is the area of the electrodes, z the unit vector pointing through the sample thickness and q_s the charge density, see Fig. 2.3. We emphasize that our study is dedicated to the bulk response of ferroelectric ceramics and not to thin films exhibiting considerable free-surface effects. As a consequence, the depolarization field plays only a marginal role, such that the above relations hold and we may assume that the applied voltage differential can be directly interpreted as the average applied electric field at the RVE-level.

Finally, since both the electric field $\bar{\boldsymbol{e}} = \langle \boldsymbol{e}\rangle = \boldsymbol{e}^0$ and the electric displacement $\bar{\boldsymbol{d}} = \langle \boldsymbol{d}\rangle$ are related to their measured counterparts, the average polarization $\bar{\boldsymbol{p}}$ (based on an isotropic permittivity) is obtained as

$$\langle \boldsymbol{p}\rangle = \langle \boldsymbol{d}\rangle - \kappa_0 \langle \boldsymbol{e}\rangle. \tag{2.4.5}$$

This allows a for direct comparison of the measured polarization obtained in experiments at the macroscale and the homogenized polarization over a RVE based on numerical simulations at the mesoscale.

2.5 SPECTRAL SOLUTION SCHEME

We follow the approach of Vidyasagar et al. (2017) and solve all governing equations in Fourier space, encouraged by the periodic homogenization scheme. To this end, we discretize the cubic-shaped RVE of side length L into N grid points in each dimension, such that the position vector over all grid points becomes $\boldsymbol{x} = \{\boldsymbol{x}_1, \ldots, \boldsymbol{x}_{3N}\}$. For any function $f(x)$, we define its inverse discrete Fourier transform as

$$f(\boldsymbol{x}) = \mathcal{F}^{-1}\left(\hat{f}\right) = \sum_{\boldsymbol{k}\in\mathcal{T}} \hat{f}(\boldsymbol{k})\, \exp\left(i\boldsymbol{k}\cdot\boldsymbol{x}\right) \qquad \text{and} \qquad i = \sqrt{-1}, \tag{2.5.1}$$

where $\boldsymbol{k} = \{\boldsymbol{k}_1, \ldots, \boldsymbol{k}_{3N}\}$ denotes the wave vector in the reciprocal lattice (the complete set being $\mathcal{T}$), and $\hat{f}(\boldsymbol{k})$ are the Fourier coefficients.

2.5.1 *Electrical and mechanical problem*

In the absence of free charges, negligible body, and acceleration forces, the electrical and mechanical problems simplify both to equilibrium equations, which can be solved independently from one another for a given polarization $\boldsymbol{p}(\boldsymbol{x}, t)$ at a certain time t. To this end, we solve Gauss' law (2.2.2) in Fourier space to obtain the complex electric field as, respectively,

$$\hat{\phi}_p(\boldsymbol{k}) = -i\frac{\boldsymbol{k}\cdot\hat{\boldsymbol{p}}(\boldsymbol{k})}{\kappa_0|\boldsymbol{k}|^2} \quad \Rightarrow \quad \hat{\boldsymbol{e}}(\boldsymbol{k}) = -i\boldsymbol{k}\hat{\phi}_p(\boldsymbol{k}) = \begin{cases} -\dfrac{\boldsymbol{k}\cdot\hat{\boldsymbol{p}}(\boldsymbol{k})}{\kappa_0|\boldsymbol{k}|^2}\boldsymbol{k}, & \text{if } \boldsymbol{k} \neq \boldsymbol{0}, \\ \boldsymbol{e}^0, & \text{if } \boldsymbol{k} = \boldsymbol{0}, \end{cases} \tag{2.5.2}$$

where we impose the average electric field $\boldsymbol{e}^0$ through the case $\boldsymbol{k} = \boldsymbol{0}$. The voltage potential ϕ is not an independent variable in our ferroelectric constitutive model. For completeness, nevertheless, it can be computed by adding the non-periodic contribution to the symmetric potential field $\phi_p(\boldsymbol{x})$ through the imposed average electric $\boldsymbol{e}^0$ as follows:

$$\phi(\boldsymbol{x}) = \phi_p(\boldsymbol{x}) - \frac{1}{\kappa_0}\boldsymbol{e}^0 \cdot \left(\boldsymbol{x} - \frac{\boldsymbol{L}}{2}\right) + \phi^0. \tag{2.5.3}$$

Note that the second term is an odd function, i.e., it does not contribute to the average electric potential $\langle\phi\rangle$, which is imposed by ϕ^0.

The mechanical problem governed by the balance of linear momentum (2.2.1) requires an iterative solution strategy with a perturbation stress $\boldsymbol{\tau}(\boldsymbol{x})$ and a reference stiffness tensor $\mathbb{C}^0 = \langle\mathbb{C}(\boldsymbol{x})\rangle$ to account for the heterogeneity of the elastic stiffness tensor $\mathbb{C}(\boldsymbol{x})$ (see references Lebensohn et al. (2012) and Moulinec and Suquet (1998, 2003)), such that the stress tensor takes the form

$$\sigma_{ij}(\boldsymbol{x}) = \mathbb{C}^0_{ijkl}\varepsilon_{kl}(\boldsymbol{x}) - \tau_{ij}(\boldsymbol{x}). \tag{2.5.4}$$

Applying the divergence operator to the equation above and solving for the complex strains in Fourier space results in

$$\hat{\varepsilon}_{ij}(\boldsymbol{k}) = \begin{cases} \dfrac{1}{2}\left[A^{-1}_{ni}(\boldsymbol{k})k_m k_j + A^{-1}_{nj}(\boldsymbol{k})k_m k_i\right]\left[\hat{\tau}_{nm}(\boldsymbol{k}) + \tilde{\mathbb{C}}^0_{nmkl}\hat{\varepsilon}^r_{kl}(\boldsymbol{k})\right], & \boldsymbol{k} \neq \boldsymbol{0}, \\ \varepsilon^0_{ij}, & \boldsymbol{k} = \boldsymbol{0}, \end{cases} \tag{2.5.5}$$

where ε^r_{kl} denotes the electrostrictive strain, ε^0_{ij} the imposed average strain tensor, and $A_{ik}(\boldsymbol{k}) = \mathbb{C}^0_{ijkl}k_j k_l$ is the acoustic tensor. The strain dependence

of the perturbation stress $\boldsymbol{\tau}$ demands an iterative solution scheme, which makes this solution strategy computationally expensive.

2.5.2 *Ferroelectric problem*

We discretize the modified Allen-Cahn equation by an implicit backward-Euler finite-difference scheme, based on time increments $\Delta t > 0$ such that $t^n = n\,\Delta t$. Thus, (2.3.25) is turned into

$$\mu\,\frac{p_i^{n+1} - p_i^n}{\Delta t} = \left[-\frac{\partial W}{\partial p_i}(\boldsymbol{p}^{n+1}) + \left(\frac{\partial W}{\partial p_{i,j}}(\boldsymbol{p}^{n+1})\right)_{,j}\right] + \mu\,\eta_i^n \tag{2.5.6}$$

for every grid point inside the RVE, where $\boldsymbol{p}^{n+1} = \boldsymbol{p}(\boldsymbol{x}, t^n + \Delta t)$ and $\boldsymbol{p}^n = \boldsymbol{p}(\boldsymbol{x}, t^n)$ denote the polarization at the current and previous time increment, respectively, and $\boldsymbol{\eta}^n = \boldsymbol{\eta}(\boldsymbol{x}, t^n)$ the thermal fluctuations introduced in Section 2.3.2. Note that the first and second term represent the deterministic contribution to the polarization evolution, whereas the last term is purely stochastic, due to the constraints (2.3.26)-(2.3.28). For convenience, we define a thermodynamic driving force with components

$$f_i(\boldsymbol{\varepsilon}, \boldsymbol{e}, \boldsymbol{p}) = -\frac{\partial W}{\partial p_i} = \left[e_i - \frac{\partial \Psi_{\text{coupl}}}{\partial p_i} - \frac{\partial \Psi_{\text{pol}}}{\partial p_i}\right], \tag{2.5.7}$$

and the nonlocal gradient term, which is computed in Fourier space, is evaluated as

$$g_i(\boldsymbol{p}) = \left(\frac{\partial W}{\partial p_{i,j}}\right)_{,j} = \left(\frac{\partial \Psi_{\text{inter}}}{\partial p_{i,j}}\right)_{,j} = G_0 p_{i,jj} = \mathcal{F}^{-1}\left\{G_0\,|\boldsymbol{k}|^2\,\hat{p}_i\right\}. \tag{2.5.8}$$

The overall ferroelectric problem is solved in a time-incremental, staggered manner. We first solve for the electric field $\hat{\boldsymbol{e}}^{n+1}$ and the strains $\hat{\boldsymbol{\varepsilon}}^{n+1}$ in Fourier space, using Eqns. (2.5.5) and (2.5.2) based on the polarization $\boldsymbol{p}^n$ from the previous time step. Applying the inverse Fourier transform yields the real-space quantities $\boldsymbol{e}^{n+1}$ and the strains $\boldsymbol{\varepsilon}^{n+1}$ at all RVE grid points. Next, using implicit Euler time integration to solve

$$p_i^{n+1} = p_i^n + \frac{\Delta t}{\mu}\left[f_i(\boldsymbol{\varepsilon}^{n+1}, \boldsymbol{e}^{n+1}, \boldsymbol{p}^{n+1}) + g_i(\boldsymbol{p}^{n+1})\right] + (\eta_{\Delta t})_i^n, \tag{2.5.9}$$

leads to the sought new polarization $\boldsymbol{p}^{n+1}$, where last term stems from Eqn. (2.3.29). The time step size Δt was verified by numerical experiments to be sufficiently small to achieve convergence of this staggered scheme.

2.6 SIMPLIFYING ASSUMPTIONS

In this section, we discuss the simplifying assumptions to the general solution strategy, described in the previous Section 2.5. As a first assumption, we assume an isotropic interface energy with $\mathbb{G}_{ijkl} = G_0 \delta_{ij} \delta_{kl}$ (using the Kronecker delta δ) in (2.2.12), such that the interface energy simplifies to

$$\Psi_{\text{int.}}(\nabla \boldsymbol{p}) = \frac{G_0}{2} |\nabla \boldsymbol{p}|^2 , \tag{2.6.1}$$

where G_0 denotes the interface energy constant. An anisotropic formulation of the interface energy, as suggested by Völker et al. (2011), is generally not possible due to practical reasons, e.g., experimental validation is challenging and the anisotropy in combination with an FFT-based approach involves severe computational costs requiring an iterative solution scheme when studying heterogeneous materials. Therefore, an isotropic interface energy is assumed, which is a common assumption in the research field (Shu & Bhattacharya, 2001; Su & Landis, 2007; Woldman & Landis, 2016, 2019; W. Zhang & Bhattacharya, 2005). As previously described, the effective material response is generally computed by solving the governing equations (2.2.1),(2.2.2), and (2.3.25) within a RVE, using spectral homogenization to impose volume-average strains $\langle \boldsymbol{\varepsilon} \rangle$ and average electric fields $\langle \boldsymbol{e} \rangle$, see Section 2.5 for details.

Second, by assuming elastic homogeneity (which is the case in (an)isotropic single-crystals as well as in polycrystals when assuming elastic isotropy), we avoid an iterative FFT-based solution scheme (Lebensohn et al., 2012; Moulinec & Suquet, 1998, 2003) and can impose average stresses directly, which is elaborated. Therefore, we assume a homogeneous material and approximate an isotropic elastic material behavior with Voigt stiffness moduli C_{11}, C_{12} (as obtained from first principles by Völker et al. (2011)) and define $C_{44} = (C_{11} - C_{12})/2$, so that the components of the fourth-order elasticity tensor can be written as

$$\mathbb{C}_{ijkl} = \lambda_e \delta_{ij} \delta_{kl} + \mu_e (\delta_{ik} \delta_{jl} + \delta_{il} \delta_{jk}) \tag{2.6.2}$$

with Lamé moduli λ_e and μ_e, listed in Tab. 2.1 for PZT. Of course, this is a simplifying assumption and we admit that the elastic anisotropy may have an impact on the ferroelectric response (especially when considering, e.g., the elastic mismatch near GBs). However, given the variations of reported (experimental and computed) elastic moduli, especially for PZT near the

morphotropic phase boundary, we are not in a position to quantify the exact influence of elastic anisotropy and therefore limit our study to isotropy.

Consequently, defining the associated coupling stress tensor as

$$\sigma_{ij}^{\mathrm{r}} = \partial \Psi_{\mathrm{coupl}} / \partial \varepsilon_{ij} = \mathbb{B}_{ijmn} p_m p_n \tag{2.6.3}$$

and applying the Fourier transform to the balance of linear momentum leads to

$$\hat{\varepsilon}_{ij}(\boldsymbol{k}) = \begin{cases} -\frac{1}{2}\left[A_{ni}^{-1}(\boldsymbol{k}) k_m k_j + A_{nj}^{-1}(\boldsymbol{k}) k_m k_i\right] \hat{\sigma}_{nm}^{\mathrm{r}}(\boldsymbol{k}), & \text{if } \boldsymbol{k} \neq \boldsymbol{0}, \\ \varepsilon_{ij}^{0}, & \text{if } \boldsymbol{k} = \boldsymbol{0}, \end{cases} \tag{2.6.4a}$$

$$\hat{u}_k(\boldsymbol{k}) = \frac{i}{h} A_{ik}^{-1}(\boldsymbol{k}) \hat{\sigma}_{ij}^{\mathrm{r}}(\boldsymbol{k}) k_j, \tag{2.6.4b}$$

where $A_{ik}(\boldsymbol{k}) = \mathbb{C}_{ijkl} k_j k_l$ is the acoustic tensor, and $\hat{\sigma}_{nm}^{\mathrm{r}}(\boldsymbol{k})$ represents the Fourier-transformed coupling stresses (which are computed in real space from the constitutive law (2.6.3)). Equations (2.6.4a)-(2.6.4b) can be solved directly in Fourier space without iterations, which enables fast and efficient simulations without the need for computing or storing a consistent tangent (hence enabling the presented high-resolution simulations).

Furthermore, since samples in experiments were unconstrained (Kannan & Kochmann, 2022; Kannan et al., 2022; W. L. Tan et al., 2019; Vidyasagar et al., 2017), we assume a negligible average stress in the sample and hence inside the RVE:

$$\langle \sigma_{ij} \rangle = \langle \mathbb{C}_{ijkl} \varepsilon_{kl} \rangle + \langle \mathbb{B}_{ijmn} p_m p_n \rangle = 0. \tag{2.6.5}$$

When exploiting the assumption of elastic isotropy, (2.6.5) allows us to compute the average strain in the RVE as

$$\varepsilon_{kl}^{0} = \langle \varepsilon_{kl} \rangle = \mathbb{C}_{ijkl}^{-1} \left(\langle \sigma_{ij} \rangle - \langle \mathbb{B}_{ijmn} p_m p_n \rangle \right) = -\mathbb{C}_{ijkl}^{-1} \langle \mathbb{B}_{ijmn} p_m p_n \rangle = \langle \varepsilon_{kl}^{r} \rangle , \tag{2.6.6}$$

where $\langle \boldsymbol{\varepsilon}^{r} \rangle$ on the right-hand side is computed by homogenization of (2.2.5).

Third, to optimize the computational efficiency and for practical reasons, e.g., ease of visualization and comparability, we perform primarily two-dimensional (2D) simulations but consider out-of-plane strains. The description of the plane-stress model in the following is briefly adapted from Indergand (2019) for the sake of completeness. We assume vanishing out-of-plane components $e_3 = 0$, $p_3 = 0$, $d_3 = 0$, and $\sigma_{i3} = 0$ $(i = 1, 2, 3)$,

whereas $\varepsilon_{33} \neq 0$ in general. By applying these assumptions to (2.2.4), the out-of-plane strain writes

$$\varepsilon_{33} = -\left[\frac{C_{12}}{C_{11}}\left(\varepsilon_{11}+\varepsilon_{22}\right)+\frac{q_{12}}{C_{11}}\left(p_1^2+p_2^2\right)\right]. \tag{2.6.7}$$

Unfortunately, the in-plane strains depend on the normal stresses, e.g. $\varepsilon_{11} = \varepsilon_{11}(\sigma_{11},\sigma_{22},\sigma_{33})$, such that a system of equations must be solved. From (2.6.5) we know that the average strain follows from (2.6.6), viz.

$$\bar{\varepsilon}_{ij} = \langle\varepsilon_{ij}\rangle = \mathbb{C}^{-1}_{ijkl}\left(\langle\sigma_{ij}\rangle - \langle\mathbb{B}_{ijkl}p_k p_l\rangle\right) = \mathbb{C}^{-1}_{ijkl}\left(\langle\sigma_{ij}\rangle - \langle\sigma^r_{ij}\rangle\right), \tag{2.6.8}$$

or, written component by component where use is made of the compliance tensor $\mathbb{S} = \mathbb{C}^{-1}$ for convenience,

$$\langle\varepsilon_{11}\rangle = S_{11}\left(\langle\sigma_{11}\rangle - \langle\sigma^r_{11}\rangle\right) + S_{12}\left(\langle\sigma_{22}\rangle - \langle\sigma^r_{22}\rangle + \cancelto{0}{\langle\sigma_{33}\rangle} - \langle\sigma^r_{33}\rangle\right), \tag{2.6.9a}$$

$$\langle\varepsilon_{22}\rangle = S_{11}\left(\langle\sigma_{22}\rangle - \langle\sigma^r_{22}\rangle\right) + S_{12}\left(\langle\sigma_{11}\rangle - \langle\sigma^r_{11}\rangle + \cancelto{0}{\langle\sigma_{33}\rangle} - \langle\sigma^r_{33}\rangle\right), \tag{2.6.9b}$$

$$\langle\varepsilon_{33}\rangle = S_{11}\left(\cancelto{0}{\langle\sigma_{33}\rangle} - \langle\sigma^r_{33}\rangle\right) + S_{12}\left(\langle\sigma_{11}\rangle - \langle\sigma^r_{11}\rangle + \langle\sigma_{22}\rangle - \langle\sigma^r_{22}\rangle\right). \tag{2.6.9c}$$

It is important to note that the plane-stress assumption imposes the total stress $\sigma_{33} = 0$, but not necessarily the elastic and coupling stresses, expressed as $\sigma^e_{33} \neq 0$ and $\sigma^r_{33} \neq 0$. Since we enforce the average stress $\langle\boldsymbol{\sigma}\rangle$ in the RVE as a boundary condition, the only unknown in the above system of equations is the coupling stress $\boldsymbol{\sigma}^{\mathrm{r}} = \partial\Psi_{\mathrm{coupl}}/\partial\boldsymbol{\varepsilon}$, which results from applying the plane-stress assumption to (2.6.3), viz.

$$\sigma^r_{11} = q_{11}p_1^2 + q_{12}p_2^2, \tag{2.6.10a}$$

$$\sigma^r_{22} = q_{11}p_2^2 + q_{12}p_1^2, \tag{2.6.10b}$$

$$\sigma^r_{33} = q_{12}(p_1^2 + p_2^2), \tag{2.6.10c}$$

$$\sigma^r_{12} = q_{44}p_1 p_2. \tag{2.6.10d}$$

Using the spectral solution scheme introduced in Section 2.5, the in-plane strains $\varepsilon_{11}(\boldsymbol{x})$, $\varepsilon_{22}(\boldsymbol{x})$, and $\varepsilon_{12}(\boldsymbol{x})$ at each position $\boldsymbol{x}$ are calculated in Fourier space via (2.6.4a). Finally, with (2.6.7), the out-of-plane strain $\varepsilon_{33}(\boldsymbol{x})$ can be computed. This model distinguishes itself from other approaches (e.g. W. Zhang and Bhattacharya (2005), who used a 2D model, or Su and Landis (2007) with a generalized plane-strain model (uniform out-of-plane strain ε_{33})) by considering a spatial dependence of the out-of-plane strain ε_{33} to ensure better energy relaxation, closer to a 3D model.

Numerical case studies on the bipolar electric cycling hysteresis showed that results of the plane-stress model for a single-crystal setup are consistent with the corresponding results from the 3D model in the case of a 2D loading scenario (Indergand, 2019). It is important to note that polycrystals are, strictly speaking, always 3D, since they are composed of multiple grains with different crystallographic orientations in all three directions. Nevertheless, the 2D plane-stress model can closely approximate the material response of tetragonal ceramics, e.g., a uniaxial polycrystal (all grains having a common $\langle 100 \rangle$-axis.)

This allows us to use 3D material constants (as obtained from first principles) while simulating a planar RVE (thus allowing the out-of-plane strains to accommodate the remnant strains as in a bulk ferroelectric that is stress-free on average). The planar assumption allows for an inexpensive computation of the bulk material response, in which the mechanical and electric fields are restricted to the plane without thin-film effects (e.g., thickness-dependent material response, and depolarization fields).

A pseudo-code of the described plane-stress algorithm is shown in Alg. 1. By utilizing the simplifying assumptions discussed in this section, the electrical as well as the mechanical problem are solved without iterations in Fourier space. Furthermore, the temporal update of the coupled mechanical, electrical, and ferroelectric problem is performed in a fully implicit manner, improving the stability of the numerical scheme and allowing larger time steps Δt (Gottlieb & Orszag, 1977).

Algorithm 1: Implementation of the Plane-Stress Model

Data: Simulation time t_{end}, time step size Δt, initial polarization $\boldsymbol{p}(\boldsymbol{x}, t=0)$, tangent stiffness $\mathbb{C}$.

Declaration and initialization of variables, assignment of the initial guess for $\boldsymbol{p}^n$;

while $t^n \leq t_{\text{end}}$ **do**

  $\boldsymbol{\eta}^n_{\Delta t} = \sqrt{\frac{2k_{\text{B}}\theta\,\Delta t}{\mu V_{\text{char}}}}\boldsymbol{X} \qquad \text{with} \qquad \{X_1, X_2, X_3\} \sim \mathcal{N}(0,1)$;

  Reset of the m count and assign initial guess of $\boldsymbol{p}^{n+1}_m$;

  while $\left\| p^{n+1}_{m+1}(\boldsymbol{x}) - p^{n+1}_m(\boldsymbol{x}) \right\| \geq tol$ **do**

    $\boldsymbol{\sigma}^{\text{r}}(\boldsymbol{x}) = \mathbb{B}(\boldsymbol{p}^{n+1}_m \otimes \boldsymbol{p}^{n+1}_m)$;

    for *loop over* $\boldsymbol{k}$*-space* **do**

      $\hat{\boldsymbol{\sigma}}^r(\boldsymbol{k}) = \text{FFT}\left(\boldsymbol{\sigma}^r(\boldsymbol{x})\right)$;

      $\hat{\boldsymbol{p}}(\boldsymbol{k}) = \text{FFT}\left(\boldsymbol{p}^{n+1}_m(\boldsymbol{x})\right)$;

      if $\boldsymbol{k} == \boldsymbol{0}$ **then**

        $\boldsymbol{e}(\boldsymbol{k}) = \boldsymbol{e}^0$;

        $\boldsymbol{\varepsilon}(\boldsymbol{k}) = \left\langle \boldsymbol{\varepsilon}^r(p^{n+1}_m) \right\rangle$; `/* stress-free BC */`

      else

        $\boldsymbol{e}(\boldsymbol{k}) = -\dfrac{\boldsymbol{k}\cdot\hat{\boldsymbol{p}}(\boldsymbol{k})}{\kappa_0|\boldsymbol{k}|^2}\boldsymbol{k}$;

        $\boldsymbol{\varepsilon}(\boldsymbol{k}) = -\frac{1}{2}\left[\hat{\boldsymbol{\sigma}}^{\text{r}}(\boldsymbol{k})\boldsymbol{k}A^{-1} \otimes \boldsymbol{k} + A^{-\text{T}}\hat{\boldsymbol{\sigma}}^{\text{r}}(\boldsymbol{k})\boldsymbol{k} \otimes \boldsymbol{k}\right]$

      end

      $\hat{\boldsymbol{g}}(\boldsymbol{k}) = G_0\,|\boldsymbol{k}|^2\,\hat{\boldsymbol{p}}(\boldsymbol{k})$

    end

    iFFT to obtain $\boldsymbol{e}^{n+1}(\boldsymbol{x})$, $\boldsymbol{\varepsilon}^{n+1}(\boldsymbol{x})$, and $\boldsymbol{g}^{n+1}(\boldsymbol{x})$

    $\varepsilon^{n+1}_{33}(\boldsymbol{x}) = -\left[\frac{C_{12}}{C_{11}}\text{tr}\left(\boldsymbol{\varepsilon}^{n+1}\right) + \frac{q_{12}}{C_{11}}\text{tr}\left(\boldsymbol{p}^{n+1}_m \otimes \boldsymbol{p}^{n+1}_m\right)\right]$;

    $\boldsymbol{f}^{n+1}(\boldsymbol{x}) = \boldsymbol{e}^{n+1} - \frac{\partial\Psi_{\text{coupl}}}{\partial\boldsymbol{p}}(\boldsymbol{\varepsilon}^{n+1}, \boldsymbol{p}^{n+1}_m, \varepsilon^{n+1}_{33}) - \frac{\partial\Psi_{\text{pol}}}{\partial\boldsymbol{p}}(\boldsymbol{p}^{n+1}_m)$;

    $\boldsymbol{p}^{n+1}_{m+1} = \boldsymbol{p}^n + \frac{\Delta t}{\mu}\left[\boldsymbol{f}^{n+1} + \boldsymbol{g}^{n+1}\right] + \boldsymbol{\eta}^n_{\Delta t}$, reassign to $\boldsymbol{p}^{n+1}_m$, and increment m;

  end

  $\boldsymbol{p}^n = \boldsymbol{p}^{n+1}_{m+1}$ and increment n;

end

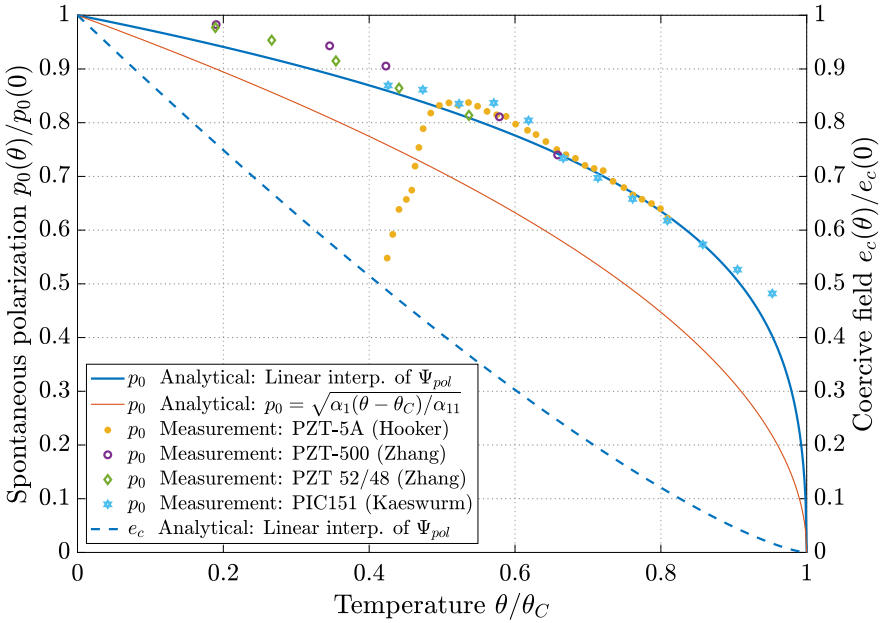

Figure 2.4: The computed spontaneous polarization $p_0(\theta)$ from (2.3.2) (solid blue line) in comparison with Devonshire's theory (solid orange line) and measurements of PZT-5A (yellow asterisk), PZT-500 (violet open circle), PZT 52/48 (green open diamond) and PIC151 (blue open star). The spontaneous polarization $p_0(\theta)$ is normalized by its value at 0 K (reference values are listed in Tab. 2.2). The predicted normalized (single-crystal, single-domain) coercive field $e_c(\theta)$ is also included (dashed blue line).

2.7 RESULTS: FERROELECTRIC SWITCHING

2.7.1 *Influence of the temperature-dependent polarization potential*

To assess the accuracy of the chosen linear interpolation of the polarization potential with temperature, Fig. 2.4 illustrates the spontaneous polarization p_0 vs. temperature – comparing computed results obtained from the linearly interpolated polarization potential (2.3.1) as well as from the approximation by Devonshire (1954) to experimental data for different types of PZT. Unfortunately no complete set of data for a single type of PZT across the full temperature range is available to our knowledge. Hence, for an accurate

comparison the temperature and spontaneous polarization are normalized by, respectively, the Curie temperature θ_C and the extrapolated polarization at 0K, $p_o(0)$, for each material (see Tab. 2.2 for the exact reference values used for normalization).

Table 2.2: Material properties of PZT ceramics used for normalization. The spontaneous polarization at 0K, $p_o(0K)$, is obtained by extrapolation from the following experiments: [1] Hooker (1998), [2] CeramTec (2020), [3] Q. Zhang et al. (1994), [4] Bernhard Jaffe (1971), [5] Kaeswurm et al. (2018), and [6] PICeramic (2020).

material constants used for normalization		
composite [−]	spontaneous polarization $p_0(0K)$ [C/m^2]	Curie temperature θ_C [K]
PZT-5A	0.32 [1]	643 [2]
PZT-500	0.43 [3]	650 [2]
PZT-52/48	0.34 [3]	640 [4]
PIC 151	0.35 [5]	523 [6]

We note that the drop in the experimental data of Hooker (1998) at low temperatures is questionable in our view (one may question whether complete polarization reversal was achieved at those low temperatures, since all other data clearly report a different trend). If we ignore the low-temperature data of Hooker (1998), the normalized spontaneous polarization measurements in Fig. 2.4 coincide reasonably well with the prediction by our finite-temperature model for all shown PZT compositions (also demonstrating the continuous, second-order phase transition expected for PZT).

In comparison to measured data, the spontaneous polarization from first-principle DFT calculations at zero temperature is noticeably higher, viz. $p_o^{DFT}(0) = 0.58\,\mathrm{C/m^2}$ for $Pb(Zr_{0.5}Ti_{0.5})O_3$. This can be expected since simulations are based on an ideal, defect-free, single-crystal, whereas experiments deal with a polycrystalline sample with imperfections.

Important characteristics of ferroelectrics are their electric hysteresis and butterfly curve, which we extract from single-crystal RVE simulations at different temperature levels, using bipolar electric field cycling. To this end, a triangular-shaped average electric field in the x_3-direction with

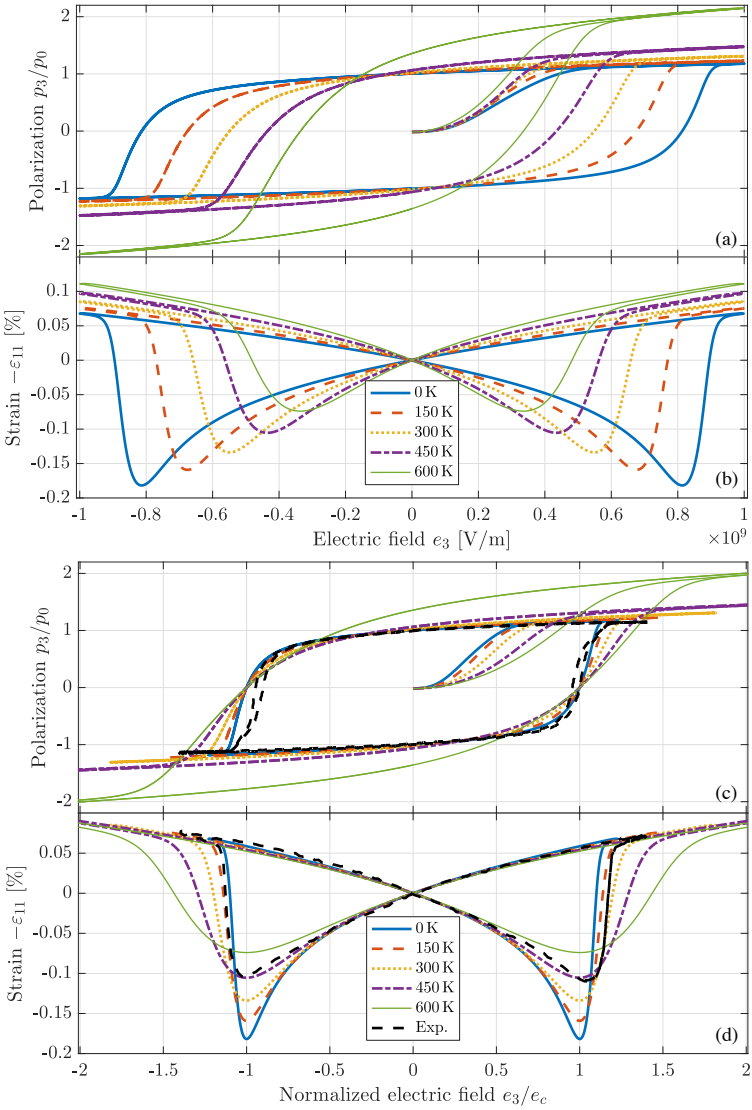

Figure 2.5: Influence of the temperature-dependent polarization potential $\Psi_{\text{pol}}(\boldsymbol{p}, \theta)$ on the bipolar cycling hysteresis (a,c) and on the (negative) lateral strain ε_{11} (b,d) computed with a 2D model at 0 K, 150 K, 300 K, 450 K, and 600 K. A triangular wave with cycling period $T = 21\mu/|\alpha_1|$ and amplitude $e_3 = 10^9\,\text{V/m}$ is applied. Experimental measurements on polycrystalline PZT-5A by W. L. Tan et al. (2019) are added for comparison.

amplitude e_3 and cycling period T is applied; simultaneously, the average electric displacement parallel and the average strain perpendicular to the electric field, d_3 and ε_{11}, respectively, are recorded. Numerical results of the bipolar switching hysteresis at different temperatures, computed with a single-crystal 2D RVE of grid resolution 256×256, are plotted in Fig. 2.5(a). Similar to the predicted temperature dependence of the coercive field in Fig. 2.4, we notice an approximately linear decrease of the coercive field $e_c = e|_{p=0}$ with increasing temperature. In Fig. 2.5(c) we plot the normalized polarization (i.e., the polarization normalized by its value $p_0 = p|_{e=0}$ for each temperature) vs. the normalized electric field (i.e., the applied electric fields normalized by the coercive field at each temperature). The normalized polarization at zero electric field is approximately 1 across the full temperature range tested, so the polarization converges to its equilibrium state, which implies that the simulation indeed captures the quasistatic material response at the chosen cycling rate. As the only exception, results for 600K reveal a polarization at zero electric field that is considerably higher than the spontaneous polarization at that temperature, so we observe a strong effect of temperature on the hysteresis. Also included in Fig. 2.5(c) are experimentally measured data for (polycrystalline) PZT-5A at room temperature (W. L. Tan et al., 2019), whose normalized curve agrees well with the simulated hystereses.

As a further characteristic of ferroelectric ceramics we compute the evolution of strain with electric field. Fig. 2.5(b) plots the negative lateral strain ε_{11} vs. the applied electric field as the classical butterfly curve. Analogous to the polarization hysteresis, an increase in temperature leads to a decrease of the electric field at maximum strain (e_c^ε), which is slightly higher than the corresponding field from the polarization hysteresis curve (e_c). Furthermore, we observe a decrease of the strain magnitude from polarization reversal with increasing temperature. The corresponding normalized curves are shown in Fig. 2.5(d), again indicating good qualitative agreement with experimental data.

From the bipolar switching hysteresis and the butterfly curves, small-signal properties such as the piezoelectric coefficients d_{31}, d_{33} and dielectric constants κ_{11}, κ_{33} can be determined as (no summation implied)

$$d_{ij} = \left.\frac{\partial \varepsilon_{(jj)}}{\partial e_i}\right|_{\sigma=\mathbf{0}} \quad \text{and} \quad \kappa_{ij} = \left.\frac{\partial d_j}{\partial e_i}\right|_{e=\mathbf{0}} \quad \text{for } i,j = 1,2,3. \tag{2.7.1}$$

The dielectric constant or relative permittivity κ_{33} (the slope of the polarization hysteresis at zero electric field) is a measure of the capacitance of a

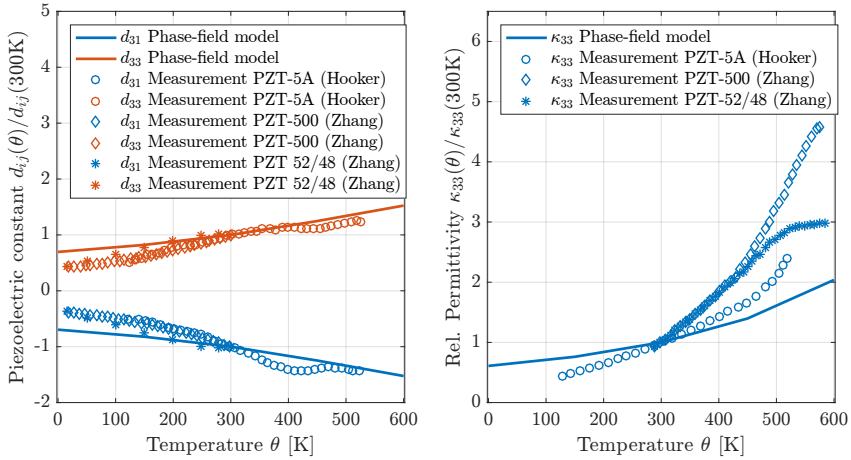

Figure 2.6: Influence of the temperature-dependent polarization potential $\Psi_{\text{pol}}(\boldsymbol{p}, \theta)$ on small-signal properties such as the piezoelectric constants d_{31}, d_{33} (left) and the dielectric constant κ_{33} (right) computed with a 2D model (line) in comparison with measurements of PZT-5A (open circles), PZT-500 (open diamonds) and PZT 52/48 (asterisks). The piezo-/dielectric constants are normalized with respect to their corresponding value at 300K

medium. The piezoelectric coefficients d_{31} and d_{33} (the slopes of the strain perpendicular and parallel to the switching direction, ε_{11} and ε_{33}, respectively, at zero electric field) provide a relation between the induced strain and the applied electric field and can be interpreted as a force sensitivity (i.e. charge released per Newton force). The temperature dependence of the piezoelectric coefficient and of the dielectric constant as obtained from our phase-field model is shown in Fig. 2.6 in comparison with experimental data. Since the bipolar switching hysteresis and the butterfly curve depend strongly on a particular material's microstructure and composition (i.e., its grain size and texture, defect distribution, titanium concentration, dopants, etc.) which are not considered in our model, all reported small-signal properties are normalized with respect to their value at 300 K, see Tab. 2.3. The overall trends of the temperature-dependent piezoelectric coefficients d_{31} and d_{33} are captured reasonably well, independent of the specific ferroelectric ceramic (and unbiased by microstructural variations). We note that the dielectric constant κ_{33} shows a stronger dependence on the particular material. Our model (based on the first-principles-informed 0K potential of

Völker et al. (2011)) comes closest to Hooker's (1998) measurements of PZT-5A. However, effects at the polycrystalline mesoscale, such as domain wall motion and defect pinning, are known to have an impact on the large-signal and small-signal properties. Considering that we used a single-crystal in our simulations, the agreement with measurements is reasonably good.

Table 2.3: Small signal properties of PZT ceramics at 300 K (used for normalization) stem from the following experiments: [1] Hooker (1998) and [2] Q. Zhang et al. (1994).

Piezoelectric and dielectric constants at 300K			
composite	piezoelectric const. d_{31} [pC/N]	piezoelectric const. d_{33} [pC/N]	dielectric const. κ_{33} [-]
PZT-5A [1]	-195	354	1320
PZT-500 [2]	-170	361	1861
PZT-52/48 [2]	-114	248	1230

2.7.2 *Influence of thermal fluctuations*

To assess the impact of the thermalized random noise on the ferroelectric switching kinetics, we deliberately deactivate the temperature dependence of the polarization potential (discussed in the previous section) in order to isolate the effect of the stochastic noise (this ensures that varying the temperature does not alter the coercive field, so that a constant applied electric field is a legitimate test case for evaluating the influence of the introduced random noise for varying temperature levels). The combined effects of temperature-dependent potential and thermal noise will be investigated in the following Section 2.7.3. Subsequent numerical examples use a 2D RVE with 1024×1024 grid points and resolve the ferroelectric microstructure down to the atomic level; i.e., as discussed before, every pixel mimics exactly one tetragonal atomic-level unit cell and exhibits temperature-dependent Brownian motion through the space-time random process.

As an instructive scenario, we use the well-defined environment of a single-crystal to study the kinetics of domain nucleation and growth under the influence of thermal noise. To initialize the nucleus, we seed an elliptic-

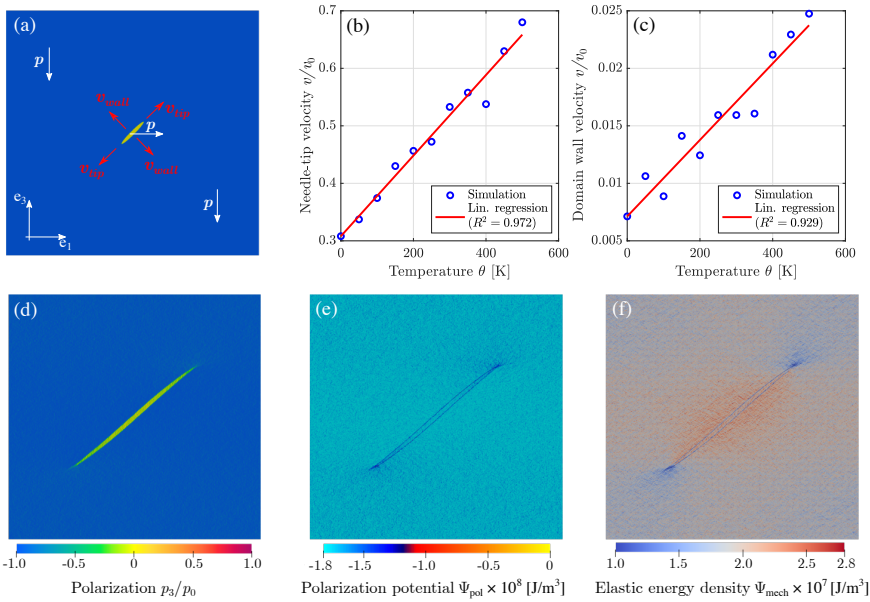

Figure 2.7: Simulation results for a single-crystalline RVE with periodic boundary conditions and an isolated nucleus at its center, kept at a constant electric field of $e_3 = 10^8$ V/m (considering only thermal fluctuations). (a) The initial polarization distribution $\boldsymbol{p}(\boldsymbol{x}, 0)/p_0$ is indicated by small white arrows, starting from which the nucleus grows in two directions at speeds v_{tip} and v_{wall} of the nucleus, as indicated in red. (b) Needle-tip velocity $v_{\text{tip}}(e, \theta)$ and (c) domain wall velocity $v_{\text{wall}}(e, \theta)$ were computed for various temperatures θ, and the corresponding estimate based on a linear regression, is indicated as a red line (speeds are normalized by $v_0 = 2.93|\alpha_1|a_{\text{cub}}/\mu$). Snapshots of the computed growth of the ferroelectric nucleus at $t = 170\mu/|\alpha_1|$ illustrate (d) polarization component $p_3(\boldsymbol{x}, t)/p_0$, (e) polarization potential $\Psi_{\text{pol}}(\boldsymbol{p}, \theta)$, and (f) elastic energy density $\Psi_{\text{mech}}(\boldsymbol{\varepsilon})$ at room temperature $\theta = 300$ K.

shaped a^+-domain at the center of the RVE, as depicted in Fig. 2.7(a), and – for its stabilization – apply a constant electric field $e_3 = 10^8$ V/m significantly below the coercive field (which in this case is $e_c = 5 \cdot 10^8$ V/m). At varying noise levels, we observe the isolated nucleus grow in two directions: in the longitudinal direction (spreading with the needle-tip speed v_{tip}) and in the transverse direction (accommodated by classical domain wall motion at a speed v_{wall}), see Fig. 2.7(a). As shown in Fig. 2.7(b) and (c), both velocities are strongly influenced by the thermal fluctuations, with

the propagation speeds increasing approximately linearly with temperature and consistent with 0K results obtained at the athermal limit without thermal fluctuations. Independent of temperature, the needle-tip velocity v_{tip} is considerably higher (about a factor of 33) than the domain wall velocity v_{wall}, which consequently results in a slender, needle-like shape of the growing a^+-domain. This predominant growth in the longitudinal direction is illustrated in Fig 2.7(d), showing the computed polarization in the vertical direction $p_3(\boldsymbol{x}, t)/p_0$ after an elapsed time of $t = 170\mu/|\alpha_1|$. Fig 2.7(f) reveals that the bulk of the nucleus occupies an equilibrium polarization state (a^+-domain) with a low polarization energy, whereas the domain walls and the needle-tip are in a non-equilibrium polarization state with a locally high polarization energy. This high-energy polarization state makes the needle tip and walls prone to thermally-driven switching due to the lower energy barrier ΔE_{90} in the polarization energy $\Psi_{\text{pol}}(\boldsymbol{p}, \theta)$ that stands in competition with the thermal energy $k_{\text{B}}\theta$.

2.7.3 *Combined effects of thermal fluctuations and temperature-dependent energetics*

To understand the behavior observed when including both the temperature-dependent polarization potential (affecting the energetic switching barriers) and the thermal noise (causing fluctuations that help overcome those barriers), we illustrate in Fig. 2.8(a) a typical landscape of the polarization enthalpy density $W_{\text{pol}}(\boldsymbol{p}, \boldsymbol{e}, \theta)$ vs. the (normalized) polarization $\boldsymbol{p} = (p_1, p_3)^{\text{T}}$ in 2D, at a fixed applied electric field $e_3 = 8 \cdot 10^7\,\text{V/m}$ and temperature $\theta = 300\,\text{K}$. Consider as the initial state $\boldsymbol{p} = (0, -p_0)^{\text{T}}$. Under the applied field, switching from $\boldsymbol{p} = (0, -p_0)^{\text{T}}$ to $\boldsymbol{p} = (0, p_0)^{\text{T}}$ is most easily accommodated by two subsequent 90°-switching events. The minimum energy pathway (MEP) connecting those two polarization states is obtained by using the simplified string method (Sheppard et al., 2008) and is indicated as a magenta curve in Fig. 2.8(a). Plotting the polarization enthalpy density along this MEP reveals the energy barrier ΔE_{90} of a 90°-domain wall, see Fig. 2.8(b). (The barrier for 180°-switching is significantly higher.) As summarized in Fig. 2.8(c), the energy threshold ΔE_{90}, which separates two 90°-adjacent polarization states, depends on the applied electric field e_3 as well as on temperature θ, the latter dependence enters through the polarization potential $\Psi_{\text{pol}}(\boldsymbol{p}, \theta)$ introduced in Section 2.3.1. Data in Fig. 2.8(c) indicates that increasing the temperature reduces the energy barrier for

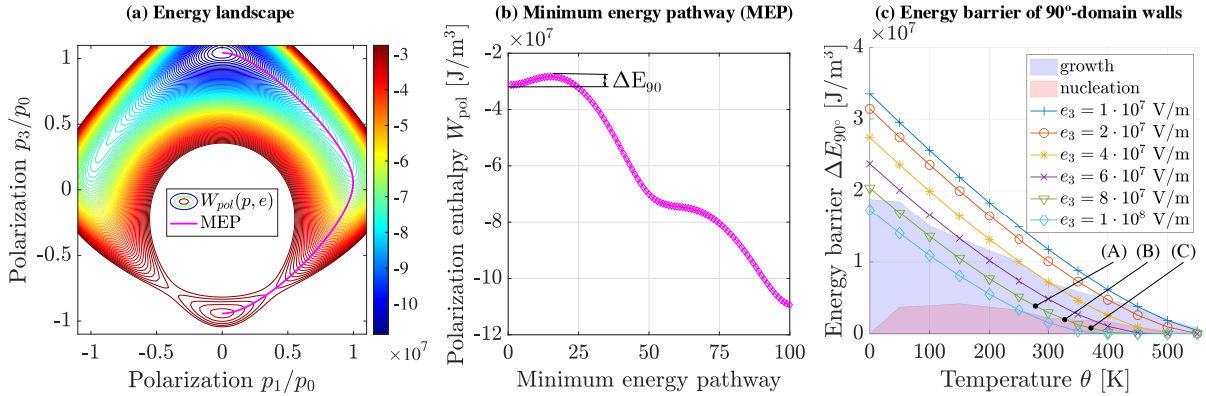

Figure 2.8: (a) 2D landscape of the polarization enthalpy density $W_{\mathrm{pol}}(\boldsymbol{p}, \boldsymbol{e}, \theta)$ vs. the (normalized) polarization $\boldsymbol{p} = (p_1, p_3)^{\mathrm{T}}$ at a fixed applied electric field $e_3 = 8 \cdot 10^7\,\mathrm{V/m}$ and temperature $\theta = 300\,\mathrm{K}$. (b) Polarization enthalpy density W_{pol} along the minimum energy pathway (MEP) shown in (a), between the two polarization states $\boldsymbol{p} = (0, -p_0)^{\mathrm{T}}$ and $\boldsymbol{p} = (0, p_0)^{\mathrm{T}}$. (c) Energy barrier ΔE_{90} of a 90°-domain wall as a function of temperature θ and electric field e_3. The two shaded regions refer to different growth mechanisms of an initial domain nucleus as observed in simulations: light blue indicates pure growth of the existing nucleus, red indicates simultaneous growth and branching of the nucleus plus nucleation of new domains, white implies the disappearance of an unstable nucleus. Markers (A), (B), and (C) denote specific thresholds of importance in Fig. 2.9.

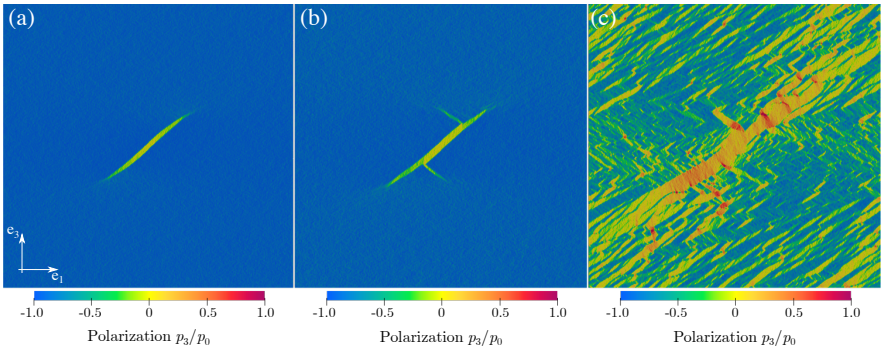

Figure 2.9: Snapshots of a simulated evolving ferroelectric domain microstructure in a single-crystal at $t = 51\mu/|\alpha_1|$, showing polarization component $p_3(\boldsymbol{x}, t)/p_0$ for an applied electric field $e_3 = 8 \cdot 10^7$ V/m at temperatures (a) $\theta = 275$ K, (b) 325 K, and (c) 375 K. The corresponding energy threshold of the 90°-domain walls for the three depicted ferroelectric microstructures is indicated in Fig. 2.8(c) as A, B, C.

90°-switching, so that maintaining a constant applied electric field induces domain switching more readily with increasing temperature.

This effect becomes apparent in Fig. 2.9, which shows the same single-crystal example from Fig. 2.7 but this time at the three temperatures $\theta = 275$ K, 325 K, and 375 K, while applying the same electric field $e_3 = 8 \cdot 10^7$ V/m. We observe three distinct switching mechanisms: (a) growth of the nucleus predominantly as a needle in the longitudinal direction at 275 K, (b) branching of the existing a^+-domain into multiple a^--domains at 325 K, and (c) nucleation of mainly a^+-domains at randomly distributed locations inside the c^--domain at 375 K. For the given choice of temperature and electric field, classical domain wall motion perpendicular to the wall plays only a minor role[1], which is in agreement with experimental observations and analytical considerations (Ayoub et al., 2017; Hayashi, 1972; Meng et al., 2015; Merz, 1956). The temperature dependence of the polarization potential hence globally reduces the energy barrier at elevated temperatures and stimulates thermally-driven polarization reversal by branching of existing domains and nucleation of new ones.

1 We acknowledge that classical domain wall motion, i.e., the growing of a domain through wall motion perpendicular to the wall, is of course an important mechanism. However, the longitudinal growth requires only ions at the needle tip to be displaced, on the contrary to lateral growth, and is therefore energetically preferred (Snoeck et al., 1994).

The conditions of the three snapshots in Fig. 2.9 correspond to points A, B, C highlighted in Fig. 2.8(c). By more broadly covering the space of electric fields and temperatures, numerical simulations were used to identify regions in Fig. 2.8(c) in which polarization switching occurs primarily by growth only as in Fig. 2.9(a) (blue shaded area), growth, branching, and nucleation as in Fig. 2.9(c) (red area), or shrinkage and extinction of the nucleus (white area). This illustrates the competing microstructural mechanisms and the influence of temperature and electric field. Other fluctuation fields (not considered in this work, caused, e.g., by thermally-driven migration of oxygen vacancies or free charges) are expected to have a similar effect as lattice vibrations. On the other hand, microstructural imperfections such as GBs, lattice defects, cracks and voids result in localized high-energy spots, leading to heterogeneous nucleation instead of at random locations as seen in the single-crystalline RVE in Fig. 2.9(c).

To probe the impact of heterogeneity, we simulate a polycrystalline RVE of PZT with randomly-oriented grains, whose orientations are assigned based on a Gaussian distribution with zero mean and 22° standard deviation. The sample is poled initially in the negative vertical direction, resulting in a single c^--domain. After equilibration, the polarization adjusts slightly according to the preferred orientation of each grain. Finally, an electric field is applied and kept constant during the domain evolution, comparable to the experimental step-load procedure described by Schultheiß et al., 2018 (this step-response loading shows the system kinetics in a clean fashion without dependence on, e.g., the frequency during bipolar electric cycling).

Fig. 2.10 shows various snapshots of the same simulated ferroelectric microstructure, showing the normalized polarization $p_3(\boldsymbol{x}, t)/p_0$ in the vertical direction, the polarization energy density $\Psi_{\mathrm{pol}}(\boldsymbol{p}, \theta)$, and the elastic energy density $\Psi_{\mathrm{mech}}(\boldsymbol{\varepsilon})$. The grain orientations within the RVE are shown schematically in Fig. 2.11. Analogous to the single-crystal example, we observe that nucleation of new a-domains inside a c^--domain lowers the polarization potential in the bulk, but the domain wall and the needle-tip of the nucleus remain in a non-equilibrium polarization state and are therefore energetically unfavorable. The red spots in the polarization energy map indicate locations where the energy has reached the threshold of a 90°-domain wall (for a grain with zero misorientation); since these are unstable states, an immediate polarization switching can be expected. We also illustrate the elastic energy density, which highlights locations of high stress concentrations, such as grain triple junctions, mismatching domain interfaces caused by c/a-lattice distortion, and perpendicular branches growing out of

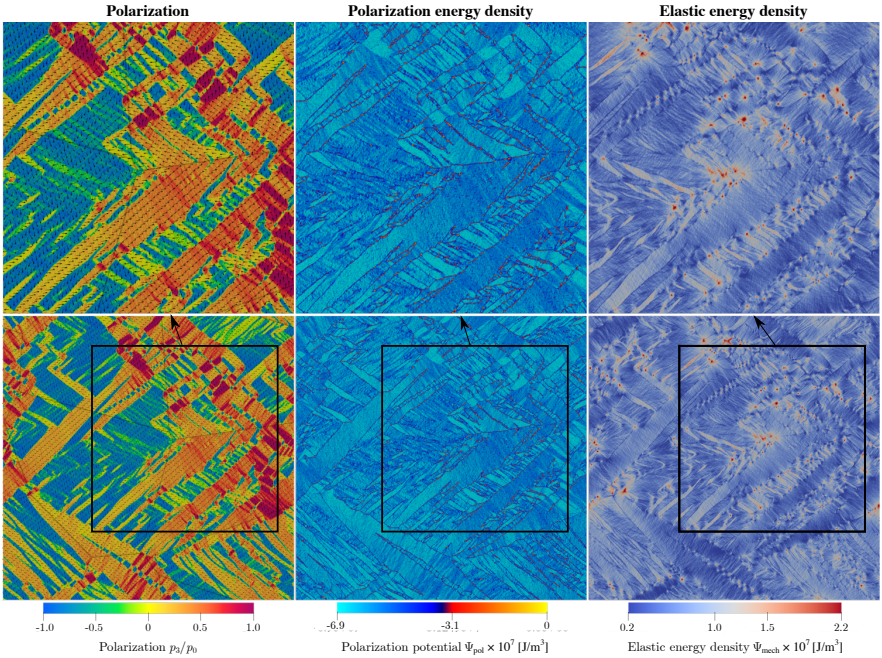

Figure 2.10: Snapshots of a simulated ferroelectric domain microstructure, showing polarization component $p_3(\boldsymbol{x}, t)/p_0$ (left column), polarization energy density $\Psi_{\text{pol}}(\boldsymbol{p}, \theta)$ (central column), and elastic energy density $\Psi_{\text{mech}}(\boldsymbol{\varepsilon})$ (right column) (snapshots were taken at time $t = 136\mu/|\alpha_1|$ under a constant electric field of $e_3 = 8 \cdot 10^7\,\text{V/m}$ at $\theta = 300\,\text{K}$). Small arrows in the left column indicate the orientation of the polarization vector $\boldsymbol{p}(\boldsymbol{x}, t)/p_0$. Top-row images show zoomed-in versions of the respective highlighted boxed areas in the bottom-row images.

existing domains. The shown microstructure reveals primarily 90°-domain patterns arranged in laminate structures, including more complex domain patterns such as second-order laminates or (in the magnified view of the polarization distribution) a wedge-like microstructure along the horizontal GB, reminiscent of ferroelectric domain patterns observed experimentally; see, e.g., the TEM images of Schmitt et al. (2007) and Woodward et al. (2005).

Figs. 2.11 and 2.12 visualize the influence of temperature on the evolution of such ferroelectric microstructures at the three temperatures $\theta = 275\,\text{K}$, $325\,\text{K}$, and $375\,\text{K}$. Under a constant electric field of $e = 8 \cdot 10^7\,\text{V/m}$, applied instantaneously at $t = 0\,\text{s}$, the polarization evolves, whose average

$\langle p_3(\boldsymbol{x},t)/p_0\rangle$ is shown in Fig. 2.11, while the corresponding microstructures at the strain polarization levels indicated as A through C, at three different temperatures, are illustrated in Fig. 2.12. That is, the shown microstructures within each row of Fig. 2.12 have the exact same average polarization $\langle p_3(\boldsymbol{x},t)/p_0\rangle$ (and the same applied electric field) but the underlying microstructures differ significantly due to the three distinct temperature levels.

The domain pattern evolution, also shown in Movies S1 and S2 (see supporting online material), shows two distinct switching mechanisms: (i) various nucleation events of needle-like domains at GBs and triple junctions, followed by (ii) subsequent growth – predominantly in the longitudinal (needle-tip) direction. The ratio of the speeds of the aforementioned mechanisms is an important factor that determines the appearance of ferroelectric microstructures. Increasing the temperature generally leads to more detailed and finer domain structures. This is traced back to the competition between nucleation and growth, yet we reiterate that two competing effects are at play here. On the one hand, with increasing temperature the polarization energy landscape becomes shallower and the coercive field e_c is reduced, see Fig. 2.8; this increases the number of possible nucleation sites at a constant electric field with increasing temperature, so it becomes easier to overcome the energy barrier between adjacent spontaneous polarization states. On the other hand, the noise amplitude increases with temperature

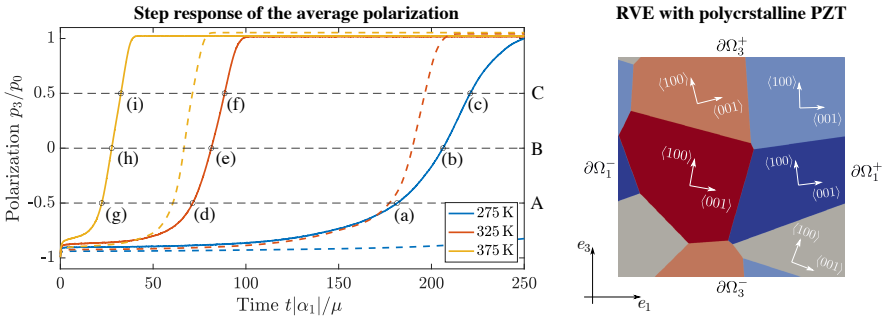

Figure 2.11: Influence of temperature on the ferroelectric step response (left) under a constant electric field $e_3 = 8 \cdot 10^7$ V/m at temperatures $\theta = 275$ K, 325 K, 375 K along with a schematic of the the polycrystal (right). The dashed lines in the step response are results obtained without thermal fluctuations under otherwise same conditions. Equal average polarization levels $\langle p_3(\boldsymbol{x},t)/p_0\rangle = -0.5, 0, 0.5$ are indicated by capital letter A, B, C. Labels (a) through (i) indicate those states whose microstructures are shown in Fig. 2.12.

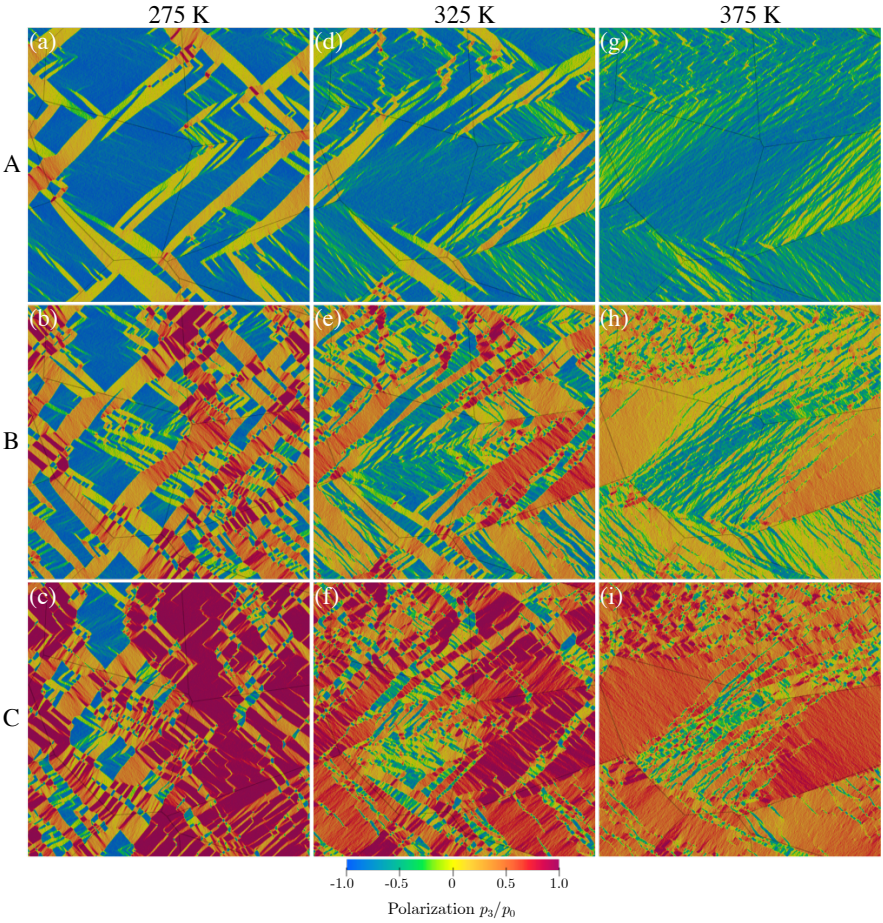

Figure 2.12: Influence of temperature on the ferroelectric domain pattern formation, showing $p_3(\boldsymbol{x}, t)/p_0$ under a constant electric field $e_3 = 8 \cdot 10^7\,\mathrm{V/m}$ at temperatures $\theta = 275\,\mathrm{K}$, $325\,\mathrm{K}$, $375\,\mathrm{K}$ (columns) and switching states: A, B, C (rows), the latter corresponding to the polarization states defined in Fig. 2.11.

($|\boldsymbol{\eta}| \propto \sqrt{\theta}$), so the larger step size of the random walk enables statistically more locations to escape from local energy minima to energetically lower polarization states. These two effects explain the temperature dependence of the domain nucleation sites, which becomes apparent in Fig. 2.12: nucleation at low temperature occurs primarily at GBs, while at high temperature the formation of new domains is not restricted to locations with high stress concentrations. Instead, the shallow energy landscape (Fig. 2.8c) in combination with higher thermal fluctuations allows the random walk to overcome the energy barrier of the polarization potential, resulting in nucleation at random locations – similar to the single-crystal results in Fig. 2.9c. For completeness, Fig. 2.11 also includes (as dashed lines) results obtained without the stochastic noise (so the temperature dependence stems solely from the polarization potential), which highlights the impact of the fluctuations: with thermal noise, we observe a considerably faster response time, which is explained by the increasing nucleation rate of a-domains and, as a consequence, polarization reversal being dominated by nucleation as opposed to domain growth.

2.8 CONCLUSIONS

We have presented a finite-temperature continuum model for ferroelectric ceramics, which is based on a temperature-dependent Landau-Devonshire potential and on a temperature-dependent stochastic Allen-Cahn equation for the evolution of the total polarization. The former was shown to provide an accurate prediction of the spontaneous polarization, the coercive field, and the piezoelectric and dielectric constants across a broad temperature range in agreement with experimental data for PZT (after normalization of the electric field by the coercive field, the computed butterfly curve also showed convincing agreement with room-temperature measurements). Because of the large spread among measured data for different PZT compositions and the fact that we do not account for dopants in the model, the piezoelectric and dielectric constants required normalization for comparison. However, when considering that we compare measurements from different types of polycrystalline PZT at the macroscale with numerical results computed with a single-crystalline 2D model at the mesoscale, the presented framework captures the salient macroscopic temperature effects reasonably well.

Based on statistical mechanics, we introduced a temperature-dependent Gaussian noise into the evolution equation for the polarization, which mimics atomic-level lattice vibrations at the continuum scale. Typical for diffusive processes such as ferroelectric domain wall motion, the noise amplitude is proportional to the square root of temperature and time increment. Simulations revealed that the thermal noise has a considerably effect on the ferroelectric switching kinetics. First, superimposing random small perturbations onto the deterministic gradient-flow kinetics breaks the symmetry of the single-crystalline polarization energy, such that 180°-switching becomes less probable. Instead, the utilization of pathways with lower energy barriers leads to switching predominantly by two consecutive 90°-rotations. Second, thermal noise leads to significantly faster growth of a domain nucleus at elevated temperature in both the longitudinal and transverse directions – whose relation $|v_{\text{tip}}| \gg |v_{\text{wall}}|$ is responsible for the characteristic needle-like shape of ferroelectric domains. In addition, thermal fluctuations promote the branching of existing domains and nucleation of new domains. While the nucleation spots are randomly distributed in a defect-free single-crystal, grain boundaries in a polycrystal (like any other location with stress or charge concentrations) act as natural sites for nucleation. The emerging simulated microstructures during polarization switching incorporate qualitatively various characteristic features known from experimental observation, including first- and higher-order laminates, and wedge-like structures. A detailed comparison with experiments is unfortunately out of reach since in-situ measurements of ferroelectric microstructures, especially over a broad temperature range and under applied electric fields, are a rare find. Our simulations capture general qualitative trends while a quantitative comparison will require further experimental data and may require a re-calibration of model parameters (specifically of the drag coefficient μ, which may also be assumed temperature-dependent in general). Yet, our model demonstrated the salient features of finite-temperature ferroelectric switching in a promising fashion (based on energetic potentials obtained from first principles). We have thus presented an approach to "thermalize" a 0K first-principles-based model for finite-temperature phase-field simulations.

We close by pointing out that we linked the stochastic noise in our model to thermal lattice vibrations. By using as the normalization volume the primitive unit cell of the crystal lattice (known from DFT calculations), we ensure that the noise amplitude is intrinsically connected to material properties without any fitting parameter. As a downside, this restricts

simulations to small length scales (effectively limiting the pixel or voxel size to that of an atomic unit cell), as demonstrated in the presented examples with RVEs at the nanoscale. This also results in realistic domain wall thicknesses in simulations, not achievable at considerably larger scales. Note that one may alternatively interpret the introduced fluctuation field at larger scales, e.g., as the joined impact of temperature and fluctuating point defects and charges on the mesoscale, in which case larger spatial simulation domains are feasible but at the cost of rendering the random noise phenomenological and its amplitude a fitting parameter. Irrespectively, we conclude that the presence of random fluctuations is key to achieving realistic predictions of ferroelectric microstructures not predictable in a perfect, noise-free system.

3

EFFECT OF TEMPERATURE ON DOMAIN WALL–PORE INTERACTIONS IN PZT

This Chapter has been adapted from:

Indergand, R. and Kochmann, D.M. (2021). "Effect of temperature on domain wall–pore interactions in lead zirconate titanate: A phase-field study." *Applied Physics Letters*, Vol. 119, 222901, URL: https://doi.org/10.1063/5.0066612

3.1 INTRODUCTION

Ferroelectric materials have a permanent electric dipole moment (or spontaneous polarization), which can be altered by electric fields. This unique property—in combination with their electro-mechanical (Curie & Curie, 1880), thermoelectric (Brewster, 1824), and electro-optical coupling (Parravano, 1952)—makes ferroelectrics a versatile class of materials for, e.g., transducers, actuators, sensors, and memory devices. Since the effective kinetics of polarization switching at the macroscale is strongly determined by the collective motion (Bintachitt et al., 2010; Gorfman et al., 2018) of individual domain walls at smaller scales (Bassiri-Gharb et al., 2007; Marincel, Zhang, et al., 2015; Pramanick et al., 2011), understanding the underlying physics of domain wall motion and its interaction with defects in realistic materials (which typically show high sintering-induced porosity with nano- to micrometer-sized pores (Mercadelli et al., 2010)) is key for accurate predictions of microstructure-property relations. Pores can introduce substantial local mechanical (Johnson-Wilke et al., 2015; Xu & Wang, 2015; Zeng et al., 2007) and electric fields (Johnson-Wilke et al., 2015; Khachaturyan et al., 2016; Zeng et al., 2007) in their vicinity, which interfere with domain wall motion, thus influencing the ferroelectric and piezoelectric properties (Skinner et al., 1978) in bulk (Schultheiß et al., 2019b) and thin films (Johnson-Wilke et al., 2015). For instance, recent studies on (an-)isometric pores investigated the effect of pore concentration, size,

anisotropy, and orientation for tuning the piezoelectric properties of lead zirconate titanate (PZT) (Guo et al., 2011; Schultheiß et al., 2019b; Y. Zhang et al., 2017). Experiments have demonstrated the effects of domain wall pinning across scales: at the macroscale, the influence of dopants, oxygen vacancies, and crystal structures in PZT on the bipolar hysteresis behavior was investigated (Carl & Hardtl, 1977; B. Li et al., 2005; Rojac et al., 2016), while insight into the microscopic kinetics of polarization reversal was gained by tracking individual domain walls via atomic force microscopy, piezoresponse force microscopy, and polarization sensitive collection mode near-field scanning optical microscopy (Jo et al., 2009; Kalinin et al., 2008; Paruch et al., 2006; Tybell et al., 2002; T. Yang et al., 1999).

When modeling domain wall motion in complex geometries at realistic scales, phase-field techniques are often the method of choice to predict material behavior. Various types of defects have been studied by phase-field models: from space charges and oxygen vacancy migration at the atomic level (Xiao & Bhattacharya, 2008) over impurities, voids (J. Wang & Kamlah, 2009), dislocations (Kontsos & Landis, 2009), and grain boundaries (N. Liu & Su, 2014) at the mesoscale to cracks (J. Wang et al., 2010), notches, and free surfaces (Fedeli et al., 2019) at the macroscopic device-level. At larger scales, scaling arguments and functional renormalization group techniques have been used to study domain wall pinning in disordered elastic systems for random bond and field disorder (Nattermann, 1987; Nattermann et al., 1990), crystal-lattice and disorder pinning (Emig & Nattermann, 1999; Emig & Nattermann, 1997), and the dipolar interaction of incommensurate–commensurate transitions (Natterman, 1983). Stemming from nonlinear continuum mechanics, a theory for interface motion in homogeneous (Abeyaratne & Knowles, 1991; Ball et al., 1995; Bhattacharya, 1999; James, 2000) and heterogeneous materials (Salje, 2012; L. Tan & Bhattacharya, 2016) was established and used to study, among others, the role of the defect length scale on the pinning of interface motion as well as the influence of grain boundary, size, and triple junctions (Qiao & Radovitzky, 2016; Ueland & Schuh, 2013), and its impact on the macroscopic hysteresis.

Although various models have thus been proposed to study the influence of pores, the effect of temperature on domain wall (de-)pinning is insufficiently considered in general but plays an important role on domain wall kinetics, as evident from experiments (Jo et al., 2009; Savage & Miller, 1960; Stadler & Zachmanidis, 1964). We therefore use a finite-temperature phase-field framework (Indergand et al., 2020), which—calibrated by Density Functional Theory (DFT) data—captures the temperature dependence

of the Ginzburg-Landau energy as well as thermal fluctuations. This allows us to gain insight into the effect of temperature on domain wall-pore interactions for an enhanced predictability of the kinetics of ferroelectric materials and, more generally, it provides an efficient numerical tool to probe the temperature-dependent influence of microstructural features.

To this end, Section 3.2 briefly summarizes the finite-temperature constitutive model within the context of porous ferroelectrics, Section 3.3 provides a comparison of the electric field in the proximity of a single pore based on an analytical solution from electrostatics and on computational mechanics using phase-field modelling, Section 3.4 discusses the influence of pores on the ferroelectric domain wall motion for various pore sizes and densities at finite temperature, and finally, Section 3.5 summarizes the key findings in comparison with experiments and open challenges of this study.

3.2 FINITE-TEMPERATURE PHASE-FIELD MODEL

As the length and time scales of interest lie outside the realm of first-principles techniques, we use a phase-field description based on the well-established Devonshire-Ginzburg-Landau theory (Devonshire, 1954; L. Landau, 1937) with the total polarization vector $\boldsymbol{p}$ as the order parameter, describing the evolution of the ferroelectric microstructure by resolving the diffuse interfaces between ferroelectric domains. We simulate a Representative Volume Element (RVE) of a ferroelectric material, whose electro-mechanical response is described by the mechanical displacement field $\boldsymbol{u}(\boldsymbol{x}, t)$ and electric potential $\phi(\boldsymbol{x}, t)$, both dependent on position $\boldsymbol{x}$ and time t. The mechanical problem is governed by the balance of linear momentum (in the absence of body forces and inertial effects),

$$\nabla \cdot \boldsymbol{\sigma} = 0, \tag{3.2.1}$$

where $\boldsymbol{\sigma}$ is the Cauchy stress tensor. The electrical problem obeys Gauss' law (assuming no free charges),

$$\nabla \cdot \boldsymbol{d} = 0, \qquad \text{where} \qquad \boldsymbol{d} = \kappa_0 \boldsymbol{e} + \boldsymbol{p} \tag{3.2.2}$$

is the electric displacement field linked to the electric field $\boldsymbol{e} = -\nabla\phi$ through the permittivity of free space, κ_0. We assume a uniform temperature

θ within the material, whose electric enthalpy density is of the form (Su & Landis, 2007; W. Zhang & Bhattacharya, 2005)

$$\begin{aligned} W(\boldsymbol{\varepsilon}, \boldsymbol{e}, \boldsymbol{p}, \nabla \boldsymbol{p}, \theta) = \Psi_{\text{mech.}}(\boldsymbol{\varepsilon}) + \Psi_{\text{coupl.}}(\boldsymbol{\varepsilon}, \boldsymbol{p}) + \Psi_{\text{pol.}}(\boldsymbol{p}, \theta) \\ + \Psi_{\text{el.}}(\boldsymbol{e}) + \Psi_{\text{inter.}}(\nabla \boldsymbol{p}) - \boldsymbol{e} \cdot \boldsymbol{p}, \end{aligned} \tag{3.2.3}$$

comprising the mechanical energy density $\Psi_{\text{mech.}}$ dependent on strain tensor $\boldsymbol{\varepsilon} = \frac{1}{2}(\nabla \boldsymbol{u} + \nabla \boldsymbol{u}^{\intercal})$, coupling energy density $\Psi_{\text{coupl.}}(\boldsymbol{\varepsilon}, \boldsymbol{p})$, polarization (Landau) potential $\Psi_{\text{pol.}}$ as well as electric and interface energy densities $\Psi_{\text{el.}}$ and $\Psi_{\text{inter.}}$, respectively. Material constants (which have been adapted from DFT calculations for tetragonal PZT by Völker et al. (2011)) and the specific form of the above energy densities are summarized in Tab. 2.1. Constitutive relations follow as $\boldsymbol{\sigma} = \partial W / \partial \boldsymbol{\varepsilon}$ and $\boldsymbol{d} = -\partial W / \partial \boldsymbol{e}$. The polarization potential $\Psi_{\text{pol}}(p, \theta)$—and hence its minimizer, the spontaneous polarization p_0—is temperature-dependent. Below the Curie temperature θ_{C} (for PZT $\theta_{\text{C}} = 650\,\text{K}$) we find, from minimizing $\Psi_{\text{pol.}}(\boldsymbol{p}, \theta)$,

$$p_{\text{o}}(\theta) = \sqrt{\frac{\sqrt{\alpha_{11}^2 - 3\alpha_1\alpha_{111}\frac{\theta_{\text{C}}-\theta}{\theta_{\text{C}}}} - \alpha_{11}}{3\alpha_{111}}}. \tag{3.2.4}$$

The evolution of the polarization $\boldsymbol{p}$ is generally described by gradient flow kinetics (Chen, 2008; Su & Landis, 2007; W. Zhang & Bhattacharya, 2005). Since the latter applies only in the athermal limit (at 0 K), we here model finite temperature via a stochastic extension of the Allen-Cahn equation:

$$\mu \dot{\boldsymbol{p}} = -\frac{\partial W}{\partial \boldsymbol{p}} + \nabla \cdot \frac{\partial W}{\partial \nabla \boldsymbol{p}} + \mu \boldsymbol{\eta} \tag{3.2.5}$$

with an inverse mobility $\mu > 0$. $\boldsymbol{\eta}$ represents uncorrelated random noise, which accounts for atomic-level thermal fluctuations at the mesoscale. Under the assumption of thermal equilibrium, the stochastic process $\boldsymbol{\eta}(\boldsymbol{x}, t)$ is identified as a centered Gaussian random variable, which is unbiased and uncorrelated in space and time and whose variance depends on temperature (Indergand et al., 2020):

$$\left\langle \boldsymbol{\eta}(\boldsymbol{x}, t), \boldsymbol{\eta}(\boldsymbol{x}', t') \right\rangle = \frac{2k_{\text{B}}\theta}{\mu V_{\text{char}} \Delta t} \delta(t - t')\, \delta(\boldsymbol{x} - \boldsymbol{x}'), \tag{3.2.6}$$

where k_{B} denotes Boltzmann's constant, Δt the numerical time increment, and $V_{\text{char}} = a_{\text{tetr}}^2 c_{\text{tetr}}$ the volume of a perovskite atomic unit cell (which is assumed to be constant). The effect of temperature hence enters the

model through (i) the polarization potential and the resulting spontaneous polarization in Eq. (3.2.4) and (ii) the thermalized kinetics in Eq. (3.2.5). This phase-field model, which was validated against experimental data and shown to produce realistic domain microstructures (Indergand et al., 2020), is the basis for studying the influence of temperature on domain wall pinning in porous single-crystalline PZT. Pores are modeled as non-switchable cavities with polarization $\boldsymbol{p} = \boldsymbol{0}$ and vacuum permittivity κ_0.

We solve Eqns. (3.2.1), (3.2.2) and (3.2.5) within a cubic RVE by an FFT-based homogenization scheme with periodic boundary conditions (Section 2.5). Experimental conditions of free-standing, electrically loaded samples are realized by enforcing a vanishing average stress, $\langle \boldsymbol{\sigma} \rangle = \boldsymbol{0}$, along with a prescribed average electric field $\langle \boldsymbol{e} \rangle$, representing the applied field. While for small pores relative to the RVE size ($R/L \ll 0.1$) this setup accurately approximates the analytical solution for an isolated pore in an infinite medium (see Section 3.3, including a discussion on numerical accuracy), larger pores ($R/L > 0.1$ at fixed RVE size) model periodic arrays of voids and are viewed representative of porous samples.

3.3 SINGLE-VOID BENCHMARK

To assert the accuracy of the phase-field model to predict the electric field in the proximity of voids, we study as a benchmark an isolated cavity within an infinite dielectric material, for which an analytical solution derived from electrostatics can be used to validate numerical results.

3.3.1 *Analytical solution from electrostatics*

We solve Laplace's equation, $\Delta\phi = 0$, on an infinite dielectric body Ω with a circular cavity Ω_d of radius R. We use cylindrical polar coordinates r and φ and assume the origin at the center of the RVE, see Fig. 3.1(a). For the electric potential we use the ansatz

$$\phi(r,\varphi) = \alpha_0 \log r + \beta_0 + \sum_{m=1}^{\infty} (\gamma_m r^m + \delta_m r^{-m}) \sin(m\varphi), \tag{3.3.1}$$

where $m \in \mathbb{N} \setminus \{0\}$ and $\alpha_0, \beta_0, \gamma_m, \delta_m \in \mathbb{R}$ are constants. At the dielectric-cavity interface at $r = R$ we assume a curl-free electric field ($[\![\boldsymbol{e}]\!] \cdot \boldsymbol{t} = 0$) and open-circuit boundary conditions ($[\![\boldsymbol{d}]\!] \cdot \boldsymbol{n} = 0$), where $\boldsymbol{t}$ and $\boldsymbol{n}$ denote,

respectively, unit vectors parallel and normal to the interface and $\boldsymbol{d} = \kappa \boldsymbol{e}$ is the electric displacement with permittivity $\kappa = \kappa_0 \kappa_r$. Furthermore, by imposing boundary conditions in the far-field limit, i.e., $\boldsymbol{e}(r \to \infty) = E_0 \mathbf{e}_2$ and $\phi(r \to \infty) = -E_0 x_2$, and considering axial symmetry with respect to the $\mathbf{e}_2$-direction, the electric potential is obtained as

$$\phi(r, \varphi) = \begin{cases} -\frac{2}{1/\kappa_r + 1} E_0 r \sin\varphi & \text{in } \Omega_d, \\ \left(-r + \frac{1/\kappa_r - 1}{1/\kappa_r + 1} \frac{R^2}{r^2}\right) E_0 \sin\varphi & \text{in } \Omega, \end{cases} \tag{3.3.2}$$

where κ_r is the relative permittivity of the dielectric. From the electrostatic relation $\boldsymbol{e} = -\nabla\phi$ we determine the electric field in Cartesian coordinates (x_1, x_2) as

$$\boldsymbol{e}(\boldsymbol{x}) = \begin{cases} \frac{2}{1/\kappa_r + 1} E_0 \mathbf{e}_2 & \text{in } \Omega_d, \\ -2E_0 R^2 \frac{1/\kappa_r - 1}{1/\kappa_r + 1} \frac{x_1 x_2}{|\boldsymbol{x}|^4} \mathbf{e}_1 + E_0 \left[R^2 \frac{1/\kappa_r - 1}{1/\kappa_r + 1} \left(\frac{2x_2^2}{|\boldsymbol{x}|^4} - \frac{1}{|\boldsymbol{x}|^2} \right) + 1 \right] \mathbf{e}_2 & \text{in } \Omega, \end{cases} \tag{3.3.3}$$

where $|\boldsymbol{x}| = \sqrt{x_i x_i}$ denotes the Euclidean length of the position vector $\boldsymbol{x}$. By rearranging the electric field (3.3.3) along the vertical direction, one can obtain an estimate for the electric field interaction of nearest-neighbor pores at distance vectors $\boldsymbol{x} = (0, L)^{\mathrm{T}}$ based on the relative electric field decay $|\Delta e|$, defined as

$$|\Delta e| = \left| \frac{e_2}{E_0} - 1 \right| = \frac{1}{4} \left| \frac{1/\kappa_r - 1}{1/\kappa_r + 1} \right| \left(\frac{2R}{L} \right)^2. \tag{3.3.4}$$

In a 3D domain with a centered spherical cavity, we follow Jackson (1999) to analogously derive a solution based on Legendre functions, such that the electric potential and electric field are obtained as, respectively,

$$\phi(r, \varphi) = \begin{cases} -\frac{3}{1/\kappa_r + 2} E_0 r \sin\varphi & \text{in } \Omega_d, \\ \left(-r + \frac{1/\kappa_r - 1}{1/\kappa_r + 2} E_0 \frac{R^3}{r^2}\right) E_0 \sin\varphi & \text{in } \Omega, \end{cases} \tag{3.3.5}$$

and, using Cartesian coordinates (x_1, x_2, x_3),

$$\boldsymbol{e}(\boldsymbol{x}) = \begin{cases} \frac{3}{1/\kappa_r + 2} E_0 \mathbf{e}_2 & \text{in } \Omega_d, \\ -3E_0 R^3 \frac{1/\kappa_r - 1}{1/\kappa_r + 2} \frac{x_1 x_2}{|\boldsymbol{x}|^5} \mathbf{e}_1 + \left[R^3 \frac{1/\kappa_r - 1}{1/\kappa_r + 2} \left(\frac{3x_2^2}{|\boldsymbol{x}|^5} - \frac{1}{|\boldsymbol{x}|^3} \right) + 1 \right] E_0 \mathbf{e}_2 & \text{in } \Omega. \end{cases} \tag{3.3.6}$$

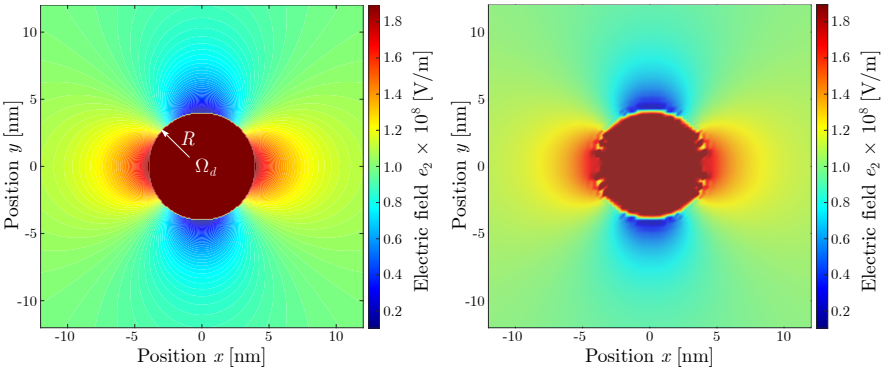

Figure 3.1: Comparison of the electric field component $e_2(\boldsymbol{x})$ in the vertical direction as predicted by theory (a) and the phase-field model (b) for a circular void inside a dielectric in 2D; shown for relative permittivity $\kappa_r = 18$ and an average electric field $\langle e_2 \rangle = 10^8\,\mathrm{V/m}$ in the vertical direction.

Note that the third component of the electric field is identical to the first by the symmetry of the problem. Finally, the decay of the electric field for a spherical pore is

$$|\Delta e| = \left| \frac{e_2}{E_0} - 1 \right| = \frac{1}{4} \left| \frac{1/\kappa_r - 1}{1/\kappa_r + 2} \right| \left(\frac{2R}{L} \right)^3 . \tag{3.3.7}$$

By comparing the electric field in (3.3.3) and (3.3.6), we find that its magnitude within a cylindrical pore is approximately 33% higher compared to a spherical pore, showing the difference between a 2D and a 3D pore geometry.

3.3.2 *Isolated void vs. array of voids*

While the above theoretical solutions are based on solving the Laplace equation for the electric potential on an infinite domain by imposing a far-field $\boldsymbol{e}(r \to \infty)$ and electric potential $\phi(r \to \infty)$, the phase-field model with its FFT-based numerical implementation is restricted to a finite and periodic domain with averages imposed for $\langle \boldsymbol{e} \rangle$ and $\langle \phi \rangle$. Despite these differences, the phase-field model predicts the induced electric field for small voids reasonable well in comparison with the analytical solution, as

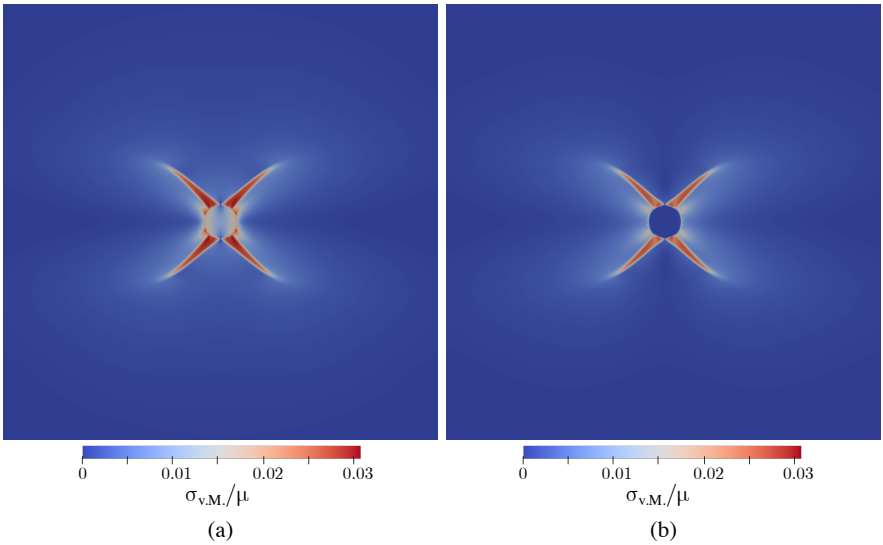

Figure 3.2: Influence of the artificial void stiffness $\mathbb{C}^{\mathrm{v}}$ on the von Mises stress $\sigma_{\mathrm{v.M.}}/\mu_{\mathrm{e}}$ (normalized by the shear modulus μ_{e}) for a stiffness ratio of $\mathbb{C}^{\mathrm{v}}_{ij}/\mathbb{C}^{\mathrm{FE}}_{ij} = 1$ (a) and $\mathbb{C}^{\mathrm{v}}_{ij}/\mathbb{C}^{\mathrm{FE}}_{ij} = 0.01$ (b), where $\mathbb{C}^{\mathrm{FE}}$ denotes the elastic stiffness tensor of the ferroelectric, computed for a circular void of radius $R = 8\,\mathrm{nm}$ in 2D under shorted and stress-free boundary conditions, $\langle \boldsymbol{e} \rangle = \mathbf{0}$ and $\langle \boldsymbol{\sigma} \rangle = \mathbf{0}$, respectively, at room temperature.

shown in Fig. 3.1 (for a circular void embedded in a dielectric material with relative permittivity $\kappa_r = 18$ at an imposed average electric field $E_0 = \langle e_2 \rangle = 10^8\,\mathrm{V/m}$). Only small discrepancies at the fringes of the cavity are visible, which originate from the staggered discretization of curved surfaces leaving few pixels with only one nearest-neighbor pixel within the inclusion, which results in Gibbs oscillations caused by the discontinuity of the permittivity $\kappa(\boldsymbol{x})$ and non-uniform convergence of the truncated Fourier Series; see, e.g., Anglin et al. (2014), Lebensohn and Rollett (2020), and Vidyasagar et al. (2017) for a detailed discussion on the accuracy of FFT-based methods depending on homogeneity, geometry, and resolution.

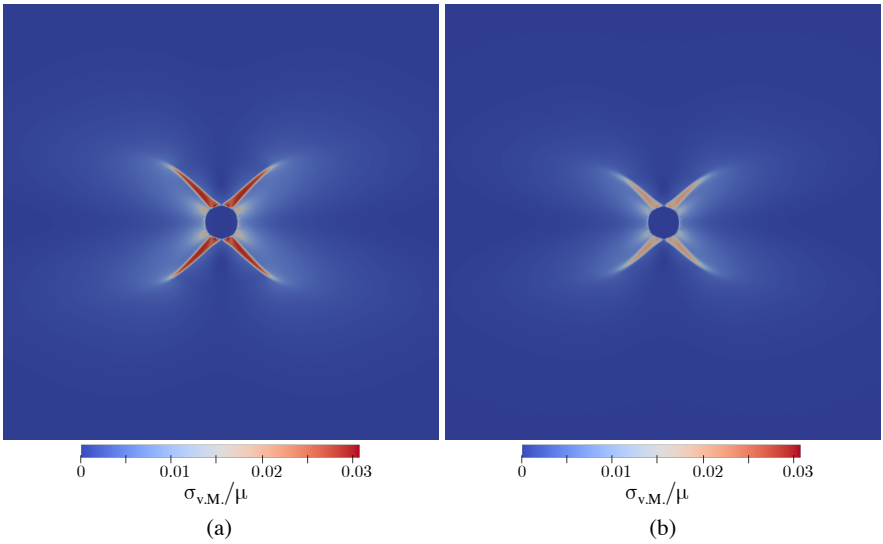

Figure 3.3: Influence of temperature on the von Mises stress $\sigma_{\text{v.M.}}/\mu_{\text{e}}$ (normalized by the shear modulus μ_{e}) at 200 K (a) and 400 K (b), computed for a circular void of radius $R = 8\,\text{nm}$ with a stiffness contrast of $\mathbb{C}_{ij}^{\text{pore}}/\mathbb{C}_{ij}^{\text{FE}} = 0.01$ in 2D under shorted and stress-free boundary conditions, $\langle \boldsymbol{e} \rangle = \mathbf{0}$ and $\langle \boldsymbol{\sigma} \rangle = \mathbf{0}$, respectively.

3.3.3 *Heterogeneous vs. homogeneous elastic stiffness tensor*

We briefly asses the impact of the heterogeneous and homogeneous elastic stiffness model in the contrast of a circular pore in PZT by utilizing (2.5.5) and (2.6.4a), respectively, in the FFT-based spectral solution scheme, described in Section 2.5. The stiffness contrast between the cavity and the dielectric material under on average stress-free conditions within the RVE ($\langle \boldsymbol{\sigma} \rangle = \mathbf{0}$) in combination with the small cavity size relative to the RVE size leads to additional stress concentrations on the surface of the void, as shown in Fig. 3.2, which shows the von Mises stress distribution for a stiffness contrast $\mathbb{C}_{ij}^{\text{v}}/\mathbb{C}_{ij}^{\text{FE}} = 0.01$. (Of course, the stiffness of the cavity is practically 0, yet for numerical purposes we assign a finite stiffness that is significantly smaller than that of the surrounding medium with only a marginal impact on the numerical solution.) As seen in Fig. 3.2 and Fig. 3.3, the heterogeneity of the elastic stiffness tensor for the given setup plays only a minor role for the depinning field in comparison to the thermo-electrical impact and temperature-related changes in the stress field are

primarily concentrated within the needle domains, which is why we make the simplifying assumption of a homogeneous isotropic material to avoid an iterative solution scheme.

3.4 RESULTS: DOMAIN WALL-PORE INTERACTION AT FINITE TEMPERATURE

Pores in a ferroelectric act as hot spots for domain switching and domain nucleation under an applied electric field, which is amplified to significantly larger local electric fields induced near the pore. This effect becomes apparent in Fig. 3.4a, which shows the evolution of the polarization around a spherical cavity of radius $R = 12\,\mathrm{nm}$ and, for improved visibility, 2D results for the polarization p_2/p_0 and the electric field e_2 at 100 K (Fig. 3.4b/c) and at 300 K (Fig. 3.4d) for comparison. Initially poled with $\boldsymbol{p} = p_0\mathbf{e}_2$, symmetric needle-shaped a-domains grow under 45° to compensate for the strain mismatch and the induced electric fields in the proximity of the pore. The induced electric field above and below the pore favors b^--domains and disfavors the existing b^+-domain. The lowest-energy transition for polarization reversal to occur is by polarization rotation, which corresponds to two subsequent 90°-switching steps, e.g., from a b^+-domain via $a^\pm$-domains to a b^--domain. These newly formed a-domains are a consequence of the induced electric field by the pore and the minimization of the polarization potential $\Psi_{\mathrm{pol.}}$.

In the absence of free charges, the electric field $\boldsymbol{e}^-$ inside the cavity is related to the electric field $\boldsymbol{e}^+$ and polarization $\boldsymbol{p}$ outside the cavity by the jump condition $[\![\boldsymbol{d}]\!] \cdot \boldsymbol{n} = 0$, where $\boldsymbol{n}$ is the outward-pointing surface normal. Inserting Eq. (3.2.2) gives the electric field outside the cavity as

$$\boldsymbol{e}^+ = \boldsymbol{e}^- - \frac{1}{\kappa_0}(\boldsymbol{p}\cdot\boldsymbol{n})\boldsymbol{n}, \tag{3.4.1}$$

i.e., as a function of the electric field $\boldsymbol{e}^-$ inside the pore and the outside polarization $\boldsymbol{p}$ (whose magnitude is the spontaneous polarization p_0 in the absence of external loads). Since the spontaneous polarization depends on temperature, cf. Eq. (3.2.4), the induced electric field also varies with temperature. This is observed when comparing the computed electric field component $e_2(\boldsymbol{x})$ at the two temperatures of 100 K and 300 K in Fig. 3.4c and Fig. 3.4d, respectively. Due to the smaller spontaneous polarization at 300 K, the induced electric field in Fig. 3.4d is lower in amplitude and

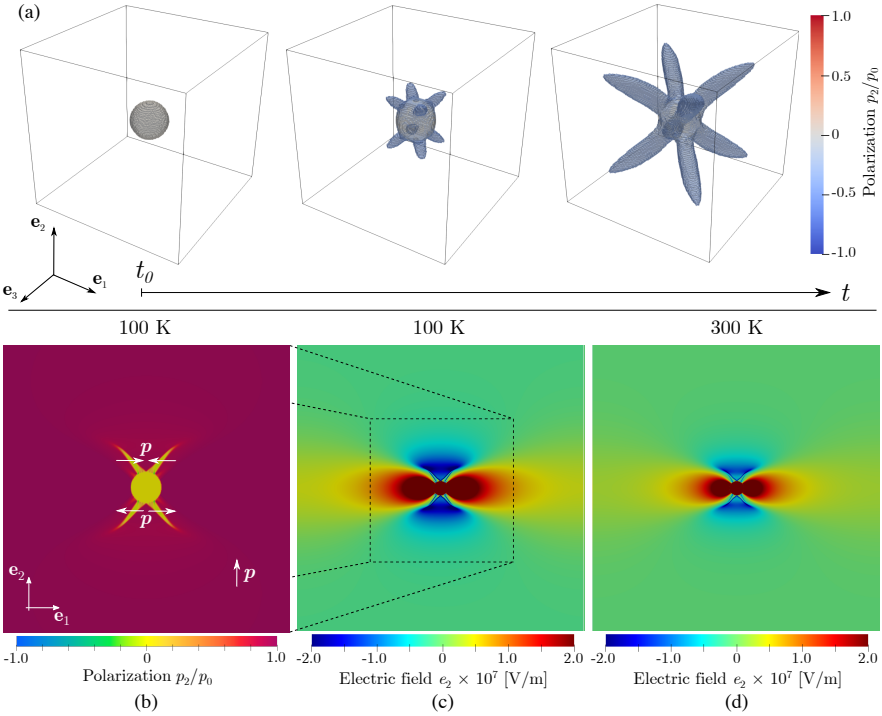

Figure 3.4: (a) Snapshots of the 3D polarization evolution ($L = 51\,\text{nm}$), showing regions with a vertical polarization component $\boldsymbol{p}_2(\boldsymbol{x})/p_0 \in [-0.5, 0.5]$ in the vicinity of a spherical cavity with radius $R = 12\,\text{nm}$ for an imposed average field $\langle \boldsymbol{e} \rangle = \mathbf{0}$ and average stress-free conditions ($\langle \boldsymbol{\sigma} \rangle = \mathbf{0}$). Comparison of the electric field in the vertical direction, $e_2(\boldsymbol{x})$, for an imposed average field $\langle \boldsymbol{e} \rangle = \mathbf{0}$ at temperatures $\theta = 100\,\text{K}$ and $300\,\text{K}$ is shown in (c) and (d), respectively. A zoomed-in version of the region highlighted in (c) visualizes polarization component $p_2(\boldsymbol{x})/p_0$ in (b).

extends less into the surroundings than at 100 K (shown in Fig. 3.4c). As a consequence, a decreasing influence of pores onto domain wall motion with increasing temperature may be expected.

To systematically investigate the influence of pore size and pore separation distance on domain walls, we simulate domain wall-pore interactions in the simpler 2D setting, which gains significant efficiency while not affecting the physics at play (cf. Fig. 3.4). We consider a 180°-domain wall interacting with a periodic array of circular pores of equal radii R (simulating a square-shaped RVE of side length $L = \{102, 205, 410\}$ nm with periodic boundary conditions, see Fig. 3.5). Independent of parameters R and L, the single-crystalline RVE contains initially two ferroelectric domains: the b^+-domain (red) and b^--domain (blue), whose polarizations point up and down, respectively. When applying an average electric field e_2 in the vertical direction, the lower-energy b^+-domain grows by moving the domain walls towards the outer boundaries of the RVE. The non-switchable pores, whose size exceeds the thickness of domain walls ($l_0 \approx$ 0.7-2 nm (Cho et al., 2003; Völker et al., 2011)), serve as obstacles to the moving domain walls. Their interaction is already apparent before the domain wall reaches the pore, as shown in Fig. 3.5b, where the growing b^+-domain (red) is locally eroded close to the pore by the induced electric field to the left of the cavity. Such erosion of the 180°-domain wall near defects under an applied field was observed in experiments (T. Yang et al., 1999) using near-field scanning optical microscopy. The spreading a^-- and a^+-domains above and below the pore, respectively, connect to the b^+-domain by forming 90°-domain walls. Local electric fields in the proximity of the cavity reduce the driving force on the domain wall, thus slowing down the propagating interface, until it is pinned at the pore (Fig 3.5d). Such pinning of an individual domain wall at an isolated defect (Kalinin et al., 2008), a dislocation (Gao et al., 2011), precipitates (Zhao et al., 2021), secondary phases (Riemer et al., 2017), a twin (Jesse et al., 2008) and grain (Marincel, Zhang, et al., 2015; Marincel, Zhang, et al., 2015) boundary has been confirmed experimentally. To unpin from the obstacle, the applied electric field must be increased, which in case of the cavity promotes the following mechanism (Fig. 3.5e): domains with polarization parallel to the cavity's surface grow, until the top and bottom regions merge to grow a new b$^+$-domain to the right of the pore. This newly formed domain then expands by domain wall motion and eventually merges with the initial b^+-domain from the center of the RVE (Fig. 3.5e). We define the *depinning field* as the minimum applied electric field required to unpin the domain wall from the pore(s); it is obtained in simulations

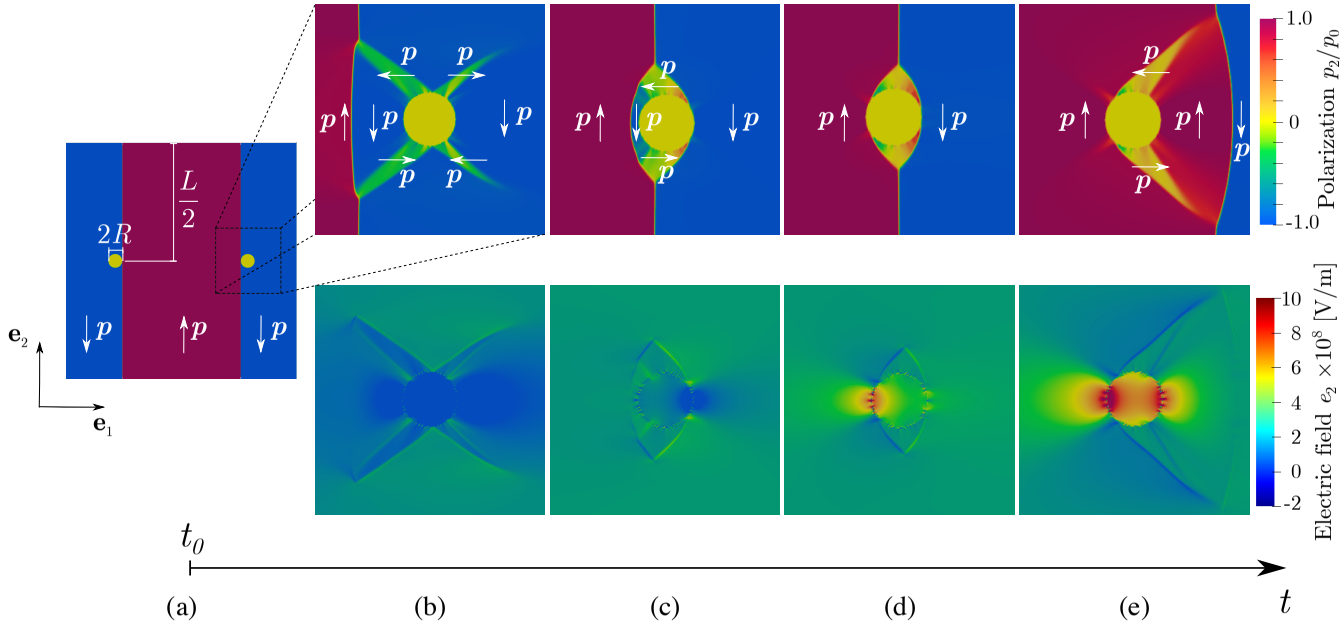

Figure 3.5: Snapshots of a simulated ferroelectric domain wall interacting with a circular cavity, showing polarization component $p_2(\boldsymbol{x}, t)/p_0$ (top row) and electric field component $e_2(\boldsymbol{x}, t)$ (bottom row) at temperature $\theta = 300\,\mathrm{K}$. (a) The initial configuration includes two ferroelectric domains separated by 180°-domain walls with two circular pores of radius R at a distance L, considering periodic boundary conditions. Snapshots (b) to (e) show zoomed-in versions of the highlighted section in (a) for the three cases when (b-c) the domain wall is approaching the void, (d) the domain wall is pinned by the pore, and (e) the domain wall unpins from the void. Small arrows indicate the polarization vector directions. For the full simulation see Supplementary Video 1.

by increasing the applied electric field incrementally (with sufficient dwell time between increments, so finite-temperature Brownian motion can show its effect). The recurring pinning and unpinning of domain walls at pores appears as stick-slip behavior of mesoscopic domain wall motion, or as a pronounced hysteresis at the macroscale (L. Tan & Bhattacharya, 2016).

The impact of pore size (radius R) and pore separation (distance L) on the depinning field is summarized in Fig. 3.6a-c for the three temperatures of $\theta = 200, 300, 400\,\mathrm{K}$. Overall, the depinning field increases monotonically with pore size, and the slope of the pore-radius-vs.-electric-field curve indicates a higher sensitivity of the depinning field to larger pore densities (assuming uniform pore radii). We hence conclude that at least two characteristic length-scales are at play: (i) pore radius R determines the locally induced near-field in the vicinity of the void according to Gauss' law, and (ii) distance L between pores accounts for the far-field interference of overlaying electric fields from adjacent pores. To account for these distinct length scales, we define the linear pore density $v_d = 2R/L$ as the ratio of the pore diameter and their distance (which is the domain of influence of a single pore within the ferroelectric). The resulting plot of depinning field vs. v_d collapses onto a single master curve $e(v_d)$ at each temperature (Fig. 3.6d-f), each following a linear relation. Note that the phase-field model is valid in the "large-defect" regime, i.e., for large pores with $2R > l_0$, below which a more accurate (atomistic) description is required and where other mechanisms are at play. (The largest domain wall thickness observed in simulations is about 1 nm at 500K.)

The interplay of pore size, pore separation distance, and temperature becomes apparent in Fig. 3.7a-c, showing the depinning field over a wide temperature range. The effect of temperature is generally dominant over both pore size and concentrations. The pore size gains importance with decreasing temperature and with decreasing pore separation distance. When approaching the Curie temperature $\theta_C = 650\,\mathrm{K}$, the homogeneous disordering of the ferroelectric polarization makes domain wall motion negligible and significantly reduces the pinning field (seen in the slope $\partial f/\partial v_d$ vs. temperature in Fig. 3.6g). By contrast, in the athermal limit $\theta \to 0\,\mathrm{K}$ thermal fluctuations are absent, so the associated Brownian motion cannot promote barrier-crossing events in non-coercive regions (Indergand et al., 2020) to lower the depinning field. While for the largest separation distance ($L = 410\,\mathrm{nm}$) the depinning field depends noticeably on pore size only at low temperatures below 200 K, the effect of pore size is more pronounced at $L = 102\,\mathrm{nm}$.

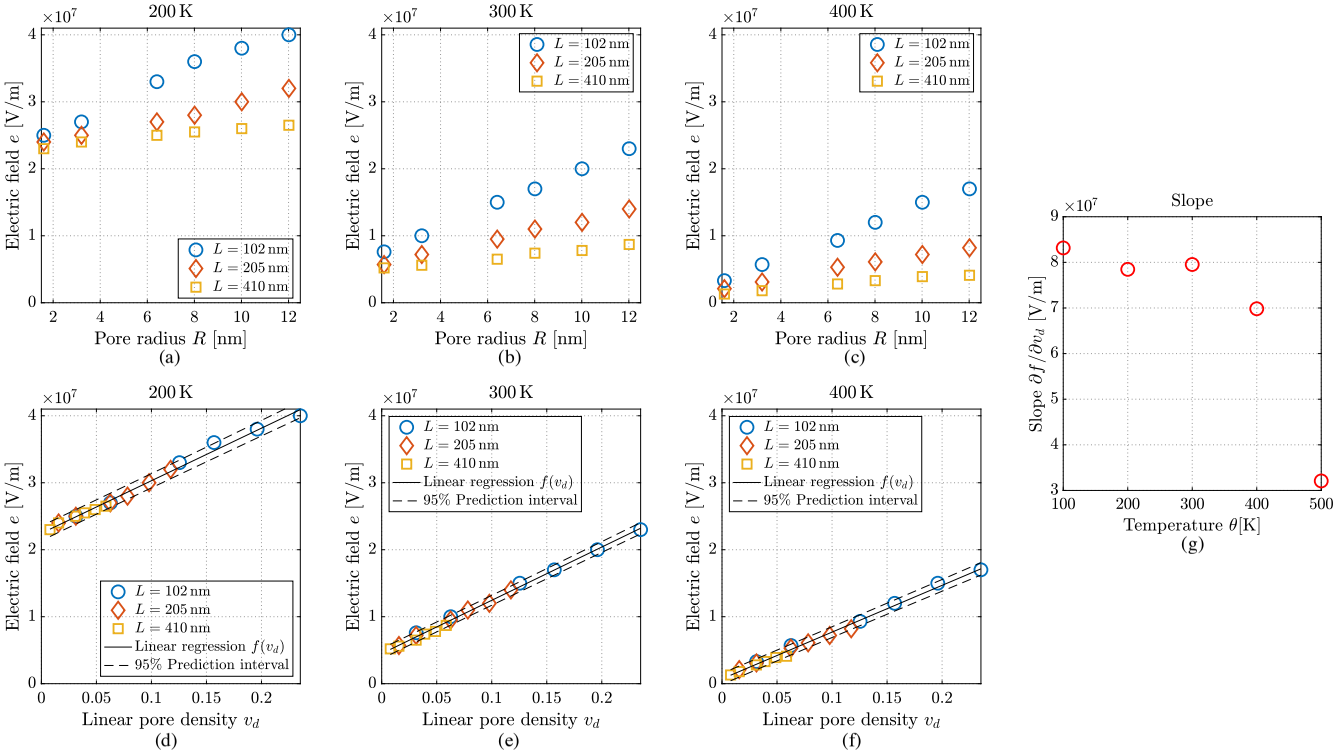

Figure 3.6: Influence of the pore radius R (a-c) and linear pore density $v_d = 2R/L$ (d-f) on the depinning electric field e_2, required for a 180°-domain wall to unpinn from and overcome an array of pores separated at distances $L = \{102, 205, 410\}$nm (line colors) at temperatures $\theta = \{200, 300, 400\}$K (columns). (g) Slope of the depinning field vs. v_d for all examined temperatures.

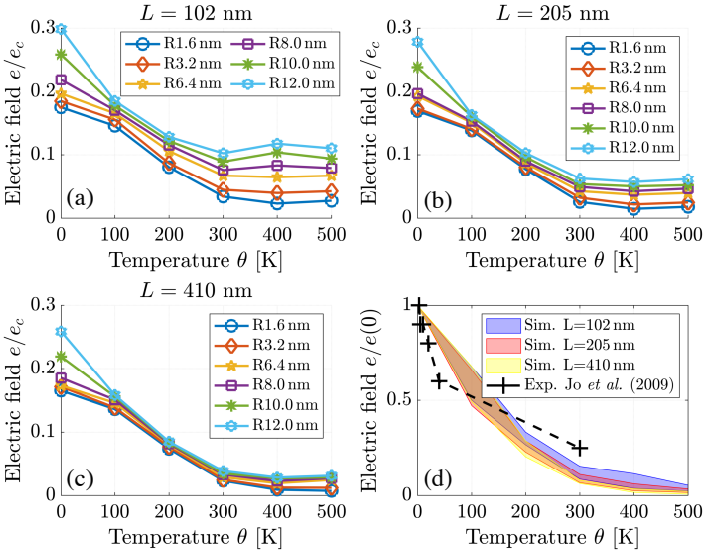

Figure 3.7: (a-c) Influence of temperature on the electric field e_2 (normalized by the temperature-dependent coercive field e_c) required for a 180°-domain wall to unpin and overcome an array of pores of radii $R = \{1.6, 3.2, 6.4, 8.0, 10.0, 12.0\}$ nm separated by distances $L = \{102, 205, 410\}$ nm. (d) Summary of all simulated data (each curve normalized by its athermal value $e(0\,\mathrm{K})$, showing the margin between minimum and maximum field per temperature) in comparison with experimental data (Jo et al., 2009).

Comparing the obtained depinning field at room temperature, $e/e_c \approx 0.044$ (averaged over all radii R at $L = 205\,\text{nm}$), with hysteresis measurements of PZT-5A (Hooker, 1998; W. L. Tan et al., 2019), reporting $e/e_c = 0.006$, reveals that in reality domain wall motion is active even below the electric field values reported here; this is expected due to simplifying assumptions and the 2D approximation of a spherical pore, overestimating the local electric field. Despite this difference in the depinning field magnitude, our model captures several key features previously reported from experiments. For example, the nonlinear temperature dependence of the depinning field is in good qualitative agreement with measurements of the domain wall velocity under random-field pinning in the creep regime (Jo et al., 2009) in epitaxial PZT films at finite temperature, as shown in Fig. 3.7d, where simulated data (normalized by the athermal limit) are compared to experiments (Jo et al., 2009). Moreover, the observed stick-slip behavior of domain wall motion interacting with pores is in agreement with local piezoresponse force spectroscopy measurements that identified the fine structure in the hysteresis loops as a fingerprint of an isolated defect (Kalinin et al., 2008).

3.5 CONCLUSION

In summary, using a temperature-aware phase-field model, we have investigated the pinning of domain walls at nano-sized pores in tetragonal PZT under an applied bias field across a wide temperature range. Domain wall pinning strongly affects ferroelectric switching through its impact on domain wall kinetics. We have highlighted the influence of pore size, pore concentration, and temperature.

Of course, such a model comes with limitations. First, the 2D simplification overestimates the electric field induced by the pore by 33% (Section 3.3.1). In a 3D ferroelectric material, we expect even smaller depinning fields due to two additional tetragonal variants, which increase the available switching paths and hence the probability of thermally induced barrier-crossing events. Second, we focused on 180°-domain walls and excluded pinning of initially 90°-domain wall configurations. Due to the differences in energy barriers, we have observed in analogous studies that depinning fields of 90°-domain walls can be orders of magnitude lower that the ones reported here. However, other physical effects, such as nucleation are dominant with 90°-domain walls and result in a different depinning mechanism,

such that a direct transfer of the reported depinning fields to 90°-domain wall pinning is challenging. Finally, the strain mismatch near pores, which is important for pinning, has not been investigated thoroughly in this study (see Section 3.3.3 for a discussion).

Despite these simplifying assumptions, the reported microscale interactions of nano-sized pores with 180°-domain walls are in general agreement with experimental observations. For example, the induced electric field in the proximity of the pore leads locally to polarization reversal, which appears as bending of the domain wall around the void. This effect has been optically captured and reported as bowing of domain walls (J. Yang, 2006). Furthermore, we observed a stick-slip behavior of domain walls at pores, which is characteristic for the large-defect-regime kinetics (L. Tan & Bhattacharya, 2016) and has been verified experimentally on isolated defects (Kalinin et al., 2008), twin boundaries (Jesse et al., 2008), and dislocations (Gao et al., 2011). In addition, theoretical (Khachaturyan et al., 2016) and experimental (Y. Zhang et al., 2018) studies suggest a decrease in the macroscale remanent polarization for higher porosity, which agrees with our findings that more densely packed pores (at constant size) increase microscale domain wall-pinning. Moreover, the computed temperature dependence of the depinning field shows agreement with measurements of PZT thin films (Jo et al., 2009). Our finite-temperature model hence reproduces salient features of domain wall pinning seen in experiments and in agreement with theoretical considerations. It improves the predictability of properties of realistic, porous ferroelectric materials at finite temperature, accounting for domain wall interactions with dielectric impurities at the microscale for wide ranges of electric field and temperature.

4

DOMAIN PATTERN FORMATION IN TETRAGONAL FERROELECTRIC CERAMICS

This Chapter has been adapted from:

Indergand, R., Bruant, X., and Kochmann, D.M. (2023). "Domain Pattern Formation in Tetragonal Ferroelectric Ceramics." *Under review.*

4.1 INTRODUCTION

A unique property of ferroelectric materials is their permanent (spontaneous) polarization, which can be reoriented by a sufficiently high applied electric field. This feature, together with various physical coupling mechanisms including the piezoelectric (Curie & Curie, 1880), pyroelectric (Brewster, 1824), electrooptic (Haertling, 1987), and electrocaloric (Olsen et al., 1985) effects, makes ferroelectrics versatile multipurpose materials for numerous applications such as sensors, actuators, capacitors, random access memory (FeRAM) (Buck, 1952), energy conversion devices (Bucsek et al., 2020), and micro-electro-mechanical systems (MEMS) (Lines & Glass, 2001; Uchino, 2009).

Most technically relevant ferroelectrics have a perovskite crystal structure, which undergoes a phase transition at the Curie temperature—with decreasing temperature from a high-symmetry non-polar state to a low-symmetry polar state, e.g., from a cubic crystal to a tetragonal, orthorhombic, or rhombohedral crystal (Cohen, 1992; Cohen & Krakauer, 1992). The symmetry-lowering transformation is a polar distortion that comes with a displacement of the atoms that breaks the centrosymmetry of the charge distribution, such that a spontaneous polarization emerges (Lines & Glass, 2001). The degeneracy of different low-symmetry states and long-range ordering of individual polar unit cells leads to the formation of regions of homogeneous polarization separated by interfaces of a few atomic layers thickness (Jia

et al., 2011; Meyer & Vanderbilt, 2002; Nataf et al., 2020), known as *ferroelectric domains* and *ferroelectric domain walls*, respectively (Lines & Glass, 2001). Analogously, a symmetry-lowering transformation that entails a change of shape of the crystal lattice gives rise to a spontaneous strain and *ferroelastic domains*. Adjacent pairs of ferroelastic domains with different spontaneous strains form *ferroelastic domain walls* at the interface, which are mobile under applied mechanical fields (Janovec & Privratska, 2013; Tagantsev et al., 2010).

Domain walls can be considered as two-dimensional (2D) topological defects with distinct physical properties compared to the bulk, according to experimental observations (Catalan et al., 2012; Meier, 2015; Seidel, 2012) and theoretical models (Aird & Salje, 1998; Janovec et al., 1999; N. Lawless & Fousek, 1970). Recent interest in the special attributes of domain walls, e.g., the conductivity in domain walls (Guyonnet et al., 2011; Meier et al., 2012; Rojac et al., 2017; Seidel et al., 2010; Seidel et al., 2009) or domain-wall polarity in non-polar materials (Goncalves-Ferreira et al., 2008; Nataf et al., 2017; Salje et al., 2013; Scott et al., 2012; Yokota et al., 2019) led to the exciting new field of *domain wall engineering*—with promising applications such as domain-wall nanoelectronics (Catalan et al., 2012; Nataf et al., 2020) comprising nonvolatile memory (Jiang et al., 2018; Sharma et al., 2017), diodes (Whyte & Gregg, 2015), and tunnel junctions (Sanchez-Santolino et al., 2017). A profound understanding of the domain pattern formation is key for future applications of ferroelectrics, e.g., as non-volatile memory devices, whose information storage capacity is strongly dependent on the density of domain walls (Nataf et al., 2020).

While the classification of compatible ferroelectric and ferroelastic domain structures and domain walls based on the underlying crystal symmetry is generally well understood (Janovec & Privratska, 2013; Tagantsev et al., 2010), other areas are far less well established. For example, the polarity of domain walls, is an active field of research, in which the symmetry of a wall is described by a layer group, using geometrical arguments in real space (Janovec et al., 2004; Janovec & Privratska, 2013) and in the order parameter space of the Grinzburg-Landau theory (Schranz et al., 2019; Tolédano et al., 2014) to derive the properties of the wall. A remarkable theoretical finding showed that all mechanically compatible ferroelastic domain walls are non-centrosymmetric and hence polar (Janovec et al., 1999) (even in non-polar materials), which was confirmed experimentally by second harmonic generation (SHG) microscopy (Yokota et al., 2019; Yokota et al., 2014).

Apart from the special properties of domain walls, the formation of intricate ferroelectric structures, e.g., arrays of polarization flux-closure vorticies (Yadav et al., 2016), polar-skyrmion bubble domains (Das et al., 2019), and polarization flux-closure domains (Jia et al., 2011) offer exciting features and have recently caught the interest of the ferroelectrics community. The latter structure is well known in ferromagnetics and was examined in early studies by theoreticians (Kittel, 1946; L. Landau & Lifshitz, 1935) and later by experimentalists (Hubert & Schäfer, 2008; Özdemir et al., 1995). Nevertheless, transition layers, such as *closure domains*[1], are also relevant in ferroelectrics (Tagantsev et al., 2010), primarily in thin films or phase boundaries (Jia et al., 2011; McQuaid et al., 2011). Although the appearance of closure arrangements can mostly be traced back to the effect of uncompensated boundary conditions such as an electric field induced by electric dipoles at a free surface (depolarization field) (Aguado-Puente & Junquera, 2008; Batra & Silverman, 1972; Junquera & Ghosez, 2003; Prosandeev & Bellaiche, 2007; Spaldin, 2004) or mechanical incompatibility of ferroelastic domains at phase boundaries (Ball & James, 1992; Z. Zhang et al., 2009), the understanding of closure-like structures is by far not complete. While the former boundary condition generates an electric field that can be neutralized by the screening effect of mobile charge carriers provided by metallic electrodes, the latter (mechanical) boundary condition locally induces a strain field which cannot be compensated easily (Gruverman et al., 1996; Kolosov et al., 1995; Simons et al., 2018). In ferroelectrics, closure domains have been studied in theory (Arlt & Sasko, 1980), in first-principle calculations (Aguado-Puente & Junquera, 2008; Lai et al., 2007; Prosandeev & Bellaiche, 2007), in piezoresponse force microscopy (PFM) experiments at the meso scale (McGilly et al., 2010; McQuaid et al., 2011), and in transmission electron microscopy (TEM) measurements at the atomic scale (Jia et al., 2011; Nelson et al., 2011).

Another important attribute of the domain pattern formation for next-generation ferroelectric devices is the size of domains, which influences the dielectric and piezoelectric properties and, therefore, determines the storage capacity of high-density memories, defines the size of nanoelectronics and the performance of ferroelectric transducers (Scott et al., 2012; Wada et al., 2006). Based on a simple model of a 180°-laminate of ferromagnetic domains with an open boundary condition, a scaling law was derived (Kittel, 1946; L. Landau & Lifshitz, 1935) by balancing the energy contained

1 For simplicity, we use this term for both vortex structures (complete flux closure) as well as vertex structures (incomplete flux closure).

within the domain vs. in the interface. This is better known as *Kittel's law*, which relates the domain width to the sample thickness in a square root-like manner. This square-root scaling law was later extended for ferroelectric films (Daraktchiev et al., 2008; Mitsui & Furuichi, 1953; Roitburd, 1976) and is generally applicable for any periodic domain pattern (Catalan et al., 2009; Catalan et al., 2006; Craik & Cooper, 1970; De Guerville et al., 2005; Kinase & Takahasi, 1957; Thiele, 1970).

Furthermore, *Kittel's law* is not limited to thin films but also of significance for polycrystalline bulk materials, where the domain width scales with the square root of the grain size, as early investigations on barium titanate (BT) showed (Arlt, 1990). Later studies on lead zirconate titanate (PZT) ceramics generally verified previous results and narrowed down the scope of validity of the square-root law depending on the grain size (Cao & Randall, 1996; Hoffmann et al., 2001; Randall et al., 1998; Webber et al., 2009). Besides governing the width of the twin lamellae, the competition between elastic strain energy and interface energy (Arlt, 1990; Arlt & Sasko, 1980) is responsible for a critical grain size, above which more intricate domain patterns (e.g., rank-2 laminates or bundle domains) emerge and act as a stress-reducing mechanism that minimize the energy. Recent PFM and *in situ* synchrotron x-ray experiments on donor-doped PZT observed such a decrease in the complexity of domain structures and an increase in internal stress with decreasing grain size (Picht et al., 2020).

Aside from the size of the crystallite, their orientation distribution is a decisive factor in determining the anisotropy of the effective material properties of a ferroelectric ceramic. Various high-energy synchrotron x-ray and neutron diffraction experiments reported a strong correlation of the domain switching fraction within a grain during electric-field poling and the crystallographic orientation (Hall et al., 2004; Hall et al., 2005; Jones et al., 2006; Jones et al., 2007; Jones et al., 2005; Pramanick et al., 2011)—thus emphasizing the role of texture and the contribution of 90°-domain wall motion towards the polycrystalline material response.

To study the ferroelectric microstructure, different models have been utilized to predict the domain evolution at the mesoscale under applied electric fields. First, sharp-interface models have been used for many years to compute equilibrium domain structures based on energy minimization, which seeks to satisfy the compatibility conditions not locally but on average (Ball & James, 1987; Davi & Rizzoni, 2004; De Simone, 1993; J. Li & Liu, 2004; Shu & Bhattacharya, 2001). More recently, the criteria

for exact compatibility (i.e., local compatibility) were used to identify all energy-minimizing rank-2 laminate structures in a tetragonal crystal (Tsou et al., 2011) as well as all possible low-energy transition paths between different types of compatible laminates (Tsou et al., 2013). While the discontinuous description of ferroelectric domain walls offers mathematical advantages, it becomes computationally expensive for large numbers of domains and requires an additional model to account for nucleation, which makes it unsuitable to predict the complex ferroelectric microstructure in a polycrystal. In contrast to sharp-interface models, diffuse-interface or phase-field models represent domain walls as diffusive interfaces with a finite thickness. This, in turn, requires sufficient spatial resolution to track the motion of individual walls. Such models are generally based on solving the time-dependent Ginzburg-Landau (GLD) equation within a finite-element (FE) (Su & Landis, 2007; W. Zhang & Bhattacharya, 2005) or spectral framework based on the fast Fourier transform (FFT) (Vidyasagar et al., 2017). We recently introduced (Indergand et al., 2020) a statistical mechanics-based extension of the GLD, which accounts for the effects of finite temperature by considering both the temperature dependence of the Ginzbug-Landau potential and thermal fluctuations. The latter promote the nucleation of needle-like domains at locations of high heterogeneity (e.g., at grain boundaries) and therefore predicts a more realistic domain pattern evolution.

Based on the aforementioned finite-temperature phase-field framework, we here present the results of ultra-high-resolution simulations of the ferroelectric microstructure evolution in a micron-sized polycrystal. By leveraging the parallel efficiency of the FFT-based numerical implementation, our simulations contain hundreds of grains, admitting statistics of the grain and domain evolution during ferroelectric switching. We demonstrate the capability to predict realistic domain pattern formation for various grain sizes at the mesoscale, discuss different types of emerged domain structures (monodomains, laminates, and flux-closure domains), link them to the underlying polycrystalline microstructure, and we highlight their implication on the ferro- and piezoelectric properties at the macroscale in close comparison with experiments and theoretical models. The remainder of this contribution is structured as follows. Section 4.2 briefly summarizes the phase field model. Section 4.3 details how we automatically detect the different types of domain walls from simulation data, followed by simulation results presented in Section 4.5. Finally, Section 4.6 concludes our study.

4.2 FERROELECTRIC CONSTITUTIVE MODEL

We adopt the ferroelectric constitutive model recently presented in Indergand et al. (2020), which accounts for the effects of finite temperature by including thermal fluctuations and which is summarized in the following to the extent required for subsequent discussions. The interested reader is referred to Chapter 2 for more details.

Based on the continuum description of ferroelectric ceramics, the electromechanically coupled behaviour of a ferroelectric body $\Omega \subset \mathbb{R}^n$ in a n-dimensional space is defined by the mechanical displacement vector $\boldsymbol{u}(\boldsymbol{x}, t)$, the infinitesimal strain tensor $\boldsymbol{\varepsilon}(\boldsymbol{x}, t) = \frac{1}{2}\left(\nabla \boldsymbol{u} + \nabla \boldsymbol{u}^{\mathrm{T}}\right)$, the electric potential $\phi(\boldsymbol{x}, t)$, and the electric field vector $\boldsymbol{e}(\boldsymbol{x}, t) = -\nabla \phi$, as functions of position $\boldsymbol{x} \in \Omega$ and time $t \geq 0$. The evolution of the ferroelectric microstructure is described by the polarization vector $\boldsymbol{p}(\boldsymbol{x}, t)$, which acts as the order parameter in the Devonshire-Ginzburg-Landau (DGL) theory (Devonshire, 1954; L. Landau, 1937). To evolve these fields with time, we solve the quasistatic mechanical and electrical problems (assuming sufficiently slow loading rates) as well as a kinetic law for the polarization.

The *mechanical problem* is described by the balance of linear momentum (with suitable boundary conditions), which yields under the assumption of negligible inertial effects and volumetric forces

$$\nabla \cdot \sigma = \mathbf{0}, \tag{4.2.1}$$

where $\sigma(\boldsymbol{x}, t)$ denotes the Cauchy stress tensor. The *electrical problem* is governed by Gauss' law, which in the absence of free charges reads

$$\nabla \cdot \boldsymbol{d} = \mathbf{0}, \quad \text{with} \quad \boldsymbol{d} = \kappa_0 \boldsymbol{e} + \boldsymbol{p}, \tag{4.2.2}$$

where the electric displacement vector field $\boldsymbol{d}(\boldsymbol{x}, t)$ is coupled to the electric field $\boldsymbol{e}$ via the permittivity of vacuum, κ_0, and the polarization vector field $\boldsymbol{p}$.

Assuming thermal equilibrium with a uniform temperature θ within the material, we follow Indergand et al. (2020), Su and Landis (2007), and W. Zhang and Bhattacharya (2005) and use the following additive structure for the electric enthalpy density:

$$W(\boldsymbol{\varepsilon}, \boldsymbol{e}, \boldsymbol{p}, \nabla \boldsymbol{p}, \theta) = \Psi_{\text{elastic}}(\boldsymbol{\varepsilon}, \boldsymbol{p}) + \Psi_{\text{pol.}}(\boldsymbol{p}, \theta) + \Psi_{\text{el.}}(\boldsymbol{e}) + \Psi_{\text{int.}}(\nabla \boldsymbol{p}) - \boldsymbol{e} \cdot \boldsymbol{p}. \tag{4.2.3}$$

$\Psi_{\text{elastic}}(\boldsymbol{\varepsilon}, \boldsymbol{p}) = \frac{1}{2}\left(\boldsymbol{\varepsilon} - \boldsymbol{\varepsilon}^r\right) \cdot \mathbb{C}\left(\boldsymbol{\varepsilon} - \boldsymbol{\varepsilon}^r\right)$ is the elastic strain energy density, where $\boldsymbol{\varepsilon}^r$ denotes the remanent strain and $\mathbb{C}$ is the fourth-order elasticity

tensor. The temperature-dependent polarization potential $\Psi_{\text{pol.}}(\boldsymbol{p}, \theta)$ follows from DGL theory, $\Psi_{\text{el.}}(\boldsymbol{e})$ is the electrostatic energy density, and the isotropic interface energy density is denoted by $\Psi_{\text{int.}}(\nabla \boldsymbol{p})$. The mechanical stress tensor and the electric displacement vector derive from the electric enthalpy density as, respectively, $\boldsymbol{\sigma} = \partial W / \partial \boldsymbol{\varepsilon}$ and $\boldsymbol{d} = -\partial W / \partial \boldsymbol{e}$. The complete expressions of all energy contributions along with the corresponding material constants for tetragonal PZT (Völker et al., 2011) are listed in Tab. 2.1.

To describe the evolution of the polarization at finite temperature, we use a statistical mechanics-based extension of the well-established *Allen-Cahn equation*, in which thermal fluctuations are added on top of the deterministic gradient-flow kinetics (Indergand et al., 2020), viz.

$$\mu \dot{\boldsymbol{p}} = -\frac{\partial W}{\partial \boldsymbol{p}} + \nabla \cdot \frac{\partial W}{\partial \nabla \boldsymbol{p}} + \mu \boldsymbol{\eta}, \tag{4.2.4}$$

where $\mu > 0$ is an inverse mobility constant, and $\boldsymbol{\eta}(\boldsymbol{x}, t)$ is a random noise vector field, which mimics thermal lattice vibrations and is elaborated in the following. The assumption of thermal equilibrium allows us to use *Maxwell-Boltzmann statistics* to identify $\boldsymbol{\eta}(\boldsymbol{x}, t)$ as centered Gaussian white noise, i.e, subject to the constraints

$$\langle \boldsymbol{\eta}(\boldsymbol{x}, t) \rangle_{\Omega} = \int_{\Omega} \boldsymbol{\eta}(\boldsymbol{x}, t) \, \mathrm{d}x = \boldsymbol{0} \quad \forall t, \tag{4.2.5a}$$

$$\langle \boldsymbol{\eta}(\boldsymbol{x}, t) \rangle_{\tau} = \int_{t}^{t+\tau} \boldsymbol{\eta}(\boldsymbol{x}, t) \, \mathrm{d}t = \boldsymbol{0} \quad \forall x \in \Omega, \tag{4.2.5b}$$

$$\left\langle \boldsymbol{\eta}(\boldsymbol{x}, t), \boldsymbol{\eta}(\boldsymbol{x}', t') \right\rangle_{\Omega, t} = \frac{2 k_{\mathrm{B}} \theta}{\mu V_{\text{char.}} \Delta t} \delta \left(x - x' \right) \delta \left(t - t' \right), \tag{4.2.5c}$$

where τ denotes a sufficiently large time window, k_{B} Boltzmann's constant, $V_{\text{char.}} = a_{tetr.}^2 c_{tetr.}$ the volume of the perovskite unit cell, and Δt the time increment. The constraints (4.2.5a) and (4.2.5b) require the random noise $\boldsymbol{\eta}$ to be unbiased in space and time; i.e, the average of $\boldsymbol{\eta}$ over the body Ω must be zero at any time t, and the average of $\boldsymbol{\eta}$ over a sufficiently large time window τ at any point $\boldsymbol{x} \in \Omega$ must tend to zero, respectively. Finally, the noise term $\boldsymbol{\eta}$ must be uncorrelated in space and time with the variance stated in (4.2.5c). The implications of thermal fluctuations onto the ferroelectric microstructure as well as the expected accuracy of the computed fields from the phase-field model will be discussed in Section 4.3.

We solve the boundary value problem (BVP) within a Representative Volume Element (RVE) of the ferroelectric ceramic, using an FFT-based

spectral method, which was described in detail in (Indergand et al., 2020; Vidyasagar et al., 2017) and is therefore summarized here only briefly. By assuming periodic boundary conditions, the mechanical problem (4.2.1) and electrical problem (4.2.2) are solved efficiently in Fourier space by using the *FFTW* library (Frigo & Johnson, 2005) to perform discrete fast Fourier transforms of the polarization, strain, and electric fields. Moreover, we use higher-order finite difference stencils to approximate gradients and to reduce ringing artifacts associated with the Gibbs phenomenon (which arise from discontinuous physical properties and differently orientated grains in our polycrystal (Vidyasagar et al., 2017)) and the non-uniform convergence of the truncated Fourier modes. After updating the aforementioned equilibrium equations, the evolution of the polarization is computed via implicit time integration of the extended Allen-Cahn equation (4.2.4), using a backward-Euler scheme. The latter provides increased numerical stability and admits a larger time step size Δt in comparison to the forward-Euler scheme. Higher-order time-integration schemes, e.g., Runge-Kutta, Adams-Bashforth, or Crank-Nicolson, showed no significant improvement in terms of the computational performance.

Due to improved computational efficiency and ease of visualization, we use a 2D plane-stress model in the following numerical examples, which spatially resolves the out-of-plane strain $\varepsilon_{33}(\boldsymbol{x})$ and shows realistic microstructures in comparison with experiments at various temperatures (Indergand et al., 2020). Of course, polycrystalline samples always represent a 3D problem due to grain orientations about all three crystallographic axes. Nevertheless, in case of tetragonal symmetry (as we consider in this study), a 2D model provides a reasonable approximation of a uniaxial polycrystal, where all grains have a common $\langle 100 \rangle$-axis. The agreement of 2D simulation results presented in Section 4.5 with several physical laws experimentally observed on 3D polycrystals supports the validity of our approach. To create the polycrystalline RVE, we subdivide the simulation domain into n_g grains, whose shapes are determined via Voronoi tessellation, and we assign to each grain a 2D orientation angle γ, which describes the rotation $\boldsymbol{R} \in \mathrm{SO}(2)$ from the global reference frame into the local crystal frame $\{\hat{e}_1, \hat{e}_2\}$. Consequently, the governing equations are transformed into the respective coordinate system of each grain, followed by an inverse transformation to compute the homogenized material response.

4.3 METHODS: DOMAIN WALL IDENTIFICATION AND ANALYSIS

The diffuse-interface setting of the phase field model makes it challenging to identify domain walls, especially in an automated fashion and in non-equilibrium situations. Therefore, we introduce a method to identify different types of ferroelectric domain walls and trace them not only in equilibrium but also in non-equilibrium situations (such as during polarization reversal with a transient applied electric field). An added complication arises from the random noise introduced to capture the effects of thermal lattice vibrations. Our approach is based on a few characteristic features of domain walls explained in the following. Although the following procedure has been developed and calibrated for tetragonal crystal symmetries, it can be adapted and generalized to other crystal symmetries.

4.3.1 *Interface energy density*

The most unique property to differentiate between domains and their boundaries (i.e., between, respectively, regions of homo- and heterogeneous polarization distribution $\boldsymbol{p}(\boldsymbol{x}, t)$ at a given time t) is naturally the interface energy density $\Psi_{\text{int.}}(\boldsymbol{\nabla p})$, which writes for an isotropic case

$$\Psi_{\text{int.}}(\boldsymbol{\nabla} p) = \frac{G_0}{2}|\boldsymbol{\nabla} p|^2, \tag{4.3.1}$$

where $G_0 > 0$ is an interface energy constant. Within our phase-field framework, domain walls are modelled as diffusive interfaces, whose thickness is calibrated based on density functional theory (DFT) and atomistic simulations at zero temperature (Völker et al., 2011). This results in differences in the thickness and therefore in the polarization gradient $\boldsymbol{\nabla} p$ within the two types of domain walls in a tetragonal crystal. As a consequence, the interface energy density $\Psi_{\text{int.}}(\boldsymbol{\nabla} p)$ exhibits different profiles when plotted across a 90°- vs. 180°-type wall, as shown in Fig. 4.1(a). We utilize this (interface) energy signature as a fingerprint of a certain type of domain wall to uniquely identify and track its motion during polarization switching. Therefore, we define the subset of nodes within the simulation domain which are associated with a specific domain wall type as

$$\Omega^{\text{int.}}_{90/180} = \left\{ \boldsymbol{x} \in \Omega : \zeta^{\text{min.}}_{90/180} \leq \Psi_{\text{int.}}\left(\nabla \boldsymbol{p}(\boldsymbol{x})\right) \leq \zeta^{\text{max.}}_{90/180} \right\}, \tag{4.3.2}$$

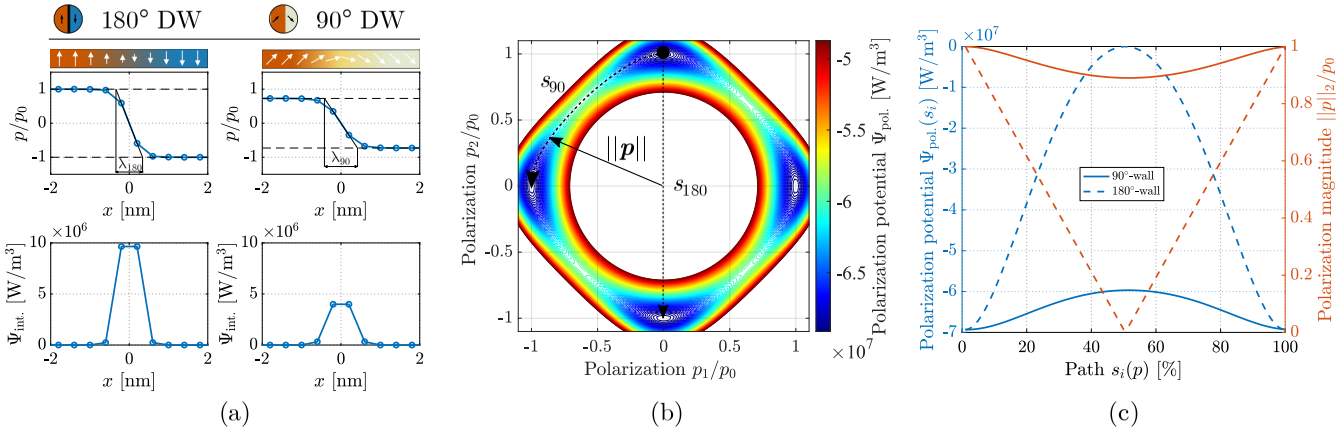

Figure 4.1: (a) Simulated domain wall properties of PZT, showing the polarization component parallel to the interface p/p_0 (top row) and interface energy density $\Psi_{\text{int.}}$ (bottom row) vs. the distance x from the wall for a 180°- and 90°-domain wall in the left and right column, respectively. (b) 2D contour plot of the polarization potential $\Psi_{\text{pol.}}(\boldsymbol{p})$ vs. the polarization $\boldsymbol{p} = (p_1, p_2)$, revealing the transition paths s_{90} and s_{180} (black dashed line) between the polarization states $\boldsymbol{p}_0$ (blue regions) for the depicted 180°- and 90°-domain wall in (a) as well as the magnitude of the polarization vector $||\boldsymbol{p}||$ (black solid arrow). (c) Polarization potential $\Psi_{\text{pol.}}(\boldsymbol{p})$ (left axis) and the magnitude of the polarization vector $||\boldsymbol{p}||$ (right axis) along the transition paths s_{180} and s_{90}, indicated by the straight and dashed lines, respectively.

where $\zeta^{\text{max.}}_{90/180}$ and $\zeta^{\text{min.}}_{90/180}$ denote, respectively, upper and lower bounds (and set of bounds for each of the two types of domain walls), which are listed in Tab. 4.2. While the subsets in (4.3.2) are usually sufficient to accurately capture the emergent ferroelectric microstructure at equilibrium, it becomes imprecise in the presence of imposed external loads, which can distort the energy landscape. To improve the accuracy and reliability of our predictions, we include additional features, as detailed in the following.

4.3.2 *Polarization energy density*

Instead of specifying and utilizing the conditions at the interface as an indicator, as we did in the previous section, we may also exploit differences in the polarization potential $\Psi_{\text{pol.}}(\boldsymbol{p}, \theta)$ across the domain wall, i.e., along the path between the two polarization states associated with the adjacent domains. Fig. 4.1(b) shows the polarization potential $\Psi_{\text{pol.}}(\boldsymbol{p}, \theta)$ at room temperature together with the polarization trajectories of the 90°- and 180°-type domain walls, denoted as $s_{90}(\boldsymbol{p})$ and $s_{180}(\boldsymbol{p})$, respectively. A direct comparison of the polarization energy density $\Psi_{\text{pol.}}(s(\boldsymbol{p}), \theta)$ along the two trajectories, illustrated in Fig. 4.1(c), reveals significant differences in the energy barrier associated with an interface type. This may serve as an additional indicator to distinguish different interfaces as follows by defining

$$\Omega^{\text{pol.}}_{90/180} = \left\{ \boldsymbol{x} \in \Omega : \xi^{\text{min.}}_{90/180} \leq \Psi_{\text{pol.}}\left(\boldsymbol{p}(\boldsymbol{x})\right) \leq \xi^{\text{max.}}_{90/180} \right\}, \tag{4.3.3}$$

with suitable upper and lower bounds for the polarization potential $\xi^{\text{max.}}_{90/180}$ and $\xi^{\text{min.}}_{90/180}$, respectively, listed in Tab. 4.2.

4.3.3 *Polarization magnitude*

As a third metric, we use the change in the magnitude of the order parameter, $|\boldsymbol{p}|$, as a measure to separate different types of domain walls. As visualized in Fig. 4.1(b)-(c), the path s_{180} of an antiparallel 180° (Ising-type) domain wall follows the shortest distance between the two polarization states $\boldsymbol{p}_0 = (0, \pm 1)^{\mathrm{T}}$, which results in a pure stretch of the polarization vector $\boldsymbol{p}$. By contrast, the trajectory s_{90} of a 90° (Néel-type) domain wall follows the minimum energy path (Indergand et al., 2020), which requires primarily a rotation of the polarization vector $\boldsymbol{p}$. Therefore, imposing con-

strains on the norm of the polarization vector $|\boldsymbol{p}|$ allows us to separate the two types of domain walls with the help of

$$\Omega^{\text{mag.}}_{90/180} = \left\{ \boldsymbol{x} \in \Omega : v^{\text{min.}}_{90/180} \leq |\boldsymbol{p}(\boldsymbol{x})| \leq v^{\text{max.}}_{90/180} \right\}, \tag{4.3.4}$$

again with suitable upper and lower bounds $v^{\text{max.}}_{90/180}$ and $v^{\text{min.}}_{90/180}$, respectively, for the polarization potential; values are listed in Tab. 4.2.

4.3.4 *Domain wall identification and the implications of thermal fluctuations*

By combining all three of the above measures (interface energy, polarization energy, and polarization magnitude), we define those nodes lying within 90/180-type interfaces as the intersections of all three previously defined subsets (using Dirac measure $\delta_x(\Omega)$), and the set of all nodes contained in domain walls as the union of both interface types:

$$\Omega_{90/180} = \Omega^{\text{int.}}_{90/180} \cap \Omega^{\text{pol.}}_{90/180} \cap \Omega^{\text{mag.}}_{90/180}, \tag{4.3.5a}$$

$$\Omega_{\text{DWs}} = \Omega_{90} \cup \Omega_{180}. \tag{4.3.5b}$$

Of course, the choice of measures used for the identification of domain walls is not unique, e.g., one could utilize the elastic strain energy density $\Psi_{\text{ES}}(\boldsymbol{\varepsilon}, \boldsymbol{p})$ as an alternative (or additional) measure. Here, we choose those energies showing the most pronounced contrast between the two interface types. Furthermore, we defined in (4.3.5a) a certain domain wall type as the intersection (and not as the union) of the aforementioned measures to narrow down our selection, thus making it more robust. Note that, strictly speaking, the 90/180 types of domain walls are only defined for equilibrium conditions.

As an illustrative example to benchmark our proposed method, we consider a ferroelectric single-crystal with a well-known rank-2 laminate structure (Hooton & Merz, 1955; Rödel, 2007), which contains both types of domain walls of a tetragonal crystal. Fig. 4.2(a) illustrates the computed ferroelectric domain pattern of the aforementioned laminate, showing the polarization orientation angle (colors) as well as the polarization vector $\boldsymbol{p}$ (white arrows) within each domain. Based on (4.3.5), we identified and highlighted all nodes within the RVE in Fig. 4.2(a) that are associated with a 180°-type wall ($\boldsymbol{x} \in \Omega_{180}$) and with a 90°-type wall ($\boldsymbol{x} \in \Omega_{90}$) in red and blue, respectively. The results is shown in Fig. 4.2(b)—demonstrating that both types of domain walls are successfully recognized by the algorithm.

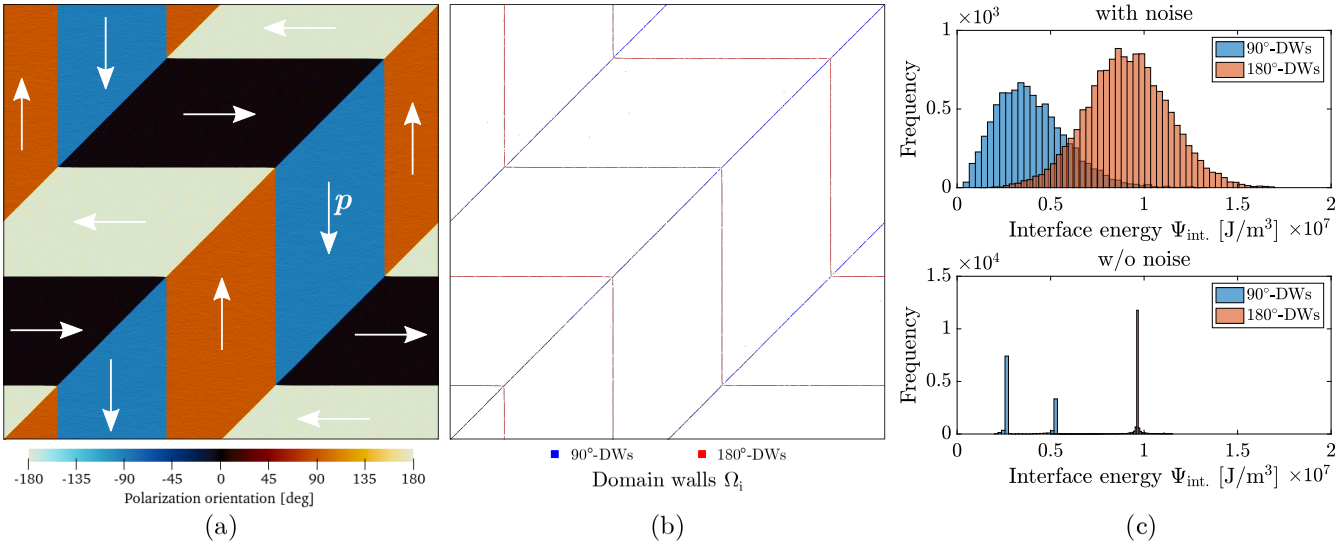

Figure 4.2: Domain pattern formation of a rank-2 laminate simulated in a single-crystalline RVE with periodic boundary conditions at equilibrium and in the absence of external loads. The ferroelectric microstructure is visualized by (a) the polarization orientation angle in degrees (colors) and the polarization vector $\boldsymbol{p}$ (white arrows) within each domain. (b) The corresponding point sets Ω_{90} and Ω_{180} highlighting domain walls (DWs) of 90°-type (blue) and 180°-type (red); white indicates regions without domain walls. (c) Domain wall statistics showing the frequency of observations (nodes) based on the interface energy density $\Psi_{\text{int.}}$ for both interface types $\Omega_{90/180}$ (blue/red) under the influence of thermal fluctuations (top) and without thermal noise (bottom).

The statistics of the two domain wall types are plotted in Fig. 4.2(c), visualizing the frequency of occurrences in Ω_i as a function of the interface energy density Ψ_{int} for a simulation with and without thermal noise. The distribution of the interface energy in the absence of thermal noise shows relatively well-separated distinct energy bands for each interface type, while the energy under thermal lattice fluctuations is broadly smeared out, resulting in multiple overlapping Gaussian distributions for the different types of walls. This demonstrates the necessity for additional measures, besides the interface energy density Ψ_{int}, to distinguish different types of domain walls accurately, when thermal noise is present in the simulated data. Based on the geometry of the laminate structure, the spatial discretization Δx of the grid of nodes, and the domain wall thicknesses $\lambda_{180/90}$, we can analytically estimate the average number of nodes for each type of domain wall as $n_i = l_i a_i$, where l_i denotes the number of nodes along the length of the domain wall ($l_{180} = 4N$ and $l_{90} = 2N$ in this example), N the number of nodes per RVE side, and $a_i = \lfloor \lambda_i / \Delta x \rfloor + 1$ the number of nodes across a domain wall. This analytical estimate serves as a reference for the numerical detection algorithm. Tab. 4.1 lists the amount of detected domain wall nodes, i.e., $|\Omega_i|$, relative to the aforementioned reference number of nodes n_i, showing excellent agreement without thermal noise and generally an underestimation in the presence of thermal fluctuations. The exact numbers, of course, strongly depend on the parameters used for calibration. Tab. 4.1 shows that, in the presence of thermal noise, 180°-type interfaces are detected more accurately compared to the 90°-type (which is more common in tetragonal PZT). One of the reasons that determines the accuracy of our method is the contrast between the interface energy $\Psi_{\text{int.}}$ of a certain type of domain wall and the contribution to $\Psi_{\text{int.}}$ stemming from the background noise within domains due to thermal lattice vibrations. As the Gaussian distribution of the thermal noise is centered at zero, it

Table 4.1: Number of detected nodes associated with both interface types, using the identification method (4.3.5a).

	Accuracy $\lvert\Omega_i\rvert / n_i$	
DW	w/o noise	with noise
90°	99 %	74 %
180°	97 %	91 %

interferes more strongly with the 90°-type, whose Gaussian is more closely located (see Fig. 4.2). Simply put, in terms of the interface identifiers used here, it is easier to confuse a noisy pixel within a homogeneous domain with a 90°-type wall than with a 180°-type wall. Moreover, the reported values in Tab. 4.1 under the influence of thermal noise should be interpreted as an estimated accuracy (relative to an unperturbed situation), since the *exact* number of nodes cannot be determined. The limits used to define the subset of the interface energy $\Omega^{\text{int.}}_{90/180}$, the polarization potential $\Omega^{\text{pol.}}_{90/180}$, and the polarization magnitude $\Omega^{\text{mag.}}_{90/180}$ are listed in Tab. 4.2.

Table 4.2: Upper and lower bounds used to define the subsets of the interface energy $\Omega^{\text{int.}}_{90/180}$, polarization potential $\Omega^{\text{pol.}}_{90/180}$, and polarization magnitude $\Omega^{\text{mag.}}_{90/180}$.

	90°-DW		180°-DW	
Type	min.	max.	min.	max.
Interface energy ζ	$2.0 \cdot 10^6$	$8.5 \cdot 10^6$	$5.0 \cdot 10^6$	$5.0 \cdot 10^7$
Polarization potential ξ	$-1.0 \cdot 10^9$	$-4.3 \cdot 10^7$	$-4.0 \cdot 10^7$	$1.0 \cdot 10^8$
Polarization magnitude ν	0.45	∞	0	0.6

4.4 EFFECTIVE MATERIAL PROPERTIES BASED ON MINIMIZATION OF THE ELECTRIC ENTHALPY DENSITY

We here present a simple model to estimate the energetic preference of monodomain vs. laminate domain patterns in grains whose orientation does not generally align with the applied electric field. To this end, we neglect the mechanical and electro-mechanical coupling effects and only consider the Ginzburg-Landau potential and the electric energy density, based on which we compute the energy-minimizing volume fractions of domains in a laminate pattern and compare the latter to the energy-minimizing configuration in a monodomain constellation. This is, of course, only a simplified model, yet it captures some of the salient microstructural features well, as we show.

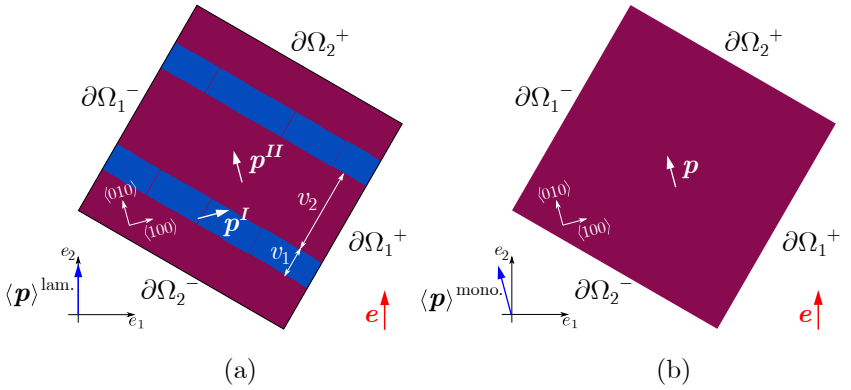

Figure 4.3: Schematic of two energy-minimizing domain structures considered here: (a) the 90°-laminate pattern, comprised of domain pairs $\boldsymbol{p}^I$ and $\boldsymbol{p}^{II}$, and (b) the monodomain structure. Colors indicate the polarization orientation, blue arrows represent the polarization vectors of the homogenized domain structure $\langle \boldsymbol{p} \rangle$, and the red arrows show the direction of the applied electric field $\boldsymbol{e}$ in each case.

4.4.1 *Effective properties of a simple 90°-domain laminate*

We consider a three-dimensional body $\Omega \in \mathbb{R}^3$ subject to periodic boundary conditions, which forms a periodically repeating ferroelectric laminate structure in the x_1-x_2-plane over the entire body. The laminate is composed of 90°-domain pairs, separated by sharp interfaces. The volume fraction v_i of each domain $i \in \{1, 2\}$, satisfying $v_1 + v_2 = 1$, can vary depending on the difference in the poling direction and the crystal orientation γ (denoting the rotation about the $\boldsymbol{e}_3$-axis, measured against the vertical axis). For simplicity, we consider only the polarization energy density $\Psi_{\text{pol.}}(\boldsymbol{p})$ and the applied electric field $\boldsymbol{e}$ and hence neglect all mechanical and electro-mechanical coupling effects. For a given crystal orientation γ, we seek to find a low-energy construction of the laminate pattern, by minimizing the total energy of the material with respect to the polarization field:

$$\boldsymbol{p}(\boldsymbol{x}) = \arg\min \int_\Omega \left[\Psi_{\text{pol.}}(\boldsymbol{p}) - \boldsymbol{e} \cdot \boldsymbol{p} \right] \mathrm{d}V. \tag{4.4.1}$$

Minimization of the first term requires the polarization in each domain, $\boldsymbol{p}^i$, to be in one of the spontaneous polarization states $\boldsymbol{p}_0 / p_0 \in \{(1,0,0)^{\mathrm{T}}, (-1,0,0)^{\mathrm{T}}, (0,1,0)^{\mathrm{T}}, (0,-1,0)^{\mathrm{T}}, (0,0,1)^{\mathrm{T}}, (0,0,-1)^{\mathrm{T}}\}$, whereas maximization of the second term drives the polarization $\boldsymbol{p}$ to be aligned with the applied

electric field $\boldsymbol{e}$ on average over the laminate. Without loss of generality, we assume an electric field in the vertical $\boldsymbol{e}_2$-direction, and the polarization vectors $\boldsymbol{p}^1$ and $\boldsymbol{p}^2$ within the homogeneous domains 1 and 2, respectively, are given by

$$\boldsymbol{p}^1 = \begin{cases} p_0\hat{\boldsymbol{e}}_1, & \text{if } \gamma \geq 0, \\ -p_0\hat{\boldsymbol{e}}_1, & \text{if } \gamma < 0, \end{cases}, \qquad \boldsymbol{p}^2 = p_0\hat{\boldsymbol{e}}_2, \tag{4.4.2}$$

where $\{\hat{\boldsymbol{e}}_1, \hat{\boldsymbol{e}}_2, \hat{\boldsymbol{e}}_3\} = \{\langle 100\rangle, \langle 010\rangle, \langle 001\rangle\}$ denote the crystal axis orientations. In other words, if $\gamma = 0$, we expect no laminate but a monodomain ($v_1 = 0$, $v_2 = 1$) with polarization $\boldsymbol{p} = p_0\boldsymbol{e}_2$. If $\gamma \neq 0$, then we expect a laminate ($v_1, v_2 \in (0, 1)$) composed of 90°-domain walls with alternating polarizations $\boldsymbol{p} = p_0(\pm\hat{\boldsymbol{e}}_1 + \hat{\boldsymbol{e}}_2)$. Letting the rotation matrix $\boldsymbol{R} = \mathrm{SO}(3)$ account for the transformation from the reference frame to the grain's crystal axes $\{\hat{e}_1, \hat{e}_2, \hat{e}_3\} = \{\langle 100\rangle, \langle 010\rangle, \langle 001\rangle\}$ (dependent on angle γ), the average polarization in the laminate follows as

$$\langle \boldsymbol{p} \rangle^{\text{lam.}} = \sum_{i=1}^{2} v_i \boldsymbol{R}^{\mathrm{T}} \boldsymbol{p}^i. \tag{4.4.3}$$

Solving (4.4.1) under the constraints $v_1 + v_2 = 1$ and $\langle p_1 \rangle^{\text{lam.}} = 0$ yields the volume fractions in an energy-minimizing laminate as

$$v_2 = \frac{1}{|\tan\gamma| + 1} \quad \text{and} \quad v_1 = 1 - v_2 \quad \forall \gamma \in \mathbb{R}. \tag{4.4.4}$$

Analogously, the infinitesimal strain tensors in domain 1, domain 2, and on average over the laminate are, respectively,

$$\boldsymbol{\varepsilon}^1 = \mathrm{diag}\left(\varepsilon_\beta, \varepsilon_\alpha, \varepsilon_\alpha\right), \ \boldsymbol{\varepsilon}^2 = \mathrm{diag}\left(\varepsilon_\alpha, \varepsilon_\beta, \varepsilon_\alpha\right), \text{ and } \langle \boldsymbol{\varepsilon} \rangle^{\text{lam.}} = \sum_{i=1}^{2} v_i R^{\mathrm{T}} \boldsymbol{\varepsilon}^i R, \tag{4.4.5}$$

where ε_β and ε_α denote the spontaneous strains parallel and perpendicular to the spontaneous polarization direction, respectively. When utilizing the

obtained volume fractions in (4.4.4), the average polarization and strain of the laminate become, respectively,

$$\langle \boldsymbol{p} \rangle^{\text{lam.}} = p_0 \begin{pmatrix} 0 \\ \frac{1}{|\cos\gamma| + |\sin\gamma|} \\ 0 \end{pmatrix} \quad \text{and} \tag{4.4.6}$$

$$\langle \boldsymbol{\varepsilon} \rangle^{\text{lam.}} = \begin{pmatrix} \langle \boldsymbol{\varepsilon}_{11} \rangle^{\text{lam.}} & \langle \boldsymbol{\varepsilon}_{12} \rangle^{\text{lam.}} & \langle \boldsymbol{\varepsilon}_{13} \rangle^{\text{lam.}} \\ & \langle \boldsymbol{\varepsilon}_{22} \rangle^{\text{lam.}} & \langle \boldsymbol{\varepsilon}_{23} \rangle^{\text{lam.}} \\ \text{sym.} & & \langle \boldsymbol{\varepsilon}_{33} \rangle^{\text{lam.}} \end{pmatrix} \tag{4.4.7}$$

with strain components

$$\begin{aligned}
\langle \boldsymbol{\varepsilon}_{11} \rangle^{\text{lam.}} &= \frac{\left(\varepsilon_\alpha \sin^2\gamma + \varepsilon_\beta \cos^2\gamma\right)|\sin\gamma| + \left(\varepsilon_\alpha \cos^2\gamma + \varepsilon_\beta \sin^2\gamma\right)|\cos\gamma|}{|\cos\gamma| + |\sin\gamma|}, \\
\langle \boldsymbol{\varepsilon}_{22} \rangle^{\text{lam.}} &= \frac{\left(\varepsilon_\alpha \sin^2\gamma + \varepsilon_\beta \cos^2\gamma\right)|\cos\gamma| + \left(\varepsilon_\alpha \cos^2\gamma + \varepsilon_\beta \sin^2\gamma\right)|\sin\gamma|}{|\cos\gamma| + |\sin\gamma|}, \\
\langle \boldsymbol{\varepsilon}_{33} \rangle^{\text{lam.}} &= \varepsilon_\alpha, \\
\langle \boldsymbol{\varepsilon}_{12} \rangle^{\text{lam.}} &= \frac{\left(\varepsilon_\alpha - \varepsilon_\beta\right)\left(|\cos\gamma| - |\sin\gamma|\right)\sin 2\gamma}{2\left(|\cos\gamma| + |\sin\gamma|\right)}, \\
\langle \boldsymbol{\varepsilon}_{23} \rangle^{\text{lam.}} &= 0, \\
\langle \boldsymbol{\varepsilon}_{13} \rangle^{\text{lam.}} &= 0.
\end{aligned}$$

These effective quantities are plotted in Fig. 4.4 vs. the grain orientation angle γ.

Note that the maximization of the $\boldsymbol{e} \cdot \boldsymbol{p}$-term under the aforementioned constraints in (4.4.1) determines effectively the volume fractions of the domains in a 90° laminate. This is in contrast to a 180° laminate, where there is no mechanism to align the polarization with an external field on average, such that the domains remain locally in a spontaneous polarization state and complying with the boundary conditions, due to the symmetry of the antiparallel oriented domains.

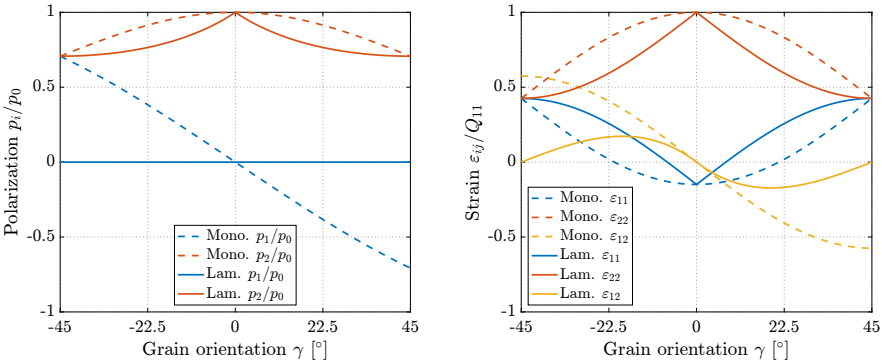

Figure 4.4: Comparison of the analytically derived effective polarization $\langle \boldsymbol{p} \rangle$ (left) and strain $\langle \boldsymbol{\varepsilon} \rangle$ (right) of a monodomain (dashed line) and a rank-1 laminate (straight line) as functions of the grain orientation γ, for the case of an applied electric field in the vertical direction, i.e., $\boldsymbol{e} = (0, e, 0)^{\mathrm{T}}$.

4.4.2 *Effective properties of a monodomain*

Analogous to the obtained effective properties of a 90°-laminate structure above, the average polarization and strain of a *monodomain*, respectively, evaluate to

$$\langle \boldsymbol{p} \rangle^{\text{mono.}} = p_0 \begin{pmatrix} -\sin\gamma \\ \cos\gamma \\ 0 \end{pmatrix} \quad \text{and} \tag{4.4.8}$$

$$\langle \boldsymbol{\varepsilon} \rangle^{\text{mono.}} = \begin{pmatrix} \varepsilon_\alpha + (\varepsilon_\beta - \varepsilon_\alpha)\sin^2\gamma & (\varepsilon_\alpha - \varepsilon_\beta)\sin(2\gamma)/2 & 0 \\ & \varepsilon_\alpha + (\varepsilon_\beta - \varepsilon_\alpha)\cos^2\gamma & 0 \\ \text{sym.} & & \varepsilon_\alpha \end{pmatrix}, \tag{4.4.9}$$

where we considered the range $\gamma \in (-45°, 45°)$. Alternatively, one can expand $\langle \boldsymbol{p} \rangle^{\text{mono.}}$ as a $\frac{\pi}{2}$-periodic function. The calculated effective properties of a monodomain are included in Fig. 4.4, in comparison with the analytical solution for a 90°-laminate structure.

4.5 RESULTS: FERROELECTRIC DOMAIN PATTERN FORMATION

In the following, we consider a 2D volume domain filled with a polycrystal of n_g randomly oriented grains with a spatial discretization of $N \times N$ grid points. As elaborated in Chapter 2, we choose the spatial resolution to match the crystallographic lattice spacing, i.e., $\Delta x = a_{tetr.}$, so that each node in the grid represents exactly one atomic-level unit cell. The sample is initially poled in the negative vertical direction, followed by a spontaneous relaxation, during which the polarization adjusts based on the orientation of each grain. The ferroelectric specimen is free to deform and hence has a zero stress on average, i.e, $\langle \boldsymbol{\sigma} \rangle = \mathbf{0} \ \forall t$. After pre-equilibration, an average electric field $e_2(t) = \langle e_2(t) \rangle$ is imposed in the positive vertical direction, followed by an equilibration phase, during which the ferroelectric microstructure is relaxed.

4.5.1 *Influence of the RVE and grain size*

We first asses the influence of the different length scales at play—reaching from the thickness l of a domain wall over the grain size g in a polycrystal to the size L of the computational domain—on the statistics of domain pattern formation. To this end, we successively enlarge the sample $\Omega(L)$, while keeping all microstructural features (such as the average grain size g) constant, until convergence is approximately achieved of the effective material response and of the microstructural statistics. The limiting size L_∞ of the computational domain, at which the statistics converge to the macroscale limit, is statistically representative, which is why the corresponding simulation domain is referred to as Representative Volume Element (RVE).

This effect becomes apparent in Fig 4.5, where snapshots of the ferroelectric microstructure at equilibrium are shown the domain sizes $L = \{0.10, 0.21, 0.41, 0.82, 1.64\}$ µm at a temperature of $\theta = 300\,\mathrm{K}$. The emerged ferroelectric microstructures appear self-similar across the different sizes, such that the domain pattern at a certain size can be approximated through tessellation of the domain pattern of the next smaller size. This observation visually indicates statistical homogeneity of ferroelectric microstructure, which is confirmed in Fig. 4.5(b), showing the frequency of domains within RVEs of different sizes, measured by the average interface energy density $\langle \Psi_{\text{int.}}(N) \rangle$ and the average number of nodes associated with domain

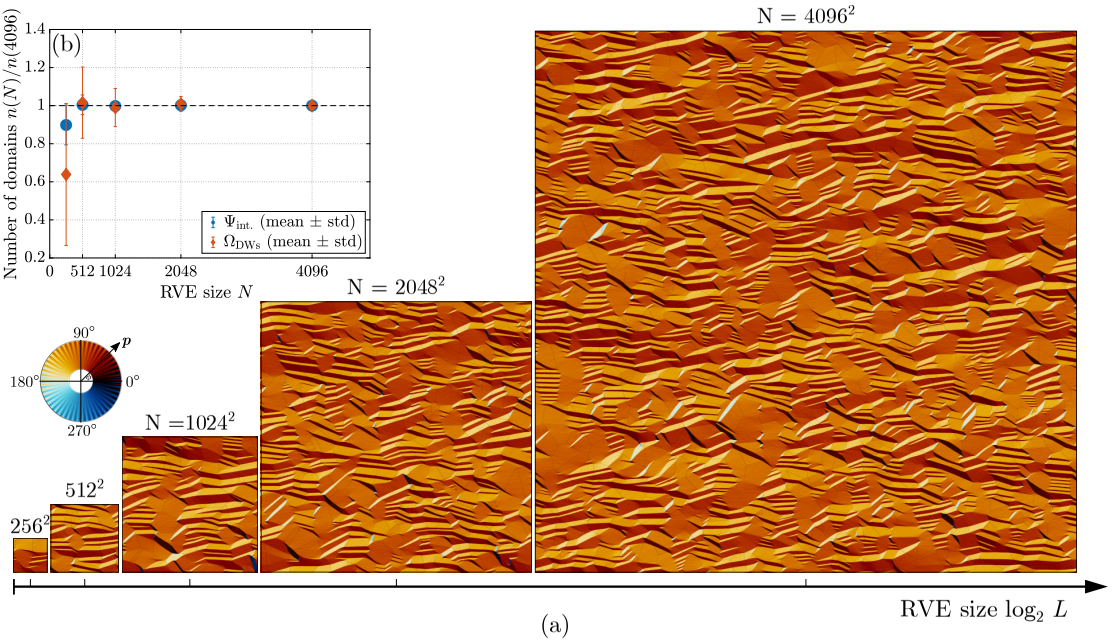

Figure 4.5: Effect of sample enlargement on the ferroelectric microstructure visualized by (b) the average number of ferroelectric domains $\langle n_D \rangle$ and (a) the polarization orientation angle $\phi(\boldsymbol{x})$ for various sample sizes $L = \{0.10, 0.21, 0.41, 0.82, 1.64\}$ µm. The snapshots in (a) show the domain pattern formation at equilibrium of a polycrystal with an average grain size $\langle g \rangle = 46\,\text{nm}$ after a step load of $e_2 = 8 \times 10^7\,\text{V/m}$ in the positive vertical direction. The plot in (b) shows the ensemble average based on ten randomly generated microstructures of the average interface energy density $\langle \Psi_{\text{int.}}(N) \rangle / \langle \Psi_{\text{int.}}(4096) \rangle$ (circle) and the average number of domain walls $\langle \Omega_{\text{DWs}}(N) \rangle / \langle \Omega_{\text{DWs}}(4096) \rangle$ (diamond) and the standard derivation (error bar).

walls, $\langle \Omega_{\mathrm{DWs}}(N) \rangle$. Both measures are normalized by their corresponding value at the largest size ($N = 4096$) and exhibit convergence of the average to the macroscale limit at a sample size of $N = 512$ and 20 grains.

Having established suitable simulation domain sizes, we proceed to investigate the influence of the grain size on the ferroelectric microstructure and the effective material response. Therefore, we study domain pattern statistics under grain size enlargement by varying the average grain size $\langle g \rangle$, while keeping the RVE size $N = 4096$ constant. We utilize image segmentation and analysis on the emerged lamellar bands to extract the average width $\langle w \rangle$ of all ferroelectric domains for a given average grain size $\langle g \rangle$. Fig. 4.6(a) shows snapshots of the ferroelectric domain pattern formation visualized by the polarization orientation angle for various average grain sizes $\langle g \rangle = \{23, 46, 92, 183, 367, 734\}$ nm. These results indicate a reduction in the total number of domains within the RVE and an increase in the average domain width $\langle w \rangle$ with increasing average grain size $\langle g \rangle$. This observation is more clearly visible in the average interface energy $\langle \Psi_{\mathrm{int.}} \rangle$ in Fig. 4.6(b), which is a measure of the domain density. It follows a $\langle \Psi_{\mathrm{int.}} \rangle \propto \langle g \rangle^{-1/2}$ scaling, as the regression curve $f(\langle g \rangle)$ shows. This scaling law was previously postulated through theoretical considerations of balancing the domain wall energy and the elastic strain energy (Arlt, 1990; Kittel, 1946; Salje, 1990) and seems to capture the most dominant grain size effect, as the agreement with our significantly more intricate phase-field model reveals. Moreover, the average width of domains is closely approximated by the parabolic scaling $\langle w \rangle \propto \langle g \rangle^{1/2}$. This scaling law was originally proposed by Arlt in (Arlt, 1990) as an adaption from thin films to polycrystals, based on minimization of the sum of elastic strain energy and domain wall energy within a clamped, cubic-shaped grain, assuming a negligible contribution of the electric energy at GBs due to compensation by mobile charges. The regression curve in Fig. 4.6(c) shows that our data suggest a slightly lower scaling exponent, which leads to a more accurate description of the domain width especially for smaller grain sizes $\langle g \rangle < 1\,\mu\mathrm{m}$. (To provide a meaningful characterization of the average domain width $\langle w \rangle$ and to account for the higher variance for larger grains, a weighted regression $h_w(g)$ is used, whose weight is inverse proportional to the variance of the domain width.)

Another interesting effect associated with the domain density is its extrinsic contribution to the small-signal properties through mobile 90°-domain walls (Ihlefeld et al., 2016). The observed increase in the density of domain walls (measured via $\langle \Psi_{int.} \rangle$) with decreasing grain sizes $\langle g \rangle$ in Fig. 4.6(b) results in an increase of the dielectric and piezoelectric constants. This effect

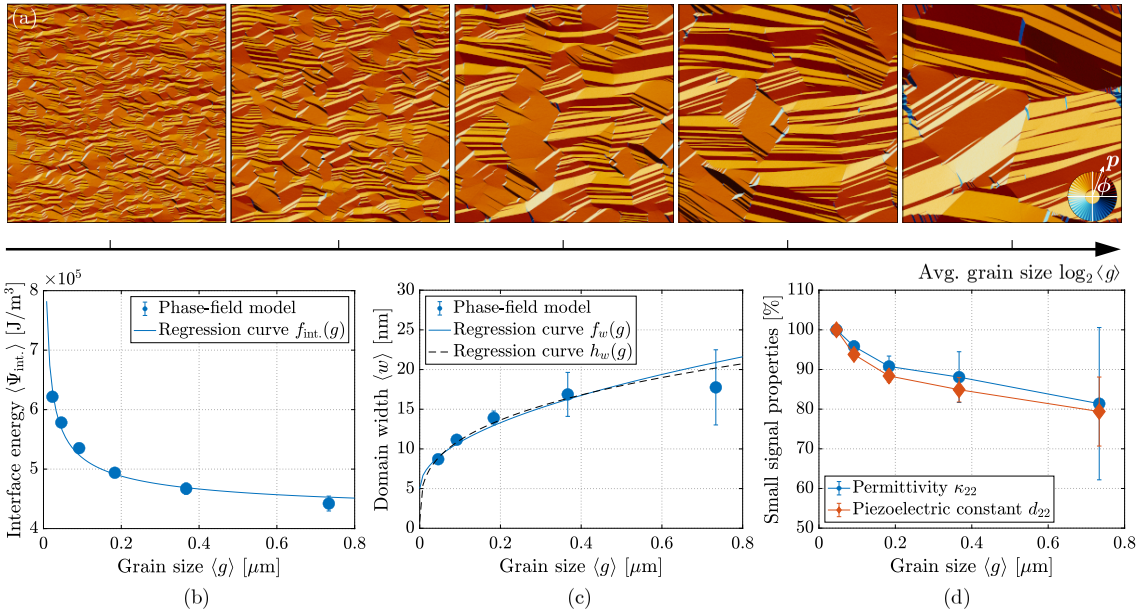

Figure 4.6: Influence of the average grain size $\langle g\rangle$ on the ferroelectric domain pattern formation, showing (a) the polarization orientation angle, (b) the average interface energy density $\langle\Psi_{\text{int.}}\rangle$, (c) the average domain width $\langle w\rangle$, and (d) the relative change of the permittivity κ_{22} and of the piezoelectric constant d_{22} parallel to the electric field direction for various average grain sizes $\langle g\rangle = \{23, 46, 92, 183, 367, 734\}$ nm within an RVE of side length $L = 1.64\,\mu$m ($N = 4096$). The circular/diamond-shaped markers in (b) to (d) represent the ensemble average based on ten realizations, each with a randomly generated polycrystalline microstructure, while the solid and dashed lines indicate the corresponding regression curves $f_{\text{int.}}(g) = C_1 g^{-0.5} + C_2$, $f_{\text{w}}(g) = C_1 g^{0.5} + C_2$, and $h_{\text{w}}(g) = C_1 g^{0.32} + C_2$.

is shown in Fig. 4.6(d) and in agreement with measurements on barium titanate ceramics with grains larger than 1 μm (Arlt et al., 1985; Ihlefeld et al., 2016). For submicrometer-sized grains in lead-based ceramics, however, a decrease of the permittivity and piezoelectric constant with decreasing grain size was reported (Randall et al., 1998). We assume that this change in trends for submicrometer-sized grains is attributed to two effects, which are not accounted for in our model. First, surface-to-volume ration increases with decreasing grain size, which dilutes the naturally high permittivity of PZT with the low permittivity of the grain boundary layer by the rule of mixture (Ihlefeld et al., 2016). Second, x-ray diffraction measurements have shown a decrease in the tetragonal unit cell distortion c/a from the bulk value for submicrometer-sized grains (Picht et al., 2020), which leads to a drop in the spontaneous polarization and strain; hence, a decrease of the intrinsic contribution to the dielectric and piezoelectric constants.

4.5.2 *Equilibrium grain statistics*

The formation of energy-minimizing domain patterns strongly depends on the boundary conditions and on the underlying texture (i.e., grain orientations and grain size of the ferroelectric ceramic). We assume an electric field $\boldsymbol{e}$ applied to the RVE in the vertical direction, while the local orientation of the crystal axes $\{\langle 100\rangle, \langle 010\rangle\}$ in the 2D plane is measured by the grain orientation angle γ (see Fig. 4.7i). To probe the influence of the grain orientation, we simulate a polycrystalline PZT sample of size $N = 4096$ with $n_g = 1280$ randomly-oriented grains, whose orientations are assigned based on a uniform distribution with $\gamma \in (-45°, 45°)$. The same periodic boundary conditions are used as in the previous study. After equilibration of the RVE, we compute in a post-processing step the mean fields $\langle\,.\,\rangle_{\Omega_g}$ within each grain Ω_g for ten realizations of the polycrystal, each with a randomly generated grain seed and grain orientation distribution. This allows us to examine the influence of a grain's orientation on the domain pattern within the grain.

The aforementioned dependence of various fields of interest on the grain orientation γ is depicted in Fig. 4.7, where the influence of the grain orientation γ on the grain-averaged polarization in the horizontal and vertical directions, $\langle p_1/p_0\rangle_{\Omega_g}$ and $\langle p_2/p_0\rangle_{\Omega_g}$, respectively, the polarization orientation $\langle\phi\rangle_{\Omega_g}$, the strain in the horizontal and vertical directions, $\langle\varepsilon_{11}\rangle_{\Omega_g}$ and $\langle\varepsilon_{22}\rangle_{\Omega_g}$, respectively, the interface energy density $\langle\Psi_{\text{int.}}\rangle_{\Omega_g}$, and the

domain density $\langle \Omega_{\mathrm{DW}} \rangle_{\Omega_g}$ are plotted based on a data set of 12,800 random grain samples. This data clearly demonstrates a correlation between the grain orientation γ and almost all fields shown in Fig. 4.7(a) through (g). Exceptions are the horizontal polarization component $\langle p_1/p_0 \rangle_{\Omega_g}$ (Fig. 4.7a) and the related polarization orientation $\langle \phi \rangle_{\Omega_g}$ (Fig. 4.7c).

To understand the link between the grain orientation and the observed ferroelectric domain patterns, let us discuss the correlations in Fig. 4.7(a)-(g) and relate them to the characteristics of a *monodomain* vs. a *laminate* domain structure, both illustrated in Fig. 4.8(a) and (d), respectively. To gain further insight into the competition between a homogeneous domain vs. a laminate pattern as a function of the grain orientation, we presented in Section 4.4 a simple model, which is based on minimizing the electric enthalpy and predicts the energetically optimal average polarization of a misoriented grain with or without the ability to form a laminate (see Eqs. (4.4.6) and (4.4.8)). These are used for reference here.

First, the vertical polarization component $\langle p_2/p_0 \rangle_{\Omega_g}$ peaks around $\gamma \approx 0°$ and decreases for larger grain misorientations γ. This is expected, since a homogeneous b^+-domain within a grain with a small misorientation γ minimizes the polarization potential $\Psi_{\mathrm{pol.}}$ and maximizes the vertical polarization component p_2/p_0, whereas a large grain misorientation forces the material to form an energy-minimizing sequence of domains, which geometrically has a smaller grain-averaged vertical polarization component $\langle p_2/p_0 \rangle_{\Omega_g}$ (see Fig. 4.7b). This is in good agreement with measurements of the domain switching fraction based on combined high-energy x-ray and neutron diffraction experiments on PZT (Hall et al., 2004; Hall et al., 2005; Jones et al., 2006; Jones et al., 2007; Jones et al., 2005; Pramanick et al., 2011). When compared to the analytical model (Section 4.4), the simulated vertical polarization agrees well with the orientation dependence predicted by assuming a monodomain with $\langle p_2/p_0 \rangle^{\mathrm{mono.}}$ (Section 4.4.2) for weakly misoriented grains, whereas for high grain misorientations γ the laminate solution $\langle p_2/p_0 \rangle^{\mathrm{lam.}}$ (Section 4.4.1) describes the trend more accurately (see the dashed and solid red lines in Fig. 4.7(h), respectively). Note that, although the analytical model captures these important features correctly, it is relatively simple compared to the phase-field model (cf. the lack of mechanical and electrical compatibility at the grain boundary and grain-to-grain interactions, which results in an overestimation of the maximum polarization at $\gamma \approx 0$). Nevertheless, such theoretical models help to improve our understanding and provide simple estimates. Here,

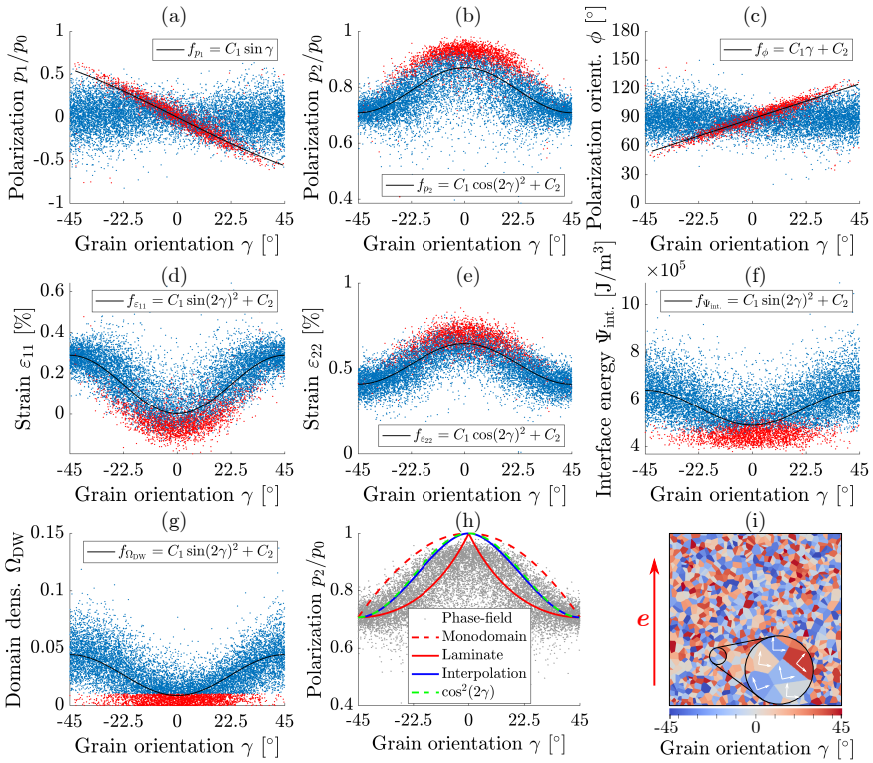

Figure 4.7: Equilibrium grain statistics showing the influence of the grain orientation γ on (a)-(b) the grain-averaged polarization $\langle \boldsymbol{p}/p_0 \rangle_{\Omega_g}$ (normalized by the spontaneous polarization p_0), (c) the polarization orientation $\langle \phi \rangle_{\Omega_g}$, (d)-(e) the normal strains $\langle \boldsymbol{\epsilon} \rangle_{\Omega_g}$, (f) the interface energy density $\langle \Psi_{\text{int.}} \rangle_{\Omega_g}$, and (g) the domain density $\langle \Omega_{\text{DW}} \rangle_{\Omega_g}$. The dataset contains 12,800 grain samples, where each dot represents the average field of a grain. Highlighted in red is a subset of all those grains with $\langle \Omega_{\text{DW}} \rangle_{\Omega_g} < 0.01$, which indicates grains with a *monodomain*-like configuration illustrated in Fig 4.8(a). The regression curves $f(\gamma)$ (black lines) indicate possible correlations in plots (a)-(g). (h) Comparison of the analytically calculated vertical polarization for a monodomain $\langle p_2/p_0 \rangle^{\text{mono.}}$ (dashed red line), a 90° laminate $\langle p_2/p_0 \rangle^{\text{lam.}}$ (straight red line), an interpolation between monodomain and laminate $\langle p_2/p_0 \rangle^{\text{interp.}}$ (blue line), and a $\cos^2(2\gamma)$ function (dashed green line). (i) Polycrystalline RVE with 1280 grains, showing the direction of the applied electric field (red arrow) and the grain orientations γ (colors).

e.g., a linear interpolation between the monodomain and laminate solutions, shown as $\langle p_2/p_0 \rangle^{\text{interp.}}$ (blue line), displays overall reasonable agreement with the phase-field results (gray dots) in Fig. 4.7(h), and it is closely approximated by a $\cos^2 2\gamma$-function (dashed green line). Analogous to the vertical polarization, the vertical strain component $\langle \varepsilon_{22} \rangle_{\Omega_g}$ follows the same line of reasoning.

Second, the horizontal strain $\langle \varepsilon_{11} \rangle_{\Omega_g}$ is typically negative for an ideal monodomain grain due to the lateral contraction $\varepsilon_{11} = -0.128\,\%$ relative to the polarization direction, and it increases for grains that form laminates (theoretically up to $\varepsilon_{11} = 0.365\,\%$ at $\gamma \approx \pm 45°$). Both features can be observed here, but note that the aforementioned reference strain values are valid only for an ideal stress-free situation, which is not the case at the local grain level; hence, minor differences must be expected. Third, the majority of emerged ferroelectric domains are arranged in energetically favored 90°-domain patterns with interfaces in the family of {110}-planes, as seen in Figs. 4.5 and 4.6. This is in agreement with experimental observations (Keve & Bye, 1975) and first-principle calculations (Meyer & Vanderbilt, 2002) on lead-based ferroelectrics. The number of domain wall pixels Ω_{DW} and the interface energy density $\Psi_{\text{int.}}$ are direct measures of the domain density and both have their minimum at $\gamma \approx 0°$ and increase for larger grain orientations γ with a clear dependence on the crystal orientation γ. In the following sections, we discuss the specifics of grains with and without lamellar domain structures in more detail.

4.5.3 *Monodomain grains*

The red dots in Fig. 4.7 indicate grains, which have most likely only a single domain and have been identified by imposing an upper bound on the domain wall density, viz. $\Omega^{\text{mono.}} = \left\{ i \in \{1, \ldots, n_g\} : \langle \Psi_{\text{DW}}(i) \rangle_{\Omega_g} \leq 0.01 \right\}$, where n_g denotes the number of grains. Analyzing this highlighted subset $\Omega^{\text{mono.}}$ reveals some interesting features. For example, the horizontal polarization $\langle p_1/p_0 \rangle_{\Omega_g}$ and the polarization orientation $\langle \phi \rangle_{\Omega_g}$ are generally uncorrelated (blue dots in Fig. 4.7bc). However, the subset $\Omega^{\text{mono.}}$ clearly exhibits a scaling $p_1 \propto \sin\gamma$, while the polarization orientation ϕ shows a linear correlation with the grain orientation (red dots in Fig. 4.7c)—the regression functions are indicated in Fig. 4.7. Note that only for fully aligned grains ($\gamma = 0°$) the polarization vector points upward, i.e., $f_\phi(0) \approx 90°$.

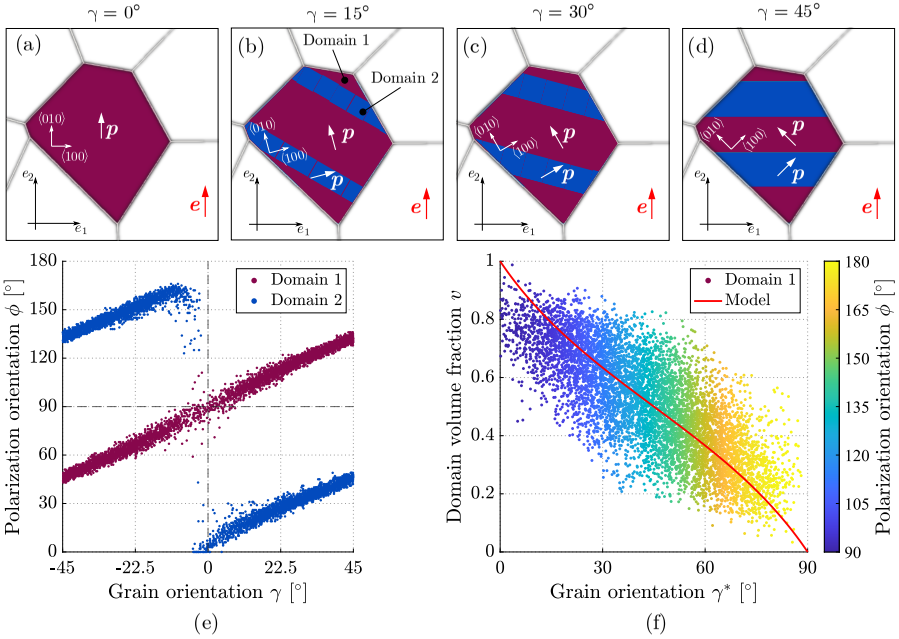

Figure 4.8: Impact of the grain orientation γ on the ferroelectric twin pattern formation in a polycrystal, illustrated by schematics in (a)-(d) and phase-field simulation results (with $N = 4096$ and $n_g = 1280$ at equilibrium) of 12,800-grain samples, showing (e) the polarization orientation ϕ of domain 1 with polarization state $\boldsymbol{p}_0 = (0,1)^{\mathrm{T}}$ and domain 2 with polarization state $\boldsymbol{p}_0 = (\pm 1,0)^{\mathrm{T}}$, and (f) the volume fraction v of domain 1 vs. the grain orientation γ^* (negative angles $\gamma < 0$ are shifted by $+90°$ by the symmetry of the tetragonal crystal). Colors in (f) indicate the polarization orientation ϕ, while the red line is the result of the simple energetic model (Section 4.4.2). Note that only grains with laminate patterns are shown in this figure; monodomain grains have been excluded for improved visibility.

This supports the above argument that $\Omega^{\text{mono.}}$ indeed represents the subset of monodomain grains, whose polarization orientation ϕ is directly related to the grain orientation γ (which is not true for grains with a lamellar domain structure). This observation is verified by the simple analytical model of a 90° laminate vs. a monodomain in Section 4.4.1, where we minimize the polarization enthalpy density in a sharp-interface setting. From this low-energy construction we indeed find that $\langle p_1/p_0\rangle_{\Omega_g} \propto \sin\gamma$ in a monodomain (see (4.4.8)). Across the full range of grain orientations γ, the preferred correlations of the vertical strain ε_{22} and horizontal strain ε_{11} generally suggest a $\cos(2\gamma)^2$ dependence, which is in agreement with high energy synchrotron x-ray diffraction experiments (Hall et al., 2004; Hall et al., 2005). However, monodomain grains (highlighted in red) appear to deviate from that trend (black line) with a disproportionately high vertical polarization, suggesting that a different mechanism is at play for this subset $\Omega^{\text{mono.}}$.

4.5.4 *Grains with lamellar domain patterns*

After discussing the specific properties of monodomain grains and conditions under which they emerge, we now focus on grains that form ferroelectric microstructure or, more precisely, the most common type of simple (rank-1) laminate or twin patterns. Through image analysis we identified all grains with more than one type of domain and plotted their polarization orientation ϕ as a function of the grain orientation γ in Fig. 4.8(e) and analogously the domain volume fraction in Fig. 4.8(f), where colors indicate the polarization orientation with respect to the crystal axis (as illustrated in the schematics of a 90° laminate in Fig. 4.8(a) to (d) for four different grain orientations). In an ideal scenario, the orientation of the domain aligned with the $\langle 010\rangle$-axis (red color in Fig. 4.8(e)) is continuous within $\gamma \in (-45°, 45°)$, whereas the domain aligned with the $\langle 100\rangle$-axis (blue color in Fig. 4.8(e)) has a discontinuity at $\gamma = 0°$, such that polarization jumps to the $\langle \bar{1}00\rangle$-axis for $\gamma < 0°$. Phase-field data in Fig. 4.8(e) closely match this trend. Overall, the difference in the polarization orientation between domains 1 and 2 is $|\phi_1 - \phi_2| \approx 90°$, suggesting primarily ferroelectric/ferroelastic domain walls in equilibrium. This is indeed energetically reasonable due to the lower energy cost per wall (Meyer & Vanderbilt, 2002; Völker et al., 2011) and complies with the higher frequency of observations in experiments (Ricote et al., 1999). Furthermore, the difference $|\phi_1 - \phi_2|$ is

generally constant and independent of the grain orientation γ, except for weakly misoriented grains $\gamma \approx 0°$. This can be explained by the transition to low-energy monodomains instead of laminate patterns, as discussed in Section 4.5.3. Note that, although a few domain structures with 180°-domain walls have been found among the examined grains, their number is negligible in comparison to the predominant 90°-domain walls.

The comparison of the volume fraction of domain 1 obtained by the phase-field model (colored dots) and the simple analytical model (red curve) as a function of the grain orientation γ^* in Fig. 4.8(f) shows that, although the analytical prediction captures the general trend of the phase-field model reasonably well, individual grains can deviate considerably from the average volume fraction at a certain orientation γ. This is explained by the simplifying assumptions of the analytical model, which neglects all other energetic contributions besides the Landau potential, and—more importantly—the assumption of periodic boundary conditions, which implies an infinite grain or exact compatibility at grain boundaries. The latter is generally implausible in a ceramic with finite-size grains and grain-to-grain misorientations and instead requires domain structures for compatibility between grains, which is discussed in the following.

4.5.5 *Domain structures at grain boundaries*

In an ideal scenario, the ferroelectric microstructure within a certain grain (laminate or monodomain) is exactly compatible with the microstructure of all neighboring grains. This demands a difference in the crystal orientation $\Delta\gamma$ between each pair of grains of exactly $\Delta\gamma = n\pi/2, n \in \mathbb{N}$ (found by solving the mechanical and electrostatic compatibility conditions (Shu & Bhattacharya, 2001)). Since this coincides with the crystal symmetries of the tetragonal material, any difference in grain orientation leads to incompatibility at the grain boundaries and therefore to local mechanical and electric fields. Nevertheless, various experiments on tetragonal PZT (Cao & Randall, 1996; Ivry et al., 2011; Marincel, Zhang, et al., 2015) have reported a collective, correlated alignment of ferroelastic domain patterns across multiple grain boundaries—providing evidence that the existence of domain patterns across grain boundaries is rather a compromise of sustaining a low-energy laminate pattern in exchange for localized high-energy spots at locations of incompatibility.

To assess the impact of grain boundaries on the ferroelectric microstructure qualitatively, we show in Fig. 4.9 representative snapshots of the equilibrium domain pattern formation in bicrystals, which are poled in the positive vertical direction and have five different misorientations $\Delta\gamma$. For *symmetrically* misorientated tilt grain boundaries in Fig. 4.9(a)-(e), we observe mostly disconnected laminar domains with triangular-shaped transition structures at low grain misorientations $\Delta\gamma$ (highlighted in the magnification in Fig. 4.9(a)). By contrast, the lamellar bands at high misorientations $\Delta\gamma$ are generally correlated across the grain boundary with only a few wedged-like transition structures. Note that the depicted domain structure adjacent to the grain boundary for $\Delta\gamma = 25°$ in Fig. 4.9(a) shows a similar pattern as observed in bright-field cross-section TEM of 24°-tilted bicrystalline epitaxial PZT (Marincel, Zhang, et al., 2015), although the electric field in the experiment was applied in the out-of-plane direction. The highlighted triangular-shaped flux-closure domain structures in the proximity of the GB account for uncompensated electric fields due to the incompatibility at the boundary to reduce the total energy of the material. They have been reported in atomic-resolution TEM (Jia et al., 2011; McGilly et al., 2010) and in mesoscale PFM (McQuaid et al., 2011). The emergence of such closure domains is partially a consequence of the charge-free assumption, i.e., that no mobile charge carriers are present within the material, which could accumulate at locations of uncompensated electric fields, such as grain boundaries.

Fig. 4.9(f)-(j) shows the other interesting case are *asymmetrically* misoriented grains, where the left grain is rotated by $\gamma_1 = -\Delta\gamma$ and the coordinate system of the right grain is aligned with the electric field direction. While the crystal on the right generally favors a monodomain configuration, the rotated grain on the left is forced to form an energy-minimizing microstructure, which is incompatible at the grain boundary. This arrangement is comparable to the situation at an austinite-martensite phase boundary in shape-memory alloys, in which the low-symmetry martensite phase forms a ferroelastic twin pattern that gradually refines towards the interface to reduce the elastic strain energy due to the incompatibility at the interface (cf. Fig. 1 in (Cui et al., 2006)). The microstructures of both materials in the vicinity of a grain boundary are similar with the main difference that in the depicted ferroelectric microstructures no refinement of the lamellar bands is visible. Instead, triangular-shaped flux-closure domains emerge to establish electrostatic compatibility at the interface. The domain structure at the boundary is also important for the switching behavior under changing

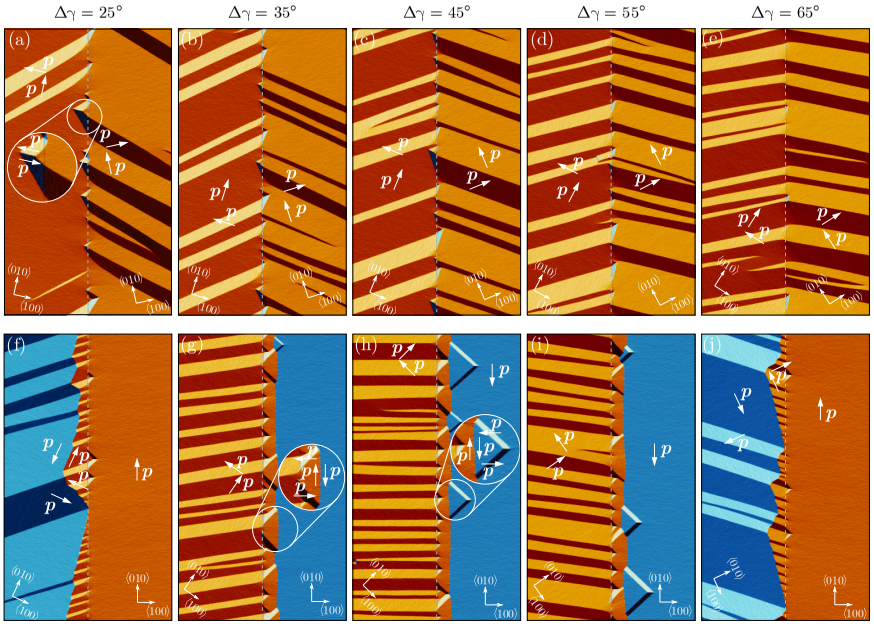

Figure 4.9: Ferroelectric domain structures at a vertical tilt grain boundary (gray dashed line) in a bicrystal, showing the polarization orientation $\phi(\boldsymbol{x})$ as a function of the grain-to-grain misorientation $\Delta\gamma = \gamma_2 - \gamma_1 \in \{25°, 35°, 45°, 55°, 65°\}$ (columns) for a symmetric misorientation $\gamma_1 = \gamma_2 = \mp\Delta\gamma/2$ in (a) to (e) and an asymmetric misorientation $\gamma_1 = -\Delta\gamma$ and $\gamma_2 = 0°$ in (f) to (j). γ_1 and γ_2 denote the orientations of the left and right grains, respectively. A polycrystalline RVE with two grains, pre-poled in the negative vertical direction, and a triangularly-shaped electric field in the positive vertical direction with amplitude $e_2 = 10^8\,\mathrm{V/m}$ and electric field rate $\dot{e}_2 = 10^8\,\mathrm{V/m \cdot s}$ were used to compute the depicted domain patterns.

electric fields. Based on the computed microstructures in the proximity of an asymmetrically misoriented bicrystal, we observe that in case of a large lattice mismatch ($\Delta\gamma \approx 45°$), the 90° laminate in the left grain reverts its polarization first and initiates 180°-domain wall motion within the grain on the right, see Fig. 4.9(g)-(i). By contrast, in case of a small lattice mismatch, the right grain switches first, followed by 180°-domain wall motion towards the left grain, see Fig. 4.9(g,i). The complete switching behavior of polycrystalline ferroelectrics is discussed next.

4.5.6 *Non-equilibrium domain patterns and switching mechanism*

To understand the role of mesoscale nucleation and domain wall motion on the macroscale material response, we study the evolution of the homogenized polarization and strain as well as the underlying domain pattern formation during polarization switching, which is illustrated in Fig. 4.10. The macroscale material response is shown by the history of the average strain $\langle \varepsilon_{22} \rangle$ parallel to the applied field direction (red, dashed line) and the average polarization $\langle p_2 / p_0 \rangle$ (blue, straight line) in Fig. 4.10(a). The underlying evolution of the ferroelectric microstructure is shown by the polarization orientation $\phi(\boldsymbol{x}, t)$ within the RVE in Fig. 4.10(b). These snapshots were taken at the discrete times indicated in Fig. 4.10(a). Fig. 4.10(c) shows a grain-scale schematic of the zoomed-in region highlighted in Fig. 4.10(b), representing a typical grain of the polycrystalline RVE with 20 grains. We explain the overall mechanism by briefly discussing the different stages of switching, using Roman numbers (I)-(VI) for the different times as shown in Fig. 4.10(a).

(I) The RVE is initially pre-poled in the negative vertical direction and equilibrated. In this initial state, the ferroelectric microstructure shows primarily 90°-laminate structures, which is a results of energy relaxation (Bernhard Jaffe, 1971; Fousek & Janovec, 1969; Lines & Glass, 2001; Sapriel, 1975) and has been observed in numerous experiments (Asada & Koyama, 2007; Cao & Randall, 1996; Goo et al., 1981; Randall et al., 1987; Ricote et al., 1999; Schmitt et al., 2007; Schönau et al., 2007; Woodward et al., 2005). In our simulation, the lamellae are composed of a^+, a^-, and b^- variants, which typically continue across grain boundaries or form localized transition layers to compensate for local stress or electric fields due to incompatibility (Dayal & Bhattacharya, 2007; Hubert & Schäfer, 2008). We refer to this initial 90°-laminate structure as the first laminate for the sake of readability.

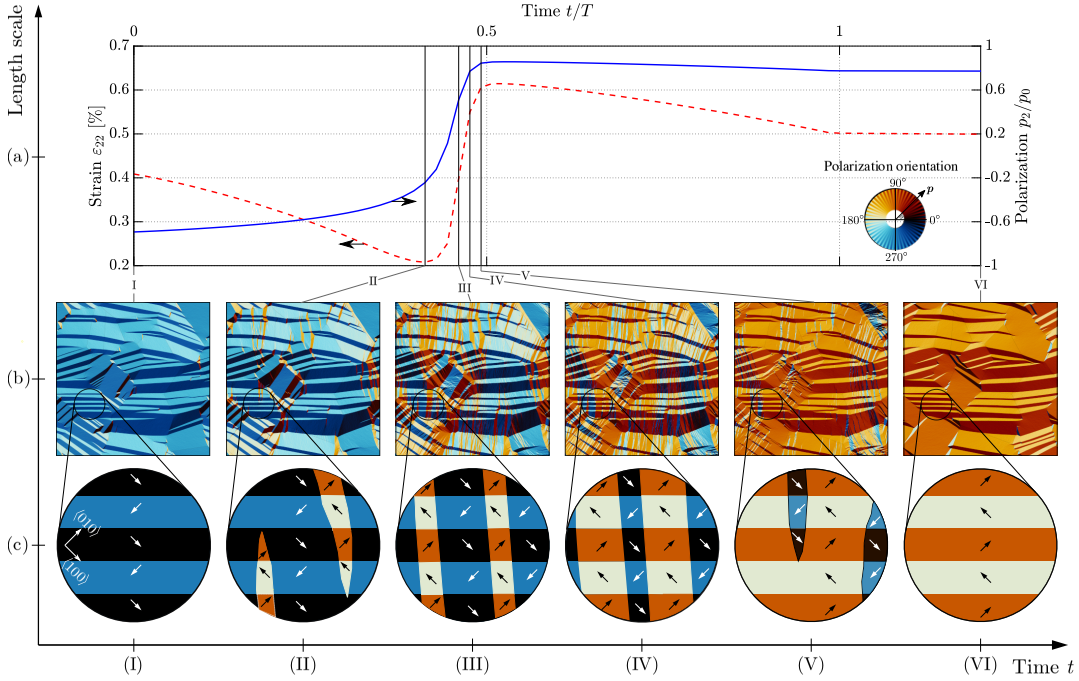

Figure 4.10: Polarization reversal is accommodated by domain switching. The switching mechanism illustrated by (a) the macroscale time evolution of the vertical strain component ε_{22} (red, dashed line) and the vertical polarization component p_2/p_0 (blue, straight line), (b) snapshots of the evolving ferroelectric microstructure during polarization reversal, and (c) a magnified schematic of the local domain pattern formation of the respective highlighted circled areas in (b). Colors indicate the polarization orientation. A polycrystalline RVE with 20 grains and a triangularly-shaped electric field with amplitude $e_2 = 8 \cdot 10^7\,\mathrm{V/m}$ and electric field rate $\dot{e}_2 = 2.5 \cdot 10^7\,\mathrm{V/m \cdot s}$ was used for simulations.

(II) As the applied electric field is slowly ramping up, the inverse piezoelectric effect leads to a linear decrease in $\langle \varepsilon_{22} \rangle$, accompanied by a nonlinear contribution from the motion of the existing 90°-domain walls (Hall, 2001; Pramanick et al., 2011; Trolier-McKinstry et al., 2006), the nucleation of new rank-2 laminates (Snoeck et al., 1994; Z. Zhang et al., 2008), and due to intergranular stresses (Hall et al., 2004). The newly emerged 90° laminate in Fig. 4.10(c) with an $a^- b^+$ domain structure nucleates primarily at GBs or other high-energy spots and grows longitudinally in a needle-like shape from the top and bottom into the existing $a^+ b^-$ laminate of the grain, as shown in Fig. 4.10(c). The longitudinal growth is energetically favored, since it requires only ions at the needle tip to be displaced as opposed to lateral growth, where all ions along the domain wall must be displaced, which makes the latter mechanism geometrically more susceptible to domain wall pinning (Snoeck et al., 1994).

(III)-(IV) Once fully established, the needles continue their longitudinal expansion, until the needle tips reach the boundaries of the grain. TEM experiments have shown that interactions of the needle tip with defects (Snoeck et al., 1994) or other domain walls (Z. Zhang et al., 2008) also leads to pinning, but the former effect is not considered here and the latter is less often observed. The intersection of the $a^- b^+$ and $a^+ b^-$ lamellae results in a rank-2 laminate (Tsou et al., 2011), forming an array of polarization vortices. After the longitudinal growth stops, the second-order laminate grows primarily in the lateral direction by moving its 90°-domain walls sideways, which is in agreement with experimental reports (Kim et al., 2013; Snoeck et al., 1994) and theoretical models (Arlt, 1997). Although we still observe occasional nucleation of new domains (since the electric field is still increasing), it appears to be outweighed by 90°-domain wall motion. The latter mechanism is highly mobile, since only small elastic forces are required (Arlt, 1997). The overall switching mechanism appears as a 180°-switching step, which does not deform the grain but only reverts the polarization orientation (Arlt, 1997; Schultheiß et al., 2018).

(V) Shortly after the second-order laminate has grown across the whole grain through domain wall motion, the first laminate slowly starts to vanish by 90°-domain wall motion. However, depending on the applied electric field, the initial $a^+ b^-$-lamellae must not necessarily be extinguished completely. Nevertheless, as more grains switch their polarization completely by the motion of ferroelastic domain walls (or become pinned), the rate of change of the macroscopic polarization and strain decreases steadily, such that $\langle \boldsymbol{p} \rangle$ and $\langle \varepsilon_{22} \rangle$ approach their saturation values at time $T = 0.5$

asymptotically or in a creep-like manner (Fett & Thun, 1998; Guillon et al., 2004; Viola et al., 2014).

(VI) During times $T/t \in (0.5, 1.0)$, the electric field is linearly ramped down, which leads to an almost linear decrease in the strain $\langle \varepsilon_{22} \rangle$—governed by the inverse piezoelectric effect. After complete removal of the applied external field $T/t \geq 1.0$, we observe equilibration of the ferroelectric microstructure through local refinement of domain walls, which straightens the interfaces to comply with the compatibility conditions (Shu & Bhattacharya, 2001). In addition, transition layers (wedge-shaped structures) form at grain boundaries with a strong orientation mismatch to locally compensate for incompatibility (Dayal & Bhattacharya, 2007; Hubert & Schäfer, 2008), while we also observe the annihilation of small domains and slight rearrangements of the domain patterns towards energy-minimizing equilibrium configurations.

4.5.6.1 *Influence of the applied electric field rate*

As ferroelectric switching is a kinetic process, which depends on the rate at which the electric field is applied (Kannan & Kochmann, 2022; Kannan et al., 2022; Schultheiß et al., 2019a), we also simulated the influence of rate-dependent loading on the macro- and mesoscale response of PZT ceramics. A triangular-shaped electric field pulse with varying pulse widths T and constant maximum field $e_2 = 8.0 \times 10^7\,\mathrm{V/m}$, resulting in rates $\dot{e}_2 = \{5.0 \times 10^6, 5.0 \times 10^7\}\,\mathrm{V/m \cdot s}$, is applied to a polycrystalline RVE, comprised of 320 grains. The homogenized polarization response is extracted along with snapshots of the ferroelectric microstructure during switching. Fig. 4.11(a) illustrates the impact of the electric field rates $\dot{e}_2 = \{5 \times 10^6, 5 \times 10^7\}\,\mathrm{V/m \cdot s}$ on the average polarization $\langle p_2/p_0 \rangle$ and the average densities of 90°- and 180°-domain walls ($\langle \Omega_{90} \rangle$ and $\langle \Omega_{180} \rangle$, respectively), and the total amount of domain walls ($\langle \Omega_{\mathrm{DWs}} \rangle$). At the lower rate, we observe a prompt polarization response with an approximately linear increase in domain wall density. The higher rate delays polarization switching but leads to a higher peak density of domain walls (which rises in a nonlinear fashion close to time $t/T = 0.5$). This difference in the domain wall density becomes apparent in the shown snapshots of the ferroelectric domain microstructure in Fig. 4.11(c,d): fewer and larger domains are visible at the slow rate (Fig. 4.11(c)), whereas denser and finer domains are observed at the high rate (Fig. 4.11(d)). This effect is traced back to the competition between *nucleation* and *growth*, which

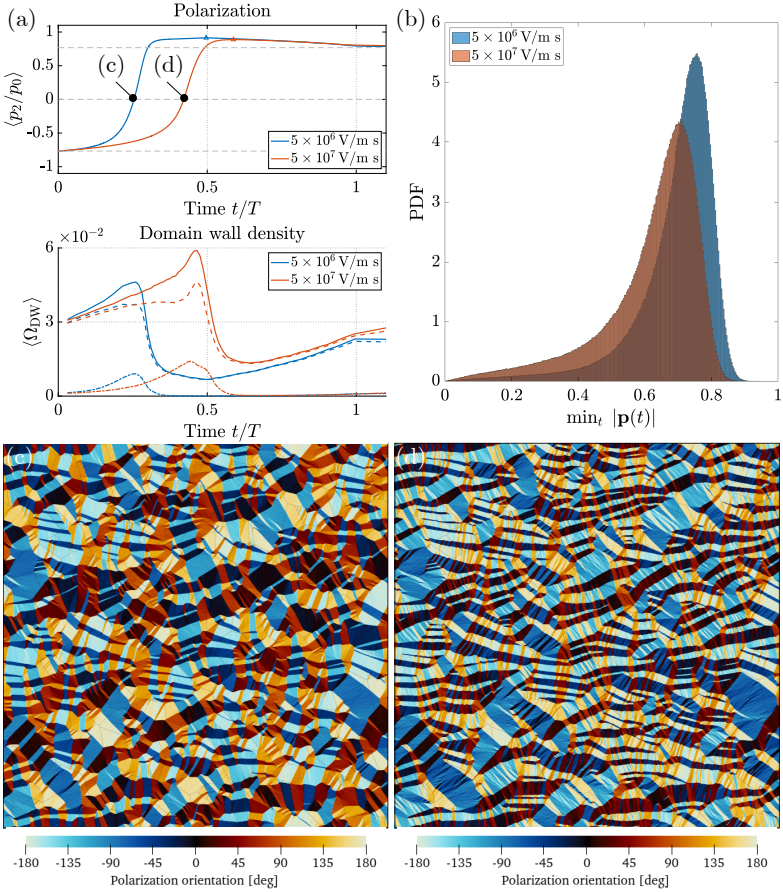

Figure 4.11: Influence of the electric field rate $\dot{e}$ on the triangular-pulse response, showing (a) the average polarization $\langle p_2/p_0 \rangle$ and average domain wall densities of 90° walls $\langle \Omega_{90} \rangle$ (dashed line), 180° walls $\langle \Omega_{180} \rangle$ (dashed-doted line), and the total amount of domain walls $\langle \Omega_{\mathrm{DWs}} \rangle$ (straight line) vs. the normalized time t/T, where T denotes the time period of the triangular pulse. Line colors indicate the electric field rates $\dot{e} = \{5 \times 10^6, 5 \times 10^7\}\,\mathrm{V/m \cdot s}$ for an electric field magnitude $e_2 = 8.0 \times 10^7\,\mathrm{V/m}$. (b) Switching statistics showing the probability density function vs. minimal length of the polarization vector during polarization reversal, $\min_t |\boldsymbol{p}(t)|$. Snapshots of representative ferroelectric domain microstructures, extracted at an average polarization $\langle p_2/p_0 \rangle = 0$ for the two rates, are depicted in (c) and (d).

influences the appearance of the domain patterns by the following two mechanisms.

First, because of the linear rise of the electric field in a triangular pulse, the electric field magnitude at slow electric field rates increases slowly, such that switching occurs primarily due to the growth of existing, incompletely switched domains at GBs or grain triple junctions. The presence of small driving forces results in quasi-equilibrium conditions with local equilibration, evident by the straight domain walls. Nucleation of new domains, by thermally-activated barrier-crossing events, is less likely at low electric fields.

Second, with increasing rates the electric field magnitude increases faster, which lowers the energy barriers in the polarization energy landscape. This, in turn, allows thermal fluctuations to escape their disadvantageous polarization states to reach lower-energy polarization states more frequently. As a result, domain wall motion becomes less dominant during polarization switching, as it is outweighed by the increase in nucleation of new domains. The impact of nucleation is apparent in the ferroelectric domain patterns, showing more detailed domain structures with rough and curvy interfaces. Higher rates favor the formation of 180°-domain walls, which is visible in the considerable increase in the 180°-domain wall density at the higher rate (Fig. 4.11(a)). 90°-domain walls evolve in a similar fashion at both rates (except for the surge in 90°-domain walls during the peak switching activity close to $t/T = 0.5$).

To assess the predominant switching type, i.e., rotation of the polarization vector vs. stretch of the polarization vector, known as 90°-switching vs. 180°-switching, we compute the change in the polarization norm $|\boldsymbol{p}|$ of each unit cell during polarization switching. This is shown in Fig. 4.11(b), where the probability density function of the smallest polarization length $|\boldsymbol{p}|$ is depicted. For both rates, the polarization norm is generally centered between $|\boldsymbol{p}| \approx 0.7 - 0.8$ and exhibits only a minor stretch; hence, switching occurs primarily by two consecutive 90°-rotations. However, statistically more 180°-switching is observed at the higher rate (Fig. 4.11(b)), since such high-energy switching trajectories become more accessible with increasing electric fields. We point out that the reported rate dependence is a transient effect, which affects the ferroelectric microstructure mainly during polarization reversal but does not alter the equilibrium microstructure significantly (as seen in the close to identical final polarization states and domain wall densities).

4.6 CONCLUSION

We have presented a high-resolution phase-field study of the complex domain pattern formation in tetragonal PZT ceramics, discussed computational techniques for automatic domain wall identification and tracking, and demonstrated their usability in comparison with analytical models and experimental reports. These are our main conclusions:

First, we demonstrated that the finite-temperature phase-field framework predicts realistic ferroelectric microstructures comprised of the typical lamellar bands (Arlt, 1990) stretching across multiple grains (Ivry et al., 2011), while also including more intricate domain structures such as wedged-shaped transition layers in the vicinity of grain boundaries (for reasons of compatibility), which have been observed in ferroelectric (Jia et al., 2011; McQuaid et al., 2011), ferromagnetic (Özdemir et al., 1995) and ferroelastic materials (Cui et al., 2006).

Second, while the phase-field setting offers a convenient way to resolve complex networks of domains in polycrystals, it makes it challenging to keep track of the number and type of interfaces present in the material. Therefore, we presented a new approach (based on the characteristics of the respective minimum-energy states) to efficiently and reliably identify different types of domain walls and trace them during polarization reversal in an automatic fashion, which extends the capability of the diffuse-interface framework.

Third, a large-scale study on the impact of domain pattern formation on the effective material properties in lead-based ceramics revealed distinct correlations between the grain orientation and the grain-averaged polarization, strain, and domain density—which agree well with experimental observations based on x-ray and neutron diffraction measurements (Hall et al., 2004; Hall et al., 2005; Jones et al., 2006; Jones et al., 2007; Jones et al., 2005; Pramanick et al., 2011).

Fourth, a simple analytical model based on minimizing the electric enthalpy yields good estimates for judging whether a grain will comprise a single domain (monodomain) or a lamellar band (laminate) structure and, for each case, predicts the average polarization and strain within the grain as a function of the grain orientation.

Fifth, by examining the domain wall density per grain in polycrystals, we showed that the grain-averaged lateral polarization and the polarization

orientation are generally uncorrelated, while—in the special case of monodomain grains—those admit strong correlations with the grain orientation (in agreement with the analytical model).

Finally, polarization reversal during switching in a pre-poled polycrystalline RVE (with existing lamellar bands) occurs in two steps: (1) the nucleation of a new 90° laminate, whose needle domains grow orthogonal to the existing 90° laminate and jointly form a rank-2 laminate (vortex structure). (2) Once the rank-2 laminate is fully established, polarization reversal in the existing laminate is achieved through domain wall motion of the new 90° laminate, which is energetically favored by the applied electric field.

5

CONCLUSION AND OUTLOOK

All models are wrong, but some are useful.
— George E. P. Box (Box, 1979)

In this thesis, the effect of temperature on the ferroelectric domain pattern formation and evolution in porous single-crystalline and dense polycrystalline lead-based ferroelectric materials has been investigated by using a diffuse-interface approach. The developed finite-temperature phase-field model provided insight into mesoscale interactions, accommodated by domain wall motion and pinning at defects and nucleation of new domains at localized high-energy spots, to advance our current understanding of the underlying mechanisms driving the macroscopic switching kinetics.

5.1 FINITE-TEMPERATURE FERROELECTRIC CONSTITUTIVE MODEL

A new finite-temperature constitutive model for ferroelectric ceramics has been presented that accounts for the temperature dependence of the DFT-informed polarization potential as well as for the effect of atomic-level thermal lattice vibrations at the mesoscale by a thermalized stochastic noise term in the well-established Allen-Cahn equation. This model demonstrated the salient features of finite-temperature ferroelectric switching in a promising fashion. Several original temperature-driven switching mechanisms were discussed, such as thermally activated nucleation of needle-shaped domains and branching of existing domains, which qualify to play a key role in the kinetics of polarization reversal at subcoercive electric fields.

The newly established stochastic noise term in the evolution equation of polarization stimulates the formation of realistic domain patterns, comprised of networks of slender, needle-shaped domains forming intricate laminate patterns, such as the well-known herringbone and vortex structures. This is accomplished primarily by the following two mechanisms.

First, thermal fluctuations randomly perturb the evolution of polarization which breaks the symmetry of the Landau potential, such that high-energy 180°-switching trajectories become improbable, whereas low-energy switching paths, realized by two consecutive 90°-rotations, are favored. The combination of primarily 90°-domain patterns and the motion of highly mobile 90°-domain walls at the mesoscale results in an increase in the effective switching kinetics at the macroscale.

Second, depending on the temperature, thermal noise can induce branching of existing domains and nucleation of new domains. Nucleation occurs naturally, as a consequence of thermally activated barrier-crossing events, without requiring an additional nucleation model and even in perfect, defect-free single crystals. These are unique features of our model. While at high temperatures more detailed and finer domains appear, at low temperatures fewer but larger domains are visible. This can be traced back to the competition between nucleation and growth which plays a key role in the effective switching kinetics.

The stochastic noise in this model accounts for thermal lattice vibrations. Alternatively, one could reinterpret the noise term as fluctuations caused by spatial disorder such as lead and oxygen vacancies, impurities, and any combined effects, cf. (Bauer et al., 2022; Glinchuk & Farhi, 1996; Pirc & Blinc, 1999; S. Wang et al., 2016) or fluctuations in the local electric field. Furthermore, by utilizing the primitive unit cell of the crystal lattice (known from DFT calculations) as the normalization volume of the non-convex energy, the noise amplitude is intrinsically connected to material properties without any fitting parameter. While this comes at the cost of being restricted to a subnanometers spatial resolution in the numerical discretization, it also ensures realistic domain wall thicknesses in simulations, which is not possible at larger scales.

5.2 EFFECT OF TEMPERATURE ON DOMAIN WALL–PORE INTERACTIONS IN PZT

In Chapter 3, the combined effect of porosity and temperature was investigated by leveraging the established finite-temperature phase-field model on porous ferroelectric materials. To this end, a circular pore was modeled, and its impact on an approaching ferroelectric domain wall was studied. The observed mechanisms of domain wall pinning and depinning on a pore were discussed, and the effect of temperature on the (depinning) electric

field required to unpin 180°-domain walls from a periodic array of pores was reported, for various pore sizes and concentrations. Results indicate that larger pore sizes and densities reduce the domain wall kinetics, while temperature mitigates the pinning effect of pores, leading to an increase in the mobility of domain walls, which is generally in good agreement with experimental reports and underlines the importance of finite-temperature effects on the effective switching kinetics.

Numerical simulations of the interaction of a 180°-domain wall with circular pores qualitatively captured several domain-wall pinning effects, which have been reported in various experiments. One such experiment observed bowing of a domain wall around a void caused by induced electric fields in the vicinity of the pore. Other experiments reported a reduction of the effective remanent polarization for increasing porosity, which is reflected by our predicted increase of domain wall pinning for more densely packed pores. A third experiment revealed mesoscale pinning and subsequent depinning of domain wall motion at pores, whose kinetics at the macroscale is reported as stick-slip behavior, which is typical for the large-defect regime.

Although the emphasis was placed on pore sizes larger than the domain wall thickness (large-defect regime), a recent phase-field study used our finite-temperature constitutive model and was conducted in the small-defect regime, showed that the creep-like domain wall motion at low electric fields can be traced back to pinning at spatial, quenched disorder, while thermal noise mitigates pinning on point defects (Bauer et al., 2022). This report on depinning at the small-scale defects, in combination with our findings at the large-defect regime, supports the conclusion that the length scale of the heterogeneity plays a decisive role in the pinning behavior. Furthermore, the aforementioned study confirmed that the effect of thermal noise leads generally to an increase in the mobility of domain walls in non-defect-free materials.

However, the study on domain wall-pore interactions, presented in Chapter 3, also revealed the limitations of our model. In particular, the simplification to 2D leads to an overestimation of the electric field induced by the pore of 33% compared to a spherical pore in 3D. Furthermore, the focus was placed on 180°-domain walls and excluded pinning of 90°-domain walls, which are expected to have a lower depinning field due to the difference in the energy barrier. Moreover, the influence of the strain mismatch between

the pore and the surrounding ferroelectric has not been studied thoroughly, since isotropic elasticity is assumed.

5.3 DOMAIN PATTERN FORMATION IN TETRAGONAL CERAMICS

Major improvements in the parallel efficiency of the FFT-based numerical implementation enabled us to study the intricate domain pattern formation and subsequent evolution in PZT ceramics by performing high-resolution simulations of micron-sized polycrystals. In addition, new computational techniques to automatically identify and track different types of domain walls while the ferroelectric microstructure is evolving were developed. As a result, distinct corrections of the grain-averaged polarization, strain, and density of domains as a function of the crystal orientation were obtained by examining the equilibrium domain structures of a statistically representative number of grain samples, which agree well with x-ray and neutron diffraction experiments. Furthermore, these correlations can be traced back analytically to two predominant types of domain arrangements, the monodomain and laminate structure, by minimizing the polarization enthalpy density in a sharp-interface setting. Moreover, the observed switching mechanism of the ferroelectric microstructure in polycrystals was detailed based on the homogenized polarization and strain responses and in close comparison with experimental reports, to shine new light on the complexities of domain pattern evolution in tetragonal PZT ceramics.

Our model predicts the typical features of ferroelectric microstructure in polycrystalline PZT, such as the characteristic striped domain patterns expanding across multiple grains and the more complex triangular-shaped transition structures in the proximity of grain boundaries. Furthermore, the average width of the emerged lamellar bands is in reasonable agreement with the theoretically predicted Kittel-Mitsui-Furuichi-Roitburd's square-root law, when plotted as a function of the grain size. Moreover, the emerged domain structures in the vicinity of grain boundaries agree qualitatively with the wedged-shaped domains observed in micrographs, but they could not be validated quantitatively, since high-resolution TEM measurements of transition layers are hard to find. In conclusion, the finite-temperature phase-field model yields a realistic prediction of the domain pattern formation in tetragonal ceramics, for which convergence of its statistics to the macroscale limit was demonstrated.

Due to the influence of domain walls on the macroscale properties, a new computational technique was discussed to efficiently identify and track different domain wall types in phase-field simulations, which is non-trivial in systems exhibiting random noise. While the presented procedure has been calibrated and benchmarked for the specific domain wall properties of tetragonal PZT, different crystal systems can also be considered by appropriate adjustments of the interface measures according to their respective symmetry groups and interface properties. In general, this extends the capability of phase-field models to provide valuable information on the types and densities of interfaces present in the RVE to determine their role in the effective material behavior.

Analyzing the equilibrium grain statistics of the emerged ferroelectric domain pattern formation of more-than-12,000-grain samples disclosed clear correlations between the grain orientation and the grain-averaged polarization, strain, and domain density, which are in agreement with x-ray and neutron diffraction experiments. Furthermore, depending on the local grain orientation, two types of domain structures were identified and their emergence was linked as a result of minimizing the electric enthalpy density with respect to their crystal orientation, using a simple analytical model of a 90° laminate and a monodomain grain.

5.4 OUTLOOK

In this thesis, several original techniques were presented to assess the kinetics of polarization switching in porous and polycrystalline ferroelectric at finite temperatures. Of course, a series of unanswered questions has remained, which provide ideas for potential future work.

Regarding theoretical and numerical methods, the finite-temperature constitutive model leaves room for improvement in several respects. First, it allows solely for isothermal conditions within the material and considers only the temperature dependence of the polarization energy density. An extension to account for further temperature effects, such as temperature-dependence of elasticity and other physical effects, e.g., thermal expansion, could be implemented analogously into the existing framework, although reliable temperature-dependent material inputs for lead-based ferroelectrics are rare. Nevertheless, this would enhance the accuracy of stress predictions significantly, especially in regions with heterogeneous material properties, e.g., grain boundaries, voids, and impurities. In contrast, heterogeneous

temperature fields are not admissible in the current framework and require an extension of the governing equations to account for heat diffusion and dissipation, subject to the second law of thermodynamics (Woldman & Landis, 2016, 2019). This could potentially open new temperature-related research directions, such as domain wall-induced self-heating, which has been measured recently in nanoparticle-assisted Raman thermometry experiments (Lundh et al., 2020).

Second, iterative solution schemes, such as the Richardson fixed-point iteration (2.5.5), solve the balance of linear momentum in a heterogeneous material in an iterative fashion and are therefore computationally expensive; hence, the elastic anisotropy is often neglected. While more sophisticated techniques, e.g., based on Newton-Krylov methods (Kabel et al., 2014) and Augmented Lagrangian (AL) schemes (Michel et al., 2000), offer some advantages for large deformations and high-contrast problems, they also require fixed-point iterations to compute the unknown strain field, which renders the Fourier-based solution strategy disproportionately time-consuming. Alternatively, recent developments and applications of neural network-based methods in mechanics, e.g., physics-informed neural networks (PINNs) that solve supervised learning tasks while respecting any given laws of physics (Raissi et al., 2019) and Fourier neural operators that learn mappings between functional spaces (Z. Li et al., 2020), allow for efficient learning of the stress-strain relation to replace iterative solution schemes in the linear momentum balance. Such models present a promising improvement as ML-based accelerators in current spectral homogenization schemes in heterogeneous materials, in semiconducting ferroelectrics to solve Gauss' law with space charges, and as a potential surrogate model of ferroelectricity.

Equally important is the experimental validation of the simulated domain pattern formations and detailed switching mechanisms for providing reliable model predictions. First, to assess the kinetics of domain evolution at the mesoscale, *in-situ* imagining during polarization reversal can be performed, where the domain structure is spatially resolved, e.g., in high-speed PLM and SHG measurements. Such experiments in a temperature-controlled environment are underway in our lab to capture the temperature- and electric-field-rate-dependent kinetics of polarization switching and their impact on the ferroelectric microstructure.

Second, a validation of the theoretically and numerically predicted dependence of monodomain and lamellar domain structures on the grain

orientation would further foster trust in our models. Therefore, in-house, *ex-situ* SEM experiments on poled PZT ceramics obtaining the grain orientation and domain structure of each grain are conducted in our lab, to bring clarity in this regard. Furthermore, combined EBSD and PFM measurements, providing grain and polarization orientation, could validate the predicted correlation functions of the grain-averaged polarization and domain volume fractions in the polycrystals.

The presented finite-temperature model to predict the domain evolution has broad applications in other fields of science, but naturally implies certain adaptations. As a first example, thin films, whose material behavior is determined by surface effects, are not realizable with the Fourier-based spectral solution scheme and require finite element methods. Second, multiaxial polycrystals represent a fully 3D problem imposing severe challenges in terms of the costs of computation and data storage. Third, ferroelectric semiconductors exhibit space-charge and oxygen-defect migrations demanding additional balance and evolution laws. Finally, actuators for micro-robotics applications are subject to large deformations and rotations that require an extension of the constitutive model to account for finite strain theory. Furthermore, application in related materials would also be interesting, e.g., in shape-memory alloys to investigate the formation of ferroelastic domains at the austenite-martensite phase boundaries, in relaxor ferroelectrics to mimic vibrations of interphase boundaries of polar regions, and in multiferroics whose numerous physical couplings would provide insight into interference and crosstalk of multiple pertubed fields.

BIBLIOGRAPHY

Abe, R. (1959). Theoretical treatment of the movement of 180° domain in $BaTiO_3$ single crystal. *Journal of the Physical Society of Japan*, *14*(5), 633.

Abeyaratne, R., & Knowles, J. K. (1991). Kinetic relations and the propagation of phase boundaries in solids. *Archive for Rational Mechanics and Analysis*, *114*(2), 119.

Aguado-Puente, P., & Junquera, J. (2008). Ferromagneticlike closure domains in ferroelectric ultrathin films: First-principles simulations. *Phys. Rev. Lett.*, *100*, 177601.

Aird, A., & Salje, E. K. H. (1998). Sheet superconductivity in twin walls: Experimental evidence of. *Journal of Physics: Condensed Matter*, *10*(22), 377.

Aizu, K. (1969). Possible species of ferroelastic crystals and of simultaneously ferroelectric and ferroelastic crystals. *Journal of the Physical Society of Japan*, *27*(2), 387.

Anglin, B., Lebensohn, R., & Rollett, A. (2014). Validation of a numerical method based on fast fourier transforms for heterogeneous thermoelastic materials by comparison with analytical solutions. *Computational Materials Science*, *87*, 209.

Arlt, G. (1990). The influence of microstructure on the properties of ferroelectric ceramics. *Ferroelectrics*, *104*(1), 217.

Arlt, G., & Dederichs, H. (1980). Complex elastic, dielectric and piezoelectric constants by domain wall damping in ferroelectric ceramics. *Ferroelectrics*, *29*(1), 47.

Arlt, G., Hennings, D., & de With, G. (1985). Dielectric properties of fine-grained barium titanate ceramics. *Journal of Applied Physics*, *58*(4), 1619
doi: 10.1063/1.336051.

Arlt, G., & Sasko, P. (1980). Domain configuration and equilibrium size of domains in $BaTiO_3$ ceramics. *Journal of Applied Physics*, *51*(9), 4956
doi: 10.1063/1.328372.

Arlt, G. (1997). A model for switching and hysteresis in ferroelectric ceramics. *Integrated Ferroelectrics*, *16*(1-4), 229.

Asada, T., & Koyama, Y. (2007). Ferroelectric domain structures around the morphotropic phase boundary of the piezoelectric material $PbZr_{1-x}Ti_xO_3$. *Phys. Rev. B*, *75*, 214111.

Avrami, M. (1940). Kinetics of phase change. ii transformation-time relations for random distribution of nuclei. *The Journal of Chemical Physics*, *8*(2), 212.

Ayoub, M., Futterlieb, H., Imbrock, J., & Denz, C. (2017). 3D imaging of ferroelectric kinetics during electrically driven switching. *Advanced Materials*, *29*(5), 1603325.

Baettig, P., Schelle, C. F., LeSar, R., Waghmare, U. V., & Spaldin, N. A. (2005). Theoretical prediction of new high-performance lead-free piezoelectrics. *Chemistry of Materials*, *17*(6), 1376
doi: 10.1021/cm0480418.

Ball, J. M., & James, R. D. (1987). Fine phase mixtures as minimizers of energy. *Archive for Rational Mechanics and Analysis*, *100*(1), 13.

Ball, J. M., & James, R. D. (1992). Proposed experimental tests of a theory of fine microstructure and the two-well problem. *Philosophical Transactions of the Royal Society of London. Series A: Physical and Engineering Sciences*, *338*(1650), 389
doi: 10.1098/rsta.1992.0013.

Ball, J. M., Chu, C., & James, R. D. (1995). Hysteresis during stress-induced variant rearrangement. *Le Journal de Physique IV*, *5*(C8), C8.

Baruffi, C., Finel, A., Le Bouar, Y., Bacroix, B., & Salman, O. U. (2019). Overdamped langevin dynamics simulations of grain boundary motion. *Materials Theory*, *3*(1), 4.

Bassiri-Gharb, N., Fujii, I., Hong, E., Trolier-McKinstry, S., Taylor, D. V., & Damjanovic, D. (2007). Domain wall contributions to the properties of piezoelectric thin films. *Journal of Electroceramics*, *19*(1), 49.

Batra, I. P., & Silverman, B. D. (1972). Thermodynamic stability of thin ferroelectric films. *Solid State Communications*, *11*(1), 291.

Bauer, N., Neumayer, S. M., Maksymovych, P., & Lavrentovich, M. O. (2022). Structures and velocities of noisy ferroelectric domain walls. *Phys. Rev. Mater.*, *6*, 124401.

Bernhard Jaffe, H. J., William Cook. (1971). *Piezoelectric ceramics*. Academic Press.

Bhattacharya, K. (1991). Wedge-like microstructure in martensites. *Acta Metallurgica et Materialia*, *39*(10), 2431.

Bhattacharya, K., & Ravichandran, G. (2003). Ferroelectric perovskites for electromechanical actuation [The Golden Jubilee Issue. Selected

topics in Materials Science and Engineering: Past, Present and Future]. *Acta Materialia*, *51*(19), 5941.

Bhattacharya, K. (1999). Phase boundary propagation in a heterogeneous body. *Proceedings of the Royal Society of London. Series A: Mathematical, Physical and Engineering Sciences*, *455*(1982), 757.

Bhide, V., Deshmukh, K., & Hegde, M. (1962). Ferroelectric properties of $PbTiO_3$. *Physica*, *28*(9), 871.

Bilz, H., Benedek, G., & Bussmann-Holder, A. (1987). Theory of ferroelectricity: The polarizability model. *Physical Review B*, *35*(10), 4840.

Binnig, G., Quate, C. F., & Gerber, C. (1986). Atomic force microscope. *Phys. Rev. Lett.*, *56*, 930.

Bintachitt, P., Jesse, S., Damjanovic, D., Han, Y., Reaney, I. M., Trolier-McKinstry, S., & Kalinin, S. V. (2010). Collective dynamics underpins rayleigh behavior in disordered polycrystalline ferroelectrics. *Proceedings of the National Academy of Sciences*, *107*(16), 7219.

Boltzmann, L. (1868). On the relationship between the second fundamental theorem of the mechanical theory of heat and probability calculations regarding the conditions for thermal equilibrium.

Bonnell, D. (2000). *Scanning probe microscopy and spectroscopy: Theory, techniques, and applications*. John Wiley & Sons.

Box, G. (1979). Robustness in the strategy of scientific model building. In R. L. Launer & G. N. Wilkinson (Eds.), *Robustness in statistics* (pp. 201–236). Academic Press.

Brewster, S. D. (1824). *Observations on the pyro-electricity of minerals*. William Blackwood.

Buck, D. A. (1952). *Ferroelectrics for digital information storage and switching*. (tech. rep.). Massachusetts Institute of Technology Cambridge.

Bucsek, A. N., Nunn, W., Jalan, B., & James, R. D. (2020). Energy conversion by phase transformation in the small-temperature-difference regime. *Annual Review of Materials Research*, *50*(1), 283.

Burcsu, E., Ravichandran, G., & Bhattacharya, K. (2004). Large electrostrictive actuation of barium titanate single crystals. *Journal of the Mechanics and Physics of Solids*, *52*(4), 823.

Cao, W., & Randall, C. A. (1996). Grain size and domain size relations in bulk ceramic ferroelectric materials [Proceeding of the 3rd Williamsburg Workshop on Fundamental Experiments on Ferroelectrics]. *Journal of Physics and Chemistry of Solids*, *57*(10), 1499.

Carl, K., & Hardtl, K. H. (1977). Electrical after-effects in $Pb(Ti, Zr)O_3$ ceramics. *Ferroelectrics*, *17*(1), 473.

Catalan, G., Lukyanchuk, I., Schilling, A., Gregg, J. M., & Scott, J. F. (2009). Effect of wall thickness on the ferroelastic domain size of $BaTiO_3$. *Journal of Materials Science*, *44*(19), 5307.

Catalan, G., Scott, J. F., Schilling, A., & Gregg, J. M. (2006). Wall thickness dependence of the scaling law for ferroic stripe domains. *Journal of Physics: Condensed Matter*, *19*(2), 022201.

Catalan, G., Seidel, J., Ramesh, R., & Scott, J. F. (2012). Domain wall nanoelectronics. *Rev. Mod. Phys.*, *84*, 119.

CeramTec. (2020). Avanced electro ceramics datasheet.

Chaplya, P. M., & Carman, G. P. (2001). Dielectric and piezoelectric response of lead zirconate–lead titanate at high electric and mechanical loads in terms of non-180° domain wall motion. *Journal Applied Physics*, *90*(10), 5278.

Chen, L. Q. (2008). Phase-field method of phase transitions/domain structures in ferroelectric thin films: A review. *Journal of the American Ceramic Society*, *91*(6), 1835.

Cho, Y., Matsuura, K., Valanoor, N., & Ramesh, R. (2003). Direct domain wall thickness measurement using scanning nonlinear dielectric microscopy. *Ferroelectrics*, *292*(1), 171.

Choudhury, S., Li, Y., Krill, C., & Chen, L.-Q. (2005). Phase-field simulation of polarization switching and domain evolution in ferroelectric polycrystals. *Acta Materialia*, *53*(20), 5313.

Cohen, R. E. (1992). Origin of ferroelectricity in perovskite oxides. *Nature*, *358*(6382), 136.

Cohen, R. E., & Krakauer, H. (1992). Electronic structure studies of the differences in ferroelectric behavior of $BaTiO_3$ and $PbTiO_3$. *Ferroelectrics*, *136*(1), 65.

Craik, D. J., & Cooper, P. V. (1970). Magnetostatic energy coefficients for cylindrical domains. *Physics Letters A*, *33*(7), 411.

Cui, J., Chu, Y. S., Famodu, O. O., Furuya, Y., Hattrick-Simpers, J., James, R. D., Ludwig, A., Thienhaus, S., Wuttig, M., Zhang, Z., & Takeuchi, I. (2006). Combinatorial search of thermoelastic shape-memory alloys with extremely small hysteresis width. *Nature Materials*, *5*(4), 286.

Curie, J., & Curie, P. (1880). Développement par compression de l'électricité polaire dans les cristaux hémièdres à faces inclinées. *Bulletin de minéralogie*, *3*(4), 90.

Dabra, N., Hundal, J. S., Nautiyal, A., Sekhar, K. C., & Nath, R. (2010). Analysis of ferroelectric polarization switching in (nh4)0.39k0.61no3

films using nucleation limited switching model. *Journal of Applied Physics*, *108*(2), 024108.

Damjanovic, D. (1998). Ferroelectric, dielectric and piezoelectric properties of ferroelectric thin films and ceramics. *Reports on Progress in Physics*, *61*(9), 1267.

Daraktchiev, M., Catalan, G., & Scott, J. F. (2008). Landau theory of ferroelectric domain walls in magnetoelectrics. *Ferroelectrics*, *375*(1), 122 doi: 10.1080/00150190802437969.

Das, S., Tang, Y. L., Hong, Z., Gonçalves, M. A. P., McCarter, M. R., Klewe, C., Nguyen, K. X., Gómez-Ortiz, F., Shafer, P., Arenholz, E., Stoica, V. A., Hsu, S. .-., Wang, B., Ophus, C., Liu, J. F., Nelson, C. T., Saremi, S., Prasad, B., Mei, A. B., ... Ramesh, R. (2019). Observation of room-temperature polar skyrmions. *Nature*, *568*(7752), 368.

Daumont, C. J. M., Mannix, D., Venkatesan, S., Catalan, G., Rubi, D., Kooi, B. J., Hosson, J. T. M. D., & Noheda, B. (2009). Epitaxial $TbMnO_3$ thin films on $SrTiO_3$ substrates: A structural study. *Journal of Physics: Condensed Matter*, *21*(18), 182001.

Davi, F., & Rizzoni, R. (2004). On twinning and domain switching in ferroelectric $PbZr_{1-x}Ti_xO_3$—part i: Twins and domain walls. *Journal of the Mechanics and Physics of Solids*, *52*(1), 113.

Dayal, K., & Bhattacharya, K. (2007). A real-space non-local phase-field model of ferroelectric domain patterns in complex geometries. *Acta Materialia*, *55*(6), 1907.

De Guerville, F., Luk'yanchuk, I., Lahoche, L., & El Marssi, M. (2005). Modeling of ferroelectric domains in thin films and superlattices. *Materials Science and Engineering: B*, *120*(1), 16.

De Simone, A. (1993). Energy minimizers for large ferromagnetic bodies. *Archive for rational mechanics and analysis*, *125*(2), 99.

DeSimone, A., & James, R. D. (2002). A constrained theory of magnetoelasticity. *Journal of the Mechanics and Physics of Solids*, *50*(2), 283.

Devonshire, A. (1949). Xcvi. theory of barium titanate. *Philosophical Magazine Series 7*, *40*(309), 1040.

Devonshire, A. (1951). Cix. theory of barium titanate: Part ii. *Philosophical Magazine Series 7*, *42*(333), 1065.

Devonshire, A. (1954). Theory of ferroelectrics. *Advances in Physics*, *3*(10), 85.

Drougard, M. (1960). Detailed study of switching current in barium titanate. *Journal of Applied Physics*, *31*(2), 352.

Duiker, H. M., & Beale, P. D. (1990). Grain-size effects in ferroelectric switching. *Phys. Rev. B*, *41*, 490.

Emig, T., & Nattermann, T. (1999). Disorder driven roughening transitions of elastic manifolds and periodic elastic media. *The European Physical Journal B - Condensed Matter and Complex Systems*, *8*(4), 525.

Emig, T., & Nattermann, T. (1997). A new disorder-driven roughening transition of charge-density waves and flux-line lattices. *Phys. Rev. Lett.*, *79*, 5090.

Eshelby, J. D. (1975). The elastic energy-momentum tensor. *Journal of Elasticity*, *5*(3), 321.

Fedeli, P., Kamlah, M., & Frangi, A. (2019). Phase-field modeling of domain evolution in ferroelectric materials in the presence of defects. *Smart Materials and Structures*, *28*(3), 035021.

Fennie, C. J., & Rabe, K. M. (2005). First-principles investigation of ferroelectricity in epitaxially strained Pb_2TiO_4. *Phys. Rev. B*, *71*, 100102.

Ferrell, R., Menyhàrd, N., Schmidt, H., Schwabl, F., & Szépfalusy, P. (1968). Fluctuations and lambda phase transition in liquid helium. *Annals of Physics*, *47*(3), 565.

Fett, T., & Thun, G. (1998). Determination of room-temperature tensile creep of PZT. *Journal of Materials Science Letters*, *17*(22), 1929.

Fiebig, M., Pavlov, V. V., & Pisarev, R. V. (2005). Second-harmonic generation as a tool for studying electronic and magnetic structures of crystals: Review. *J. Opt. Soc. Am. B*, *22*(1), 96.

Floquet, N., Valot, C., Mesnier, M., Niepce, J., Normand, L., Thorel, A., & Kilaas, R. (1997). Ferroelectric domain walls in $BaTiO_3$: Fingerprints in XRPD diagrams and quantitative HRTEM image analysis. *Journal de Physique III*, *7*(6), 1105.

Foeth, M., Sfera, A., Stadelmann, P., & Buffat, P.-A. (1999). A comparison of HREM and weak beam transmission electron microscopy for the quantitative measurement of the thickness of ferroelectric domain walls. *Microscopy*, *48*(6), 717.

Fokker, A. D. (1914). Die mittlere energie rotierender elektrischer dipole im strahlungsfeld. *Annalen der Physik*, *348*(5), 810.

Fousek, J., & Janovec, V. (1969). The orientation of domain walls in twinned ferroelectric crystals. *Journal of Applied Physics*, *40*(1), 135.

Franken, P. A., Hill, A. E., Peters, C. W., & Weinreich, G. (1961). Generation of optical harmonics. *Phys. Rev. Lett.*, *7*, 118.

Franzbach, D. J., Gu, Y. J., Chen, L. Q., & Webber, K. G. (2012). Electric field-induced tetragonal to orthorhombic phase transitions

in [110]c-oriented $BaTiO_3$ single crystals. *Applied Physics Letters*, *101*(23), 232904.

Franzbach, D. J., Seo, Y.-H., Studer, A. J., Zhang, Y., Glaum, J., Daniels, J. E., Koruza, J., Benčan, A., Malič, B., & Webber, K. G. (2014). Electric-field-induced phase transitions in co-doped PZT at the morphotropic phase boundary. *Science and Technology of Advanced Materials*, *15*(1), 015010.

Frigo, M., & Johnson, S. G. (2005). The design and implementation of fftw3. *Proceedings of the IEEE*, *93*(2), 216.

Funaki, T. (1995). The scaling limit for a stochastic pde and the separation of phases. *Probability Theory and Related Fields*, *102*(2), 221.

Gao, P., Britson, J., Nelson, C. T., Jokisaari, J. R., Duan, C., Trassin, M., Baek, S.-H., Guo, H., Li, L., Wang, Y., Chu, Y.-H., Minor, A. M., Eom, C.-B., Ramesh, R., Chen, L.-Q., & Pan, X. (2014). Ferroelastic domain switching dynamics under electrical and mechanical excitations. *Nature communications*, *5*, 3801.

Gao, P., Nelson, C. T., Jokisaari, J. R., Baek, S.-H., Bark, C. W., Zhang, Y., Wang, E., Schlom, D. G., Eom, C.-B., & Pan, X. (2011). Revealing the role of defects in ferroelectric switching with atomic resolution. *Nature Communications*, *2*(1), 591.

Garcia, A., & Vanderbilt, D. (1998). Electromechanical behavior of batio3 from first principles. *Applied Physics Letters*, *72*(23), 2981.

Gauss, C. F. (1809). *Theoria motvs corporvm coelestivm in sectionibvs conicis solem ambientivm*. Sumtibus F. Perthes et IH Besser.

Genenko, Y. A., Zhukov, S., Yampolskii, S. V., Schütrumpf, J., Dittmer, R., Jo, W., Kungl, H., Hoffmann, M. J., & von Seggern, H. (2012). Universal polarization switching behavior of disordered ferroelectrics. *Advanced Functional Materials*, *22*(10), 2058.

Ghosez, P., & Rabe, K. M. (2000). Microscopic model of ferroelectricity in stress-free pbtio3 ultrathin films. *Applied Physics Letters*, *76*(19), 2767.

Gibbs, J. W. (1902). *Elementary principles in statistical mechanics: Developed with especial reference to the rational foundation of thermodynamics*. C. Scribner's sons.

Glinchuk, M. D., & Farhi, R. (1996). A random field theory based model for ferroelectric relaxors. *Journal of Physics: Condensed Matter*, *8*(37), 6985.

Goncalves-Ferreira, L., Redfern, S. A. T., Artacho, E., & Salje, E. K. H. (2008). Ferrielectric twin walls in $CaTiO_3$. *Phys. Rev. Lett.*, *101*, 097602.

Goo, E. K. W., Mishra, R. K., & Thomas, G. (1981). Electron microscopy study of the ferroelectric domains and domain wall structure in $PbZr_{0.52}Ti_{0.48}O_3$. *Journal of Applied Physics*, *52*(4), 2940.

Gorfman, S., Bokov, A. A., Davtyan, A., Reiser, M., Xie, Y., Ye, Z.-G., Zozulya, A. V., Sprung, M., Pietsch, U., & Gutt, C. (2018). Ferroelectric domain wall dynamics characterized with x-ray photon correlation spectroscopy. *Proceedings of the National Academy of Sciences*, *115*(29), E6680.

Gottlieb, D., & Orszag, S. A. (1977). *Numerical analysis of spectral methods: Theory and applications*. SIAM.

Gränicher, H., & Müller, K. (1971). On the nature of phase transitions and nomenclature. *Materials Research Bulletin*, *6*(10), 977.

Gruverman, A., Auciello, O., & Tokumoto, H. (1996). Scanning force microscopy for the study of domain structure in ferroelectric thin films. *Journal of Vacuum Science & Technology B: Microelectronics and Nanometer Structures Processing, Measurement, and Phenomena*, *14*(2), 602
doi: 10.1116/1.589143.

Gruverman, A., Rodriguez, B. J., Dehoff, C., Waldrep, J. D., Kingon, A. I., Nemanich, R. J., & Cross, J. S. (2005). Direct studies of domain switching dynamics in thin film ferroelectric capacitors. *Applied Physics Letters*, *87*(8), 082902.

Guillon, O., Thiébaud, F., Delobelle, P., & Perreux, D. (2004). Compressive creep of PZT ceramics: Experiments and modelling. *Journal of the European Ceramic Society*, *24*(9), 2547.

Guin, L., & Kochmann, D. (2022). A phase-field model for ferroelectrics with general kinetics. part i: Model formulation.

Guo, R., Wang, C.-A., & Yang, A. (2011). Effects of pore size and orientation on dielectric and piezoelectric properties of 1–3 type porous PZT ceramics. *Journal of the European Ceramic Society*, *31*(4), 605.

Gurtin, M. E. (1982). *An introduction to continuum mechanics*. Academic press.

Gurtin, M. E. (1987). Some results and conjectures in the gradient theory of phase transitions. In S. S. Antman, J. L. Ericksen, D. Kinderlehrer, & I. Müller (Eds.), *Metastability and incompletely posed problems* (pp. 135–146). Springer New York.

Güthner, P., & Dransfeld, K. (1992). Local poling of ferroelectric polymers by scanning force microscopy. *Applied Physics Letters*, *61*(9), 1137.

Guyonnet, J., Gaponenko, I., Gariglio, S., & Paruch, P. (2011). Conduction at domain walls in insulating $PbZr_{0.2}Ti_{0.8}O_3$ thin films. *Advanced Materials*, *23*(45), 5377.

Haertling, G. H. (1987). PLZT Electrooptic materials and applications—a review. *Ferroelectrics*, *75*(1), 25.

Hall, D. A. (2001). Review nonlinearity in piezoelectric ceramics. *Journal of Materials Science*, *36*(19), 4575.

Hall, D. A., Steuwer, A., Cherdhirunkorn, B., Mori, T., & Withers, P. J. (2004). A high energy synchrotron x-ray study of crystallographic texture and lattice strain in soft lead zirconate titanate ceramics. *Journal of Applied Physics*, *96*(8), 4245.

Hall, D. A., Steuwer, A., Cherdhirunkorn, B., Withers, P. J., & Mori, T. (2005). Texture of poled tetragonal $PbZr_{1-x}Ti_xO_3$ detected by synchrotron x-ray diffraction and micromechanics analysis. *Materials Science and Engineering: A*, *409*(1), 206.

Hayashi, M. (1972). Kinetics of domain wall motion in ferroelectric switching. i. general formulation. *Journal of the Physical Society of Japan*, *33*(3), 616.

Haynes, W. M. (2014). *Crc handbook of chemistry and physics*. CRC press.

Hoffmann, M. J., Hammer, M., Endriss, A., & Lupascu, D. C. (2001). Correlation between microstructure, strain behavior, and acoustic emission of soft PZT ceramics. *Acta Materialia*, *49*(7), 1301.

Hohenberg, P., & Kohn, W. (1964). Inhomogeneous electron gas. *Phys. Rev.*, *136*, B864.

Hooker, M. W. (1998). *Properties of* PZT*-based piezoelectric ceramics between -150° and 250° celsius* (tech. rep.). NASA. NASA/CR 208708.

Hooton, J. A., & Merz, W. J. (1955). Etch patterns and ferroelectric domains in $BaTiO_3$ single crystals. *Physical Review*, *98*(2), 409.

Huber, J. E., & Cocks, A. C. F. (2008). *A Variational Model of Ferroelectric Microstructure* (Vol. Smart Materials, Adaptive Structures and Intelligent Systems, Volume 1).

Huber, J., Fleck, N., Landis, C., & McMeeking, R. (1999). A constitutive model for ferroelectric polycrystals. *Journal of the Mechanics and Physics of Solids*, *47*(8), 1663.

Hubert, A., & Schäfer, R. (2008). *Magnetic domains: The analysis of magnetic microstructures*. Springer Science & Business Media.

Hwang, S., Lynch, C., & McMeeking, R. (1995). Ferroelectric/ferroelastic interactions and a polarization switching model. *Acta Metallurgica et Materialia*, *43*(5), 2073.

Idiart, M. I., & Bottero, C. J. (2020). A phenomenological constitutive theory for polycrystalline ferroelectric ceramics based on orientation distribution functions. *European Journal of Mechanics - A/Solids*, *82*, 103982.

Ihlefeld, J. F., Harris, D. T., Keech, R., Jones, J. L., Maria, J.-P., & Trolier-McKinstry, S. (2016). Scaling effects in perovskite ferroelectrics: Fundamental limits and process-structure-property relations. *Journal of the American Ceramic Society*, *99*(8), 2537 https://doi.org/10.1111/jace.14387.

Indergand, R. (2019). *Finite-temperature phase field simulations of ferroelectric ceramics* (Master's thesis). Swiss Federal Institute of Technology Zurich. Unpublished.

Indergand, R., Vidyasagar, A., Nadkarni, N., & Kochmann, D. M. (2020). A phase-field approach to studying the temperature-dependent ferroelectric response of bulk polycrystalline PZT. *Journal of the Mechanics and Physics of Solids*, *144*, 104098.

Iniguez, J., Ivantchev, S., Perez-Mato, J. M., & Garcia, A. (2001). Devonshire-landau free energy of $BaTiO_3$ from first principles. *Phys. Rev. B*, *63*, 144103.

Ishibashi, Y., & Takagi, Y. (1971). Note on ferroelectric domain switching. *Journal of the Physical Society of Japan*, *31*(2), 506.

Ivry, Y., Chu, D., Scott, J. F., & Durkan, C. (2011). Domains beyond the grain boundary. *Advanced Functional Materials*, *21*(10), 1827 https://doi.org/10.1002/adfm.201002142.

Jackson, J. D. (1999). Classical electrodynamics john wiley & sons. *Inc., New York*, *13*.

James, R. D. (2000). New materials from theory: Trends in the development of active materials. *International Journal of Solids and Structures*, *37*(1), 239.

Janovec, V., Grocky, M., Kopsky, V., & Kluiber, Z. (2004). On atomic displacements in 90° ferroelectric domain walls of tetragonal $BaTiO_3$ crystals. *Ferroelectrics*, *303*(1), 65.

Janovec, V., & Privratska, J. (2013). *International tables for crystallography* (Vol. 500). Springer.

Janovec, V., Richterová, L., & P[rcirc]ivratská, J. (1999). Polar properties of compatible ferroelastic domain walls. *Ferroelectrics*, *222*(1), 73.

Jesse, S., Rodriguez, B. J., Choudhury, S., Baddorf, A. P., Vrejoiu, I., Hesse, D., Alexe, M., Eliseev, E. A., Morozovska, A. N., Zhang, J., Chen, L.-Q., & Kalinin, S. V. (2008). Direct imaging of the spatial and

energy distribution of nucleation centres in ferroelectric materials. *Nature Materials*, *7*(3), 209.

Ji, D. W., & Kim, S.-J. (2013). Temperature-dependent ferroelastic switching of ferroelectric ceramics and evolution of linear material properties. *Acta Materialia*, *61*(1), 1.

Jia, C.-L., Urban, K. W., Alexe, M., Hesse, D., & Vrejoiu, I. (2011). Direct observation of continuous electric dipole rotation in flux-closure domains in ferroelectric $Pb(Ti, Zr)O_3$. *Science*, *331*(6023), 1420.

Jiang, J., Bai, Z. L., Chen, Z. H., He, L., Zhang, D. W., Zhang, Q. H., Shi, J. A., Park, M. H., Scott, J. F., Hwang, C. S., & Jiang, A. Q. (2018). Temporary formation of highly conducting domain walls for non-destructive read-out of ferroelectric domain-wall resistance switching memories. *Nature Materials*, *17*(1), 49.

Jo, J. Y., Han, H. S., Yoon, J.-G., Song, T. K., Kim, S.-H., & Noh, T. W. (2007). Domain switching kinetics in disordered ferroelectric thin films. *Phys. Rev. Lett.*, *99*, 267602.

Jo, J. Y., Yang, S. M., Kim, T., Lee, H. N., Yoon, J.-G., Park, S., Jo, Y., Jung, M., & Noh, T. W. (2009). Nonlinear dynamics of domain-wall propagation in epitaxial ferroelectric thin films. *Physical review letters*, *102*(4), 045701.

Johannes, M. D., & Singh, D. J. (2005). Crystal structure and electric field gradients of $PbZrO_3$ from density functional calculations. *Phys. Rev. B*, *71*, 212101.

Johnson-Wilke, R. L., Wilke, R. H. T., Wallace, M., Rajashekhar, A., Esteves, G., Merritt, Z., Jones, J. L., & Trolier-McKinstry, S. (2015). Ferroelectric/ferroelastic domain wall motion in dense and porous tetragonal lead zirconate titanate films. *IEEE Transactions on Ultrasonics, Ferroelectrics, and Frequency Control*, *62*(1), 46.

Jona, F., Shirane, G., Mazzi, F., & Pepinsky, R. (1957). X-ray and neutron diffraction study of antiferroelectric lead zirconate $PbZrO_3$. *Physical Review*, *105*(3), 849.

Jona, F., & Shirane, G. (1962). *Ferroelectric crystals, international series of monographs on solid state physics* (Vol. 1). Pergamon press Oxford, UK:

Jones, J. L., Hoffman, M., Daniels, J. E., & Studer, A. J. (2006). Direct measurement of the domain switching contribution to the dynamic piezoelectric response in ferroelectric ceramics. *Applied Physics Letters*, *89*(9), 092901
doi: 10.1063/1.2338756.

Jones, J. L., Iverson, B. J., & Bowman, K. J. (2007). Texture and anisotropy of polycrystalline piezoelectrics. *Journal of the American Ceramic Society*, *90*(8), 2297 https://doi.org/10.1111/j.1551-2916.2007.01820.x.

Jones, J. L., Slamovich, E. B., & Bowman, K. J. (2005). Domain texture distributions in tetragonal lead zirconate titanate by x-ray and neutron diffraction. *Journal of Applied Physics*, *97*(3), 034113 doi: 10.1063/1.1849821.

Jungk, T., Hoffmann, Á., Fiebig, M., & Soergel, E. (2010). Electrostatic topology of ferroelectric domains in $YMnO_3$. *Applied Physics Letters*, *97*(1), 012904.

Junquera, J., & Ghosez, P. (2003). Critical thickness for ferroelectricity in perovskite ultrathin films. *Nature*, *422*(6931), 506.

Kabel, M., Böhlke, T., & Schneider, M. (2014). Efficient fixed point and newton–krylov solvers for FFT-based homogenization of elasticity at large deformations. *Computational Mechanics*, *54*(6), 1497.

Kaeswurm, B., Schader, F., & Webber, K. (2018). Ferroelectric, ferroelastic, piezoelectric, and dielectric properties of lead zirconate titanate from–150 ° c to 350 ° c. *Ceramics International*, *44*(2), 2358.

Kalinin, S. V., Jesse, S., Rodriguez, B. J., Chu, Y. H., Ramesh, R., Eliseev, E. A., & Morozovska, A. N. (2008). Probing the role of single defects on the thermodynamics of electric-field induced phase transitions. *Phys. Rev. Lett.*, *100*, 155703.

Kampen, N. V. (2007). Chapter v - the master equation. In N. V. KAMPEN (Ed.), *Stochastic processes in physics and chemistry (third edition)* (Third Edition, pp. 96–133). Elsevier.

Kannan, V., & Kochmann, D. M. (2022). Rate-dependent ferroelectric switching in barium titanate ceramics from modified pund experiments. *Extreme Mechanics Letters*, *57*, 101898.

Kannan, V., Trassin, M., & Kochmann, D. M. (2022). Kinetics of ferroelectric switching in poled barium titanate ceramics: Effects of electrical cycling rate. *Materialia*, *25*, 101553.

Karma, A., & Rappel, W.-J. (1999). Phase-field model of dendritic sidebranching with thermal noise. *Phys. Rev. E*, *60*, 3614.

Keve, E. T., & Bye, K. L. (1975). Phase identification and domain structure in plzt ceramics. *Journal of Applied Physics*, *46*(2), 810.

Khachaturyan, R., Zhukov, S., Schultheiß, J., Galassi, C., Reimuth, C., Koruza, J., von Seggern, H., & Genenko, Y. A. (2016). Polarization-switching dynamics in bulk ferroelectrics with isometric and ori-

ented anisometric pores. *Journal of Physics D: Applied Physics*, *50*(4), 045303.

Kim, K. L., Tsou, N. T., & Huber, J. E. (2013). Domain evolution processes during poling of a near-morphotropic $Pb(Ti, Zr)O_3$ ceramic. *Journal of Applied Physics*, *113*(19), 194104.

Kinase, W., & Takahasi, H. (1957). On the 180°-type domain wall of batio3 crystal. *Journal of the Physical Society of Japan*, *12*(5), 464 doi: 10.1143/JPSJ.12.464.

Kittel, C. (1946). Theory of the structure of ferromagnetic domains in films and small particles. *Phys. Rev.*, *70*, 965.

Kohn, R. V., Otto, F., Reznikoff, M. G., & Vanden-Eijnden, E. (2007). Action minimization and sharp-interface limits for the stochastic allen-cahn equation. *Communications on Pure and Applied Mathematics: A Journal Issued by the Courant Institute of Mathematical Sciences*, *60*(3), 393.

Kohn, W., & Sham, L. J. (1965). Self-consistent equations including exchange and correlation effects. *Phys. Rev.*, *140*, A1133.

Kolmogoroff, A. (1931). Über die analytischen methoden in der wahrscheinlichkeitsrechnung. *Mathematische Annalen*, *104*(1), 415.

Kolosov, O., Gruverman, A., Hatano, J., Takahashi, K., & Tokumoto, H. (1995). Nanoscale visualization and control of ferroelectric domains by atomic force microscopy. *Physical Review Letters*, *74*(21), 4309.

Kontsos, A., & Landis, C. M. (2009). Computational modeling of domain wall interactions with dislocations in ferroelectric crystals. *International Journal of Solids and Structures*, *46*(6), 1491.

Koyama, T. (2008). Phase-field modeling of microstructure evolutions in magnetic materials. *Science and Technology of Advanced Materials*, *9*(1), 013006.

Kramers, H. A. (1940). Brownian motion in a field of force and the diffusion model of chemical reactions. *Physica*, *7*(4), 284.

Lai, B.-K., Ponomareva, I., Kornev, I., Bellaiche, L., & Salamo, G. (2007). Thickness dependency of 180° stripe domains in ferroelectric ultrathin films: A first-principles-based study. *Applied Physics Letters*, *91*(15), 152909.

Lambeck, P. V., & Jonker, G. H. (1986). The nature of domain stabilization in ferroelectric perovskites. *Journal of Physics and Chemistry of Solids*, *47*(5), 453.

Landau, L. (1937). On the theory of phase transitions (in russian). *Zh. Eksp. Teor. Fiz.*, *7*.

Landau, L., & Lifshitz, E. (1935). On the theory of the dispersion of magnetic permeability in ferromagnetic bodies. *Phys. Z. Sowjetunion*, *8*, 153.

Landau, L. D. (1908). *Collected papers of l.d. landau* (D. ter Haar, Ed.; 1th). Oxford: Pergamon Press.

Landis, C. M. (2002). Fully coupled, multi-axial, symmetric constitutive laws for polycrystalline ferroelectric ceramics. *Journal of the Mechanics and Physics of Solids*, *50*(1), 127.

Landis, C. M. (2004). Non-linear constitutive modeling of ferroelectrics. *Current Opinion in Solid State and Materials Science*, *8*(1), 59.

Langevin, P. (1908). Sur la théorie du mouvement brownien. *Compt. Rendus*, *146*, 530.

Laplace, P.-S. (1774). Mémoire sur la probabilité des causes par les événements. *Mémoires de l'Académie Royale des Sciences de Paris (Savants étrangers)*, *6*, 621.

Lebensohn, R. A., Kanjarla, A. K., & Eisenlohr, P. (2012). An elasto-viscoplastic formulation based on fast Fourier transforms for the prediction of micromechanical fields in polycrystalline materials. *International Journal of Plasticity*, *32-33*, 59.

Lebensohn, R. A., & Rollett, A. D. (2020). Spectral methods for full-field micromechanical modelling of polycrystalline materials. *Computational Materials Science*, *173*, 109336.

le Graverend, J.-B., Wojnar, C. S., & Kochmann, D. M. (2015). Broadband electromechanical spectroscopy: Characterizing the dynamic mechanical response of viscoelastic materials under temperature and electric field control in a vacuum environment. *Journal of Materials Science*, *50*(10), 3656.

Li, B., Li, G., Yin, Q., Zhu, Z., Ding, A., & Cao, W. (2005). Pinning and depinning mechanism of defect dipoles in PMnN–PZT ceramics. *Journal of Physics D: Applied Physics*, *38*(8), 1107.

Li, J., & Liu, D. (2004). On ferroelectric crystals with engineered domain configurations. *Journal of the Mechanics and Physics of Solids*, *52*(8), 1719.

Li, Y., Cross, L., & Chen, L. (2005). A phenomenological thermodynamic potential for $BaTiO_3$ single crystals. *Journal of Applied Physics*, *98*(6), 064101.

Li, Z., Grimsditch, M., Foster, C., & Chan, S.-K. (1996). Dielectric and elastic properties of ferroelectric materials at elevated temperature [Proceeding of the 3rd Williamsburg Workshop on Fundamental

Experiments on Ferroelectrics]. *Journal of Physics and Chemistry of Solids*, *57*(10), 1433.

Li, Z., Kovachki, N., Azizzadenesheli, K., Liu, B., Bhattacharya, K., Stuart, A., & Anandkumar, A. (2020). Fourier neural operator for parametric partial differential equations.

Lines, M. E., & Glass, A. M. (2001). *Principles and applications of ferroelectrics and related materials*. Oxford university press.

Liu, N., & Su, Y. (2014). The grain-size-dependent behaviors of nano-grained ferroelectric polycrystals: A phase-field study. *Acta Mechanica*, *225*(4), 1335.

Liu, S., Grinberg, I., & Rappe, A. M. (2016). Intrinsic ferroelectric switching from first principles. *Nature*, *534*(7607), 360.

Logé, R. E., & Suo, Z. (1996). Nonequilibrium thermodynamics of ferroelectric domain evolution. *Acta Materialia*, *44*(8), 3429.

Lohse, O., Grossmann, M., Boettger, U., Bolten, D., & Waser, R. (2001). Relaxation mechanism of ferroelectric switching in pb (zr, ti) o 3 thin films. *Journal of Applied Physics*, *89*(4), 2332.

Lu, W., Fang, D.-N., Li, C., & Hwang, K.-C. (1999). Nonlinear electric–mechanical behavior and micromechanics modelling of ferroelectric domain evolution. *Acta Materialia*, *47*(10), 2913.

Lummen, T. T. A., Gu, Y., Wang, J., Lei, S., Xue, F., Kumar, A., Barnes, A. T., Barnes, E., Denev, S., Belianinov, A., Holt, M., Morozovska, A. N., Kalinin, S. V., Chen, L.-Q., & Gopalan, V. (2014). Thermotropic phase boundaries in classic ferroelectrics. *Nature Communications*, *5*(1), 3172.

Lundh, J. S., Zhu, W., Song, Y., Ko, S. W., Fragkiadakis, C., Mardilovich, P., Trolier-McKinstry, S., & Choi, S. (2020). Local measurements of domain wall-induced self-heating in released $PbZr_{0.52}Ti_{0.48}O_3$ films. *Journal of Applied Physics*, *128*(21), 214102.

Mante, A., & Volger, J. (1967). The thermal conductivity of $BaTiO_3$ in the neighbourhood of its ferroelectric transition temperatures. *Physics Letters A*, *24*(3), 139.

Manz, S., Matsubara, M., Lottermoser, T., Büchi, J., Iyama, A., Kimura, T., Meier, D., & Fiebig, M. (2016). Reversible optical switching of antiferromagnetism in $TbMnO_3$. *Nature Photonics*, *10*(10), 653.

Marincel, D. M., Zhang, H., Jesse, S., Belianinov, A., Okatan, M. B., Kalinin, S. V., Rainforth, W. M., Reaney, I. M., Randall, C. A., & Trolier-McKinstry, S. (2015). Domain wall motion across various grain

boundaries in ferroelectric thin films. *Journal of the American Ceramic Society*, *98*(6), 1848.

Marincel, D. M., Zhang, H. R., Britson, J., Belianinov, A., Jesse, S., Kalinin, S. V., Chen, L. Q., Rainforth, W. M., Reaney, I. M., Randall, C. A., & Trolier-McKinstry, S. (2015). Domain pinning near a single-grain boundary in tetragonal and rhombohedral lead zirconate titanate films. *Phys. Rev. B*, *91*, 134113.

Marsaglia, G., & Bray, T. A. (1964). A convenient method for generating normal variables. *SIAM Review*, *6*(3), 260.

Marsilius, M., Webber, K. G., Aulbach, E., & Granzow, T. (2010). Comparison of the temperature-dependent ferroelastic behavior of hard and soft lead zirconate titanate ceramics. *Journal of the American Ceramic Society*, *93*(9), 2850.

Marton, P., Klic, A., Pasciak, M., & Hlinka, J. (2017). First-principles-based landau-devonshire potential for $BiFeO_3$. *Phys. Rev. B*, *96*, 174110.

Mason, W. P. (1948). Electrostrictive effect in barium titanate ceramics. *Phys. Rev.*, *74*, 1134.

McGilly, L. J., Schilling, A., & Gregg, J. M. (2010). Domain bundle boundaries in single crystal batio3 lamellae: Searching for naturally forming dipole flux-closure/quadrupole chains. *Nano Letters*, *10*(10), 4200
doi: 10.1021/nl102566y.

McMeeking, R. M., & Landis, C. M. (2002). A phenomenological multiaxial constitutive law for switching in polycrystalline ferroelectric ceramics. *International Journal of Engineering Science*, *40*(14), 1553.

McQuaid, R. G. P., McGilly, L. J., Sharma, P., Gruverman, A., & Gregg, J. M. (2011). Mesoscale flux-closure domain formation in single-crystal $BaTiO_3$. *Nature Communications*, *2*(1), 404.

Meier, D., Seidel, J., Cano, A., Delaney, K., Kumagai, Y., Mostovoy, M., Spaldin, N. A., Ramesh, R., & Fiebig, M. (2012). Anisotropic conductance at improper ferroelectric domain walls. *Nature Materials*, *11*(4), 284.

Meier, D. (2015). Functional domain walls in multiferroics. *Journal of Physics: Condensed Matter*, *27*(46), 463003.

Meng, Q., Han, M.-G., Tao, J., Xu, G., Welch, D. O., & Zhu, Y. (2015). Velocity of domain-wall motion during polarization reversal in ferroelectric thin films: Beyond merz's law. *Physical Review B*, *91*(5), 054104.

Mercadelli, E., Sanson, A., & Galassi, C. (2010). Porous piezoelectric ceramics. In E. Suaste-Gomez (Ed.), *Piezoelectric ceramics*. IntechOpen.

Merz, W. J. (1954). Domain formation and domain wall motions in ferroelectric $BaTiO_3$ single crystals. *Phys. Rev.*, *95*, 690.

Merz, W. J. (1956). Switching time in ferroelectric $BaTiO_3$ and its dependence on crystal thickness. *J. Appl. Phys.*, *27*(8), 938.

Meyer, B., & Vanderbilt, D. (2002). Ab initio study of ferroelectric domain walls in $PbTiO_3$. *Phys. Rev. B*, *65*, 104111.

Michel, J., Moulinec, H., & Suquet, P. (2000). A computational method based on augmented lagrangians and fast fourier transforms for composites with high contrast. *CMES - Computer Modeling in Engineering and Sciences*, *1*(2), 79.

Miehe, C., & Rosato, D. (2011). A rate-dependent incremental variational formulation of ferroelectricity [Theoretical-Read 05/14/13]. *International Journal of Engineering Science*, *49*(6), 466.

Miehe, C., Schröder, J., & Becker, M. (2002). Computational homogenization analysis in finite elasticity: Material and structural instabilities on the micro- and macro-scales of periodic composites and their interaction. *Computer Methods in Applied Mechanics and Engineering*, *191*(44), 4971.

Miller, R. C., & Weinreich, G. (1960). Mechanism for the sidewise motion of 180 domain walls in barium titanate. *Physical Review*, *117*(6), 1460.

Mitsui, T., & Furuichi, J. (1953). Domain structure of rochelle salt and kH_2pO_4. *Phys. Rev.*, *90*, 193.

Mohan, C., Seeger, M., Kronmüller, H., Murugaraj, P., & Maier, J. (1998). Critical behaviour near the ferromagnetic–paramagnetic phase transition in lao.8sro.2mno3. *Journal of Magnetism and Magnetic Materials*, *183*(3), 348.

Moulinec, H., & Suquet, P. (1998). A numerical method for computing the overall response of nonlinear composites with complex microstructure. *Computer Methods in Applied Mechanics and Engineering*, *157*(1-2), 69.

Moulinec, H., & Suquet, P. (2003). Comparison of FFT-based methods for computing the response of composites with highly contrasted mechanical properties. *Physica B: Condensed Matter*, *338*(1-4), 58.

Moyal, J. (1949). Stochastic processes and statistical physics. *Journal of the Royal Statistical Society. Series B (Methodological)*, *11*(2), 150.

Muller, M. E. (1958). An inverse method for the generation of random normal deviates on large-scale computers. *Mathematical Tables and Other Aids to Computation*, *12*(63), 167.

Mulvmill, M. L., Uchino, K., Li, Z., & Cao, W. (1996). In-situ observation of the domain configurations during the phase transitions in barium titanate. *Philosophical Magazine B*, *74*(1), 25.

N. Lawless, W., & Fousek, J. (1970). Small-signal permittivity of the stationary (100)-180° domain wall in batio3. *Journal of the Physical Society of Japan*, *28*(2), 419.

Nakatani, N. (1973). Ferroelectric domain structure of tri-glycine sulfate observed using a scanning electron microscope. *Japanese Journal of Applied Physics*, *12*(11), 1723.

Nakatani, N. (1979). Microscopic structure of cleavage surface of ferroelectric tri-glycine sulfate. *Japanese Journal of Applied Physics*, *18*(3), 491.

Nataf, G. F., Guennou, M., Gregg, J. M., Meier, D., Hlinka, J., Salje, E. K. H., & Kreisel, J. (2020). Domain-wall engineering and topological defects in ferroelectric and ferroelastic materials. *Nature Reviews Physics*, *2*(11), 634.

Nataf, G. F., Guennou, M., Kreisel, J., Hicher, P., Haumont, R., Aktas, O., Salje, E. K. H., Tortech, L., Mathieu, C., Martinotti, D., & Barrett, N. (2017). Control of surface potential at polar domain walls in a nonpolar oxide. *Phys. Rev. Materials*, *1*, 074410.

Natterman, T. (1983). Interface phenomenology, dipolar interaction, and the dimensionality dependence of the incommensurate-commensurate transition. *Journal of Physics C: Solid State Physics*, *16*(21), 4125.

Nattermann, T. (1987). Interface roughening in systems with quenched random impurities. *Europhysics Letters (EPL)*, *4*(11), 1241.

Nattermann, T., Shapir, Y., & Vilfan, I. (1990). Interface pinning and dynamics in random systems. *Phys. Rev. B*, *42*, 8577.

Nelson, C. T., Winchester, B., Zhang, Y., Kim, S.-J., Melville, A., Adamo, C., Folkman, C. M., Baek, S.-H., Eom, C.-B., Schlom, D. G., Chen, L.-Q., & Pan, X. (2011). Spontaneous vortex nanodomain arrays at ferroelectric heterointerfaces. *Nano Letters*, *11*(2), 828 doi: 10.1021/nl1041808.

Nye, J. F., et al. (1985). *Physical properties of crystals: Their representation by tensors and matrices*. Oxford university press.

Ojovan, M. I., & Lee, W. E. (2006). Topologically disordered systems at the glass transition. *Journal of Physics: Condensed Matter*, *18*(50), 11507.

Olsen, R. B., Bruno, D. A., & Briscoe, J. M. (1985). Pyroelectric conversion cycles. *Journal of applied physics*, *58*(12), 4709.

Özdemir, Ö., Xu, S., & Dunlop, D. J. (1995). Closure domains in magnetite. *Journal of Geophysical Research: Solid Earth*, *100*(B2), 2193 https://doi.org/10.1029/94JB02874.

Panagiotou, A. D., Curtin, M. W., Toki, H., Scott, D. K., & Siemens, P. J. (1984). Experimental evidence for a liquid-gas phase transition in nuclear systems. *Phys. Rev. Lett.*, *52*, 496.

Park, B.-E., Ishiwara, H., Okuyama, M., Sakai, S., & Yoon, S.-M. (2016). *Ferroelectric-gate field effect transistor memories*. Springer.

Parravano, G. d. (1952). Ferroelectric transitions and heterogenous catalysis. *The Journal of Chemical Physics*, *20*(2), 342.

Paruch, P., Giamarchi, T., Tybell, T., & Triscone, J.-M. (2006). Nanoscale studies of domain wall motion in epitaxial ferroelectric thin films. *Journal of applied physics*, *100*(5), 051608.

PICeramic. (2020). Pi ceramic datasheet.

Picht, G., Khansur, N. H., Webber, K. G., Kungl, H., Hoffmann, M. J., & Hinterstein, M. (2020). Grain size effects in donor doped lead zirconate titanate ceramics. *Journal of Applied Physics*, *128*(21), 214105.

Pirc, R., & Blinc, R. (1999). Spherical random-bond–random-field model of relaxor ferroelectrics. *Phys. Rev. B*, *60*, 13470.

Planck, M. (1917). Uber einen satz der statistischen dynamik and seine erweiterung in der quantetheorie. *Sitzber. Preuss. Akad. Wiss*, *45*, 324.

Pramanick, A., Damjanovic, D., Daniels, J. E., Nino, J. C., & Jones, J. L. (2011). Origins of electro-mechanical coupling in polycrystalline ferroelectrics during subcoercive electrical loading. *Journal of the American Ceramic Society*, *94*(2), 293.

Prosandeev, S., & Bellaiche, L. (2007). Asymmetric screening of the depolarizing field in a ferroelectric thin film. *Phys. Rev. B*, *75*, 172109.

Puchberger, S., Soprunyuk, V., Schranz, W., Tröster, A., Roleder, K., Majchrowski, A., Carpenter, M. A., & Salje, E. K. H. (2017). The noise of many needles: Jerky domain wall propagation in $PbZrO_3$ and $LaAlO_3$. *APL Materials*, *5*(4), 046102.

Qiao, L., & Radovitzky, R. (2016). Computational modeling of size-dependent superelasticity of shape memory alloys [Special Issue in honor of Michael Ortiz]. *Journal of the Mechanics and Physics of Solids*, *93*, 93.

Rabe, K. M., & Joannopoulos, J. D. (1987). Ab initio determination of a structural phase transition temperature. *Phys. Rev. Lett.*, *59*, 570.

Radhakrishnan, B., Gorti, S. B., Turner, J. A., Acharya, R., Sharon, J. A., Staroselsky, A., & El-Wardany, T. (2019). Phase field simulations of microstructure evolution in in718 using a surrogate Ni − Fe − Nb alloy during laser powder bed fusion. *Metals*, *9*(1), 14.

Raissi, M., Perdikaris, P., & Karniadakis, G. (2019). Physics-informed neural networks: A deep learning framework for solving forward and inverse problems involving nonlinear partial differential equations. *Journal of Computational Physics*, *378*, 686.

Randall, C. A., Barber, D. J., & Whatmore, R. W. (1987). Ferroelectric domain configurations in a modified-pzt ceramic. *Journal of Materials Science*, *22*(3), 925.

Randall, C. A., Kim, N., Kucera, J.-P., Cao, W., & Shrout, T. R. (1998). Intrinsic and extrinsic size effects in fine-grained morphotropic-phase-boundary lead zirconate titanate ceramics. *Journal of the American Ceramic Society*, *81*(3), 677 https://doi.org/10.1111/j.1151-2916.1998.tb02389.x.

Regensburger, H., Vollmer, R., & Kirschner, J. (2000). Time-resolved magnetization-induced second-harmonic generation from the Ni(110) surface. *Phys. Rev. B*, *61*, 14716.

Resta, R. (2003). Ab initio simulation of the properties of ferroelectric materials. *Modelling and Simulation in Materials Science and Engineering*, *11*(4), 69.

Ricote, J., Whatmore, R. W., & Barber, D. J. (1999). Studies of the ferroelectric domain configuration and polarization of rhombohedral PZT ceramics. *Journal of Physics: Condensed Matter*, *12*(3), 323.

Riemer, L. M., Lalitha, K., Jiang, X., Liu, N., Dietz, C., Stark, R. W., Groszewicz, P. B., Buntkowsky, G., Chen, J., Zhang, S.-T., Rödel, J., & Koruza, J. (2017). Stress-induced phase transition in lead-free relaxor ferroelectric composites. *Acta Materialia*, *136*, 271.

Robinson, G. Y., & White, R. M. (1967). Scanning electron microscopy of ferroelectric domains in barium titanate. *Applied Physics Letters*, *10*(11), 320.

Rödel, J. (2007). Effective intrinsic linear properties of laminar piezoelectric composites and simple ferroelectric domain structures. *Mechanics of Materials*, *39*(4), 302.

Rodriguez, B. J., Chu, Y. H., Ramesh, R., & Kalinin, S. V. (2008). Ferroelectric domain wall pinning at a bicrystal grain boundary in bismuth ferrite. *Applied Physics Letters*, *93*(14), Article 142901.

Roitburd, A. L. (1976). Equilibrium structure of epitaxial layers. *physica status solidi (a)*, *37*(1), 329 https://doi.org/10.1002/pssa.2210370141.

Rojac, T., Bencan, A., Drazic, G., Sakamoto, N., Ursic, H., Jancar, B., Tavcar, G., Makarovic, M., Walker, J., Malic, B., & Damjanovic, D. (2017). Domain-wall conduction in ferroelectric bifeo3 controlled by accumulation of charged defects. *Nature Materials*, *16*(3), 322.

Rojac, T., Drnovsek, S., Bencan, A., Malic, B., & Damjanovic, D. (2016). Role of charged defects on the electrical and electromechanical properties of rhombohedral $Pb(Zr, Ti)O_3$ with oxygen octahedra tilts. *Phys. Rev. B*, *93*, 014102.

Rolland, J., Bouchet, F., & Simonnet, E. (2016). Computing transition rates for the 1-d stochastic ginzburg–landau–allen–cahn equation for finite-amplitude noise with a rare event algorithm. *Journal of Statistical Physics*, *162*(2), 277.

Rondinelli, J. M., & Spaldin, N. A. (2011). Structure and properties of functional oxide thin films: Insights from electronic-structure calculations. *Advanced Materials*, *23*(30), 3363.

Ryser, M. D., Nigam, N., & Tupper, P. F. (2012). On the well-posedness of the stochastic allen–cahn equation in two dimensions. *Journal of Computational Physics*, *231*(6), 2537.

Salje, E. K. H. (1990). Phase transitions in ferroelastic and co-elastic crystals. *Ferroelectrics*, *104*(1), 111.

Salje, E. K. H. (2012). Ferroelastic materials. *Annual Review of Materials Research*, *42*(1), 265.

Salje, E. K. H., Aktas, O., Carpenter, M. A., Laguta, V. V., & Scott, J. F. (2013). Domains within domains and walls within walls: Evidence for polar domains in cryogenic $SrTiO_3$. *Phys. Rev. Lett.*, *111*, 247603.

Salje, E. K. H., & Ishibashi, Y. (1996). Mesoscopic structures in ferroelastic crystals: Needle twins and right-angled domains. *Journal of Physics Condensed Matter*, *8*(44), 8477.

Samara, G. A. (1971). Pressure and temperature dependence of the dielectric properties and phase transitions of the ferroelectric perovskites: $PbTiO_3$ And $BaTiO_3$. *Ferroelectrics*, *2*(1), 277.

Sanchez-Santolino, G., Tornos, J., Hernandez-Martin, D., Beltran, J. I., Munuera, C., Cabero, M., Perez-Muñoz, A., Ricote, J., Mompean, F., Garcia-Hernandez, M., Sefrioui, Z., Leon, C., Pennycook, S. J., Muñoz, M. C., Varela, M., & Santamaria, J. (2017). Resonant electron

tunnelling assisted by charged domain walls in multiferroic tunnel junctions. *Nature Nanotechnology*, *12*(7), 655.

Sapriel, J. (1975). Domain-wall orientations in ferroelastics. *Phys. Rev. B*, *12*, 5128.

Saurenbach, F., & Terris, B. D. (1990). Imaging of ferroelectric domain walls by force microscopy. *Applied Physics Letters*, *56*(17), 1703.

Savage, A., & Miller, R. C. (1960). Temperature dependence of the velocity of sidewise 180° domain-wall motion in $BaTiO_3$. *Journal of Applied Physics*, *31*(9), 1546.

Schmitt, L. A., Schönau, K. A., Theissmann, R., Fuess, H., Kungl, H., & Hoffmann, M. J. (2007). Composition dependence of the domain configuration and size in $Pb(Zr_{1-x}Ti_x)O_3$ ceramics. *Journal of applied physics*, *101*(7), 074107.

Schoenherr, P., Giraldo, L. M., Lilienblum, M., Trassin, M., Meier, D., & Fiebig, M. (2017). Magnetoelectric force microscopy on antiferromagnetic 180° domains in Cr_2O_3. *Materials*, *10*(9).

Schönau, K. A., Knapp, M., Kungl, H., Hoffmann, M. J., & Fuess, H. (2007). In situ synchrotron diffraction investigation of morphotropic $Pb[Zr_{1-x}Ti_x]O_3$ under an applied electric field. *Phys. Rev. B*, *76*, 144112.

Schrade, D., Müller, R., & Gross, D. (2013). On the physical interpretation of material parameters in phase field models for ferroelectrics. *Archive of Applied Mechanics*, *83*(10), 1393.

Schranz, W., Rychetsky, I., & Hlinka, J. (2019). Polarity of domain boundaries in nonpolar materials derived from order parameter and layer group symmetry. *Phys. Rev. B*, *100*, 184105.

Schröder, J. (2009). Derivation of the localization and homogenization conditions for electro-mechanically coupled problems [Proceedings of the 18th International Workshop on Computational Mechanics of Materials IWCMM-18]. *Computational Materials Science*, *46*(3), 595.

Schultheiß, J., Kungl, H., & Koruza, J. (2019a). Influence of crystallographic structure on polarization reversal in polycrystalline ferroelectric/ferroelastic materials. *Journal of Applied Physics*, *125*(17), 174101.

Schultheiß, J., Roscow, J. I., & Koruza, J. (2019b). Orienting anisometric pores in ferroelectrics: Piezoelectric property engineering through local electric field distributions. *Phys. Rev. Materials*, *3*, 084408.

Schultheiß, J., Liu, L., Kungl, H., Weber, M., Venkataraman, L. K., Checchia, S., Damjanovic, D., Daniels, J. E., & Koruza, J. (2018). Revealing

the sequence of switching mechanisms in polycrystalline ferroelectric/ferroelastic materials. *Acta Materialia*, *157*, 355.

Scott, J. F., Salje, E. K. H., & Carpenter, M. A. (2012). Domain wall damping and elastic softening in $SrTiO_3$: Evidence for polar twin walls. *Phys. Rev. Lett.*, *109*, 187601.

Seidel, J., Maksymovych, P., Batra, Y., Katan, A., Yang, S.-Y., He, Q., Baddorf, A. P., Kalinin, S. V., Yang, C.-H., Yang, J.-C., Chu, Y.-H., Salje, E. K. H., Wormeester, H., Salmeron, M., & Ramesh, R. (2010). Domain wall conductivity in la-doped $BiFeO_3$. *Phys. Rev. Lett.*, *105*, 197603.

Seidel, J., Martin, L. W., He, Q., Zhan, Q., Chu, Y. .-., Rother, A., Hawkridge, M. E., Maksymovych, P., Yu, P., Gajek, M., Balke, N., Kalinin, S. V., Gemming, S., Wang, F., Catalan, G., Scott, J. F., Spaldin, N. A., Orenstein, J., & Ramesh, R. (2009). Conduction at domain walls in oxide multiferroics. *Nature Materials*, *8*(3), 229.

Seidel, J. (2012). Domain walls as nanoscale functional elements. *The Journal of Physical Chemistry Letters*, *3*(19), 2905.

Seo, Y.-H., Franzbach, D. J., Koruza, J., Ben čan, A., Mali č, B., Kosec, M., Jones, J. L., & Webber, K. G. (2013). Nonlinear stress-strain behavior and stress-induced phase transitions in soft $PbZr_{1-x}Ti_xO_3$ at the morphotropic phase boundary. *Phys. Rev. B*, *87*, 094116.

Sepliarsky, M., Phillpot, S. R., Wolf, D., Stachiotti, M. G., & Migoni, R. L. (2001). Long-ranged ferroelectric interactions in perovskite superlattices. *Phys. Rev. B*, *64*, 060101.

Sepliarsky, M., Wu, Z., Asthagiri, A., & Cohen, R. E. (2004). Atomistic model potential for pbtio3 and pmn by fitting first principles results. *Ferroelectrics*, *301*(1), 55.

Seshadri, R., & Hill, N. A. (2001). Visualizing the role of Bi 6s "lone pairs"in the off-center distortion in ferromagnetic $BiMnO_3$. *Chemistry of Materials*, *13*(9), 2892
doi: 10.1021/cm010090m.

Shang, S., Guo, Z., & Han, Z. (2016). On the kinetics of dendritic sidebranching: A three dimensional phase field study. *Journal of Applied Physics*, *119*(16), 164305.

Shardlow, T. (2000). Stochastic perturbations of the allen-cahn equation. *Electronic Journal of Differential Equations*, (47), 1.

Sharma, P., Zhang, Q., Sando, D., Lei, C. H., Liu, Y., Li, J., Nagarajan, V., & Seidel, J. (2017). Nonvolatile ferroelectric domain wall memory. *Science Advances*, *3*(6), e1700512.

Shenoy, V. B., Xiao, Y., & Bhattacharya, K. (2012). Effect of doping on polarization profiles and switching in semiconducting ferroelectric thin films. *Journal of Applied Physics*, *111*(8), 084105.

Sheppard, D., Terrell, R., & Henkelman, G. (2008). Optimization methods for finding minimum energy paths. *The Journal of chemical physics*, *128*(13), 134106.

Shilo, D., Burcsu, E., Ravichandran, G., & Bhattacharya, K. (2007). A model for large electrostrictive actuation in ferroelectric single crystals [Physics and Mechanics of Advanced Materials]. *International Journal of Solids and Structures*, *44*(6), 2053.

Shiojiri, M., Isshiki, T., Saijo, H., Tsujikura, M., Nakada, A., Nakano, Y., Ikeda, M., & Nomura, T. (1992). High-resolution electron microscopy study of domain boundaries and dislocation loops in $BaTiO_3$ crystals. *Physica Status Solidi A*, *129*(2), 353.

Shirane, G., & Hoshino, S. (1954). X-ray study of phase transitions in $PbZrO_3$ containing Ba or Sr. *Acta Crystallographica*, *7*(2), 203.

Shu, Y. C., & Bhattacharya, K. (2001). Domain patterns and macroscopic behaviour of ferroelectric materials. *Philosophical Magazine B*, *81*(12), 2021
doi: 10.1080/13642810108208556.

Simons, H., Haugen, A. B., Jakobsen, A. C., Schmidt, S., Stöhr, F., Majkut, M., Detlefs, C., Daniels, J. E., Damjanovic, D., & Poulsen, H. F. (2018). Long-range symmetry breaking in embedded ferroelectrics. *Nature Materials*, *17*(9), 814.

Skinner, D., Newnham, R., & Cross, L. (1978). Flexible composite transducers. *Materials Research Bulletin*, *13*(6), 599.

Sluka, T., Tagantsev, A. K., Damjanovic, D., Gureev, M., & Setter, N. (2012). Enhanced electromechanical response of ferroelectrics due to charged domain walls. *Nature Communications*, *3*(1), 748.

Slutsker, J., Artemev, A., & Roytburd, A. (2008). Phase-field modeling of domain structure of confined nanoferroelectrics. *Phys. Rev. Lett.*, *100*, 087602.

Snoeck, E., Normand, L., Thorel, A., & Roucau, C. (1994). Electron microscopy study of ferroelastic and ferroelectric domain wall motions induced by the in situ application of an electric field in $BaTiO_3$. *Phase Transitions*, *46*(2), 77.

Spaldin, N. A. (2004). Fundamental size limits in ferroelectricity. *Science*, *304*(5677), 1606
doi: 10.1126/science.1099822.

Spaldin, N. A., & Fiebig, M. (2005). The renaissance of magnetoelectric multiferroics. *Science*, *309*(5733), 391.

Stadler, H. L., & Zachmanidis, P. J. (1964). Temperature dependence of 180° domain wall velocity in $BaTiO_3$. *Journal of Applied Physics*, *35*(10), 2895.

Stark, S., Neumeister, P., & Balke, H. (2016). A hybrid phenomenological model for ferroelectroelastic ceramics. part i: Single phased materials. *Journal of the Mechanics and Physics of Solids*, *95*, 774.

Stemmer, S., Streiffer, S. K., Ernst, F., & Rüuhle, M. (1995). Atomistic structure of 90° domain walls in ferroelectric $PbTiO_3$ thin films. *Philosophical Magazine A*, *71*(3), 713.

Su, Y., & Landis, C. M. (2007). Continuum thermodynamics of ferroelectric domain evolution: Theory, finite element implementation, and application to domain wall pinning. *J. Mech. Phys. Solids*, *55*, 280.

Surowiak, Z., Mukhortov, V. M., & Dudkevich, V. P. (1993). Phase transitions and domain structure in heteroepitaxial ferroelectric thin films. *Ferroelectrics*, *139*(1), 1.

Suryanarayana, P., & Bhattacharya, K. (2012). Evolution of polarization and space charges in semiconducting ferroelectrics. *Journal of Applied Physics*, *111*(3), 034109.

Tagantsev, A. K., Stolichnov, I., Setter, N., Cross, J. S., & Tsukada, M. (2002). Non-kolmogorov-avrami switching kinetics in ferroelectric thin films. *Physical Review B*, *66*(21), 214109.

Tagantsev, A. K., Cross, L. E., & Fousek, J. (2010). *Domains in ferroic crystals and thin films* (1th, Vol. 13). Springer.

Tan, L., & Bhattacharya, K. (2016). Length scales and pinning of interfaces. *Philosophical Transactions of the Royal Society A: Mathematical, Physical and Engineering Sciences*, *374*(2066), 20150167.

Tan, W. L., Faber, K. T., & Kochmann, D. M. (2019). In-situ observation of evolving microstructural damage and associated effective electromechanical properties of PZT during bipolar electrical fatigue. *Acta Materialia*, *164*, 704.

Tan, W. L., & Kochmann, D. M. (2017). An effective constitutive model for polycrystalline ferroelectric ceramics: Theoretical framework and numerical examples. *Computational Materials Science*, *136*, 223.

Taylor, G. (1985). *Piezoelectricity*. Gordon; Breach Science Publishers.

Thiele, A. A. (1970). Theory of the static stability of cylindrical domains in uniaxial platelets. *Journal of Applied Physics*, *41*(3), 1139 doi: 10.1063/1.1658846.

Tinte, S., Stachiotti, M. G., Sepliarsky, M., Migoni, R. L., & Rodriguez, C. O. (1999). Atomistic modelling of batio3 based on first-principles calculations. *Journal of Physics: Condensed Matter*, *11*(48), 9679.

Toda, M., Kubo, R., & Saitô, N. (1983). *Statistical physics i*. Springer, Berlin, Heidelberg.

Tolédano, P., Guennou, M., & Kreisel, J. (2014). Order-parameter symmetries of domain walls in ferroelectrics and ferroelastics. *Phys. Rev. B*, *89*, 134104.

Tomaszewski, P. E. (1992a). Structural phase transitions in crystals. i. database. *Phase Transitions*, *38*(3), 127.

Tomaszewski, P. E. (1992b). Structural phase transitions in crystals. ii. statistical analysis. *Phase Transitions*, *38*(3), 221.

Tonkov, E. I., & Tonkov, E. Y. (1992). *High pressure phase transformations: A handbook* (Vol. 2). CRC Press.

Trolier-McKinstry, S., Bassiri Gharb, N., & Damjanovic, D. (2006). Piezoelectric nonlinearity due to motion of 180 ° domain walls in ferroelectric materials at subcoercive fields: A dynamic poling model. *Applied Physics Letters*, *88*(20), 202901.

Tsou, N. T., Huber, J. E., & Cocks, A. C. F. (2013). Evolution of compatible laminate domain structures in ferroelectric single crystals. *Acta Materialia*, *61*(2), 670.

Tsou, N. T., Potnis, P. R., & Huber, J. E. (2011). Classification of laminate domain patterns in ferroelectrics. *Phys. Rev. B*, *83*, 184120.

Tsou, N., & Huber, J. (2010). Compatible domain structures and the poling of single crystal ferroelectrics. *Mechanics of Materials*, *42*(7), 740.

Tu, C.-S., Tsai, C. .-., Schmidt, V. H., Luo, H., & Yin, Z. (2001). Dielectric, hypersonic, and domain anomalies of $(PbMg_{1/3}Nb_{2/3}O_3)_{1-x}(PbTiO_3)_x$ single crystals. *Journal of Applied Physics*, *89*(12).

Tybell, T., Paruch, P., Giamarchi, T., & Triscone, J.-M. (2002). Domain wall creep in epitaxial ferroelectric $Pb(Zr_{0.2}Ti_{0.8})O_3$ thin films. *Physical review letters*, *89*(9), 097601.

Uchino, K. (2009). *Ferroelectric devices*. CRC Press.

Ueland, S. M., & Schuh, C. A. (2013). Grain boundary and triple junction constraints during martensitic transformation in shape memory alloys. *Journal of Applied Physics*, *114*(5), 053503.

Valasek, J. (1921). Piezo-electric and allied phenomena in rochelle salt. *Physical review*, *17*(4), 475.

Van Aken, B. B., Palstra, T. T. M., Filippetti, A., & Spaldin, N. A. (2004). The origin of ferroelectricity in magnetoelectric $YMnO_3$. *Nature Materials*, *3*(3), 164.

Vanderbilt, D. (1997). First-principles based modelling of ferroelectrics. *Current Opinion in Solid State and Materials Science*, *2*(6), 701.

Veithen, M., Gonze, X., & Ghosez, P. (2005). Nonlinear optical susceptibilities, raman efficiencies, and electro-optic tensors from first-principles density functional perturbation theory. *Phys. Rev. B*, *71*, 125107.

Vidyasagar, A., Tan, W., & Kochmann, D. (2017). Predicting the effective response of bulk polycrystalline ferroelectric ceramics via improved spectral phase field methods. *Journal of the Mechanics and Physics of Solids*, *106*, 133.

Viola, G., Boon Chong, K., Guiu, F., & John Reece, M. (2014). Role of internal field and exhaustion in ferroelectric switching. *Journal of Applied Physics*, *115*(3), 034106.

Völker, B., Marton, P., Elsässer, C., & Kamlah, M. (2011). Multiscale modeling for ferroelectric materials: A transition from the atomic level to phase-field modeling. *Continuum Mechanics and Thermodynamics*, *23*(5), 435.

Vopsaroiu, M., Blackburn, J., Cain, M. G., & Weaver, P. M. (2010). Thermally activated switching kinetics in second-order phase transition ferroelectrics. *Physical Review B*, *82*(2), 024109.

Wada, S., Yako, K., Yokoo, K., Kakemoto, H., & Tsurumi, T. (2006). Domain wall engineering in barium titanate single crystals for enhanced piezoelectric properties. *Ferroelectrics*, *334*(1), 17 doi: 10.1080/00150190600689647.

Waghmare, U., Sluiter, M. H. F., Kimura, T., Goto, T., & Kawazoe, Y. (2004). A lead-free high-tc ferroelectric $BaTi_2O_5$: A first-principles study. *Applied Physics Letters*, *84*(24), 4917.

Waghmare, U., & Rabe, K. (2005). Dielectric properties of simple and complex oxides from first principles. In A. A. Demkov & A. Navrotsky (Eds.), *Materials fundamentals of gate dielectrics* (pp. 215–247). Springer Netherlands.

Wang, J., Neaton, J. B., Zheng, H., Nagarajan, V., Ogale, S. B., Liu, B., Viehland, D., Vaithyanathan, V., Schlom, D. G., Waghmare, U. V., Spaldin, N. A., Rabe, K. M., Wuttig, M., & Ramesh, R. (2003). Epitaxial $BiFeO_3$ multiferroic thin film heterostructures. *Science*, *299*(5613), 1719.

Wang, J., & Kamlah, M. (2009). Three-dimensional finite element modeling of polarization switching in a ferroelectric single domain with an impermeable notch. *Smart Materials and Structures*, *18*(10), 104008.

Wang, J., Wu, P., Ma, X., & Chen, L. (2010). Temperature-pressure phase diagram and ferroelectric properties of $BaTiO_3$ single crystal based on a modified landau potential. *Journal of Applied Physics*, *108*(11), 114105.

Wang, S., Yi, M., & Xu, B.-X. (2016). A phase-field model of relaxor ferroelectrics based on random field theory. *International Journal of Solids and Structures*, *83*, 142.

Webber, K., Aulbach, E., Key, T., Marsilius, M., Granzow, T., & Rödel, J. (2009). Temperature-dependent ferroelastic switching of soft lead zirconate titanate. *Acta Materialia*, *57*(15), 4614.

Weng, G. J., & Wong, D. T. (2009). Thermodynamic driving force in ferroelectric crystals with a rank-2 laminated domain pattern, and a study of enhanced electrostriction. *Journal of the Mechanics and Physics of Solids*, *57*(3), 571.

Whyte, J. R., & Gregg, J. M. (2015). A diode for ferroelectric domain-wall motion. *Nature Communications*, *6*(1), 7361.

Wojnar, C. S., Le Graverend, J. B., & Kochmann, D. M. (2014). Broadband control of the viscoelasticity of ferroelectrics via domain switching. *Applied Physics Letters*, *105*(16), 1.

Woldman, A. Y., & Landis, C. M. (2016). Phase-field modeling of ferroelectric to paraelectric phase boundary structures in single-crystal barium titanate. *Smart Materials and Structures*, *25*(3), 035033.

Woldman, A. Y., & Landis, C. M. (2019). Thermo-electro-mechanical phase-field modeling of paraelectric to ferroelectric transitions. *International Journal of Solids and Structures*.

Woodward, D. I., Knudsen, J., & Reaney, I. M. (2005). Review of crystal and domain structures in the $PbZr_xTi_{1-x}O_3$ solid solution. *Phys. Rev. B*, *72*, 104110.

Xiao, Y., & Bhattacharya, K. (2008). A continuum theory of deformable, semiconducting ferroelectrics. *Archive for Rational Mechanics and Analysis*, *189*(1), 59.

Xiao, Y., Shenoy, V. B., & Bhattacharya, K. (2005). Depletion layers and domain walls in semiconducting ferroelectric thin films. *Phys. Rev. Lett.*, *95*, 247603.

Xu, T., & Wang, C.-A. (2015). Grain orientation and domain configuration in 3-1 type porous PZT ceramics with ultrahigh piezoelectric properties. *Journal of the American Ceramic Society*, *98*(9), 2700.

Yadav, A. K., Nelson, C. T., Hsu, S. L., Hong, Z., Clarkson, J. D., Schlepütz, C. M., Damodaran, A. R., Shafer, P., Arenholz, E., Dedon, L. R., Chen, D., Vishwanath, A., Minor, A. M., Chen, L. Q., Scott, J. F., Martin, L. W., & Ramesh, R. (2016). Observation of polar vortices in oxide superlattices. *Nature*, *530*(7589), 198.

Yang, J. (2006). *An introduction to the theory of piezoelectricity*. Springer US.

Yang, T., Gopalan, V., Swart, P., & Mohideen, U. (1999). Direct observation of pinning and bowing of a single ferroelectric domain wall. *Physical review letters*, *82*(20), 4106.

Yen, J., Shu, Y., Shieh, J., & Yeh, J. (2008). A study of electromechanical switching in ferroelectric single crystals. *Journal of the Mechanics and Physics of Solids*, *56*(6), 2117.

Yokota, H., Matsumoto, S., Salje, E. K. H., & Uesu, Y. (2019). Polar nature of domain boundaries in purely ferroelastic $Pb_3(PO_4)_2$ investigated by second harmonic generation microscopy. *Phys. Rev. B*, *100*, 024101.

Yokota, H., Usami, H., Haumont, R., Hicher, P., Kaneshiro, J., Salje, E. K. H., & Uesu, Y. (2014). Direct evidence of polar nature of ferroelastic twin boundaries in $CaTiO_3$ obtained by second harmonic generation microscope. *Phys. Rev. B*, *89*, 144109.

Zeng, T., Dong, X., Chen, S., & Yang, H. (2007). Processing and piezoelectric properties of porous PZT ceramics. *Ceramics International*, *33*(3), 395.

Zhang, Q., Wang, H., Kim, N., & Cross, L. (1994). Direct evaluation of domain-wall and intrinsic contributions to the dielectric and piezoelectric response and their temperature dependence on lead zirconate-titanate ceramics. *Journal of Applied Physics*, *75*(1), 454.

Zhang, W., & Bhattacharya, K. (2005). A computational model of ferroelectric domains. part i: Model formulation and domain switching. *Acta Materialia*, *53*(1), 185.

Zhang, Y., Roscow, J., Lewis, R., Khanbareh, H., Topolov, V. Y., Xie, M., & Bowen, C. R. (2018). Understanding the effect of porosity on the polarisation-field response of ferroelectric materials. *Acta Materialia*, *154*, 100.

Zhang, Y., Xie, M., Roscow, J., Bao, Y., Zhou, K., Zhang, D., & Bowen, C. R. (2017). Enhanced pyroelectric and piezoelectric properties of PZT with aligned porosity for energy harvesting applications. *J. Mater. Chem. A*, *5*, 6569.

Zhang, Z., Qi, X., & Duan, X. (2008). Two-step evolution mechanism of multi-domains in $BaTiO_3$ single crystal investigated by in situ transmission electron microscopy. *Scripta Materialia*, *58*(6), 441.

Zhang, Z., James, R. D., & Müller, S. (2009). Energy barriers and hysteresis in martensitic phase transformations. *Acta Materialia*, *57*(15), 4332.

Zhao, C., Gao, S., Yang, T., Scherer, M., Schultheiß, J., Meier, D., Tan, X., Kleebe, H.-J., Chen, L.-Q., Koruza, J., & Rödel, J. (2021). Precipitation hardening in ferroelectric ceramics. *Advanced Materials*, *33*(36), 2102421.

Zhong, W., Vanderbilt, D., & Rabe, K. M. (1994). Phase transitions in $BaTiO_3$ from first principles. *Phys. Rev. Lett.*, *73*, 1861.

Zhong, W., Vanderbilt, D., & Rabe, K. M. (1995). First-principles theory of ferroelectric phase transitions for perovskites: The case of $BaTiO_3$. *Phys. Rev. B*, *52*, 6301.

Zhou, D., Kamlah, M., & Munz, D. (2001). Rate dependence of soft PZT ceramics under electric field loading. *Proc. SPIE*, *4333*, 64.

Zhu, J., Wu, H., Wang, D., Gao, Y., Wang, H., Hao, Y., Yang, R., Zhang, T.-Y., & Wang, Y. (2017). Crystallographic analysis and phase field simulation of transformation plasticity in a multifunctional β-ti alloy. *International Journal of Plasticity*, *89*, 110.

Zhukov, S., Fedosov, S., Glaum, J., Granzow, T., Genenko, Y. A., & von Seggern, H. (2010). Effect of bipolar electric fatigue on polarization switching in lead-zirconate-titanate ceramics. *Journal of Applied Physics*, *108*(1), 014105.

Zuo, Y., Genenko, Y. A., Klein, A., Stein, P., & Xu, B. (2014). Domain wall stability in ferroelectrics with space charges. *Journal of Applied Physics*, *115*(8), 084110.

PUBLICATIONS

ARTICLES IN PEER-REVIEWED JOURNALS:

Indergand, R., Vidyasagar, A., Nadkarni, N., and Kochmann, D.M. (2020). "A phase-field approach to studying the temperature-dependent ferroelectric response of bulk polycrystalline PZT." *Journal of the Mechanics and Physics of Solids*, Vol. 144, 104098,
URL: https://doi.org/10.1016/j.jmps.2020.104098

Indergand, R. and Kochmann, D.M. (2021). "Effect of temperature on domain wall–pore interactions in lead zirconate titanate: A phase-field study." *Applied Physics Letters*, Vol. 119, 222901,
URL: https://doi.org/10.1063/5.0066612

Indergand, R., Bruant, X, and Kochmann, D.M. (2023). "Domain Pattern Formation in Tetragonal Ferroelectric Ceramics." *Under review.*

CONFERENCE CONTRIBUTIONS:

Indergand, R. and Kochmann, D.M. (2020). "The impact of temperature on the ferroelectric material response: A phase-field study of bulk polycrystalline PZT." Presentation at the *57th Society of Engineering Science (SES) Technical Meeting*, Minneapolis, USA (virtual).

Indergand, R. and Kochmann, D.M. (2021). "Finite-Temperature Phase-Field Simulations of Ferroelectric Ceramics: A New Statistical-Mechanics Based Approach." Presentation at the *14th Congress WCCM & ECCOMAS 2020*, Paris, France (virtual).

Indergand, R. and Kochmann, D.M. (2021). "Temperature-Dependent Domain Pattern Evolution in Ferroelectric Ceramics: A Phase-Field Investigation." Presentation and proceeding at the *25th International Congress of Theoretical and Applied Mechanics*, Milano, Italy (virtual).

Indergand, R. and Kochmann, D.M. (2022). "The Effect of Thermal Fluctuations on the Ferroelectric Microstructure." Presentation at the *21st GAMM Seminar on Microstructures*, Wien, Austria (virtual).

Indergand, R. and Kochmann, D.M. (2022). "Kinetics of Ferroelectric Ceramics: A large-scale phase-field study on bulk polycrystalline PZT." Presentation at the *15th World Congress on Computational Mechanics & 8th Asian Pacific Congress on Computational Mechanics*, Yokohama, Japan (virtual).